UNIVERSITY OF SOUTHAMPTON

Faculty of Natural and Environmental Sciences
School of Chemistry

High-Throughput Synthesis and Screening of Chalcogenide Thin Films for Phase-Change Memory

by

Jaffar Saleh Subaie

A thesis submitted in partial fulfilment
of the requirements for the degree of

Doctor of Philosophy

January 2017

UNIVERSITY OF SOUTHAMPTON

ABSTRACT

FACULTY OF NATURAL AND ENVIRONMENTAL SCIENCES

SCHOOL OF CHEMISTRY

Doctor of Philosophy

High-Throughput Synthesis and Screening of Chalcogenide Thin Films for Phase-Change Memory

by Jaffar Saleh Subaie

The limitations of Flash memory as an electronic storage medium have driven the development of new technologies. Amongst these, Phase-Change Random Access Memory (PCRAM) has emerged as a viable replacement for Flash due to its greater number of write cycles and faster write speeds. However, while phase-change materials have been known for over 50 years interest has only picked up over the past decade. This has created a gap in understanding of the structural and functional properties of these materials, which is only now being addressed one material at a time. The research presented here introduces a high-throughput (HT), combinatorial approach to the synthesis and screening of phase-change chalcogenide glasses. This approach focused on the screening of properties relevant to the use of chalcogenides as potential PCRAM materials. Starting with the seminal Ge:Sb:Te system, a HT workflow was developed that utilised Raman spectroscopy and X-ray diffraction to study the structure of both its amorphous and crystalline phases. The crystallisation temperature and electrical resistivity were chosen as pertinent functional properties to be evaluated under this approach. Using HT physical vapour deposition, thin film libraries of the largest reported Ge:Sb:Te compositional space were synthesised, covering the majority of the ternary space. HT software tools enabled the analysis of the film's structural evolution before and after crystallisation, revealing the formation of 5 distinct phases after annealing at 200 °C. These tools also facilitated the analysis of functional properties along six pseudobinary lines, four of which are novel to the literature. Specifically, the GeTe–Sb and GeSb–Te lines were most useful towards understanding the relationship between the structure and function in the Ge:Sb:Te system. The HT approach was applied to the less studied N-doped Ge:Sb:Te system, for which the most extensive compositional space yet was also synthesised. After annealing at 300 °C two types of materials, related to N-Sb_2Te_3 and N-$Ge_2Sb_2Te_5$, were identified through the first systematic Raman and XRD analyses of this system. Their functional properties were studied along pseudobinary lines and the results contrasted to those of Ge:Sb:Te. This led to the conclusion that N-Ge:Sb:Te materials would be more suitable for PCRAM use than Ge:Sb:Te in high temperature applications. A novel parametric testing platform, the Integrated Microelectrode Testing System (IMTS), was developed in order to characterise the electrical threshold switching field of both Ge:Sb:Te and N-Ge:Sb:Te materials, resulting in the first systematic analysis of this parameter on both systems. In the process, a model to calculate the dielectric constant of $Ge_2Sb_2Te_5$ using I-V data from the IMTS was derived. Overall, the results of these experiments established the validity of the high-throughput approach as a means to produce and evaluate phase-change chalcogenides more quickly and as reliably as traditional materials research techniques.

Contents

List of Figures

List of Tables

Declaration of Authorship

I, **Jaffar Saleh Subaie**, declare that this thesis and the work presented in it are my own and has been generated by me as the result of my own original research.

Thesis title: **High-Throughput Synthesis and Screening of Chalcogenide Thin Films for Phase Change Memory**.

I confirm that:

1. This work was done wholly or mainly while in candidature for a research degree at this University;
2. Where any part of this thesis has previously been submitted for a degree or any other qualification at this University or any other institution, this has been clearly stated;
3. Where I have consulted the published work of others, this is always clearly attributed;
4. Where I have quoted from the work of others, the source is always given. With the exception of such quotations, this thesis is entirely my own work;
5. I have acknowledged all main sources of help;
6. Where the thesis is based on work done by myself jointly with others, I have made clear exactly what was done by others and what I have contributed myself;
7. None of this work has been published before submission.

Signed: _____

Date: _____

Acknowledgements

In their study of acknowledgement sections in postgraduate dissertations Hyland and Tse[1] found that most tend to follow a three-move pattern consisting of the main thanking move framed by optional "reflecting" and "announcing" moves. Their study also serves as evidence that any subject is worthy of further enquiry provided that both funding and time are in supply. The present section will predictably follow this structure before proceeding to the main matter of this dissertation.

Ever since the dawn of the Modern Age humanity has accumulated knowledge derived from scientific endeavours at an increasingly accelerated rate. No longer can a single person like say, Aristotle or Newton in their time, master whole fields of knowledge in their entirety. As a result, narrow specialisation and the paradoxical quest to know as much as possible about as little as possible are necessary conditions to achieve scientific progress. Science as a process has thus become a collective effort where individuals with different specialisations lend their expertise to put "the big picture" together. A multidisciplinary research project like the one presented in this thesis would not have been accomplished without a similar effort, and the following paragraphs are an acknowledgement of this fact.

I sincerely thank my supervisor Prof Brian Hayden for his mentorship and near-infinite patience throughout my PhD project. I would not have been able to complete this project without his support, both academic and financial. I am also grateful to the Mexican Science and Technology Council (CONACyT) for sponsoring my research and stay at the University of Southampton.

Throughout the years I received invaluable help from the fine scientists at Ilika. In particular, I would like to express my deep gratitude to Dr Sam Guerin for sharing his high-throughput GST data, and Dr Chris Newman and James Barnett for their insight and help while putting together the PCRAM testing kit. I also appreciate the kind assistance of Drs Chris Vian and Louise Turner with matters related to the Paradise software. Conversations with Drs Alexandros Anastasopoulos, Owain Clark, John Davies, Sarah Frost, Dave Laughman, Claire Mormiche and Rob Noble helped me understand the intricacies of the various experimental

[1] Hyland, K.; Tse, P. *Int. J. Appl. Linguist.* **2004,** 14, 259–275.

techniques used in this thesis.

I am grateful to my colleagues at the Advanced Composite Materials Facility: Dr Jin Yao for making sputtered GST225 films; Dr Fiona McBride for sharing her knowledge of UHV systems and proofreading this work, may this serve as proof that the blood tributes to the PVD were not in vain; Jovine Emmanuel, Sandy Kerr and Fiona Rogers for their friendship and stimulating conversations; Carmen Villa García for her friendship, technical help and keeping me well fed while writing up.

Appreciation is given to Prof Dan Hewak and his research group for their collaboration in the field of glassy chalcogenides and for granting access to the ORC clean room and in particular to Dr Behrad Gholipour for his help with the fabrication of deposition masks.

I am deeply indebted to my mother Najieh and my siblings Faissal and Nabila for their love and encouragement. Thank you for being there for me even when I was not.

To all my friends, local and foreign, thank you for putting up with me during these long years. Aga, Alfredo, Bernie, Colin, León Guillermo, Jorge M. Jorge S. Karol, Kinga, Lupita, Marcela, Mayte, Melanie, Michi und Michi, Óscar, Sonia, Tasaffy, Tivadar, Yoana: Your friendship helped me retain the little sanity I still had before I decided to do a PhD.

Special thanks are owed to Dr Matthias Fenner of Keysight Technologies for his assistance with the AFM system. To the crew of the Mechanical Workshop: Alan, Rob and Constantin, who stoically kept complying with our lab's repairs and special requests. To Ron Leizrowice for being the best undergrad project student any postgraduate could wish for.

Finally, I cannot go on without mentioning AFM tip #7, for being nearly indestructible and taking more punishment and abuse than any tip is designed to endure.

Any intellectual errors or omissions in this thesis are entirely of my own making, and should not be blamed on the people who have kindly lent me their assistance these past few years.

Abbreviations and Acronyms

4PP ..... Four Point Probe

AFM ..... Atomic Force Microscope

AIMD ..... Ab Initio Molecular Dynamics

AIST ..... Silver Indium Antimony Telluride (Ag:In:Sb:Te)

BCE ..... Bottom contact electrode

BCT ..... Bond Constraint Theory

c-AFM ..... Conductive Atomic Force Microscopy

CD ..... Compact Disc

CG ..... Control Gate

CMOS ..... Complementary Metal Oxide Semiconductor

CPU ..... Central Processing Unit

CRN ..... Continuous Random Network

C-V ..... Capacitance-Voltage

DC ..... Direct Current

DFT ..... Density Functional Theory

DRAM ..... Dynamic Random Access Memory

DUT ..... Device Under Test

DVD ..... Digital Versatile Disc

EDS ..... Energy-dispersive X-ray Spectroscopy

E\PCOS ..... European Symposium on Phase Change and Ovonic Science

EXAFS ..... Extended X-ray Absorption Fine Structure

FCC ..... Face-centred Cubic

FeRAM ..... Ferroelectric Random Access Memory

FG ..... Floating Gate

GLS ..... Galium Lanthanum Sulfide (Ga:La:S)

GST ..... Germanium Antimony Telluride (Ge:Sb:Te)

HDD ..... Hard Disk Drive

HT ..... High-throughput

HTOMPT ..... High-throughput Optical Mapping of Phase Transitions

ICDD ..... International Centre for Diffraction Data

IMTS ..... Integrated Microelectrode Testing System

ITRS ..... International Technology Roadmap for Semiconductors

I-V ..... Current-Voltage

MBE ..... Molecular Beam Epitaxy

MLC ..... Multilevel Cell

MRAM ..... Magnetoresistive Random Access Memory

NVM ..... Non-volatile Memory

PCA ..... Principal Component Analysis

PCM ..... Phase-change Material

PCRAM ..... Phase-change Random Access Memory

PDF ..... Powder Diffraction File

PVD ..... Physical Vapour Deposition

RAM ..... Random Access Memory

RF ..... Radio Frequency

SEM ..... Scanning Electron Microscope

SMU ..... Source/Monitor Unit

SPGU ..... Semiconductor Pulse Generator Unit

SRAM ..... Static Random Access Memory

SSD ..... Solid State Drive

SSTOP ..... $Si/SiO_2/TiO_2/Pt$ substrate

STT-RAM ..... Spin-torque Transfer Random Access Memory

TEM ..... Transmission Electron Microscope

UHV ..... Ultra-high Vacuum

VAP ..... Valence Alternation Pair

XANES ..... X-ray Absorption Near-edge Spectroscopy

XAS ..... X-ray Absorption Spectroscopy

XPS ..... X-ray Photoelectron Spectroscopy

XRD ..... X-ray Diffraction

A mi mamá, por enseñarme a amar los libros.

Chapter 1

Introduction

1.1 Motivation

Consumer electronic devices such as personal computers, mobile phones, portable music players, digital cameras, e-readers, tablets and even smart watches are at the centre of the public's interaction with technology. From this interaction vast amounts of information are generated and accessed every day. For example, it has been estimated that in 2013 humanity generated or copied about 4,400 exabytes (10^{18} bytes) of digital data across all forms of media.[1] As devices become cheaper and more ubiquitous there will be an increasing demand for faster, more compact and reliable storage.

Current electronic devices use a combination of volatile and non-volatile memories (NVM) in their operation. Volatile memories such as Static Random Access Memory (SRAM, used in microprocessor cache) or Dynamic RAM (DRAM, used as the main operating memory in devices) cannot retain information for long after power has been switched off. On the other hand, NVM do retain information after power cut-off and are typically used as long-term storage in technologies like magnetic hard disk drives (HDD), optical disks, magnetic tape and Flash memory, amongst others.

As of the time of this writing, the predominant NVM media continue to be magnetic HDD. While these have high theoretical information densities (of up to 100 TB in^{-2}),[2] they suffer from a relatively high mechanical failure rate after prolonged use. HDD also have higher power consumption requirements and slower access times (3–5 ms)[3] than solid state drives (SSD) utilising NAND Flash, their nearest competitor technology.

In recent years Flash memory has become greatly popular in consumer devices due to increased information density and progressively lower cost. In particular, due to its circuit design NAND Flash allows for higher memory cell density and reduced manufacturing cost

compared to NOR Flash. Memory density in NAND Flash can be enhanced by designing multilevel cells (MLC), which can store multiple bits per cell. However, NAND Flash suffers from scaling issues like reduced data retention, as well as important physical limitations when attempting to produce memory cells smaller than 22 nm.[4] Even without these issues typical NAND flash devices currently in the market are rated for 10^5 write cycles[5] which limits their usefulness in high-capacity applications such as database servers.

Given the limitations of NAND Flash, several competing NVM alternatives are under investigation. These rely on a variety of physical principles in order to store information. A number of these technologies have been identified in the International Technology Roadmap for Semiconductors (ITRS), an industry initiative that assesses the state of semiconductor technology, as either *prototypical* or *emerging* RAM technologies as judged by the state of their development.[5] The prototypical memories will be discussed more thoroughly in Chapter 2. However, amongst them phase-change RAM (PCRAM) has become one of the most promising NVM under investigation and will be the subject of the present dissertation.

Over the past ten years the field of PCRAM research has seen a marked increase in activity. Figure 1.1 shows the results of a literature search for the term "Phase Change Memory OR Phase Change Chalcogenide OR PCRAM OR ovonic" using the Web of Science indexing service. It is evident that interest in this technology was renewed towards the end of the last decade and has remained consistent until the time of this writing. In addition to these research efforts, commercially there have been PCRAM chips used in consumer grade devices such as the GT-E2550 feature phones by Samsung[6] and Nokia's Asha smartphones.[7] However, despite this increased attention, most research and development has focused on the Ge:Sb:Te (GST) and Ag:In:Sb:Te (AIST) families of chalcogenides due to their successful implementation as phase-change materials (PCM) in optical storage discs.

Research into novel materials is affected by the classical limitations of materials preparation, whereby the chosen synthesis method, typically involving metal powder processing, sputtering or a form of reactive deposition, can only produce one stoichiometric composition at a time. This may result in extended development times while searching for the optimal composition for a given application, such as phase-change memory. High-throughput (HT) combinatorial synthesis methods like those developed by our group,[8] coupled with HT screening methodologies are intended to overcome these limitations and accelerate the discovery of the optimal composition of a given class of materials.

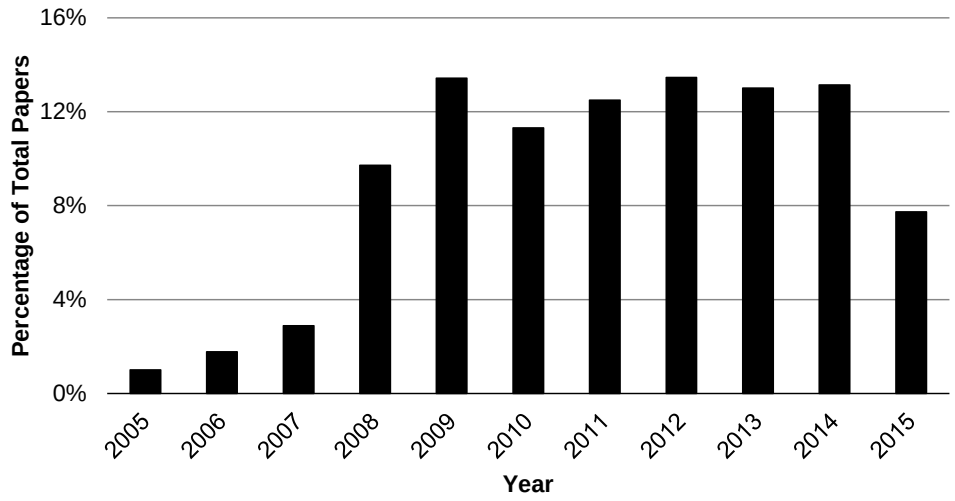

Figure 1.1: Number of publications per year as a percentage of the total for the 2005–2015 period as cited in Web of Science. Search included the terms "Phase Change Memory OR Phase Change Chalcogenide OR PCRAM OR ovonic" (n=6,849).

1.2 Project Aims

The aim of this project is to understand the relationship between the structural and functional properties of phase-change chalcogenides prepared as combinatorial thin films, with a specific focus on properties relevant for phase-change random access memory applications.

In order to achieve this aim, the following objectives have been set:

- Syntheses of combinatorial thin film libraries of phase-change chalcogenides using a high-throughput, physical vapour deposition (PVD) technique. In order to establish the validity of this technique, the nature of the materials in question must be well understood, thus allowing a comparison of results with existing literature. For these reasons, the seminal Ge:Sb:Te system has been chosen as the model material for this project. Energy-dispersive X-ray spectroscopy will be used to quantify the concentration of each element across the resulting combinatorial libraries.
- Structural characterisation using an array of high-throughput and traditional techniques. HT Raman spectroscopy will be used to probe the local order of the materials, while their long range order and structure will be characterised by HT X-ray diffraction. Atomic force microscopy (AFM) will be used to determine the thickness of the thin films and to characterise their surface at specific points of interest.

- Characterisation of primary functional properties relevant to PCRAM applications. Resistivity measurements will be done using a HT four point probe. Determination of the crystallisation temperature will take advantage of a novel technique for HT optical mapping of phase transitions developed by Ilika plc.
- Characterisation of secondary functional properties relevant to PCRAM applications. Specifically, threshold voltage will be measured using a novel parametric tester, developed in-house, that incorporates an AFM and a semiconductor device analyser. For this purpose, suitable memory test devices incorporating our combinatorial thin film libraries were also devised.
- Extension of the synthesis and characterisation methodologies outlined above to the N-doped Ge:Sb:Te system, which has been selected for its promising and not fully understood phase-change material properties.
- Understanding the logic behind the concept of pseudobinary lines, such as GeTe–Sb_2Te_3, commonly used in explaining the behaviour of phase-change materials by extending analysis to other pseudobinary lines like GeSb-Te and GeTe-SbTe, amongst others.

To enable the analysis of the large high-throughput datasets generated during the course of this project, the proprietary Paradise informatics suite developed by Ilika plc will be used.

1.3 Thesis Synopsis

The present chapter has already introduced the context and motivation behind this dissertation, as well as the overall aim of the project. In addition, the objectives required to achieve the aim have been outlined.

Chapter 2 gives a general background to electronic memory systems and the different memory types commercially available and under investigation. Then, the working principles behind optical and electrical phase-change memories are explained followed by a discussion of the structural and functional properties of chalcogenide glasses. Specific phase-change materials are also mentioned, including a detailed overview of the Ge:Sb:Te system, the effect of dopants and a discussion of some non-telluride chalcogenides. A brief overview of current computational techniques employed in the discovery and optimisation complements

the discussion on phase-change materials. The synthesis methods used to prepare these materials are summarised before moving on to an in-depth discussion of HT synthesis methods in materials science.

Chapter 3 details the experimental systems and techniques used in the synthesis and characterisation of combinatorial thin film libraries of phase-change chalcogenides. This chapter is divided into sections detailing the HT synthesis methodology (PVD, aided by EDS for composition determination), the structural characterisation techniques (XRD, Raman, AFM) and the functional characterisation methods (resistivity, crystallisation temperature, electrical parametric testing).

Chapters 4 to 6 provide the bulk of the experimental work carried out for this project and the results that were obtained. Chapter 4 focuses on the synthesis and characterisation of the undoped Ge:Sb:Te system. After discussing previous work carried out beyond compositions on the GeTe–Sb_2Te_3 pseudobinary, the synthesis of the high-throughput combinatorial libraries is detailed. This is followed by a systematic examination of the results of both sets of structural and functional characterisation experiments. A summary of the results in view of the project's objectives concludes the chapter. A similar treatment is given to the N-doped Ge:Sb:Te system in Chapter 5. Additionally, a comparison of the results obtained for both the doped and undoped Ge:Sb:Te systems may be found within this chapter.

Chapter 6 explains the core concepts underpinning the construction of PCRAM devices. This is followed by a short review on the use of conductive AFM to perform tests on memory devices. The bulk of the chapter is devoted to the development of a novel parametric tester that incorporates an AFM and a semiconductor device analyser. The Integrated Microelectrode Testing System is designed to operate as a full-fledged parametric testing platform dedicated to analyse PCRAM devices that incorporate the combinatorial thin film libraries syntesized by HT-PVD. The chapter concludes with a discussion of the results obtained using this system and a summary in view of the project's objectives.

The final chapter summarises and puts into context the results of this dissertation. Areas of further advancement and research deriving from this project are also suggested.

Chapter 2

Background

2.1 Memory Systems

Memory refers to the hardware devices used to store information for use in computer systems and therefore are fundamental to their operation. The current design of memory devices is the result of the von Neumann computer architecture originally described in 1945.[9] In the modern usage, this model has come to describe a computer where both the code and data are stored in memory. Information may be transferred between the memory and other system components, such as the central processing unit (CPU) and input/output devices, via a shared system bus. This arrangement is illustrated schematically in Figure 2.1.

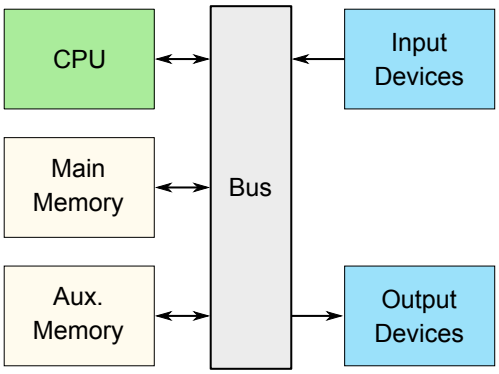

Figure 2.1: Schematic representation of the von Neumann computer architecture.

The main limitation of the von Neumann architecture arises from the fact that the shared bus has a limited data throughput between the CPU and memory. Because of the shared bus, fetching instructions from the CPU and performing data operations in memory cannot happen simultaneously. As a result, data throughput is typically lower than the rate at which the CPU can work. This is known as *the von Neumann bottleneck* and was first described by John Backus in 1978 during his Turing Award lecture.[10]

At any point during processing there could be a request for an instruction or datum stored

in the memory. In practical terms, there is no requirement for data to be located in special proximity to the code that interprets it, or that two sequential code instructions be stored next to each other. Therefore, the memory system must be able to deal with random access requests in a way that does not favour any particular request. On top of this, memory may be required to fulfil multiple, often competing, requirements such as latency, longevity, energy use, and cost. To date no single technology exists that could provide every single desired characteristic (often referred to as *universal memory* in the literature).[11] A memory hierarchy[12] thus arises where multiple types of memory are designed to accomplish different roles:

- *Main memory* is only directly accessible by the CPU, and is designed to offer nano- or pico-second latency, high bandwidth and have low energy requirements (nJ or lower). Main memory is volatile and requires a constant power input to maintain the store information. SRAM and DRAM are the representative technologies of this type of memory.
- *Auxiliary memory* can only be accessed indirectly by the CPU via input/output channels. Being non-volatile, this memory provides long-term storage at low cost per megabyte compared to main memory. However, it has millisecond latency, comparatively low bandwidth and energy requirements in the order of mJ. As discussed in Chapter 1, magnetic HDDs and NAND Flash drives are the predominant NVM technologies.

In addition to the above classification the ITRS provides a simple taxonomy of different memory technologies, which is reproduced in Figure 2.2. At the highest level, memories are separated by their ability to store data without power (i.e. volatile or not). Non-volatile memories are further divided into *baseline* (i.e. flash-type memory, due to its maturity), *prototypical* (which are mature enough to be commercially available) and *emerging* (which are the least mature but have shown to have significant potential as memory devices). The following discussion will be focused on the prototypical NVM technologies since PCRAM, the subject of this thesis, is found within this classification.

2.2 Prototypical Non-volatile Memories

There are several NVM technologies which have been proposed as being capable of replacing HDDs. In the interest of brevity, the discussion here will be limited to those technologies

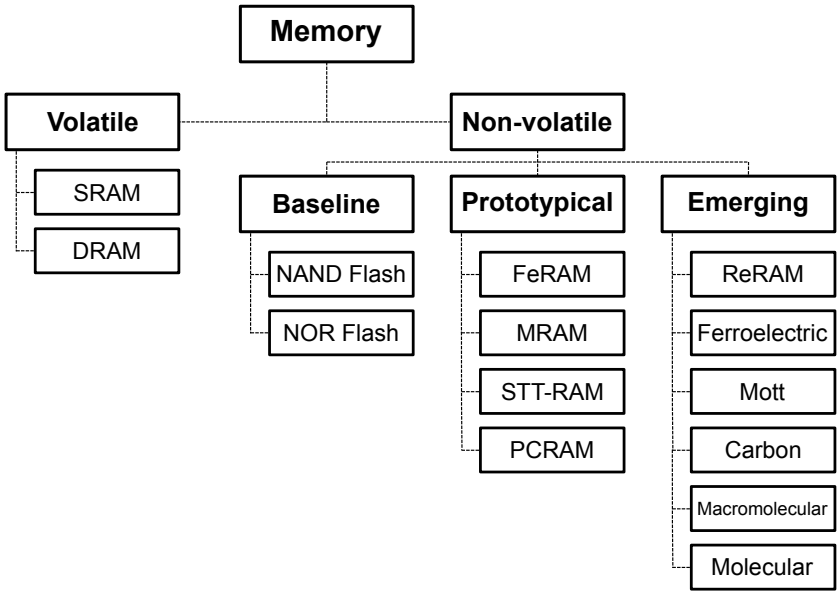

Figure 2.2: Memory taxonomy as defined by the ITRS. Note that emerging ferroelectric memory is distinct from capacitor-based FeRAM. Adapted from the 2013 ITRS report.[5]

identified as *prototypical* by the ITRS. These are ferroelectric RAM (FeRAM), magnetoresistive RAM (MRAM), spin-torque transfer RAM (STT-RAM) and phase-change RAM (PCRAM).

A useful metric to compare the memory density of devices produced using lithographic processes is the minimum feature size F. Also known as the critical dimension, F represents the overall resolution that can be consistently achieved under manufacturing conditions. It is defined as follows for a given lithographic node with a minimum pitch P:[13]

$$F = \frac{P}{2} \tag{2.1}$$

The fundamental building block of a memory device is the memory cell. It is an electronic circuit which stores one bit of information that can be set to a binary 1 (SET state) or binary 0 (RESET state). The area of an individual cell (A) is given by the square of the feature size (F^2) times the cell area factor (x), which describes the number of features needed to make the cell:

$$A = xF^2 \tag{2.2}$$

Thus, for example, in a $4F^2$ cell in a lithography process with $F = 45\,\text{nm}$ the density of the resulting memory is equal to 1.2×10^{10} cells/cm^2.

FeRAM: Ferroelectric materials such as lead zirconate titanate, $\text{Pb}(\text{Zr}_x\text{Ti}_{1-x})\text{O}$, form ferroelectric capacitors when placed between two metallic electrodes. These capacitors are char-

acterized by the presence of two stable polarization states that can be reversed when a field higher than the coercive field is applied. FeRAM devices have relatively high memory densities (currently $22F^2$),[5] offer low latency and have low power requirements. However, a few disadvantages preclude their use as a replacement to flash memory. The most important limitation arises from the destructive nature of the memory access process, which requires a retracing of the hysteresis loop of the ferroelectric capacitor. As a result, a rewrite cycle is required after each read thus doubling the memory access time while halving cycle endurance. In addition, ferroelectric materials can be degraded by conventional fabrication procedures for complementary metal oxide semiconductors (CMOS), which limits their integration into existing assembly lines. Finally, FeRAM devices lack MLC capability.[2] These characteristics make FeRAM more suitable for embedded[14] applications such as smart cards.

MRAM: The basic structure of an MRAM device consists of a magnetic tunnel junction (MTJ) comprising two ferromagnetic layers separated by a dielectric layer. When the magnetic moment of the dynamic layer is switched using a magnetic field to either align or oppose the magnetic moment of the fixed layer, the resistance to current flow through the MTJ changes. Thus the magnitude of the tunnelling current can be used to differentiate between memory states. Due to their principle of operation MRAM devices could, in principle, be cycled indefinitely and have fast writing speeds. However, producing a magnetic field within integrated circuits is an inherently inefficient process which results in higher writing currents as the memory cell size decreases.[15] Therefore it is expected that MRAM operating under field-induced switching will not see major improvements beyond the current state of the art.[5]

STT-RAM: Also considered a sub-type of MRAM, this memory has been proposed as an alternative approach to induce polarity reversal in a magnetic layer without the introduction of an external magnetic field.[16] This is achieved by running a spin-polarized electron current through the MTJ that transfers angular momentum to the spins of the electrons in the dynamic layer, causing them to switch orientation. Through this process cell sizes for STT-RAM devices can be reduced significantly (from $51F^2$ of conventional MRAM down to $28F^2$ as per the current state of the art).[5] In addition, it may be possible to extend the MLC capability of this technology to 4 bits per cell.[17] However, this scaling may subject the memory cells to thermal noise and novel technological solutions to overcome this problem, such as perpendicular magnetization using CMOS, are being investigated.[18]

PCRAM: These devices take advantage of the resistivity difference between the amorphous and crystalline phases of chalcogenide glasses (particularly Ge:Sb:Te alloys) to store data in different memory states. The amorphous phase has high electrical resistance, whereas the crystalline state has low electrical resistance. Currently manufactured PCRAM devices have high memory densities ($4F^2$), but suffer from slow writing times (typically ~100 ns).[5] Another challenge to overcome is the high current required to return the cell to an amorphous state. Since PCRAM is a highly scalable technology,[19] it is expected that these issues will be easier to address as the volume of phase-change material per memory cell decreases. It can also be incorporated into MLC thus increasing memory density.[20] As such, PCRAM is one of the most promising NVM technologies and will be the focus of the work described in this thesis.

Table 2.1 offers an overview of the state of the art as of 2013 for the prototypical NVMs by presenting the comparison of some key operational parameters. A comparison is also given to SRAM, DRAM and NAND flash for informational purposes.

Table 2.1: Comparison of several volatile and non-volatile memory technologies. Adapted from Table ERD3 found in the 2013 ITRS report.[5]

	DRAM	**SRAM**	**NAND Flash**	**FeRAM**	**STT-RAM**	**PCRAM**
Cell Area	$6F^2$	$140F^2$	$4F^2$	$22F^2$	$20F^2$	$4F^2$
Read Time	< 10 ns	0.2 ns	0.1 ms	40 ns	35 ns	12 ns
Write/Erase Time	< 10 ns	0.2 ns	1/0.1 ms	65 ns	35 ns	100 ns
Retention Time	64 ms	4 ms	10 yr	10 yr	> 10 yr	> 10 yr
Write Cycles	$> 1 \times 10^{16}$	$> 1 \times 10^{16}$	1×10^5	1×10^{14}	$> 1 \times 10^{12}$	1×10^9
Write Voltage (V)	2.5	1	15–20	1.3–3.3	1.8	3
Read Voltage (V)	1.8	0.7	4.5	1.3–3.3	1.8	1.2

2.2.1 Flash Memory

The prototypical memory types described above are regularly compared against the performance of flash memory, the current baseline technology. Flash memory was invented by Fujio Masuoka[21] during his tenure at Toshiba in the 1980s and has been the object of

sustained research and development ever since.

In this type of memory, information is stored in an array of memory cells made from floating-gate transistors, each storing a single bit of information. The transistor contains a control gate (CG) on top of an electrically insulated floating gate (FG). When the FG is charged, the electrons screen the electric field from the CG resulting in an increased threshold voltage in the cell (V_{T1}). Due to the insulation of the FG, electrons are trapped within until an applied electrical field induces their removal. As a result the voltage of this field (V_{T2}) must be higher than V_{T1}. For a read operation, a voltage V_R is applied to the CG whereby $V_{T1} < V_R < V_{T2}$. If the channel is found to be conductive then the FG would be uncharged (not containing an electron) and thus in binary 1 state. Alternatively, if the channel is non-conductive then the FG must be charged and therefore in binary 0 state.

The two types of flash memory currently in use are named after the logic gates their memory cells resemble: NOR and NAND. In NOR flash the memory cells can be addressed individually because they are connected to each other in parallel, whereas NAND cells are connected in series and can only be addressed as blocks. As a result, the area of NOR cells is much larger than NAND cells ($10F^2$ compared to $4F^2$) but are better suited for random data access albeit at a slow read/write speed. On the other hand NAND cells allow for higher memory densities and their performance is higher when working with file or sequential data, but still suffer from slow random data access. For these reasons, NOR flash has seen most adoption in embedded applications where program code rarely needs to be updated, whereas NAND flash is commonly found in mass-storage devices where data may be updated on a regular basis.

2.3 Phase-Change Memory

Having covered the different types of NVM used in electronic systems attention will now turn to phase-change memory. The following sections will present an overview of the history, mode of operation and general properties of the materials used in both optical and electrical phase-change storage media.

2.3.1 History

The principle of reversible switching between the crystalline and amorphous phases of chalcogenides (in particular $Te_{48}As_{30}Si_{12}Ge_{10}$) and their potential use as a memory storage mechanism was identified by Ovshinsky in the 1960s.[22,23] During this timeframe Pearson *et al.* at Bell Labs identified the current-voltage characteristics of As-Te-I glass[24] but did not attempt to explain or exploit them for practical applications. The viability of phase-change devices was further demonstrated by Sie through the incorporation of the chalcogenide material into a diode array.[25] This included investigation of the switching mechanism during which the phenomenon of current-induced filament growth across a thin film of chalcogenide material was first observed.[26,27]

Shanefield was tasked with the development of a phase-change memory device for the International Telephone & Telegraph after licensing one of Ovshinsky's patents. Shanefield performed the first composition optimization of the chalcogenide layer of the memory and identified in a patent[28] three compositions that showed the most desirable switching characteristics: $Te_{60}As_{20}Se_{20}$, $Te_{70}As_{20}Se_{10}$ and $Te_{70}As_{10}Se_{20}$. Further research into PCRAM devices took place during the earlier part of the 1970s, with devices of capacities up to 1024 bits being demonstrated.[29] Soon after, however, interest in this area waned due to the much greater energy requirements of PCRAM compared to other contemporaneous memories.

Also in the 1970s research on phase-change optical data storage was underway. It was soon discovered that reversible phase transitions between an amorphous and a crystalline phase could be triggered by short laser pulses in a material $Te_{81}Ge_{15}Sb_2S_2$.[30] Chen *et al.* demonstrated in 1985 the optical reversibility of a $Te_{87}Ge_8Sn_5$ film where the process was not limited by phase segregation but by the laser ablation process itself.[31] A year later while studying the $Te_{1-x}Ge_x$ system it was found that films made of either Te or GeTe could be crystallized using laser pulses of less than 100 ns.[32] Towards the end of the 1980s optical storage based on chalcogenide phase-change technology was first developed by Ohta *et al.* at Matsushita.[33] The writing layer of these discs comprised materials within the Sb_2Te_3–GeTe–Sb pseudo-ternary compositional space that were observed to crystallise into a cubic phase using a laser pulse less than 100 ns long. In 1991 Yamada *et al.* found that materials along the GeTe–Sb_2Te_3 pseudobinary line, particularly the $GeSb_2Te_4$ and $Ge_2Sb_2Te_5$ compositions, had a large optical contrast between the amorphous and crystalline phases and could be

switched with pulses less than 50 ns long, thus making them good candidate materials for optical storage.[34] Finally, Iwasaki *et al.* proposed the $Ag_{11}In_{11}Sb_{55}Te_{23}$ (AIST) system as a material for rewritable discs.[35]

With the advent of sub-micrometre lithographic processes in the 1990s the energy requirements to switch a much smaller PCRAM cell became comparable to competitor memories. In 1999 a company called Ovonyx arose from a partnership between Ovshinsky and semiconductor memory experts Lowrey and Parkinson. By the early 2000s a series of licensing agreements and investments between Ovonyx and other industrial partners such as BAE Systems, Intel and STMicroelectronics resulted in the development of the first viable PCRAM chips for modern computer systems. In 2005, an analysis[36] of over 500 United States patents issued between 1966 and 2004 concluded that the field of PCRAM was undergoing a period of extreme growth and, as may be concluded from Figure 1.1, that interest remains high to this day. While the most recent developments on PCRAM devices are usually closely-guarded trade secrets due to fierce competition, from time to time manufacturers offer a glimpse of their current state of the art in public forums; one such case being the 8 GB PCRAM chip developed by Samsung in 2012.[6] The 3D XPoint™ technology, developed by Intel Corporation and Micron Technology in 2015, is a new type of low-latency solid state memory widely rumoured to be based on PCRAM.[37] Finally, the European Symposium on Phase Change and Ovonic Science (E\PCOS) established in 2001 and modelled after its older Japanese counterpart has served as a forum for sharing both academic and industrial research into PCRAM technologies.

Recently other applications of PCMs have been considered, including their use in photonic multilevel NVM,[38] neural network computing,[39] logic devices[40] and flexible displays.[41] The use of these materials in such broad applications opens the way to produce a class of devices that would be both optically and electrically active, and could eventually be more efficient than their CMOS-based counterparts.

2.3.2 Optical Phase-Change Memory

Optical phase change is the principle of operation behind rewritable optical storage discs such CD-RW, DVD-RAM, DVD±RW and recordable Blu-ray discs. In these devices the recording layer consists of a thin film of PCMs. Recording and erasing can be achieved by heating

the recording layer with laser pulses of varying intensity to switch between amorphous and crystalline phases. Reproduction of the stored information takes advantage of the large difference in refractive index between these two phases.

Before any data is recorded on an as-deposited amorphous phase-change thin film the material is typically initialised (i.e. crystallised). During recording, the amorphous state is achieved by irradiating the recording layer with a laser with enough power to take the material above its melting temperature T_m. The material is then quenched by rapidly removing the heat source. During the melting process the atoms in the phase-change layer are found in a disordered state, and the rapid cooling rate of the material during the quench prevents the formation of an ordered, crystalline structure. Therefore, spots of amorphous material are formed on the recording layer. To achieve crystallisation a medium power laser pulse anneals the material at a temperature below T_m but above the crystallisation temperature T_x. This allows the atoms in the material to rearrange into an ordered structure. A lower intensity reading pulse leaves the material undisturbed but is strong enough to detect the 30 % reflectivity contrast between the amorphous and crystalline phases. The profile of these laser pulses is similar to the electrical pulses used to switch PCRAM, which are shown in Figure 2.3.

Optical disc drives utilise a semiconductor laser to read and write data. The laser beam is collimated, passed through a beam splitter and quarter-wave plate. It is then delivered to an objective lens that focuses it onto the recording layer, and the reflected beam is detected by a photodiode. The spot size of the focused laser beam (ϕ) is modelled by the equation:

$$\phi = \frac{\lambda}{2NA} \tag{2.3}$$

where λ is the laser wavelength and NA is the numerical aperture of the lens.[42] Combinations of these parameters as used in modern optical media systems are detailed in Table 2.2. As a general rule the shorter the laser wavelength is, the higher the recording and storage capacity of the disc. Higher storage densities can be achieved by adding multiple recording layers to the discs, as is the case in double-layer DVDs or four-layered Blu-ray discs.

Table 2.2: Optical parameters and storage capacities of commercial optical storage discs.

Disc	Wavelength (nm)	NA	Spot size (µm)	Storage capacity (GB)	Release year
CD	780	0.45	1.0	0.7 – 0.9	1982
DVD	640	0.60	0.6	4.7 – 17	1996
Blu-ray	405	0.85	0.3	25 – 128	2003

2.3.3 Electrical Phase-Change Memory

As outlined in section 2.2 PCRAM operates on the principle of resistivity contrast between the amorphous and crystalline states of a chalcogenide material. The crystalline phase is known as the SET state and has low resistivity. On the other hand, the amorphous phase is highly resistive and is known as the RESET state. As fabricated, PCRAM devices come preprogrammed in the SET state due to the high temperatures generated during their production.

In order to switch a PCRAM cell an electrical pulse must be applied. This pulse will dissipate power into the material as per the following equation:

$$P = VI = I^2R \tag{2.4}$$

where P is the dissipated power, V is the applied potential, I is the electric current and R is the resistance of the material. For a crystalline material the value of R will be low and thus a large current would be necessary to melt it. This would require a very high voltage, short duration, RESET pulse that would melt the material and allow it to quench rapidly, thus returning it to the amorphous state. Conversely, for an amorphous material the resistance would be high, thus requiring a lower current to crystallise. A SET pulse would only need to be of medium voltage intensity (compared to the RESET pulse) but of longer duration. This pulse would take the material above its crystallisation temperature, but below its melting point. Finally, a memory cell can be read by passing a current small enough not to disturb its state, but sufficiently large to measure the resistivity of the material. A summary of the pulses just described can be seen in Figure 2.3.

The electrical switch to the SET state depends on the threshold switching effect that takes place at the threshold voltage (V_{th}). While V_{th} is commonly discussed in the literature, it

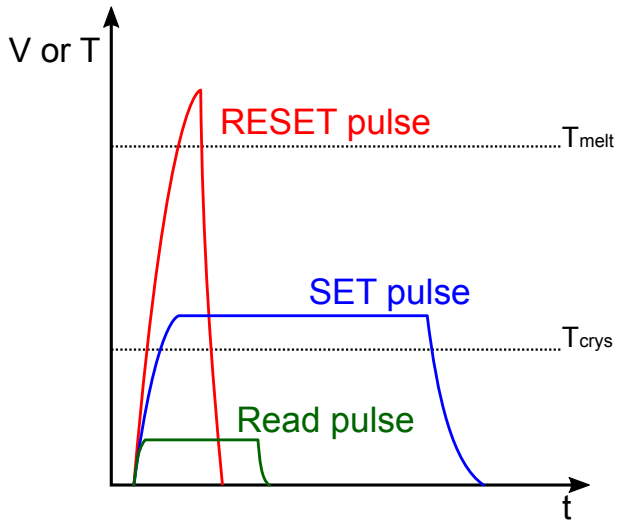

Figure 2.3: Diagram of the pulses applied to program and read a PCRAM memory cell. T_{melt} is the temperature required to melt the material, achieved with an high amplitude pulse of short duration. T_{crys} is the temperature necessary for crystallisation, achieved with a middle amplitude pulse of longer duration than the RESET pulse.

has been demonstrated that the critical parameter to understand switching behaviour of a device is the applied electrical field.[43] This is because V_{th} tends to increase linearly with the thickness of the material.[44] Regardless, at this voltage the RESET state stops behaving as per Ohm's law and shows a negative differential resistance. Threshold switching is reversible if the voltage is removed at this point, in which case the material will return to the amorphous, high-resistance state. However, if a voltage continues to be applied for longer than the crystallisation time, the supplied current will create a crystalline filament in the material and memory switching to the SET state occurs. Once this has taken place the current can be withdrawn from the device and the filament will not return to the amorphous state without application of a RESET pulse. This switching process is highly repeatable; as shown in Table 2.1, the current state of the art in PCRAM devices uses materials that can retain information for 10^{11} cycles.[45] Figure 2.4 shows idealised current-voltage (I-V) characteristic for a PCM exhibiting threshold voltage operating in both states.

The physical processes at work during threshold switching are not fully understood and several mechanisms have been proposed:

- The thermal instability model proposes threshold switching occurs through thermal runaway caused by Joule heating of the material. However, it was rapidly recognised

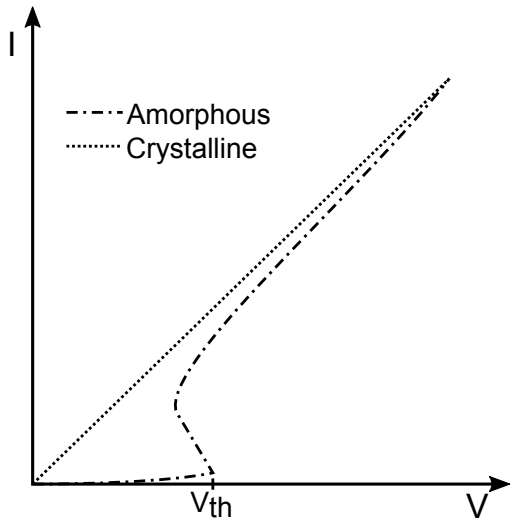

Figure 2.4: Idealised I-V characteristic for the amorphous and crystalline states of a PCRAM cell. Threshold switching behaviour occurs at the threshold voltage (V_{th}). The amorphous RESET state retains high-resistance below V_{th}, and switches to the crystalline low-resistance SET state if a voltage continues to be applied beyond this point.

that a purely thermal mechanism was insufficient to account for this phenomenon.[46] This is because the thermal time constant is slower than the typical threshold switching speed of a device. However, this model seems to hold true when dealing with thick films of material, as the contribution of the electric field towards switching is smaller.

- An electronic model posits that threshold switching takes place after carrier traps in the material become filled due to field-induced carrier generation.[47] This model also demonstrated quantitatively that heating is not essential for switching to occur.
- A crystallisation based-model proposes the origin of switching on the formation of crystalline nuclei facilitated by the electric field. The reversible nature of the switch would be explained by the breakdown of the nuclei upon removal of the field.[48] However this model would fail to account for switching in materials were crystallisation is a growth-dominated mechanism.

Bogoslovski and Tsendin in their review of switching effects in chalcogenide glasses[49] proposed that the most likely threshold mechanism is an electronic model where the charge traps become ionised by the electric field and Joule heating. However, full experimental validation of these models has not been achieved to date and it is likely that the dominant mechanism would be dependent on the PCM itself.

2.3.3.1 Properties of Materials for Phase-Change Memory

One of the characteristics of chalcogenide materials is their ability to threshold switch. Even though this property has been known since the 1910s (Waterman made a series of related observations on the conductivity of MoS_2 salts[50,51]) it was only in the 1980s when materials along the GeTe–Sb_2Te_3 pseudo-binary line were found to fulfil many of the requirements for reliable phase-change storage. Among these properties are rapid and repeated switching, as well high optical contrast between phases,[52] as discussed in section 2.3.2, which has also motivated the investigation of non-volatile photonic PCRAM.[38] The viability of optical phase-change memory generated an interest to apply this technology to PCRAM and research efforts to optimise PCMs are underway.[53,54]

In addition to the aforementioned material properties, there are several others that influence device performance, summarised in Table 2.3. The seemingly contradictory nature of some of these properties highlights the challenges faced during PCM design. Therefore, it is likely that materials will have to be optimised according to specific device requirements.[55] The discovery and optimisation process of PCMs may be accelerated through the use of high-throughput, combinatorial synthesis and characterisation methods, such as those described throughout this thesis.

2.4 Chalcogenide Glasses and their Properties

Phase-change memory relies on the use of chalcogenide materials as the switchable layer of the memory cell. Some of these chalcogenides can solidify into an amorphous, vitreous state whose properties have been found to be useful in phase-change memory applications. The following sections will provide an introduction to chalcogenide glasses and their properties. Sections 2.5 and 2.6 will then discuss the properties of specific chalcogenides used in PCRAM, of which the Ge:Sb:Te is the better characterised system to date.

2.4.1 Chalcogenides

Etymologically, the term chalcogenide derives from the Greek words *khalkós* (“copper”, but later by association, “ore”) and *-genés* (“producer of”), therefore meaning *ore former*.[56]

Table 2.3: List of PCM properties and their impact on PCRAM devices. Table adapted from Wuttig and Raoux.[55]

Property	Desired Value	Impact on PCRAM
Melting temperature	Low	Reset current will be lower for low melting point materials
Crystallisation temp.	Relatively high	Improved data retention
Thermal conductivity	Low	Better heat confinement, reduced switching currents
Crystallisation activation energy	High	Improved data retention
Resistance (crystalline)	Relatively high	Reduced RESET current, improved cyclability
Resistance (amorphous)	Relatively high	Increased SET/RESET ratio, improved cyclability
Resistance levels	Stable and multiple	Reduced resistance drift and MLC operation possible
Crystallisation speed	High	Data writing rate increased
Threshold switching field	Depends on cell size	Increased for smaller cells to avoid cell switching with reading pulse
Chemical stability	High	Increased cycle numbers without elemental segregation

Chalcogenides are the elements found in Group 16 of the periodic table (O, S, Se, Te, Po and Lv). Oxides tend not to have the desirable properties for use in phase-change memory, with the notable exception of VO_2,[57] and are generally treated as a distinct class of materials. Of the remaining chalcogenides, polonium is too radioactive and livermorium too short-lived to be of use. Therefore, only sulphur, selenium and tellurium are considered in phase-change memory material discussions.

Chalcogenides are glass-forming materials, of which the most recognised example is silicon dioxide.[58] Most oxide glasses are insulators due to the wide gap between their conduction and valence bands, which is typically around 10 eV. However, the other chalcogenides form glasses which normally have small band gaps (1–3 eV), thus making them semiconductive.[59]

Chalcogenide ores and materials can be found in either crystalline or vitreous states. For non-glass-forming compositions, it is possible to induce glass formation by alloying with a third element. Binary, glass-forming chalcogenides can be considered analogous to SiO_2, whereby two chalcogenide atoms are bound to a single Group 14 atom. Another class of chalcogenide glasses involves three chalcogenide atoms bound to two Group 15 atoms. Most stable binary chalcogenides belong to these two classes. A review by Elliott has compared the typical properties of these different chalcogenide classes.[59] Furthermore, ternary and more complex chalcogenides may be prepared by alloying materials with any other elements, although the alloying capacity of these glasses may be limited.[60]

2.4.2 Glass Formation and Crystallisation

Typically, a melt of material will form a crystalline solid if the temperature is taken below the melting temperature T_m. However, a material can bypass the crystallisation process if the melt is cooled down at a fast rate (i.e. it is quenched or supercooled) down to the glass-transition temperature T_g and instead "freezes" into a disordered, glassy state. Typically, T_g is defined as temperature at which the viscosity of the material (η) is equal to 10^{12} Pa s.[54] It is important to note that while all glasses are amorphous materials, not all amorphous materials show a glass transition. Figure 2.5 shows a schematic representation of the crystallisation and glass-formation dynamics as a function of volume/entropy.

Thermodynamically, crystallisation is a first-order phase transition process characterised by the discontinuity of parameters such as volume and entropy. These discontinuities are not seen during glass formation because the process does not involve any latent heat, and should instead be considered a second-order phase transition. This is due to the observed discontinuity in the first derivatives of volume and entropy with respect to temperature (i.e. heat capacity and the thermal expansion coefficient). Due to the lack of volume or entropy changes the glassy state is metastable with a free energy dependent on the cooling rate. As a result, slight changes in T_g may be observed at different cooling rates.[61] Several

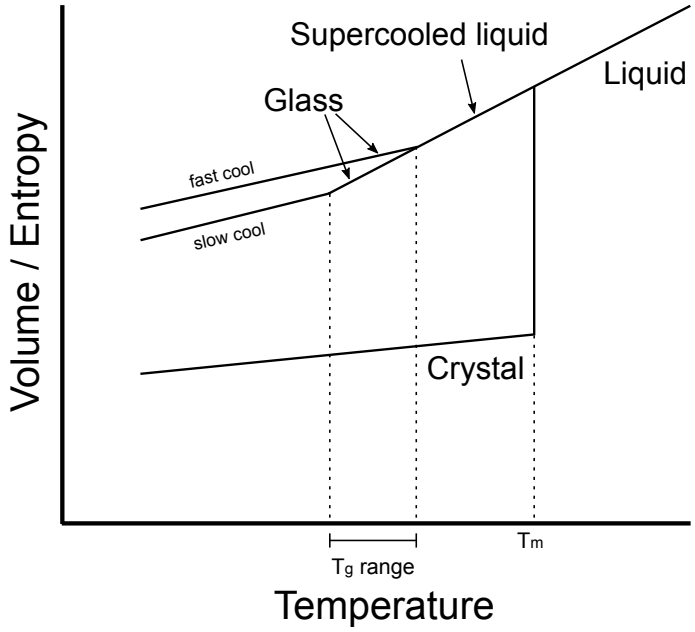

Figure 2.5: Scheme of the glass-formation and crystallisation dynamics in a melt cooled at different rates.

thermodynamic models have been put forward to explain the glass-formation mechanism, such as the configurational entropy model,[62] the free volume model,[63] the potential barrier model[64] and the bond lattice model.[65]

The relationship between T_g and T_m is defined as the reduced glass-transition temperature (T_{rg}) for glass forming materials as given by

$$T_{rg} = \frac{T_g}{T_m} \tag{2.5}$$

which can be between 0.4 and 0.85 for any glass forming composition.[66] Good glass forming materials have $T_{rg} \geq 0.7$. Following this definition, chalcogenide compounds containing S and Se are considered good glass formers; this is due to their ability to form glasses at cooling rates as low as a few degrees per second. On the other hand, Te chalcogenides require extreme cooling rates (in the order of $10^8\,\mathrm{K\,s^{-1}}$) and are considered poor glass formers.[42] Telluride glasses typically used in PCRAM have T_{rg} values between 0.45 and 0.55.[66]

Crystallisation of a chalcogenide melt is thermodynamically allowed once its temperature drops below T_m but above T_g; at this point the free energy difference favours the formation of the crystalline phase. Moreover, at T_m both the crystalline and liquid phases can coexist. Crystallisation is slow at temperatures close to T_m due to increased atomic mobility despite

there being a sufficient free energy for nucleation sites to form. At the other end of the scale, the crystallisation process is also slow at temperatures close to but above T_g due to increasingly constrained atomic movement. Therefore, the highest crystallisation rates happen at temperatures between T_m and T_g. It has been demonstrated that the rate of nucleation is inversely related to T_{rg}, as seen in good glass-forming materials ($T_{rg} \geq 0.7$) where the nucleation rate is slow.[67] As would be expected, PCMs with low T_{rg} values exhibit fast (<100 ns)[52] and even ultrafast (<1 ns)[68] recrystallisation rates as demonstrated for various Ge:Sb:Te (GST) alloys. Evidence suggests that a further contribution to this behaviour would be a low interfacial energy between the amorphous environment and the crystalline nuclei.[69] This has been argued by Lee and Elliott, using an *ab initio* molecular dynamics model (AIMD), to be due to the formation of ordered planar structures in the amorphous phase of GST.[70]

The mechanism of crystal formation is an important consideration, since nucleation time can potentially be orders of magnitude longer than the crystallisation time.[71] In the context of PCMs, two relevant mechanisms have been identified: Nucleation-dominated and growth-dominated. In a nucleation-dominated material, the majority of the crystallisation time is taken by the formation of crystallite nuclei. Examples of such materials are those found along the GeTe–Sb_2Te_3 pseudobinary of GST.[72] Growth-dominated materials tend to have fast nucleation times, but most of the crystallisation time is taken by the growth of the crystallites. Examples of these materials are the Sb:Te[72] and AIST systems.[73] Further discussion of crystallisation pertaining to GST can be found in section 2.5.2.

2.4.3 Electronic and Bonding Properties of Chalcogenide Glasses

A glass in which all atoms satisfy their valence requirements may be considered an ideal glass. In this context, valence would be defined as the number of single covalent bonds necessary for an atom to fill its outer shell of *s* and *p* orbitals with electrons. Considering that a full outer shell contains 8 electrons, atoms in chalcogenide glasses will generally obey the "$8 - N$ rule" of bonding, where N is the number of valence electrons and the coordination number is given by $8 - N$ when $N > 4$. A rule to this effect was proposed by Mott to explain the fact, first demonstrated by Kolomiets,[74] that amorphous chalcogenide glasses are insensitive to doping with elements with four or more outer electrons.[75] Satisfaction of this rule creates local energy minima leading to a reduction of the total energy of the glass so

that is closer to that of the crystalline structure, in agreement with Zachariasen's criteria for glass formation.[76]

An ideal glass would possess a similar short range order to that of its corresponding crystal, with preservation of the local stoichiometry. In reality, structural defects in the glass matrix and deviations in stoichiometry tend to be introduced during the quenching of the glass. These defects are responsible for "states in the gap" which, for example, provide recombination centres for charge carriers and are also the origin of Fermi level pinning in chalcogenide glasses.[77,78]

A continuous random network (CRN) model, with intrinsic entropy due to disorder, could be used to describe bonding within the chalcogenide glass. Atoms with broken, unsatisfied or dangling bonds give rise to topological defects within the CRN, which Mott proposed must exist in large numbers as point defects in an amorphous chalcogenide matrix.[79] Defects may also arise in stoichiometric glasses from homopolar bonds (i.e. bonds between the same type of atom). Building upon a model first developed by Anderson,[77] Mott suggested that a dangling bond may contain a single unpaired electron and is electrically neutral (defined as D^0). These dangling bonds can have a negative charge when they contain two electrons (D^-) or a positive charge (D^+) when no electrons are present. A local lattice distortion may take place upon a change in the electron population of a defect, leading to the reaction

$$2D^0 \rightarrow D^+ + D^- \tag{2.6}$$

being energetically favoured, where D^0 will only occur as an excited state.[79] As a result, the correlation energy, U, defined as the sum of positive Coulomb energy (from electron repulsion) and the negative energy from lattice interaction, can become negative. Sites with such negative correlation energy are known as "negative-U centres" in the literature.[49] Therefore, in chalcogenide glasses the electronic-lattice interaction may be so strong that the energy can only be minimised when a localised state is occupied by two electrons. Further refinements of this model have been applied to PCMs, such as the valence alternation pairs (VAPs) proposed by Kastner and Adler for chalcogenide semiconductors,[80] although their relevance is under debate.[54] Simulations recently performed by Kolobov *et al.* suggest that VAPs do exist in Ge:Te materials and are the result of transient three-centre bonds forming during the phase switching process.[81] This contradicts previous results by Robertson *et al.* which do not support the formation of VAPs in Te-based PCMs due to the tendency of Te

to over-coordinate.[82] Therefore, more research is required to fully understand the electronic properties of defects in the amorphous phase of chalcogenide glasses.

Finally, while the Fermi level is pinned in the middle of the band gap in the glass phase, a shift towards the valence band is observed upon crystallisation.[83] As a result chalcogenide glasses tend to be p-type semiconductors, although the origin of this behaviour is not fully understood. Kolobov was the first to attribute it to charged or neutral defects (e.g. neutral dangling bonds).[84] Specifically, Edwards *et al.* determined that for GeTe the formation of Ge-vacancies is particularly favourable with increasing temperature and the Fermi level is dragged down simultaneously.[85] Due to similarities between the GeTe and GST lattices, the authors predicted a similar behaviour to take place in GST materials.

2.4.3.1 Bond Constraint Theory

Bond constraint theory (BCT) introduces a conceptual framework that can relate glass forming ability to the composition of a material. BCT attempts to link the mean atomic coordination in an amorphous covalent network to its rigidity.[54] It has been proposed that for an amorphous material the maximum number of physical constraints equals the number of degrees of freedom available to the material. Thus, for an ideal three-dimensional glass this constraint metric is equal to 3 meaning the number of bonds per atom (n_c) is also 3. Moreover, *flexible* glasses have $n_c < 3$ and more degrees of freedom available for limited movement as a result, whereas *rigid* glasses have $n_c > 3$ and are more constrained.

BCT also provides a link between n_c and the average coordination number $\langle r \rangle$. In a derivation proposed by Phillips,[86] a covalent network that has a total number of bond-stretching constraints equal to half the number of bonds, and a number of bond-bending constraints adding up to $2\langle r \rangle - 3$, results in the relationship

$$\langle r \rangle = \frac{2}{5}(n_c + 3) \tag{2.7}$$

with the result that for an ideal glass with $n_c = 3$, the average coordination takes a value of 2.4. Thus it can be surmised that changing the stoichiometry of the glass would lead to a change in $\langle r \rangle$ and therefore affect the rigidity of the glass. Paesler *et al.* suggested that for a material like GST there exists an intermediate *transition* zone of isostatic rigidity as illustrated in

Figure 2.6.[87] However, simulations by Micoulaut *et al.* dismiss that idea in favour of a narrow isostatic region and a sharp transition in Te-rich regions, as will be described in section 2.5.[88]

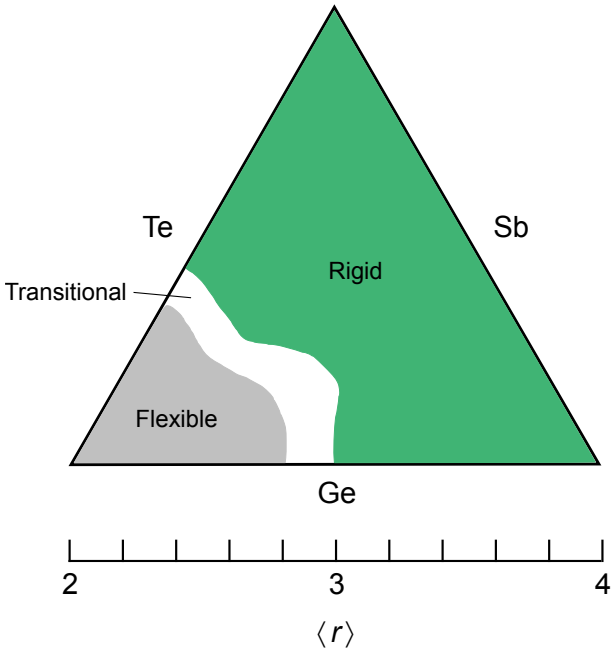

Figure 2.6: Ternary diagram of GST showing the *flexible*, *transitional* and *rigid* regions of the GST compositional space as suggested by Paesler *et al.*[87]

Consider the following for a qualitative understanding of glass rigidity. As $\langle r \rangle$ decreases so does the glass-forming ability of a flexible glass, the available degrees of freedom in the material will favour crystallisation and as result T_g will also decrease. As $\langle r \rangle$ becomes larger than 2.4, T_g will initially increase as more energy is required for atomic rearrangement due to the greater number of bonds being formed. However, as this happens, bond strength will become increasingly weaker leading to non-monotonic behaviour of T_g as a function of $\langle r \rangle$. As a result, the overall energy of the glass will increase because within a more crowded environment bond lengths will deviate from their energetic optimum and crystallisation will be favoured. Therefore, glass-forming ability also decreases as the rigidity of the glass increases.[89]

According to the $8 - N$ rule PCMs have $\langle r \rangle$ values between 2.6 and 3.2,[54] placing them in the region of rigid glasses. However, there appears to be disagreement in the literature as to whether PCMs follow this rule exactly[87,90] or tend to be more rigid than the rule would predict, due to particular atomic species having larger coordination numbers.[54] In the case of experimental data, this disagreement may arise from comparing results obtained

from materials prepared using differing methods, the use of aged materials, or different quench rates which can influence the short range order of the amorphous solid. For data derived from theoretical simulations, the discrepancy may arise from the size of the system being simulated or from ambiguities in defining the cut-off distance used to define atomic coordination. Therefore, while the use of BCT and the $8 - N$ rule may serve as a useful guide for PCM selection for further study, care must be exercised in the interpretation of the experimental data in light of these models.

2.5 Ge:Sb:Te

Initial studies on phase-change memory materials were conducted in the early 1970s.[30] These typically focused on Te and its alloys since it was known to have desirable glass forming properties. Eventually, the most frequently studied system became the Ge:Te binary. The fastest switching behaviour was found to occur at the 50/50 atomic percent composition.[32] At this composition the material can melt without phase separation as seen in the phase diagram reproduced in Figure 2.7.

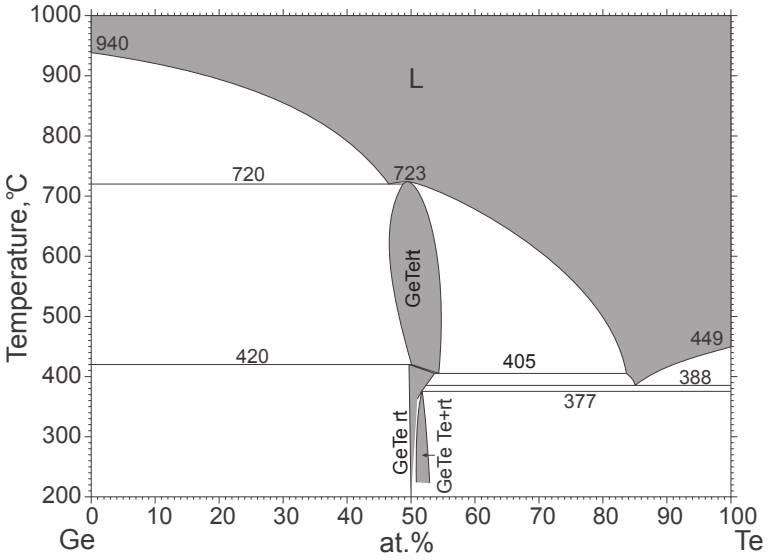

Figure 2.7: Phase diagram of the Ge:Te binary system. L = liquid; rt = room temperature (i.e. the low temperature polymorph of a given composition); ht = high temperature.[91]

The fast switching time of the GeTe alloy is possible due to the lack of atomic migration during crystallisation into a rhombohedral structure, as only bond angles change during this process.[53] From the phase diagram it can be observed that GeTe has very little compositional

tolerance. In addition, crystallisation time increases at different Ge:Te ratios away from the 1 : 1 composition due to atomic migration and rearrangement.[32] Given that the desired GeTe phase only exists within a narrow range of conditions, this motivated the search for alloys based on the Ge:Te system that allowed for greater compositional tolerance.

Doping the Ge:Te system with Sb results in the formation of a ternary system with compounds that have the desired characteristics for phase-change memory. These compounds can be found along the pseudobinary line between GeTe and Sb_2Te_3, shown in Figure 2.8. The compositions typically studied within this line are $Ge_2Sb_2Te_5$ (GST225), $GeSb_2Te_4$ (GST124) and $GeSb_4Te_7$ (GST147). Of these, GST225 is the most commonly reported in the literature. Deviation from these stoichiometric compositions results in polycrystalline films which are mixtures of the other stoichiometric crystals and individual elements.[34] These stoichiometric compositions are favoured for PCRAM because each tends to solidify into a single compound, thus minimising phase separation upon repeated SET and RESET cycles.

In addition to the materials along the GeTe–Sb_2Te_3 pseudobinary, studies of interesting compositions along other tie lines can be found in the literature. For example, Kalb *et al.* found that the crystallisation of Ge_4SbTe_5 (GST415), found along the GeTe–SbTe pseudobinary, was also nucleation dominated.[69] Paesler *et al.* used BCT to interpret extended X-ray absorption fine structure (EXAFS) data to arrive at the conclusion that GST225 had a molecular structure of Ge_2Te_3 + Sb_2Te_3 (that is, GST226)[87,92] which sits on the Ge_2Te_3–Sb_2Te_3 pseudobinary. This evaluation led to the controversial result that GST225 should be considered a good glass forming material contrary to experimental evidence (c.f. section 2.4). Further work by Micoulaut *et al.* assessed the applicability of BCT to the GST system using density functional theory (DFT) calculations.[88] They determined that GST225, together with all other phase-change compositions, were found well within the structurally rigid region of the ternary space (thus making them bad glass formers) and were separated from a flexible region delimited by the $GeTe_4$–$SbTe_4$ pseudobinary line, as shown in Figure 2.8. They also suggested that the study of materials along the $Ge_xSb_xTe_{1-2x}$ line (GeSb–Te) may lead to a better understanding of the transition between the flexible and rigid glass regions. Cheng *et al.* studied materials along the GeTe–Sb pseudobinary line for automotive PCRAM applications and found that Ge_2SbTe_2 (GST212) offered a good compromise between thermal stability and crystallisation speed.[93] In the same study they also found the properties of GST212 could be further enhanced if the Ge content were increased along the Ge–Sb_2Te_3 pseudobinary.

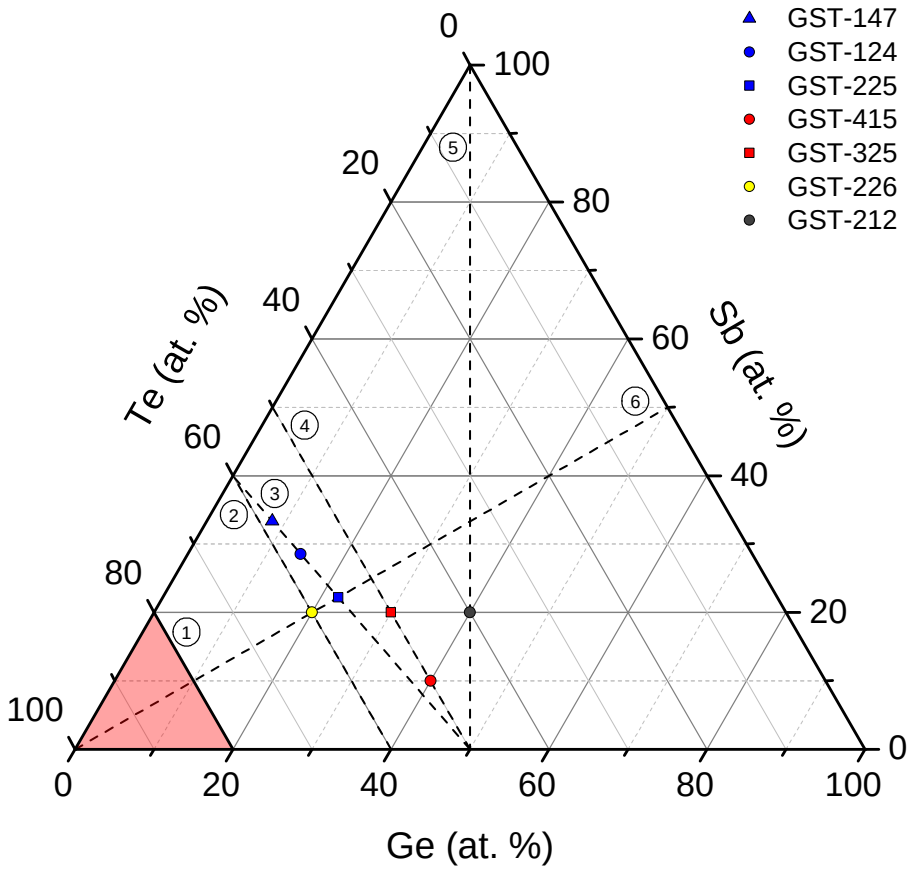

Figure 2.8: Ternary diagram of the compositional space of GST. Numbers are used to label the different pseudobinary lines described in the text: (1) $GeTe_4$–$SbTe_4$; (2) Ge_2Te_3–Sb_2Te_3; (3) GeTe–Sb_2Te_3; (4) GeTe–SbTe; (5) GeTe–Sb; (6) GeSb–Te. The locations of some stoichiometric compositions of interest are also shown. Finally, the red-shaded area delimited by the $GeTe_4$–$SbTe_4$ pseudobinary covers the "flexible" region of GST compositions as predicted by Micoulaut *et al.* using BCT.[88] The remaining compositions are expected to be in the "rigid" region.

2.5.1 Crystalline GST

The crystalline structure of the compounds along the GeTe–Sb_2Te_3 pseudobinary was studied by Yamada *et al.*[34] They proposed that these compounds consist of planar layers which form periodical hexagonal sublattices which, for the case of GST225, have a stacking sequence of Te–Sb–Te–Ge–Te–Te–Ge–Te–Sb as shown in Figure 2.9. Subsequent analysis by Kooi and Hosson proposed a Te–Ge–Te–Sb–Te–Te–Sb–Te–Ge stacking arrangement instead.[94] It appears that the preferred occupation of the cation sublattice is dependent on the thermal history of the material.[54] Regardless, GST materials crystallise through a nucleation-dominated process into a metastable[42,61] rock salt, face-centred cubic (FCC) structure at around 140 °C, with

the exact transition temperature being dependent on composition.

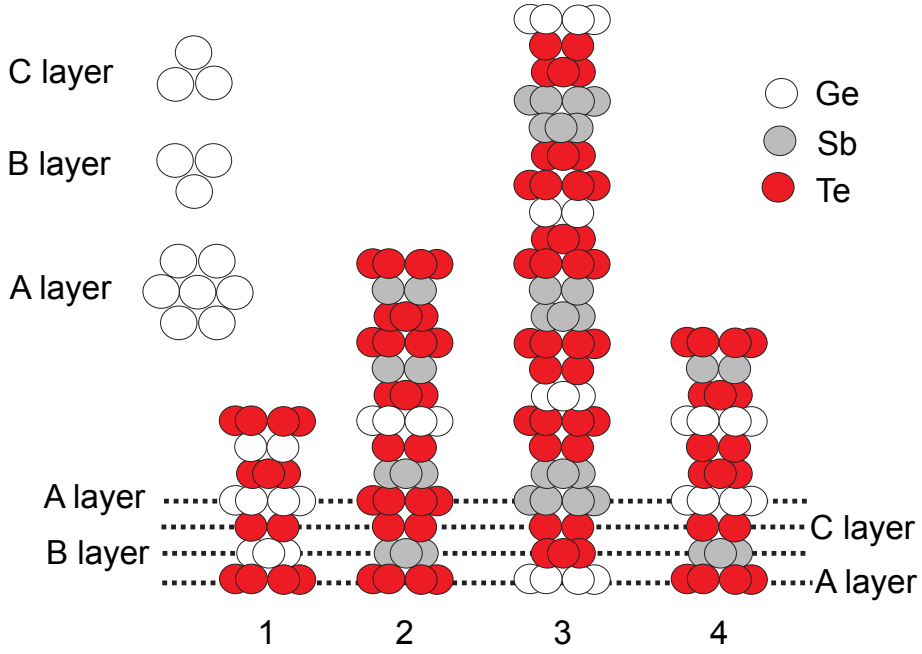

Figure 2.9: Layered arrangement of crystalline compounds along the GeTe–Sb_2Te_3 pseudobinary proposed by Yamada. 1 = GeTe; 2 = GST147; 3 = GST124; 4 = GST225.[34,95]

A second crystalline transition into the stable hexagonal phase occurs at temperatures between 140–290 °C, and melting occurs at around 600–700 °C. These transitions can be seen in the equilibrium phase diagram of the GeTe–Sb_2Te_3 pseudobinary, reproduced in Figure 2.10.

Initial crystallisation studies failed to uncover the presence of Peierls-like defects which distort the rock salt symmetry of the unit cell.[96] These distortions have the effect of reducing the lengths of both Ge–Te and Sb–Te bonds in GST255 (2.83 Å and 2.94 Å, respectively)[97] from those expected in an undistorted FCC lattice. In addition, studies have shown that the local order around the Ge atom follows a rhombohedral structure similar to GeTe, resulting in three short and three long bonds per atom.[82] This suggests the bonding around these atoms is not entirely covalent.

In materials along the GeTe–Sb_2Te_3 pseudobinary Te atoms occupy the anion sublattice whereas the cation sublattice is occupied by Ge, Sb and intrinsic vacancies, resulting in octahedral-like coordination following a $A_x^+Te_{1-x}$ general structure (A = Sb/Ge). DFT calculations have been used to understand the role of vacancies, determining that removal of Ge from a non-vacant $Ge_2Sb_2Te_4$ unit cell reduces the overall energy of the system by emptying

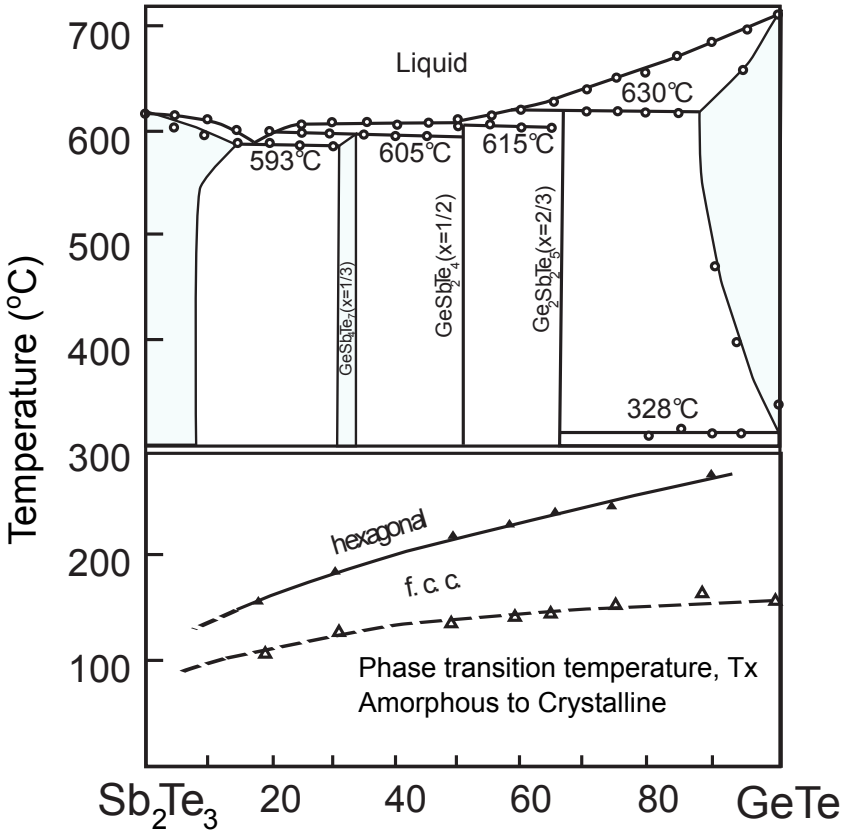

Figure 2.10: Phase diagram of the GeTe–Sb_2Te_3 pseudobinary.[95]

anti-bonding orbitals, finding a local energy minimum at a composition of $Ge_{1.5}Sb_2Te_4$.[96]

Empirically, the crystalline GST systems can be described by a formula[54] that relates the number of p-electrons per site (N_p) to the stoichiometry of the lattice site

$$N_p = \frac{2n_{\mathrm{Ge}} + 3n_{\mathrm{Sb}} + 4n_{\mathrm{Te}}}{n_{\mathrm{Ge}} + n_{\mathrm{Sb}} + n_{\mathrm{Te}} + n_V} \tag{2.8}$$

where n_i is the number of atoms of species i per formula unit, and n_V quantifies the number of intrinsic vacancies per

$$n_V = n_{\mathrm{Te}} - (n_{\mathrm{Ge}} + n_{\mathrm{Sb}}) \tag{2.9}$$

with the result that for stable materials along the GeTe–Sb_2Te_3 pseudobinary $N_p = 3$.

For an FCC crystal arrangement, achievement of the octahedral coordination requires the formation of six bonds by each atom in the unit cell. However, for both Ge and Sb atoms the number of valence electrons is insufficient to form six bonds. It has been proposed that this condition may be satisfied through resonance bonding,[98] as shown in Figure 2.11 for a GeTe network. In their original study of IV-VI semiconductors, Lucovsky and White proposed that

preservation of long-range order is a necessary condition for the formation of resonant bonds in a material.[99] This is because bonding that follows the $8-N$ rule only requires alignment of nearest neighbours, whereas resonant bonding also requires second and higher neighbours to be ordered. As a result, Peierls-like distortions of the crystalline structure mitigate the effects of resonant bonding due to misalignment of the bonding orbitals. Therefore, the search for good PCMs may be oriented towards finding materials that have good resonant bonding and suffer from limited distortion. One approach proposed by Lencer *et al.* to achieve this aim will be discussed in section 2.7.

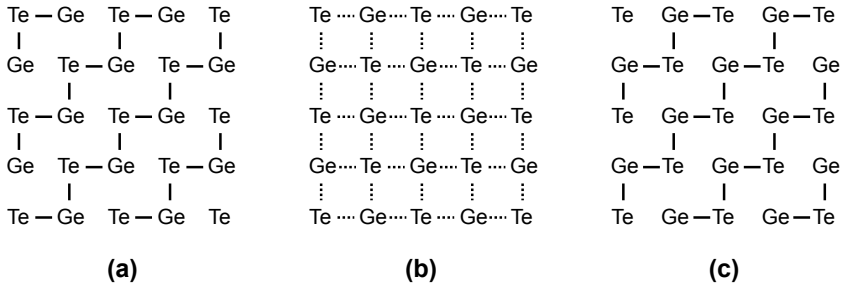

Figure 2.11: Illustration of resonant bonding in GeTe. Frames (a) and (c) show the two possible Lewis structures for the GeTe bonding network using pure covalent bonds. Frame (b) shows the resonance hybrid with delocalised bonds.

Resonant bonding has been used to explain a number of properties of the crystalline phase, such as its high optical dielectric constant (ϵ_∞) which is responsible for the optical contrast between amorphous and crystalline phases due to high electronic polarisability.[98,99] The high polarisability also results in smaller band gaps compared to the amorphous state.[100]

2.5.2 Amorphous GST

Amorphous GST has been studied using X-ray techniques such as EXAFS and X-ray absorption near-edge spectroscopy (XANES), as well as neutron diffraction, since these techniques are able to probe local atomic environments. Initial studies of the bonding environment of amorphous GST225 were done by Hyot *et al.* and found that both Ge–Te and Sb–Te bonds were shorter than in the crystalline phase at 2.62 Å and 2.84 Å respectively.[101] Further evidence confirmed these results and suggested that Ge had sp^3 hybridization in a $GeTe_4$ arrangement.[102,103] More detailed studies by Jóvári *et al.* showed a degree of chemical ordering not seen in the initial model, together with a significant number of homopolar Ge–Ge and "wrong" Ge–Sb bonds 2.47 Å and 2.69 Å long respectively.[90] In addition, the Te–Ge–Te bond

angle distribution seemed consistent with a tetrahedral environment, whereas the Te–Sb–Te bond angles indicated a predominantly octahedral one.

Kohara *et al.* used synchrotron XRD data together with Monte Carlo simulations to study the topology of GST225 and described it in terms of ring statistics.[104] They found a predominance of four- and six-fold rings, similar to the crystalline phase, with signs of chemical ordering in the form of ABAB bond alternation (where A = Sb/Ge and B = Te) as illustrated in Figure 2.12. Subsequent studies expanded upon this model[105–108] and confirmed the existence of homopolar and Ge-Sb bonds with bond angle distributions mainly around 90°. Coordination numbers for individual atoms tend to be larger than predicted by the $8 - N$ rule but smaller than six.[108] However, Xu *et al.* found that by adjusting the definition of bonding in their simulation (by using a threshold of charge localisation) on average the coordination number in GST225 was closer to three, as would be expected by the $8 - N$ rule. This result led to the conclusion that the structure of amorphous GST is composed of defective octahedral sites, mainly arising from the presence of up to one-third of the Ge atoms in a tetrahedral arrangement. In addition, the number of tetrahedral Ge sites is expected to increase as one moves along the GeTe–Sb_2Te_3 pseudobinary towards the pure GeTe composition.[104] These deviations from the mainly octahedral coordination seen in the crystalline phase result in the loss of resonant bonding and the material properties associated with it.

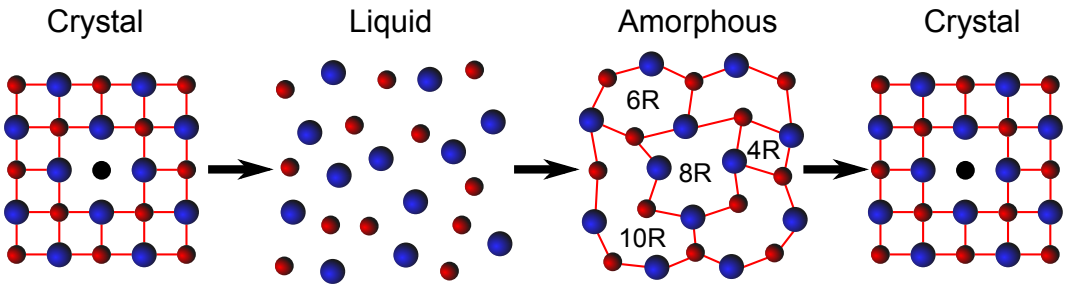

Figure 2.12: Evolution of ring statistics in GST225 as proposed by Kohara *et al.*[104] Red dots = Ge/Sb; blue dots = Te; Black dot = vacancy. The number of atoms per ring in the amorphous structure is also shown.

2.5.3 Electrical Properties and Phase Switching Mechanisms

Crystalline GST materials behave as p-type semiconductors. The origin of this behaviour has been attributed to the formation of V_{Ge} and Sb_{Te} defects in their lattice.[109] The specific conductivity properties are dependent on composition, but in general the materials along

the GeTe–Sb_2Te_3 tie line have low resistivity in the crystalline phase and low conductivity in the amorphous phase. These materials also exhibit threshold switching properties when exposed to an electric field.

The electrical conduction mechanisms of the amorphous phase at sub-V_{th} fields has been extensively reviewed by Nardone *et al.*[110] Therein they identify three regions in the electric field of the I-V characteristic of GST PCRAM devices, as illustrated in Figure 2.13. The first region generally follows Ohmic behaviour at low fields (where $F \leq 10^4\,\mathrm{V\,cm^{-1}}$). An intermediate region follows an exponential field dependence that may be described either by $\ln I \propto V$ or $\propto V^{1/2}$. At higher fields, the non-Ohmic behaviour at the V_{th} point has been attributed to the factors outlined in section 2.3.3, and the field dependence is stronger, in the order of $\ln I \propto V^2$.

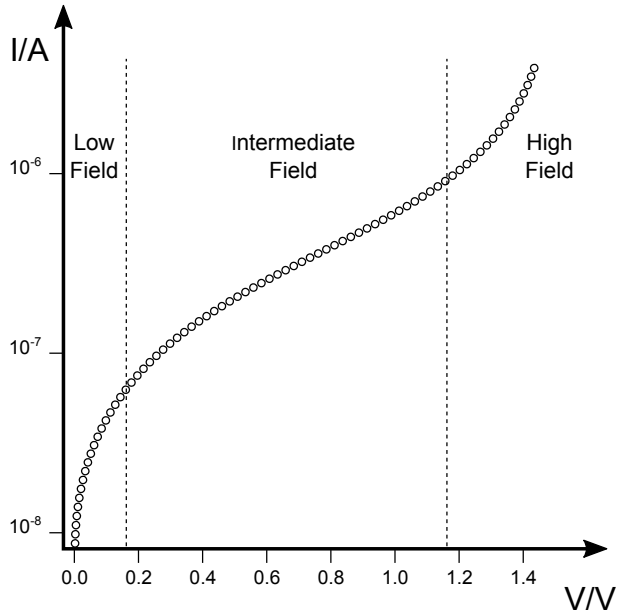

Figure 2.13: The three regions of the I-V characteristic at sub-threshold voltages in GST PCRAM devices.

Kolobov *et al.*[97] proposed the "umbrella flip" model for the crystalline to amorphous transition whereby the local environment is not disrupted around the Sb atoms and the Te layer is partially preserved. They concluded that no covalent bonds are broken and that the only structural change is the flip in the position of the Ge atom from a four-coordinated state into an eight-coordinated state. The implication is that the material may not necessarily melt during amorphisation and the local structure of the material is well defined. This phenomenon would enhance the reversibility of the switch and memory cycling. Evidence validating this

model was presented by Chong *et al.*[111] where a GeTe:Sb_2Te_3 superlattice was grown at a 2 : 1 molar ratio, thus making a $Ge_2Sb_2Te_5$ material. After 10^7 switching cycles the superlattice structure was preserved, suggesting the material never melted. Initial interpretation of this finding seemed to suggest Ge atoms adopted sp^3 hybridisation in the amorphous state, while reverting to p-bonding during crystallisation. However, it is now well understood that Ge atoms predominantly bond using p-electrons in both phases, thus avoiding rehybridisation during switching.[107]

The umbrella flip model also fails to explain threshold switching behaviour for PCMs that do not contain Ge, thus limiting its application. Hegedüs and Elliott used AIMD simulations to study the quenching of GST225 from the melt.[107] They found that the material forms four-membered rings, similar to the ABAB squares found by Akola and Jones in the AIST system, which persist into the amorphous phase, where they appear to be homogeneously distributed.[73] The concentration of connected four-membered rings increases upon annealing and these are considered to be the seeds of the crystallisation process. It is then possible to explain the switching mechanism between phases as the ordering or disordering of these rings. The existence of pre-ordered structures within the amorphous GST material may also account for its fast switching speeds. In addition, this model can be extended to other PCMs that do not contain Ge.

After melting the amorphous material undergoes structural relaxation over time resulting in resistance drift to higher values following a power law[112]

$$R = R_0 \left(\frac{t}{t_0} \right)^{\nu} \tag{2.10}$$

where R and R_0 are the current and initial resistance, t and t_0 are current and initial times and ν is the drift coefficient. For GST225 the value of ν has been found to be between $0.12 - 0.22$ depending on experimental conditions[112] and it has been shown to have a temperature dependence.[113] While this drift effectively increases device performance, by increasing the SET/RESET ratio, it may be problematic for multi-bit storage applications. The resistance drift also results in a drift in the value of V_{th}, which is similarly temperature-dependent.[114]

Additional considerations arise from the high threshold field of GST, which can lead to issues with voltage generation on nanoscale devices.[115] Another issue is the very low resistivity of the crystalline state, in particular of GST225 which requires large currents in order to RESET the material. While these problems may be partially dealt with by modifying the device

geometry,[115] others have sought to address them by investigating the properties of doped GST as well as other PCMs.

2.5.4 Doped GST

Several groups have doped GST225 and other compositions along the GeTe–Sb_2Te_3 pseudo-binary with different elements in order to enhance its phase-change properties. Nitrogen and oxygen are frequently employed as dopants because they are inexpensive, relatively non-hazardous and can be easily incorporated into sputtering processes. Table 2.4 summarises the effects of some commonly reported dopants. The following discussion will deal with the characteristics of the N-doped GST system (N-GST) as it has been studied in the work presented herein.

The first experiments using N-GST for optical phase-change memory were performed by Kojima *et al.*[138] It was determined that a dopant level of $2-3$ at. % N was the most suitable for the recording layer of optical media, with up to 8×10^5 read/write cycles. They also proposed a model for the function the N atoms have in the GST matrix: At concentrations of $1.1-2.7$ at. % N, individual Ge:Sb:Te atoms would form nitrides that would accumulate along the grain boundaries of GST crystals. The nitrides would envelop the crystals and persist through the melting process due to the higher melting point of nitrides compared to GST, thus stemming micro flow in the material. At concentrations lower than 1.1 at. %, nitrogen atoms would instead occupy vacancies within the GST matrix and these envelopes would not form. Jeong *et al.* prepared GST225 thin films with 0–31 at. % N and studied their crystal structure using XRD. They determined that crystalline N-GST has a FCC crystal structure with well-defined characteristic peaks that broaden and shift to smaller angles as N doping increases. Above 20 at. % doping the FCC structure turns into a hexagonal lattice. Their Transmission Electron Microscope (TEM) analysis also showed reduced grain size with increasing N doping due to the formation of nitrides at the grain boundary, and an increasingly strained structure due to N distortion of the lattice. Finally, their differential calorimetry studies showed an increase in crystallisation temperature from 160 °C (for pure GST225) to about 250 °C at 19 at. % doping.[139] Seo *et al.* also studied the crystallisation behaviour of $0-12$ at. % N-doped GST225 thin films, finding that it changed with increasing N content from a two-step nucleation and growth process to a single nucleation step and

Table 2.4: Summary of dopant effects on the GST system.

Dopant	Effects
N[116–121]	Reduces writing current in PCRAM. Produces crystals with small grain size due to precipitation of nitrides. Enhances thermal stability. Increases crystallisation temperature.
O[117,118,120,122]	Similar to N, but produces larger grain sizes. Increases crystallisation rate. Increases electrical resistance.
Bi[123–125]	Promotes nanosecond transition time between phases. Decreases crystallisation temperature. Material becomes n-type semiconductor.
Ag[72,126,127]	Changes crystallisation mechanism from nucleation-driven to growth-driven. Increases crystallisation temperature and rate. Increases resistance. Increases threshold voltage.
Cr[128]	Suppresses flow in molten material.
F[118]	Reduces crystallisation time.
Si[129]	Increases resistivity. Increases crystallisation temperature but decreases melting point.
Si+N[130]	Increases resistivity.
Sn[72,131]	Increases crystallisation rate.
Ga[72]	Enhances thermal stability. Increases crystallisation temperature in Sb-rich compositions.
Ce[132]	Increases phase transition temperature and thermal stability.
Al[133,134]	Increases resistance. Enhances thermal stability. Increases crystallisation temperature.
SiO_2[135]	Decreases thermal conductivity. Decreases RESET current.
In[72,136]	Increases crystallisation temperature. Enhances thermal stability.
Cu[134]	Decreases crystallisation and glass transition temperatures.
Pd[137]	Increases crystallisation speed and thermal stability of the amorphous phase.

also found evidence of grain size refinement with increasing doping.[140] Work by Kölpin *et al.* corroborated the structural information presented above and utilized AIMD simulations to determine that N doping is an energetically unfavourable process which leads to increased crystallisation temperature and reduced grain size. They also predicted that Te–N bonds would form preferentially in the amorphous matrix.[121] However, it was later shown that Ge–N bonds form preferentially instead, together with the incorporation of N_2 molecules into the lattice.[141,142] AIMD models suggest that the most favourable place for N insertion would be at the Te vacancies (N_{Te}) as they would allow for the formation of bonds with Ge.[143] Further simulations by Elliott *et al.* also supported the hypothesis that grain refinement originates from the precipitation of nitrides at grain boundaries.[144]

Shelby and Raoux observed reduced crystallisation speeds in sputtered GST thin films doped with 7 and 12 at. % N.[145] Elliott *et al.* suggest this reduced speed may be due to the formation of increasingly constrained crystallisation sites with increased N doping.[144] While this property may remove N-GST from consideration as a PCRAM material, Wang *et al.* argued that as device size decreases the crystallisation mechanism of N-GST switches from the expected nucleation-growth mechanism inherent to the material, to a hetero-crystallisation model whereby nucleation and growth take place at the boundary between a PCM and an enveloping material. They propose this crystallisation mechanism has the overall effect of reducing switching speeds, which would make N-GST a more desirable PCRAM material than GST due to its greater switching endurance.[119]

The electrical resistivity of N-GST increases with increasing N doping and is higher than that of GST in the crystalline phases.[116] The sheet resistance of sputtered N-GST films has been reported to be ca. $10^9\ \Omega$/sq. for dopant levels up to 26 at. % N in the amorphous phase, and between $10^5 - 10^6\ \Omega$/sq. in the crystalline phase after annealing up to 300 °C.[141,146] Horii *et al.* reported a N-GST PCRAM device with switching speeds of $50 - 100$ ns that required lower writing currents than similar GST devices.[116] Lai *et al.* also reported a drop in V_{th} for the N-GST system and proposed the possibility of its use in MLC designs due to the existence of three differentiated resistivity states in the material.[146]

2.6 Non-Telluride Chalcogenides

The bond strength of chalcogenide atoms decreases as one goes down the periodic table, with sulphur being the strongest, leading to a reduction in T_g.[147] Similarly, these bonds become more metallic and isotropic, resulting in less electronegative materials that have smaller band gaps and higher electrical conductivity in the crystalline phase. This is primarily the reason why telluride chalcogenides are chosen over either sulphide or selenide chalcogenides for phase-change memory applications.[126] However, as PCRAM device dimensions are decreased, it may be desirable to work with materials with lower electrical conductivity in the crystalline phase, as that would reduce the electrical current required to RESET a device. To date, most non-telluride glass research for PCRAM has been done on Se glasses and the Ga:La:S (GLS) system.

2.6.1 Selenium Glasses

Among Se glasses, the Sb:Se system has been studied for optical storage applications since the 1980s.[148,149] In the context of PCRAM, Yoon *et al.* showed that for the Sb_xSe_{1-x} system the crystallisation temperature decreased from 161 °C to 122 °C when the Sb composition x increased from 0.6 to 0.7. They also determined that a device using a $Sb_{65}Se_{35}$ as its phase-change layer had a faster crystallisation time and lower RESET current than a comparable GST225 device.[150] This system has recently been doped with Sn,[151,152] Ge[153] and Ga[154] although investigations of these materials' properties so far has been limited to studies of the band gap, crystallographic and optical properties, and no phase-change memory characterisation has been reported at the time of writing.

Another selenide system of note is the binary In:Se glass, in particular the In_2Se_3 composition. This material has been prepared and tested for PCRAM performance in both thin film[155] and nanowire form,[156] and has a high resistivity range between the SET and RESET states of up to 10^5. It can melt with electrical pulses less than 50 ns (3 V), although it requires microsecond-length pulses ($1-2$ V) to recrystallise, which could lead to the creation of energy-efficient but slow PCRAM devices based on this material.

2.6.2 Ga:La:S

GLS was first reported in 1976 by Loireau-Lozac'h *et al.*[157] It is a semiconductor with a band gap of 2.6 eV[158] and is known to be stable in both amorphous and crystalline phases.[159,160] GLS glasses attracted research interest because of their potential applications in telecommunications and sensing due to their low phonon energies. Moreover, their large, non-linear refractive index led to their investigation as optical switches,[161] waveguides and routers.[158]

In a Ga_2S_3 crystal, two out of three sulphur atoms are each bound to the three Ga atoms via two covalent bonds, while the third S–Ga bond is coordinate in nature. The third sulphur atom is bound only to Ga atoms and is believed to be a bridging atom. While Ga_2S_3 has not been observed in a glassy state, there is a GaS_4 unit within the Ga–S crystals that is thought to be glass forming. Adding an ionic sulphide to the crystal will facilitate the change of the crystalline Ga_2S_3 structure to a glassy one. Sulphur tends to form ionic bonds with rare earth elements, of which lanthanum gives the largest extent of glassy compositions.[162] The addition of La_2S_3 will modify the network of Ga–S bonds by breaking one of the coordinate bonds and replacing it with an S^{2-} anion. This has an effect of leaving the tetrahedral environment of the Ga atom unchanged, while modifying the three-fold coordinated S atom into a two-fold coordinated bridging atom. This process creates a void filled by a La^{3+} cation.[162]

The structure of GLS consists of Ga–S bonds of 2.26 Å length, and La–S bonds of 2.93 Å.[163] More importantly, these lengths have been determined to be the same in the amorphous and crystalline states.[162] Thus it is only necessary to change the bond angles of the atoms in the material in order to effect the phase change. Deriving from this property it has been hypothesised that the phase switch of these materials would be fast. GLS has an eutectic point approximately at the $0.79(Ga_2S_3)0.21(La_2S_3)$ composition.[164] With onset of crystallisation temperatures between 560 °C and 790 °C (depending on composition) and a minimum melting point of 860 °C, GLS is more thermally stable than GST.[165]

Some studies of GLS for PCRAM applications have been done in thin film and nanowire form.[95,163] These report a resistance ratio between the SET and RESET states up to 10^4. Device switching speeds were comparable to those of GST, although the switching currents were lower. In the case of Cu-doped GLS, this reduction in switching current was as high as four orders of magnitude.[166] The reduction in write current may allow for the fabrication of smaller, more efficient PCRAM devices using GLS and its derivative materials.

2.7 Computational Discovery and Optimisation of Phase-Change Materials

The use of computational methods for the discovery and development of PCMs has been limited. To date most experimental research has been a slow, empirical process involving chance discovery rather than a systematic exploration of the available chemical space. While high-throughput synthesis methods (to be discussed in section 2.8.2) can accelerate the discovery of new materials, the predictive power of computational techniques could assist the process by helping researchers make informed decisions as to where to direct their efforts. Moreover, increasing computational power has made high-throughput computational materials design a possibility, with interesting results being reported in several areas such as thermoelectric and battery materials, catalysts, and topological insulators, amongst others.[167]

Using DFT calculations Lencer *et al.*[53] produced a "treasure map" of PCMs based on the tendencies towards ionicity and hybridisation of the constituent atoms, where increasing ionicity reduces the ability of the atom to participate in resonant bonds. They concluded that good PCMs tend to possess a small value for both quantities. This result was reflected in the resulting materials map, where bands of materials grouped mainly by their constituent chalcogenide were observed. In addition, it was possible to establish a link between the crystallisation temperature of a material and its position within the map, although the authors were not able to explain the origin of this relation.

Hegedüs and Elliott[168] used an AIMD model to design and optimise a novel, non-chalcogenide, PCM. Their proposed material, $Ge_{85}Sb_{15}$, offered the best PCRAM properties when grown in contact with a suitable template material.

Molecular dynamics simulations by Skelton *et al.*[169] have predicted that 4-coordinated dopants (e.g. Zn) as well as 8-coordinated dopants (e.g. Mn) would fit into the GST225 lattice and freely move between sites with varied local geometry. Their simulations also showed that transition metal dopants would have little influence on the charge distribution around host atoms. The authors later extended this approach to simulate the entire first row of transition metal dopants in the GST system.[170]

Loke *et al.*[68] have also used AIMD models to explain the origin of ultrafast crystallisation of GST after a low voltage electrical incubation field has been applied to a PCRAM device.

Their conclusion was that incubation promotes structural ordering of GST by creating a distribution of clusters from which there is a higher probability that crystallisation nuclei would form. This alteration of the crystallisation kinetics of GST results in faster SET times in PCRAM devices.

2.8 Synthesis of Chalcogenide Thin Films

The typical preparation method of PCM thin films is through magnetron sputtering of a prefabricated target. This method yields films of composition similar to that of the target. Doped films can be achieved either through reactive sputtering with a process gas or by co-sputtering the desired dopants.

Other preparation methods include molecular beam epitaxy (MBE, a form of physical vapour deposition),[34,95] pulsed laser deposition,[95,171] electrodeposition,[172] solution-phase deposition,[81,173] atomic layer deposition,[174] and chemical vapour deposition.[61] The latter two methods are of special interest for commercial device fabrication mainly due to their conformal deposition profiles.[61,173] Most of these techniques, however, produce films of a single composition or require further treatment in order to produce combinatorial films with multiple compositions per sample. High-throughput and combinatorial materials synthesis methods can overcome these limitations and produce thin film libraries that contain multiple compositions per sample.

2.8.1 Combinatorial and High-throughput Materials Synthesis

The idea of using combinatorial synthesis methods in materials discovery was first proposed by Hanak at RCA Labs in the 1970s.[175] In his paper, he described a 30-fold increase in the output of experimental results on binary superconducting materials prepared with his technique. He fabricated a circular RF-sputtering target divided into two equal halves (A and B) with each half made of a different material. By placing a strip of substrate perpendicular to the A-B interface it was possible to synthesize a thin film with a linear change in composition along the strip. By placing a substrate strip comprising 50 gold electrodes he was able to deposit a library of Mg–Mo superconducting materials at 2 at. % intervals. Electrical resistivity and superconducting transition temperature for each composition were measured

and analysed using novel computerized methods. He was also able to extend this process to ternary systems by placing a circular section on top of a target divided into three 120° sections of material. The main limitation of this approach was the lack of automated technology to collect and analyse large datasets. Thus, it was not until the early 1990s that some of these methods were used once again, with the first applications to be found in the context of drug discovery.[176] A few years later renewed interest in combinatorial materials discovery led to the development of two main methods for combinatorial library deposition: Sequential masking and continuous gradient of materials.

Sequential masking requires the evaporation of individual materials through a series of masks, which could be either lithographic, shadow or shutter masks. By combining several masks and rotating them between deposition steps it is possible to build arrays of libraries with discrete compositions on a single substrate.[177] This technique was pioneered by Schultz *et al.* using a combination of sputtering and binary masks to produce a 16×8 array of superconductive Cu oxide thin films.[178] Wang *et al.* extended this technique to produce libraries of photoluminescent materials based on Gd and Ga oxides, where each substrate contained 1024 discrete sample compositions each.[179]

The principal drawback of sequential masking is the requirement to perform a large number of steps to produce a complete combinatorial library. In addition, due to the nature of the masking process the produced fields will be of a fixed composition, thus missing intermediate compositions between fields. Finally, sequential masking produces multilayer films as depositions are performed sequentially, therefore requiring an annealing step to ensure mixing of the components. This may result in the formation of intermediate phases at layer boundaries that could inhibit the formation of properly mixed compositions.

Continuous gradient deposition relies on off-axis evaporation sources located at regular intervals around the substrate. A mechanical shutter is placed in front of the sample during deposition of each precursor material and is moved across the substrate at a fixed, programmable speed. The result is a wedge of material with a linear change in thickness. Similar to sequential masking, this method also entails sequential deposition of each precursor and also results in multi-layered films that require further annealing treatment to mix the layers. The advantage of this method is that all compositions within the limits of the sample are potentially available for screening, the only limitation being the spatial resolution of the screening method. Xiang used this method to synthesise a (Ba,Sr,Ca)TiO_3 library and

used scanning evanescent microwave microscopy to determine the dielectric constant of the resulting materials.[180] Danielson *et al.* at Symyx Technologies utilised a more complex gradient deposition system (which also incorporated masking elements) to produce a library of 25,000 addressable compositions that they used to identify a novel red phosphor material ($Y_{0.845}Al_{0.070}La_{0.060}Eu_{0.025}VO_4$) for flat panel displays.[181] Ramberg *et al.* also at Symyx Technologies, used an MBE technique whereby a shutter system was used to periodically deposit thin films of various elements, creating a layered structure. The whole library was then annealed to allow the constituent atoms to mix.[182] While the materials studied (which included NiNb and ZrCuAl libraries) were not chalcogenides, this technique and the subsequent tests performed on them demonstrated the feasibility of MBE for the preparation of NVM materials.

It is possible to avoid the problem of multi-layered library deposition by using co-deposition of the source materials. Using this method each source has its own mechanical shutter allowing individual control of the deposition wedge. Simultaneous deposition of all precursors at room temperature results in films that can be considered a non-equilibrium solid solution. Metastable phases may also be formed that are not available through traditional powder metallurgy synthesis methods involving mechanical alloying, such as ball milling. Co-deposition also offers the possibility to use substrate heating *in situ* to form crystalline phases during deposition.

2.8.2 High-throughput Synthesis of Phase-Change Chalcogenides

High-throughput, combinatorial methods for synthesis and screening of chalcogenide materials were first used by Krysta *et al.*[183] They co-sputtered GST from individual sources in a way that resulted in a small compositional gradient of each element across the substrate. This was achieved by placing each source off-axis from the substrate and at an angle from each other. These initial experiments resulted in a small compositional library centred on GST225. Further refinement of this method allowed for more thorough preparation of materials along the GeTe–Sb_2Te_3 pseudobinary line.[184] These experiments demonstrated the efficacy of high-throughput techniques to catalogue memory cycle times and structural dependence on composition.

A similar combinatorial DC sputtering technique was used by Kölpin *et al.* to dope a GST225

material with Si. They achieved this placing the Si target at a 42° angle to the sample normal, thus creating a gradient of the dopant across the material. Separate samples with increasing N content were also created by reactive sputtering. It was found that the crystallisation temperature of GST225 increased with increasing Si content, but at a slower rate than with N doping. A decrease in grain size and an increase of the microstrain in the material was also observed with increasing Si concentration.[121]

Guerin and Hayden developed a combinatorial MBE system that allows co-deposition of different elements onto a substrate.[8] This system consists of two chambers, one allowing up to six individual elemental sources, the other four, using a combination of Knudsen cells (K-cells), electron-beam sources (e-guns) and a plasma atom source. Wedge shutters are used to control deposition by creating a gradient of the source element across the square substrate. The rate of deposition from each source allows full control of the compositional range of the material. This technique has been used to successfully fabricate compositional libraries of transition metal alloys for electrocatalyst screening,[185] perovskites,[186] carbides,[187] sulphides,[188] as well as chalcogenides for phase-change memory, as described below.

Simpson *et al.*[189] first used this method to produce combinatorial GST libraries covering the majority of the ternary space. The samples were screened for optical switching properties and were found to differ from sputtered materials, a result that was attributed to the higher pressure found in sputtering chambers. Further tests on GST using similar preparation techniques have been performed by Guerin *et al.*[190] Finally, GLS libraries were prepared by Gholipur for electrical phase-change screening.[163] It was determined that thin films of these materials showed a reduction of RESET current, compared to GST, due to efficient Joule heating.

2.9 Summary

This chapter has provided background information on current memory systems and NVM technologies. In addition, the principles of operation of phase-change memories were discussed. The theory behind chalcogenide glasses was also given, followed by an overview of materials used in PCRAM and a discussion of computational methods for discovery and optimisation of said materials.

Thin-film deposition methods for chalcogenide glasses were discussed, with an emphasis on high-throughput techniques. Due to its efficacy in the preparation of phase-change chalcogenides, and its ability to cover a wide compositional space, the HT-PVD method detailed in section 2.8.2 has been utilised for the preparation of the materials used in this thesis. Synthesis and characterisation techniques of the materials produced for this report will be discussed in Chapter 3, while presentation and analysis of results will begin in Chapter 4.

Highlighting the need for better memory materials and addressing the limitations of those used currently, chalcogenide glasses are ideally placed to be tuned, optimised and tested for PCRAM applications. Although various methods can be employed to fabricate these materials, HT-PVD synthesis combined with HT screening methods are the most appropriate to accelerate the identification of optimal PCRAM chalcogenides.

Chapter 3

Experimental Systems

In this chapter the methods used to synthesise and characterise phase-change chalcogenides will be presented. Synthesis of thin films was achieved by means of physical vapour deposition techniques, particularly the HT-PVD system discussed in section 2.8.2. The resulting combinatorial libraries were characterised using high-throughput techniques to understand their structural and functional properties as material composition changes across the films.

3.1 Thin Film Synthesis

3.1.1 High-throughput Physical Vapour Deposition

As discussed before, the HT-PVD system is a highly effective technique for the synthesis of combinatorial material libraries. This system was used to deposit the libraries of phase-change chalcogenides studied in this project. The apparatus, manufactured by DCA Instruments, consists of two growth chambers (A and B), a RF-sputtering chamber and an X-ray photoelectron spectroscopy (XPS) analysis chamber, all kept under ultra-high vacuum (UHV) conditions. The chambers are linked by a buffer line that permits sample transfer between them without breaking the vacuum. The relative location of the chambers in the system is shown in Figure 3.1. UHV conditions are achieved by a combination of rotary vane (Varian Inc.), turbo molecular (Pfeiffer Vacuum), ion (Varian), titanium sublimation (Varian) and cryogenic (Brooks Automation) pumps. The overall base pressure of the system is kept at around 5.0×10^{-9} Torr.

Elements are deposited within each growth chamber from either Knudsen effusion cells (K-cells, DCA Instruments) or electron beam evaporators (e-guns, Temescal Systems). Chamber A contains six sources in an alternating arrangement of K-cells and e-guns in six-fold symmetry. In addition, a plasma source can be introduced into the system in place of one of the

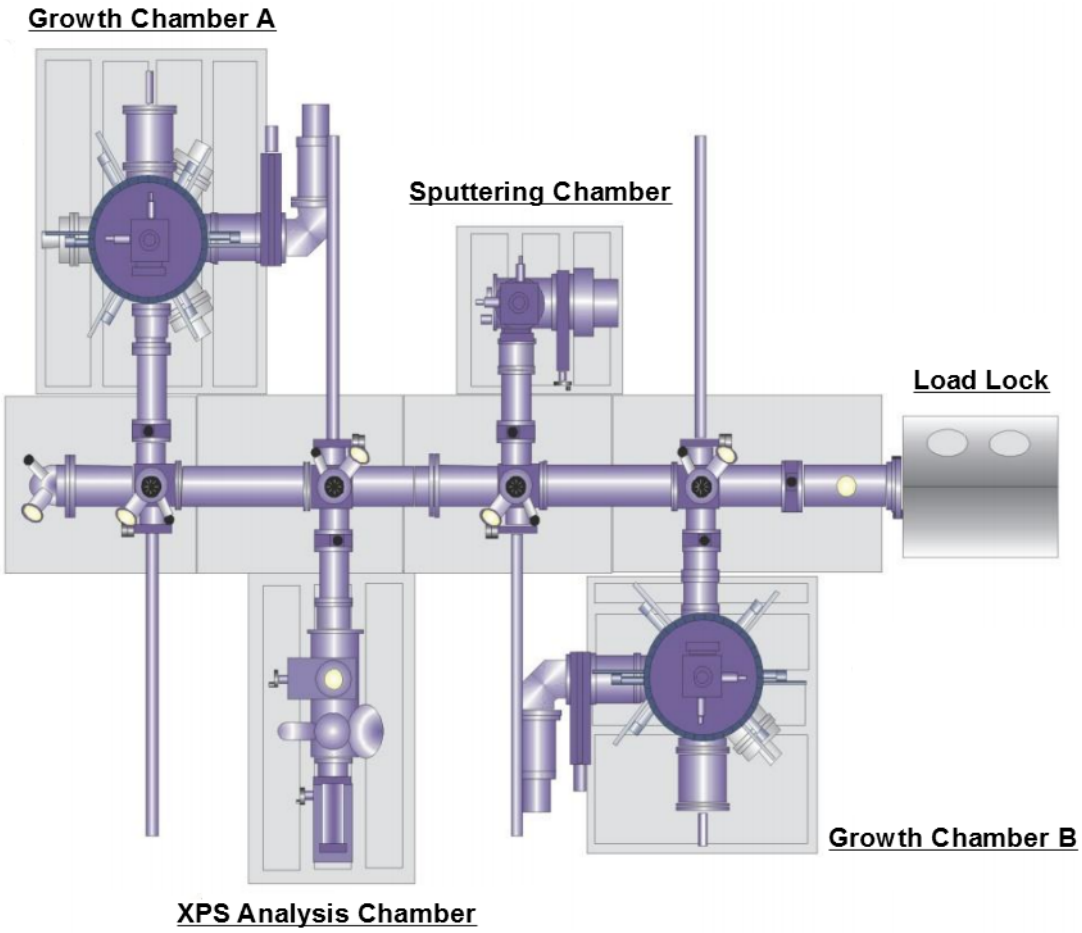

Figure 3.1: Layout of the HT-PVD system showing the different chambers and systems.

K-cells. Chamber B contains four sources (three K-cells and one e-gun) in four-fold symmetry. A top view of each chambers configuration is provided in Figure 3.2.

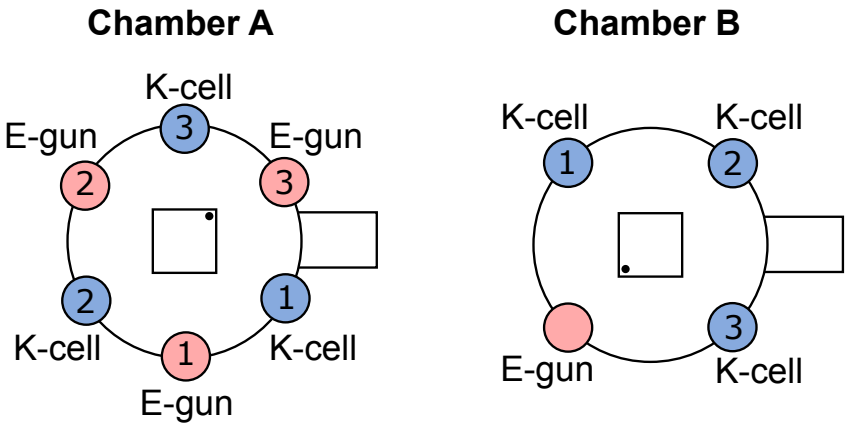

Figure 3.2: Layout of the evaporation sources available within each growth chamber. Chamber A is shown on the left and Chamber B on the right. Note that the K-cell in position blue #2 on Chamber A may be replaced with a plasma source for deposition of monoatomic gases such as H, N and O. The square at the centre of each chamber represents the position of the sample relative to each source. The dot on each square serves as point of reference for deposition and subsequent screening. Access to the central buffer line is shown to the right of each chamber.

Under UHV conditions the evaporation from the sources within the growth chambers becomes a line-of-sight process known as Molecular Beam Epitaxy (MBE). As such, it is possible to control the deposition profile of the molecular beam from of each source by using an extendable shutter. Considering that the sources are aimed towards the sample substrate and have fixed dimensions, partially blocking the molecular beam will create a reproducible shadow effect across the sample. This will have the effect of creating a gradient of material being deposited, as first demonstrated by Guerin and Hayden.[8]

The extendable shutter described above is known as a *wedge shutter* to distinguish its function from the regular shutters that fully block the molecular beam at the beginning and end of a deposition. The action of the wedge shutter is illustrated in Figure 3.3. The positioning of the wedge in between the B_{MIN} and B_{MAX} points results in different material deposition profiles. At B_{MIN} the wedge is fully retracted and does not block the beam, while at B_{MAX} the path of the beam is completely obstructed. Figure 3.4 shows cross-sections of the deposition profiles at different wedge positions. The exact position of a wedge needs to be determined empirically for each material during a calibration process prior to sample preparation.

Combinatorial thin film libraries result from the simultaneous deposition of elements from

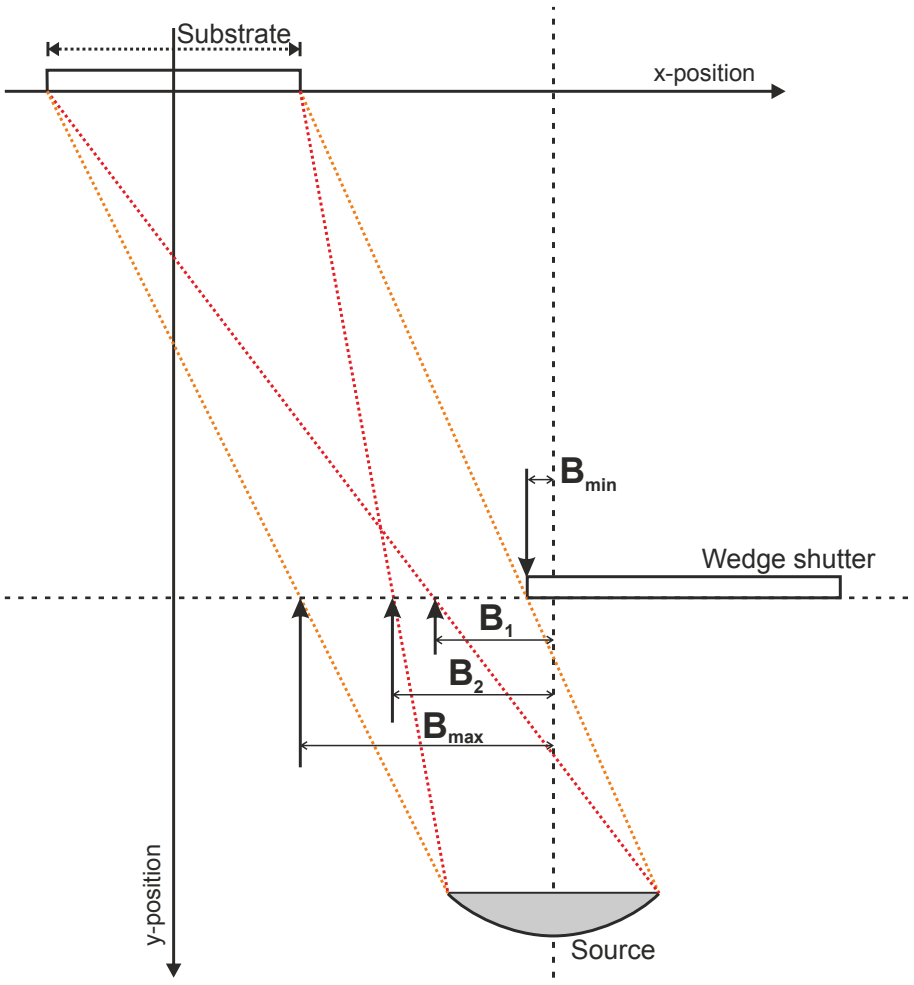

Figure 3.3: Schematic of a single off-axis evaporation source within the HT-PVD chamber. To obtain a gradient of material, the wedge shutter is moved into the path of the molecular beam between the B_{MIN} and B_{MAX} points.[8]

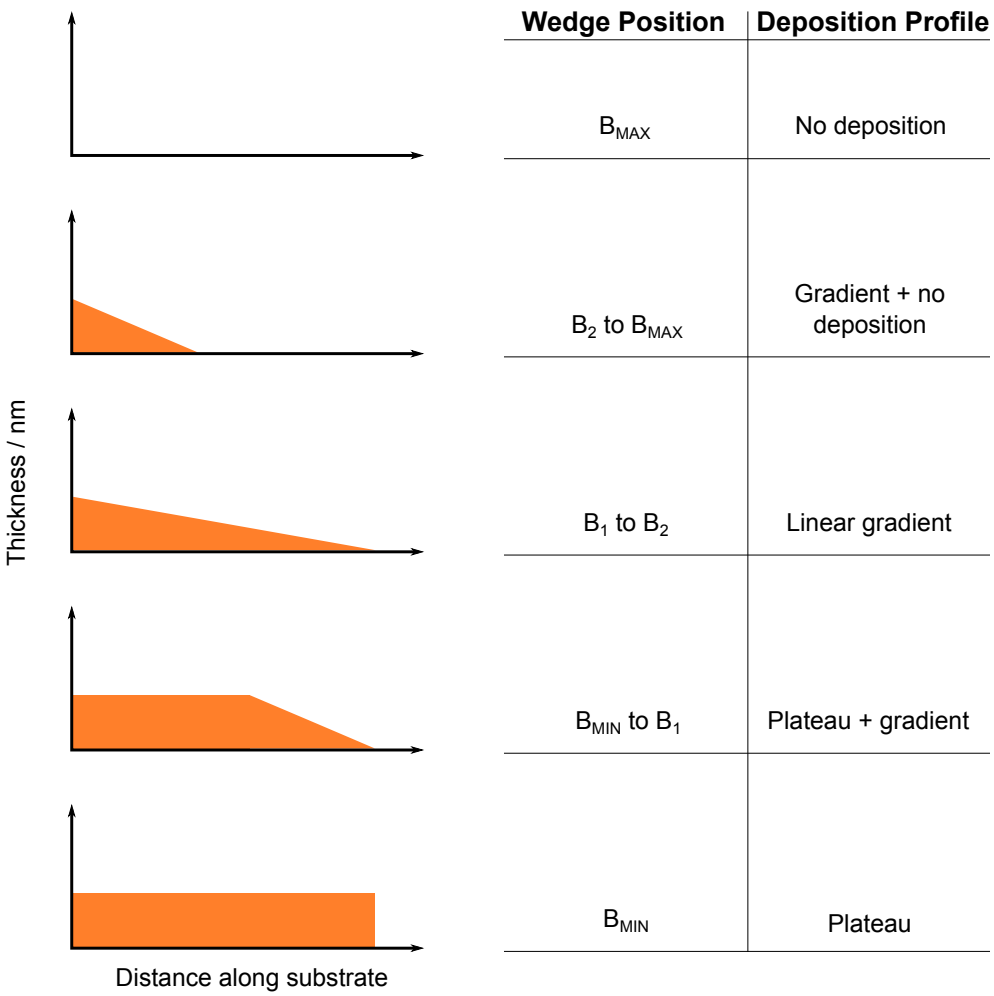

Figure 3.4: Cross section of the deposition profiles of a material deposited from a single evaporation source.[188] The profiles are shown as a function of the wedge shutter position in relation to the reference points shown in Figure 3.3.

two or more sources, as complete mixing is readily achieved. This process is easily reproducible and allows for the synthesis of metastable materials with stoichiometries not accessible through other synthesis methods. Moreover, the use of high purity elemental sources in a UHV environment produces clean samples with few impurities. In addition the sample manipulator within each growth chamber can be heated up to 600 °C, thus allowing for *in situ* annealing of samples under vacuum.

Maximum compositional spread occurs when the elemental sources are at the greatest possible separation from each other. For two sources this separation is 180° (i.e. opposite to each other) and 120° for three. While most elements can be evaporated from either an e-gun or a K-cell, some are better suited to only one of them. This is the case, for example, of W, Ta and other refractory elements which can only be evaporated with e-guns. This may pose a problem for deposition runs were maximum spread is desired, since the position of the sources cannot be exchanged within the chamber (e.g. relocating a K-cell to an e-gun position). To overcome this limitation, a further innovation of the wedge shutter concept is the use of angled wedges. These modified wedges incorporate an angle into their design which is intended to be reflected in the shape of the molecular beam and therefore in the footprint of the deposited material. As a result, the angled wedge has the effect of "shifting" the position of a source a number of degrees equal to the angle of the wedge, as illustrated in the example shown in Figure 3.5.

Thin films using the HT-PVD system are typically deposited on 35×35 mm square substrates. The choice of substrate is informed by the analysis the sample is intended to undergo after synthesis. Table 3.1 lists some common substrates and the screening techniques that can be performed on them.

Films for this project were deposited as 29×29 mm or 28×28 mm continuous films. All samples are marked with a reference dot used to keep track of its orientation during deposition and later screening. By convention, the dot is considered to be in the top right corner of the film and as such this will be the orientation used for data presentation throughout this thesis.

Table 3.1: Detail of deposition substrates and the screening techniques for which they are used.

Substrate Material	Screening Techniques
Glass	Deposition calibration; AFM
Silicon	Composition determination; phase-transition determination; Raman
Silicon nitride	X-ray diffraction; conductivity; Raman
Platinized silicon	AFM; PCRAM parametric tests

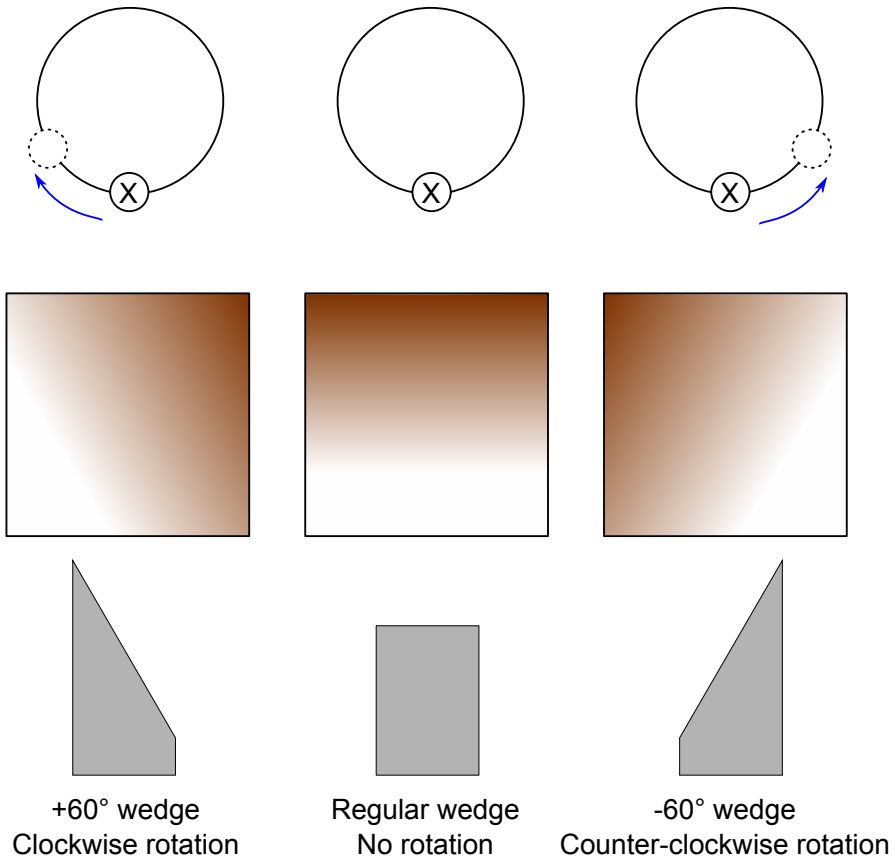

Figure 3.5: Practical example of the use of an angled wedge. The top row shows the position of the evaporation source both physical (solid circle) and emulated (dotted circle) loaded with element "X". The middle row shows the deposition footprint of X on a substrate after use of the wedge shutter illustrated in the bottom row. The use of an angled wedge can modify the deposition footprint of X to appear as if it originated from a source 60° away, either clockwise or counter-clockwise. Currently, wedges with 15°, 30°, 45° and 60° angles are available.

3.1.2 RF Sputtering

Sputtering is a physical vapour deposition process that allows the deposition of thin films of a wide variety of materials. A process gas, typically Ar, is injected into a previously evacuated vacuum chamber and ionised by a power source that generates a large electric field, thereby creating a plasma. The plasma ejects the source material from a target and travels across the vacuum to be deposited onto a sample substrate and other chamber surfaces.

Within the sputter chamber of the HT-PVD system, a circular target of material is placed in the holder located at the bottom of the chamber. The manipulator holds the sample directly above the target and it can be rotated via an electric motor to ensure the homogeneity of the resulting thin film. A mass flow controller (MKS Instruments) and an automatic adjustable gate valve (Varian) are used to set and maintain a set Ar pressure in the chamber. The process gas is then ionised by means of a radio frequency (RF) power source. RF sputtering offers the advantage that it can be used for both conducting and insulating target materials.

RF-sputtering was used to deposit thin films of GST225 (50 nm thick) on platinized silicon substrates. These films were used to calibrate the parametric measurements of PCRAM characteristics outlined in section 3.3.3 and Chapter 6 of this thesis.

Capping layers are typically deposited on top of PCM materials right after synthesis using RF-sputtering. The purpose of these layers is to protect the underlying chalcogenide film from the effects of aging through oxidation. It has been shown that, in the case of amorphous un-doped GST, aging occurs primarily through the formation of Ge and Sb oxides reaching depths of a few nanometres (< 10) from the surface the film after a 90-day exposure.[191] Apart from structural changes, aging has been shown to reduce the crystallisation temperature of GeTe and GST225 films by 5 and 8 °C respectively.[191] Oxides formed through aging may make the materials more resistive in both the amorphous and crystalline phases.

No capping layers have been used on either the GST or the N-GST thin films synthesised for this thesis. Our experience has shown that films of thickness greater than 50 nm produced using the HT-PVD system exhibit no signs of aging while stored under vacuum, even after prolonged periods of time. Risk of aging may also be mitigated by characterising the films shortly after synthesis. Additionally, N-GST films may be more resistant to aging than GST films due to the formation of Ge and Sb nitrides that would preclude the incorporation of oxygen into the materials.

3.1.3 Composition Determination using Energy-Dispersive X-ray Spectroscopy

Compositional determination of combinatorial thin film libraries was achieved by means of energy-dispersive X-ray spectroscopy (EDS). This technique takes advantage of the X-ray spectrum emitted by a sample bombarded with a focused beam of electrons. Each element produces its own characteristic X-ray lines and, barring samples containing elements with overlapping peaks, elemental identification is normally unambiguous. In principle, all elements above Be can be detected but the quality of the equipment, in particular the sensitivity of the detector, makes identification of lighter elements ($Z < 10$) difficult. However, modern silicon drift detectors benefit from high count rates and high energy resolution that improve the detection and quantification of light elements.

Characteristic X-rays are generated by electron transitions from inner orbitals closer to the atomic nucleus. An electron must first be removed in order to create a vacancy that can later be filled by another electron from an orbital further away from the nucleus. X-ray lines are identified by a capital letter indicating the shell from which the vacancy occurs (K, L, or M, as per the Rutherford-Bohr atomic model). A Greek letter and a number further identify the transition by importance and relative intensity. For example, if a vacancy occurs in the K shell and the filling electron drops from the L shell, a Kα_1 photon is emitted. Within a given shell electrons may be located in an orbital of slightly different energy, due to bonding effects. As such, it is possible that a transition Kα_2 may take place. Figure 3.6 illustrates some common electron transitions between shells. The energy difference between adjacent shells becomes smaller further away from the nucleus, resulting in the emission of less energetic photons.

The determination of elemental abundance requires quantitative analysis of the resulting X-ray spectrum by measuring line intensities for each element in a sample. This is achieved by counting photons during the measurement and is limited by statistical error. Overall, the typical accuracy of this technique is close to ±2 % for heavier elements. In addition, during measurement a continuous X-ray background is generated (the *Bremsstrahlung*) which makes the quantification of small peaks (i.e. elements with smaller abundance) more difficult. The intensity of the *Bremsstrahlung* increases with atomic number and accelerating voltage of the excitation source.

An EDS measurement system is normally coupled with an electron microscope as these instruments are able to generate the excitation beam necessary to achieve the emission of

X-rays from the sample. This allows the option to image a sample before or during an EDS measurement, from which an elemental map of the sample could result.

For this work, all compositional measurements were performed on a JEOL JSM-5910 scanning electron microscope, fitted with an Oxford Instruments x-act 51-ADD0006 EDS silicon drift detector. The Oxford Inca 300 EDS software was used for analysis. Typically, a combinatorial library sample deposited on a Si substrate would be introduced into the analysis chamber and placed under vacuum. The working distance of the measurement was 13 mm. A magnification of 500x resulted in a measurement area of approximately 200 µm by 200 µm.

The sample sits on an X-Y stage that can be controlled manually through a console or via the Jeol microscope software. The Oxford Inca EDS software can read the stage coordinates and allows the option to programme the automated measurement of predefined sites in the

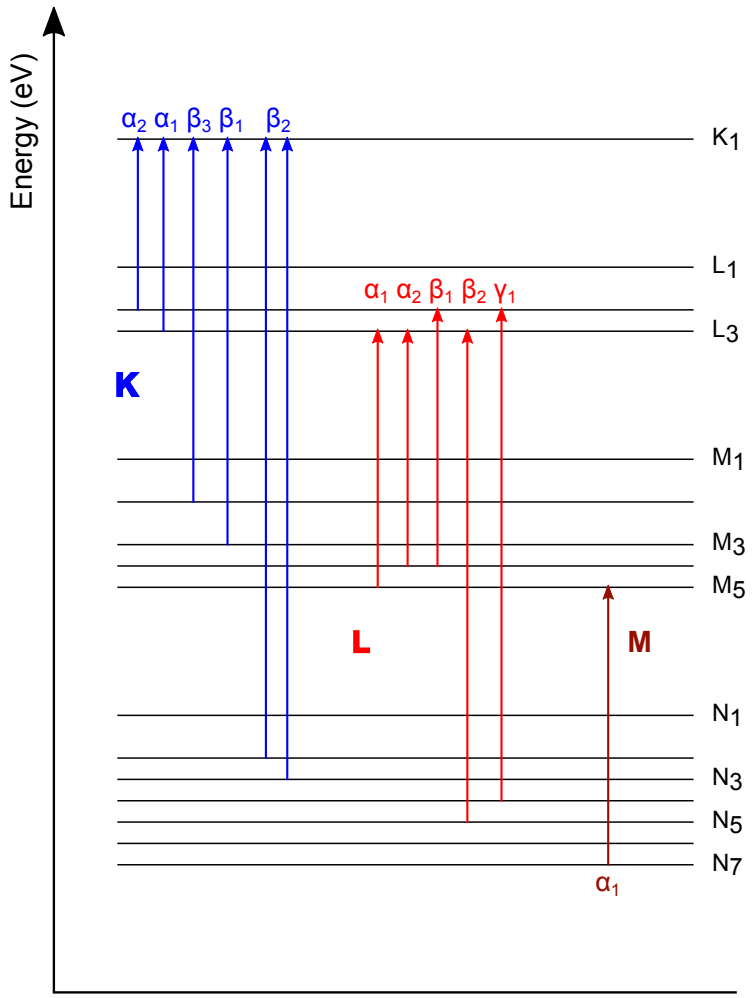

Figure 3.6: Energy level diagram showing common electronic transitions that produce X-ray photons.

form of a macro. These macros were setup in a 14×14 grid with a pitch between sites of 1.867 mm and an acquisition type of 60 s per point. A complete macro of 196 points takes around five hours to complete. Three measurements were performed on each sample in order to obtain an error estimate of the compositional data. The averaged results were imported into the Paradise analysis suite developed by Ilika plc. This bespoke software has a MATLAB backend and is used in the analysis of the large combinatorial datasets generated during the course of high-throughput experiments, such as those presented in this work.

3.2 Structural Characterisation

3.2.1 X-ray Diffraction

X-ray diffraction (XRD) is commonly used to identify the atomic structure of a crystal. X-rays are generated from a Cu source, collimated into a monochromatic beam and focused on the sample. A crystalline sample can be considered a series of stacked parallel planes, where beam diffraction takes place at each plane as per Figure 3.7.

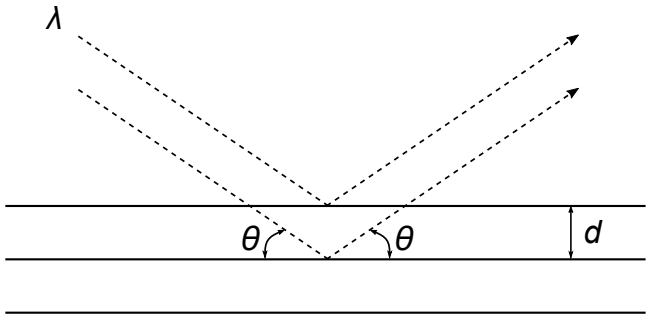

Figure 3.7: Schematic of two parallel X-rays being diffracted at parallel crystal planes. The diffracted rays will interfere either constructively or destructively depending on the d parameter of the crystal and the experimentally controlled θ angle.

The interaction of the incident beam with the sample produces constructive interference when conditions satisfy Bragg's law:

$$n\lambda = 2d \sin\theta \tag{3.1}$$

where n is the order of diffraction, λ the wavelength of the X-ray radiation, d the spacing between planes and θ the angle between the incident X-rays and the crystalline plane. The

diffracted X-rays are detected and then processed and counted by the instrument's software where they are converted into a diffraction pattern. The peaks observed in the pattern correspond to the individual planes in the material and their geometric separation. Different materials have unique diffraction patterns. This fact is particularly useful in the context of high-throughput experiments as it is possible to observe the evolution of the crystal structure of a material as its composition changes.

In a powdered sample diffraction from all available 2θ angles can be measured due to the random orientation of the material. However thin film samples tend to be highly orientated along a single crystal plane due to interaction with the substrate on which they are grown. This can have the effect of changing the relative intensities of peaks as compared to those reported in reference patterns, such as those collected by the International Centre for Diffraction Data (ICCD). In addition, some reflections may not be detected at all because they are not oriented in the correct way to allow for constructive diffraction.[192]

In a typical XRD experiment the instrumentation scans through a specified 2θ range by moving both the X-ray source and the detector. While this procedure is adequate for single samples, it is not ideal for high-throughput experiments due to long measurement times. An alternative method incorporates the use of a general area detector capable of measuring reflections at several 2θ angles simultaneously. This is advantageous as it allows the measurement of about 30° of the 2θ range without having to move either the X-ray source or the detector during the experiment. As such, it becomes possible to measure a large array of points in a matter of hours.

For this project, X-ray patterns were recorded on a D8 Bruker X-ray diffractometer fitted with Vântec-500 general area detector with a 152 cm^2 active area. The X-rays were emitted by a Cu Kα source with a 0.5 mm beam diameter. All measurements were done at a source angle of 11° from the sample normal resulting in a beam with a 0.5×2.6 mm footprint. The detector was fixed at a 25° angle from the sample normal. The resulting 2θ range was between 16° and 52°. Samples deposited on silicon nitride substrates were positioned on a stage with X-Y-Z control. Sample coordinates can be setup in the instruments GADDS software in order to define a 14×14 grid coterminous with the EDS grid defined for compositional determination. Individual scans for each macro were set to run for 10 minutes at each point. The resulting patterns were processed and analysed using Ilika's Paradise software where they were matched with their corresponding compositions.

3.2.2 Raman Spectroscopy

Raman spectroscopy is a light scattering technique used to observe the vibrational, rotational and low-frequency modes (such as phonons) of a system. Light shone onto a sample will interact with it at the molecular level by either being absorbed or scattered. Elastic light scattering is known as Rayleigh scattering, while the inelastic process is termed Raman scattering.

A scattering photon will perturb the electron cloud of a molecule and will excite it to an unobservable virtual energy state for a short time, before an inelastically scattered photon is emitted. As a result the emitted photon will have either higher or lower energy than the incoming photon. The energy difference between photons corresponds to a frequency shift known as Raman shift. If the emitted photon has increased energy relative to the incoming photon it is said to have undergone an anti-Stokes shift, whereas a photon with less energy than the incoming radiation has undergone a Stokes shift. The vast majority of photons incident on a material are scattered elastically. Since the Raman signal is very weak, modern spectrometers use lasers as their photon source due to their monochromatic nature and high beam flux. In addition, a number of filters and components are used to reduce Rayleigh scattering and obtain a higher quality Raman signal.

In a typical Raman spectroscopy experiment, an optical microscope is used to focus the laser onto a small spot of the sample. The emitted photons pass back though the microscope and into the spectrometer, where the Raman-shifted radiation is detected by a charge-coupled device (CCD) sensor. A computer connected to the instrument is used for data collection and processing. The result is a Raman spectrum of signal intensity versus the Raman shift of the material.

Raman spectroscopy has the advantage of being a non-destructive technique that requires no sample preparation prior to measurement and therefore can be used in either as-deposited or annealed thin films. It is a suitable technique to study the evolution of the local structure across combinatorial thin film libraries due to its high lateral resolution and high sensitivity to changes in chemical composition. On the other hand, given the weakness of the Raman effect multiple scans may be required in order to achieve a good signal to noise ratio. In addition, signal interference arising from fluorescence emission may be an issue in some samples due to impurities the material or the colour of the sample itself. Fluorescence can be

avoided with careful selection of the excitation wavelength, which may be sample-specific. If this is not possible, fluorescence can still be mitigated by using a confocal microscope setup, where the fluorescence from outside the lasers focus is reduced by the spatial filtering of the microscope's pinhole.

Raman spectra were collected at room temperature using an XploRA confocal Raman microscope (Horiba Jobin Yvon, Inc.) coupled to an Olympus BX41 optical microscope. The spectrometer is equipped with a 532 nm, 25 mW solid-state laser. In addition, four gratings (2400, 1800, 1200 and 600 grooves/mm) and five laser filter options can be used to improve signal quality. The spot size of the laser on the samples was approximately 1 µm. Spectra were acquired using the instrument's software (LabSpec 6), which can be programmed to run high-throughput experiments. For the measurement of combinatorial libraries, a 14×14 grid coterminous with the EDS and XRD grids was setup. As-deposited and annealed samples deposited on silicon or silicon nitride substrates were studied. The Raman signal of the combinatorial libraries studied was significantly far away from the signal arising from the substrates and therefore no baseline correction was required. The parameters for each measurement varied depending on the nature of the sample and particular care was taken not to crystallise the as-deposited samples during measurement. The resulting Raman spectra were exported into a text file and imported into Ilika's Paradise processing software for composition matching and analysis.

3.2.3 Atomic Force Microscopy

Atomic Force Microscopy (AFM) is a scanning probe technique used to obtain high resolution images of surfaces. To achieve this, a very sharp tip mounted on a cantilever is scanned across the surface and interacts with it. These interactions are normally driven by intermolecular forces and cause the cantilever holding the tip to deflect as it travels across the sample. The degree of deflection is measured by reflecting a laser off the back of the cantilever onto a two-dimensional photodetector, as shown in Figure 3.8. The AFM control software then translates the degree of deflection into topographic information. Samples are typically measured under standard ambient conditions, although specialised AFM instruments are able to measure liquid submerged samples or under high vacuum.

AFM imaging can be performed under one of three operating modes: Contact, dynamic

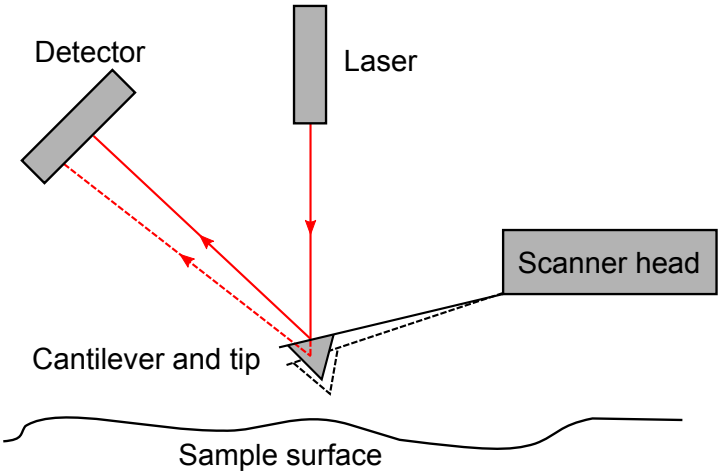

Figure 3.8: Operation mode of an AFM. As the tip interacts with the surface of the sample the laser beam will be reflected off the back of the cantilever at different angles which can be detected by a two-dimensional position-sensitive photodiode.

contact and non-contact. In contact mode the tip is approached close enough to the sample to experience repulsive forces, which deflect the cantilever. The force the tip applies to the surface is determined by the user and it defines the measurement's set point. During the experiment, the deflection of the cantilever is sensed and compared against the set point. Any deviations from the desired set point will be compensated by the instrument via a direct current (DC) feedback amplifier, and the voltage applied is a measure of the height of the features in the sample. Low stiffness cantilevers (i.e. with a low spring constant) must be used for this mode as otherwise there is a risk of snapping the tip into the surface.

In the dynamic contact mode (also known as tapping or acoustic mode) the cantilever is made to resonate at its resonance frequency, typically in the kHz range. The instrumentation aims to keep the frequency and amplitude of the resonance constant using a feedback loop. When the tip comes close to the surface intermolecular interactions change the amplitude of the cantilever oscillations and the electronic servo in the AFM scanning head will try to compensate for these changes by adjusting the height of the cantilever. The topographic scan is therefore a result of the intermittent interaction of the tip with the sample surface. This mode has the advantage of being less damaging to both the surface and tip, although some wear and tear still occurs and AFM tips will eventually lose their sharpness after a number of measurements. Finally, in non-contact mode the tip is hovered very close to the surface. As in tapping mode, the cantilever is also made to oscillate but the tip never touches the sample. Using the same feedback loop described above it is possible to detect the small cantilever

deflections caused by the attractive forces of the surface.

The AFM used in the experiments presented in this thesis was a Keysight (formerly Agilent) Technologies 5600LS Atomic Force Microscope. Measurements of thin film thickness were carried out in tapping mode using a Nanosensors Pointprobe-Plus n-doped Si tip with a resonant frequency range of 204 kHz to 497 kHz. The topography at the corner edges of the thin film samples was measured over a space of approximately 20 µm at a 0.5 lines/s scan rate and a resolution of 512 points/line. The proportional and integral gain parameters of the feedback loop had to be adjusted manually for each measurement point. Once the measurement was completed a topography cross-section was obtained three times at each point using the AFM control software, and the height difference between the substrate and the top of the film was measured. Once the thickness of the four corners of a sample was known, the values were imported into the Paradise software where the thickness was interpolated at each intermediate point, for a 14×14 grid, assuming a linear change in thickness between points.

Surface topography scans on as-deposited and annealed samples were also performed in order to observe surface features at specific points of interest within the films. These were done in tapping mode using the same probe type as described above. Scans were carried out over a 5×5 µm area, at different points of the films, at a 0.5 lines/s scan rate and 512 points/line resolution. From these measurements grain sizes were estimated when feasible.

In addition to thickness determination, the AFM tip was used as the top electrode of the probe station used to do electrical parametric testing of phase-change material devices. This probe station integrates a Keysight Technologies B1500A semiconductor device analyser (detailed in section 3.3.3) with the 5600LS AFM. A full description and discussion of this measurement method will take place in Chapter 6.

3.3 Functional Characterisation

3.3.1 Resistivity Measurements via Four Point Probe

Resistivity (ρ) is an important intrinsic property of semiconductor materials. It depends on the free electron and hole densities (n and p) and their mobility (μ_n and μ_p) as per the

relation:

$$\rho = \frac{1}{q(\mu_n + \mu_p)} \tag{3.2}$$

where q is the elementary charge. A four point probe (4PP) can be used to measure the ρ of thin film samples using the method developed by van der Pauw.[193] The probe is made of four evenly-spaced, spring loaded, conductive tips and is loaded onto a stage that permits contact between the tips and the sample surface. When in contact, a current is passed through two adjacent probes and the resulting voltage is measured across the two opposite probes, as shown in Figure 3.9. The contact resistance between the probes and sample is negligible because the instrumentation has been engineered to have much higher impedance than the rest of the circuit, so that little current passes through it.

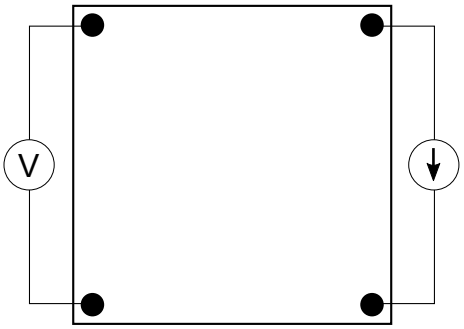

Figure 3.9: One possible resistivity measurement setup using the van der Pauw method on a square sample with a four point square probe.

For symmetrical samples the sheet resistance (R_{sh}) can be defined as follows:

$$R_{sh} = \frac{\pi}{\ln(2)} \frac{V}{I} \tag{3.3}$$

the units being in Ω/square. For thin films the thickness of the sample is smaller than the spacing of the tips, and the term $\pi/\ln(2)$ can be considered a correction factor for the measurement.[194] The resistivity of the sample can then be determined from R_{sh} if the thickness of the film (l) is known:

$$\rho = R_{sh} l \tag{3.4}$$

in units of Ω m. The conductivity (σ) of the film is simply defined as the reciprocal of the resistivity with units of $\mathrm{S\,m^{-1}}$.

For phase-change materials an important figure of merit is the resistivity contrast, $\log(\Delta\rho)$, between the as-deposited and the annealed state. This number is typically quoted in terms

of orders of magnitude, and can be calculated using the following relation

$$\log(\Delta\rho) = \log_{10} \frac{\rho_{as-deposited}}{\rho_{annealed}} \tag{3.5}$$

Sheet resistance was measured using a Four Dimensions Inc. Model 280DI four point probe. The probe had four tungsten carbide tips in a square arrangement, each with a diameter of 25 µm and 0.635 mm spacing. Prior to measurement, the tips were repeatedly cleaned by contacting them on an alumina substrate. All samples were deposited on an insulating silicon nitride substrate, thus ensuring that any readings were those of the sample itself. The instrument is equipped with a rotary translational stage, and its control software allows a measurement macro of arbitrary size and shape to be defined, thus maintaining a high-throughput workflow. A grid of 15×15 points, similar to that used for the other techniques presented above, was used for measurement. The resulting data is output as the sheet resistance at each point and was imported into Ilika's Paradise software where it was converted into resistivity by binding the thickness variable determined via AFM (see section 3.2.3). All measurements were recorded at room temperature.

3.3.2 Crystallisation Temperature Determination

The link between the reflectivity changes and the crystallographic state of PCMs is a well understood phenomenon and is the principle of operation behind optical phase-change memory. From a theoretical perspective, the reflection of light from a thin film of PCM is determined by the optical constants n and k, which are the refractive index and extinction coefficient of the material, respectively. Figure 3.10 shows the evolution of these constants between the amorphous and both crystalline phases of GST at increasing photon energies. While n and k for both crystalline phases are very similar, they are markedly different from the constants of the amorphous phase, and it is possible to conclude that the crystalline phase is generally more reflective.

Here a purpose-built system is introduced for the measurement of optical reflectivity as a function of temperature. This system has been developed at Ilika plc and is able to perform measurements in real time on the combinatorial thin film libraries described in section 3.1.1. As such, the technique is known as the High-throughput Optical Mapping of Phase Transition (HTOMPT). The apparatus, pictured in Figure 3.11, consists of a copper block

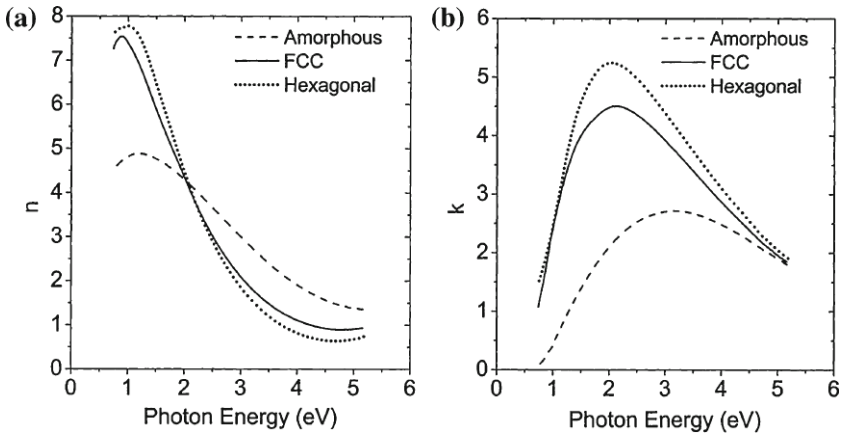

Figure 3.10: Optical constants n (a) and k (b) for amorphous and crystalline GST225 as determined by Lee *et al.*[195]

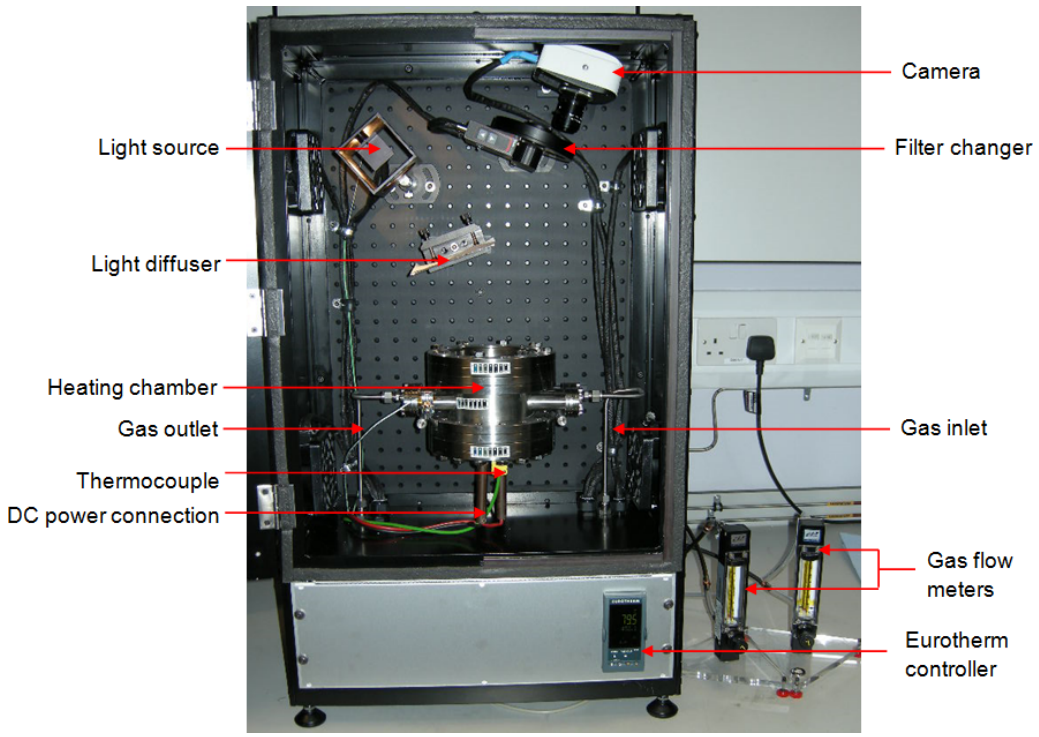

Figure 3.11: Photograph of the HTOMPT apparatus with system components labelled. Picture credit: Ilika plc.

with two embedded substrate heaters (HeatWave Labs, Inc. Model 101511) operated by a Eurotherm 3508 controller capable of delivering different heating rates. The sample is placed on top of the heating block and this setup is encased within a sealed stainless steel chamber through which an Ar flow is passed in order to prevent sample oxidation. The chamber has a top window coated with anti-reflective material that allows the recording of images of the sample during heating at defined intervals. A halogen lamp provides a source of uniform white lighting. The camera (Lumenera Infinity 2-1R) contains a 1.4 megapixel CCD sensor (1392×1040 pixels) and is positioned off-axis relative to the sample.

The experiment is controlled using a software interface written in LabView. The software allows the user to modify camera exposure settings, light filters, image frequency and the experiment's temperature profile in terms of target temperature (°C) and ramp rate (°C/min). The sequence of images generated during the experiment is saved locally in a user defined directory and can be imported for analysis into the Paradise software. The size and pitch of the analysis grid are defined by the user and once done the software will extract the intensity of the light (in arbitrary units) at each point of the grid for each frame in the sequence. The result is a plot of intensity versus temperature for each point in the grid, as shown in Figure 3.12. Further processing is then required to determine the phase transition temperature. This is achieved by performing a numerical differentiation of the intensity versus temperature plot. The Paradise software provides an interface that allows testing different differentiation parameters, such as curve smoothing, temperature range, and peak threshold and separation, before performing the analysis of the whole dataset. Once finished the phase transition temperature is stored as a variable that can be bound to a compositional dataset.

In addition to the calculated phase transition temperatures, Paradise can output time lapse videos of the experiment using either the images as captured by the camera or false-colour intensity-corrected frames. Figure 3.13 shows this difference in a comparison of individual frames from a single GST HTOMPT experiment at different temperatures. The intensity correction is calculated, for each point in the grid, as the difference (ΔI) between the intensity of the point in the current frame and the intensity of the point at the beginning of the experiment (I_0):

$$\Delta I = I - I_0 \tag{3.6}$$

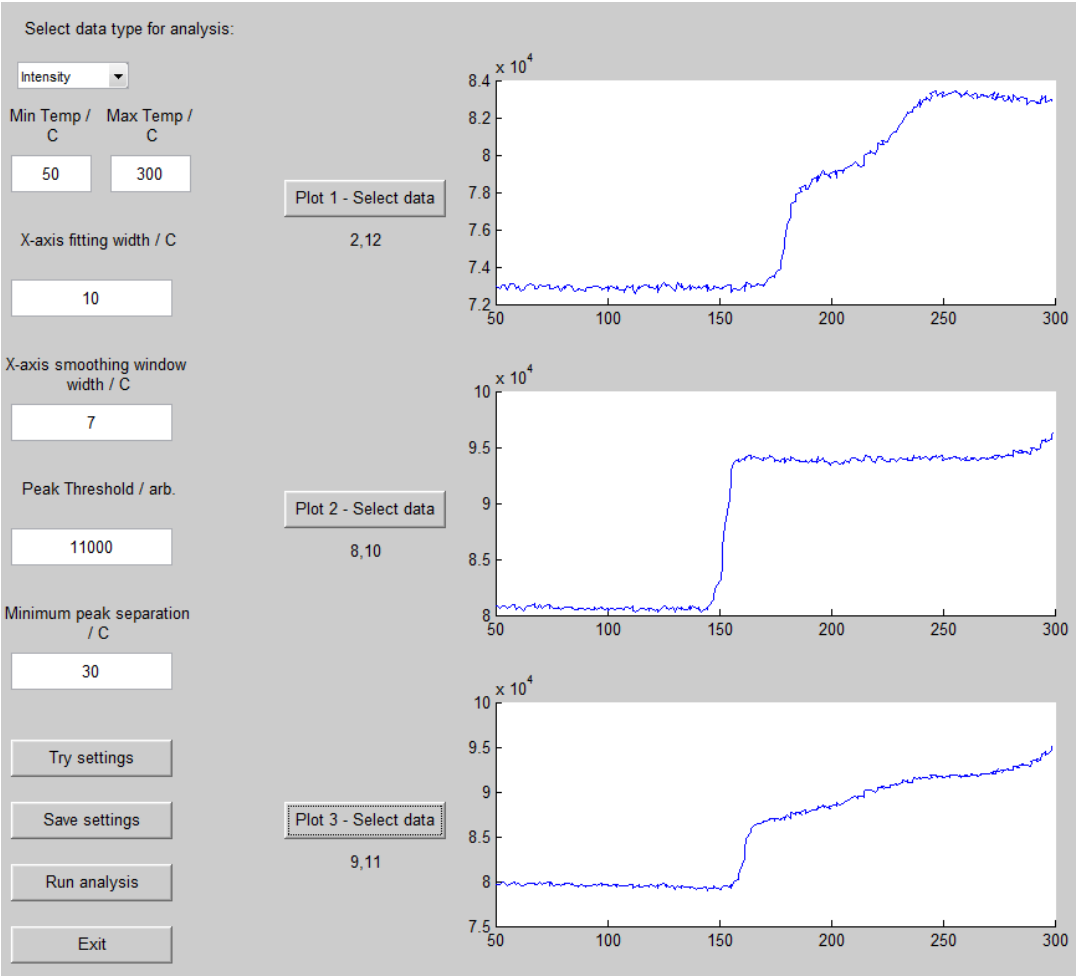

Figure 3.12: Screen capture of the numerical differentiation interface for a HTOMPT dataset. The three plots on the right are typical examples of the intensity versus temperature plots generated during the data import process into the Paradise software.

This relation can also be used in the Paradise software to produce maps of the relative intensity change across the sample at specific, user-defined temperatures.

3.3.3 Parametric Testing of PCRAM Structures

Parametric testing involves the electrical testing and characterisation of semiconductor devices, be they transistors, diodes, resistors or capacitors. Typically, the majority of tests involve direct current (DC) measurements of current versus voltage (I-V) or current versus capacitance (C-V), although alternating current measurements are also possible. Parametric testing is rarely performed on production-ready devices. Instead, it is performed on structures designed to yield information about a process or material under test.

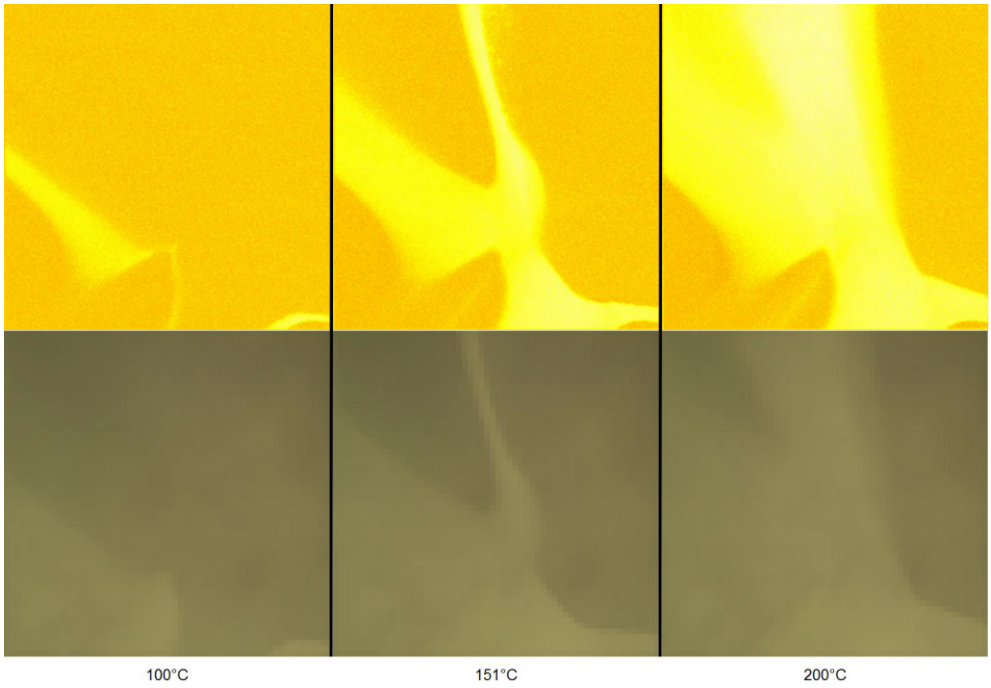

Figure 3.13: Still frames taken at different temperatures from the time lapse videos generated during a HTOMPT experiment on the GST library from sample #8294. The top row shows the false colour, intensity corrected frames generated by the Paradise software. The bottom row shows the corresponding real colour frames as taken by the camera during the experiment.

The measurement resource for parametric tests is the source/monitor unit (SMU). The SMU can force either voltage or current through the device under test (DUT) and simultaneously measure the corresponding parameter. Figure 3.14 below shows a simplified SMU circuit diagram. SMUs can be manufactured to measure currents of 1 fA or less, and therefore require triaxial outputs to minimise the leakage current that would otherwise exist between the signal wire and the outer shield of coaxial cables.

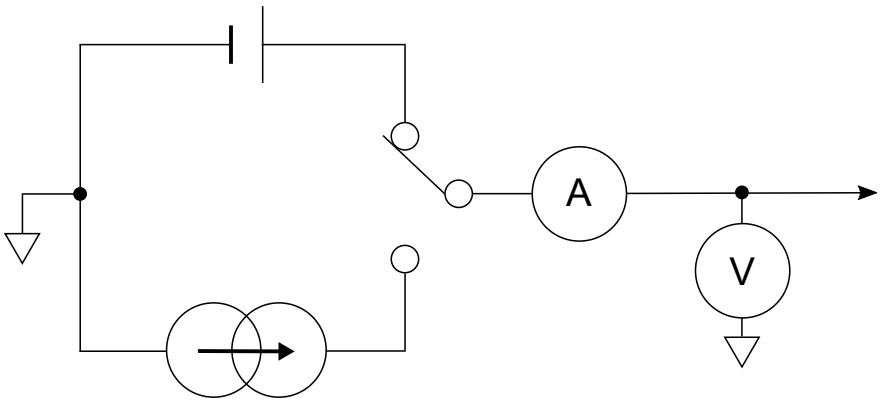

Figure 3.14: Circuit diagram of an SMU.

SMUs can be operated in three basic modes: Voltage source, current source and common. In common mode the SMU cannot perform any measurements and acts as a 0 V voltage source. In addition, it is possible to specify a device compliance setting, which is always opposite to that of the source setting in the SMU (e.g. current compliance while operating as a voltage source). When compliance is reached the SMU acts as a constant output source. This is to prevent accidental device damage that may otherwise occur if the compliance value is exceeded.

While SMUs are typically used for sweep measurements, time-domain and pulsed measurements are also possible. Their capabilities tend to be in the microsecond range and are therefore too slow for some measurement types. This is the case for example, of the pulses required to SET or RESET PCRAM devices. A semiconductor pulse generator unit (SPGU) is used instead to define pulse waveforms under a user-defined load (Figure 3.15). An SPGU can output high-frequency pulses in the nanosecond timescale required to electrically switch PCMs, and can be integrated into an I-V test workflow without the need to switch cables between measurements.

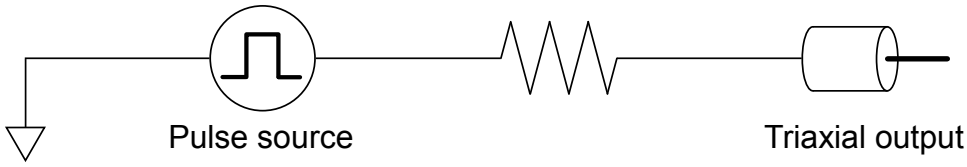

Figure 3.15: Schematic of a single-channel SPGU.

The I-V sweeps used to determine V_{th} for the materials in this project were performed using a B1500A Semiconductor Device Analyzer (Keysight Technologies) equipped with two medium power SMUs (series B1511B, Keysight) capable of ±100 V/±0.1 A output, and a minimum resolution of 0.5 µV/10 fA. In addition, a two-channel high-voltage SPGU (series B1525A, Keysight) was used to send pulses to the samples. The SPGU had an operating range ±40 V for pulse amplitude and 20 ns–10 s for pulse width. An SMU/SPGU selector (series B16440A, Keysight) allowed switching between I-V sweeps and pulse outputs automatically. The B1500A has a Windows XP-based computer integrated into its mainframe and is controlled by the EasyEXPERT software provided by the manufacturer. Collected data is stored automatically by the device in its own database, and can be exported into a variety of formats for further analysis.

Parametric tests were performed on chalcogenide PCMs deposited on platinized silicon

substrates. These substrates consist of a series of layers on top of which a 100 nm thick Pt layer has been deposited. The layers consist of Si, SiO_2, TiO_2 and Pt, hence the SSTOP shorthand used throughout this text. The conductive Pt layer functions as a bottom contact onto which a probe may be connected.

One of the aims of this PhD project was the integration of the B1500A system with 5600LS AFM, described in section 3.2.3, in order to develop a high-throughput test rig for PCRAM materials. The tip of the AFM probe was connected to one of the SMUs in the B1500A and delivered the output into the thin film samples. A full discussion of the development of this integrated system and the experimental results obtained will be presented in Chapter 6.

3.4 Summary

This chapter has presented the experimental systems used to synthesise and characterise combinatorial thin film libraries of phase-change materials. A PVD system introduced in section 3.1.1 has been used for the HT preparation of combinatorial libraries of chalcogenides. A HT workflow has also been introduced for the structural (XRD, Raman spectroscopy) and functional (resistivity, crystallisation) characterisation of these libraries. AFM has been used for film thickness determination as well as to scan the surface morphology of selected points of interest. In addition, the AFM together with a B1500A parametric tester are an integral part of the system developed for PCRAM parametric testing, which will be discussed in more depth in Chapter 6.

Chapter 4

High-Throughput Deposition and Screening of GST

4.1 Introduction

The Ge:Sb:Te system is one of the most studied PCMs, particularly along the GeTe–Sb_2Te_3 pseudobinary. The phase diagram along this tie line (Figure 2.10) was first reported by Abrikosov *et al.* in 1965.[34] They identified three intermediate compositions (GST225, GST124 and GST147) that solidified into a single compound from the melt. In their search for PCMs for optical memory in the early 1990s, Yamada *et al.* chose this pseudobinary because materials therein were expected to have "a facility for rapid crystallisation."[34] This choice had a major impact in the direction of phase-change memory research for the next two decades.

In their studies along the GeTe–Sb_2Te_3 pseudobinary Yamada *et al.* refined the phase diagram of the system and concluded that the crystallisation temperature T_x of these materials increased with increasing GeTe content.[34,52] A similar trend was observed for the laser-induced crystallisation time, with GeTe-rich compositions requiring longer pulses, albeit in the nanosecond scale. These results confirmed the facility of these materials to crystallise rapidly, which the authors attributed to the formation of the highly symmetrical, metastable, cubic phase into which they first crystallise.

Laurenzis *et al.* performed a combinatorial study of compositions near the GeTe–Sb_2Te_3 pseudobinary using samples prepared by a high-throughput sputtering technique. The resulting materials, which included the composition with the atomic ratio GST415, were studied for their optical phase-change dynamics and also reported a range of values for T_x.[52] Kalb *et al.* also reported on the crystallisation dynamics of a variety of chalcogenide glasses, which included GST225 and GST415.[69,196] Konstantinov *et al.* prepared GST225, GST124, GST147, GST326, and some substoichiometric compositions of these compounds, and reported on

their thermoelectric properties.[197] Sittner *et al.* carried on research along similar lines that included the GST72(10), GST(12)2(15) and GST(19)2(22) compositions.[198]

There have been few systematic studies outside the GeTe–Sb_2Te_3 pseudobinary reported in the literature. Navarro *et al.* studied the PCRAM characteristics of several materials in the Ge:Te system and found significant data retention improvement for materials that departed from the traditional GeTe composition.[199] Cheng *et al.* studied materials along the GeTe–Sb pseudobinary in the context of PCRAM devices. They identified GST121 as having the highest T_x along that pseudobinary but suffered from slow crystallisation speed. Instead, they choose GST212 as an optimum material with higher T_x compared to GST225 but faster crystallisation speed. Then they modified the Ge-content of GST212 along the Sb_2Te_3–Ge line in order to increase T_x without compromising other phase-change properties, and identified a Ge-rich GST212 "golden composition" that fit the desired characteristics.[93]

Micoulaut *et al.* applied BCT to the entire GST ternary space and identified a Te-rich region, delimited by the $GeTe_4$–$SbTe_4$ pseudobinary, where the materials lack enough Ge or Sb content to ensure local rigidity of the material structure and are therefore "flexible" because local deformations are allowed. They predicted that materials would undergo a rigidity transition past this pseudobinary because the constituent atoms would have more constraints than degrees of freedom. Therefore, rigidity would increase as function of Ge and Sb content.[88] Moreover, as a consequence of increased rigidity, materials would be expected to age more slowly and exhibit an increased resistance drift in the amorphous state.[200]

To date the only experimental study that covers a majority of the ternary GST space is that of Guerin *et al.* although their results remain unpublished at the time of writing.[190] Using an HT combinatorial methodology, they performed systematic studies of resistivity, crystallisation temperature and XRD.

The use of an HT approach allows for the rapid determination of trends in structural and functional relationships of the material under study over the entire compositional space. This methodology has been applied to the Ge:Sb:Te system with emphasis on pseudobinaries beyond GeTe–Sb_2Te_3 which may be used to gain further understanding of this material. The tie lines under consideration have been discussed in section 2.5 and their location within the GST compositional space is shown in Figure 2.8.

4.2 Synthesis and Compositional Analysis by EDS

Combinatorial thin film libraries of GST materials were deposited in growth chamber A of the HT-PVD system described in section 3.1.1. Germanium (99.9999%, Alfa Aesar) was loaded onto e-gun 1, while antimony (99.9999%, Goodfellow) and tellurium (99.9999%, Alfa Aesar) were loaded into k-cells 1 and 3 respectively. The source geometry is shown in the left panel of Figure 4.1. In order to achieve the maximum possible compositional spread in the samples, a +ang60ř angled wedge shutter was used at the e-gun 1 position. This would have the effect of modifying the deposition footprint of the Ge molecular beam as if the source were located in the k-cell 2 position, as depicted in the right panel of Figure 4.1.

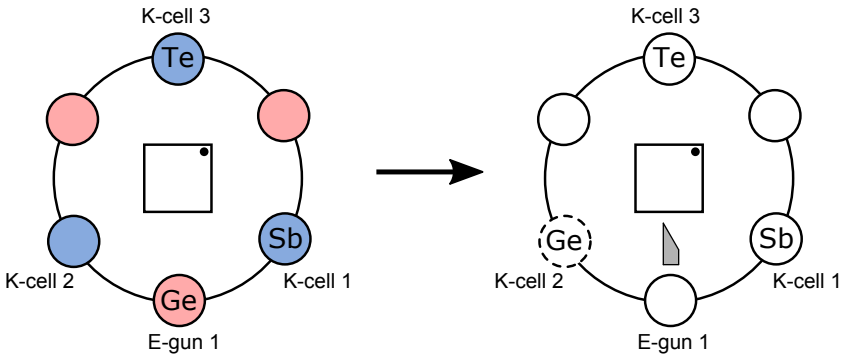

Figure 4.1: Top view of the source geometry for the HT deposition of GST. The left panel shows the physical location of the elemental sources. The right panel shows the source of the molecular beams after placing a +60° angled wedge (depicted) at the e-gun 1 position. Sample substrate position relative to each source is also shown.

The growth chamber was baked at 150 °C for 50 hours. After this process the base pressure inside the chamber was 7.5×10^{-9} Torr, within the UHV domain. Table 4.1 shows the typical deposition parameters for each element used after calibration. Samples were deposited as 29×29 mm continuous films on a variety of substrates, as per Table 3.1, provided by NOVA electronics. Before deposition substrates were cleaned in an ultrasonic bath for 15 min in a 3 : 1 solution of isopropanol and deionised water. The clean substrates were dried under a flow of Ar (99.999%, BOC).

The deposition time varied according to the desired thickness of the samples. It was found, through AFM measurements, that the mean thickness of a sample deposited over 30 min was 41 ± 7 nm. A sample deposited over 120 min had a mean thickness of 214 ± 37 nm. Knowing these rates it was possible to construct a calibration curve over which samples of

Table 4.1: Deposition parameters for the synthesis of GST libraries.

Element	Source	Rate	Temperature / °C	Wedge / mm
Germanium	e-gun	1.0 Å s^{-1}	–	35.0, +60°
Antimony	K-cell	–	610	36.5
Tellurium	K-cell	–	400	29.0

other desired thicknesses could be deposited.

For the synthesis of GST materials the aim was to deposit a large area of the ternary compositional space. A particular focus was the coverage of the six pseudobinary lines introduced in section 2.5 and shown in Figure 2.8. A series of HT EDS measurements was done on sample #8291 at an accelerating voltage of 12 kV. The measurements covered a 14×14 point grid, with a pitch between points of 1.867 mm. Figure 4.2 shows the atomic percent per element at each measurement point across the sample, where it is possible to observe the deposition gradient for each element. Of note is the deposition footprint of Ge, which exhibits the profile expected from having a +60° angled wedge.

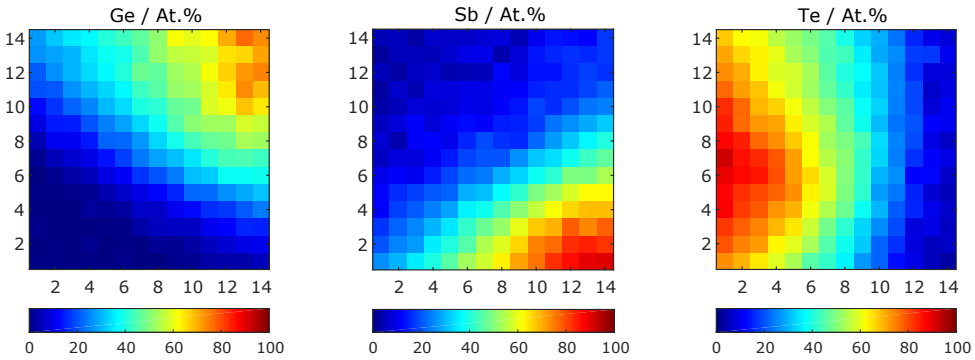

Figure 4.2: Composition gradient of each element in the combinatorial GST samples. The composition of each element is given in atomic percent, as determined by EDS. The X-Y coordinates correspond to the position of each measurement point within the sample.

Figure 4.3 shows the location of all 196 points within the ternary compositional space of GST. This plot has been used to determine the atomic percent range for each element in the

sample: Ge (0 – 78 at. %), Sb (3 – 90 at. %) and Te (5 – 91 at. %). Thus a large extent of all six targeted pseudobinary lines was covered within the produced samples.

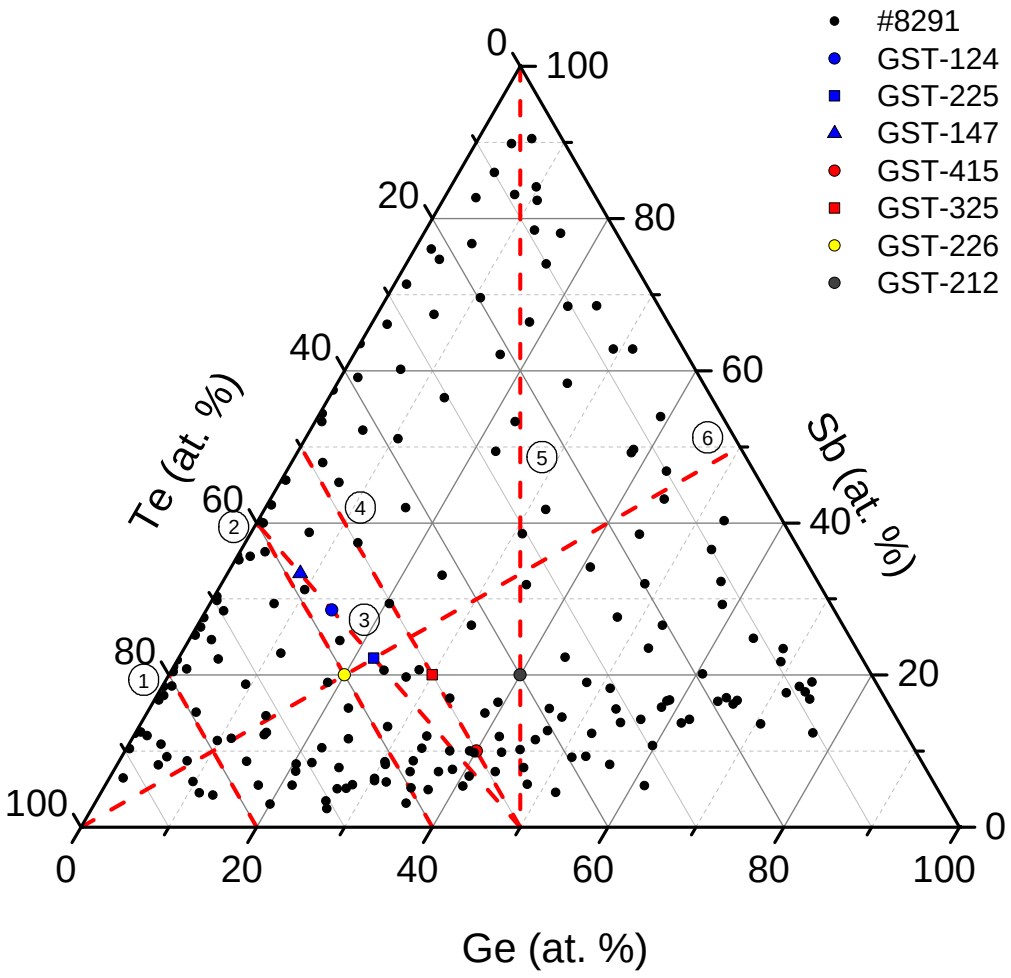

Figure 4.3: Ternary space coverage of deposited combinatorial libraries of GST. Black dots show the composition of all 196 points measured by EDS in sample #8291. Also highlighted are the locations of some compositions of interest as well as the following pseudobinary lines: (1) $GeTe_4$–$SbTe_4$; (2) Ge_2Te_3–Sb_2Te_3; (3) GeTe–Sb_2Te_3; (4) GeTe–SbTe; (5) GeTe–Sb; (6) GeSb–Te.

It is important to remember that while Figure 4.3 shows compositions as discrete points, there is a continuous gradient of compositions across the film. From the EDS measurements it was possible to calculate the rate of change for each element. This was done using an interpolation function in the Paradise software, which divided the combinatorial library in a grid of squares 1 mm by side. The results showed that for the central regions of the ternary space, where coverage is sparser, the rate of change in concentration was ~3 at. % mm^{-1}. Near the edges of the ternary space, where a higher density of points was found, the rate was ~1 at. % mm^{-1}. A list of compositions at each point quoted with their 95% confidence

levels is given in Appendix A.

4.3 Structural Characterisation

In this section the structural characterisation of the GST thin film combinatorial libraries obtained in section 4.2 will be discussed. The methods described in section 3.2 were used to characterise GST libraries in both their as-deposited condition and after *in vacuo* annealing at 200 °C. XRD was used to characterise the long-range order of the materials, whereas Raman spectroscopy was used to determine their short-range order. Analysis of the as-deposited samples will be presented first and will be followed by the discussion of the annealed materials.

4.3.1 As-deposited GST

4.3.1.1 X-Ray Diffraction

A combinatorial library of GST of 214 ± 37 nm thickness was deposited on a silicon nitride substrate for XRD analysis. Collection of the XRD patterns was performed as per the procedure described in section 3.2.1. A total of 196 XRD patterns were collected for sample #8296 and are all provided in Figure B.1 in the Appendix.

The vast majority of patterns did not exhibit any crystalline phases with the exception of a Te-rich area and a region that is centred on the Sb_2Te_3–Sb_3Te_2 compositions. Both regions were characterised for being poor in Ge content. Closer observation of the as-deposited sample (pictured in Figure 4.4) shows two areas of higher reflectivity that include these compositions. It is worth mentioning, however, that not all points within this reflective region show crystallinity. It is known that optical reflectivity in phase change chalcogenides is proportional to the volume fraction of the crystalline phase,[61] so it may be possible that those materials were not sufficiently crystalline to produce a well-defined diffraction pattern while still showing a change in optical reflectivity compared to the rest of the film.

The Te-rich, Ge-poor area of the film had a compositional range of 73−87 at. % Te, 12−26 at. % Sb and < 1 at. % Ge. Figure 4.5 compares the diffraction patterns of these compositions against the reference ICDD PDF card (01-079-0736) and shows that as Te content increases,

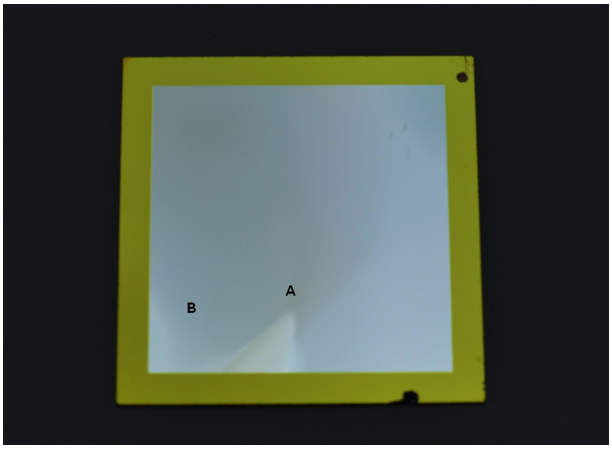

Figure 4.4: Photograph of an as-deposited GST library (#8296) with compositional points shown in Figure 4.3. The Sb_2Te_3–Sb_3Te_2 region is the bright area under A. The Te-rich region is the slightly brighter area to the left of B.

the crystallinity of the material approaches that of pure Te in the hexagonal $P3_121$ system. Suhrmann and Berndt demonstrated that it is possible to crystallise an amorphous film of Te, deposited by vapour condensation, after annealing to 25 – 30 °C.[201] This temperature range is similar to the operating temperature of the water-cooled manipulator in growth chamber A. Therefore it would be likely that any excess Te in this region of the film could begin to form a crystalline phase during deposition.

Materials of the Sb:Te system are expected to crystallise in the Sb_2Te_3 phase if they have an Sb content of 40–70 at. %.[202] For the Sb_2Te_3–Sb_3Te_2 region of sample #8296, the patterns shown in Figure 4.6 are harder to interpret as many diffraction peaks are missing. This is unsurprising as the material has not been annealed and remains only partially crystalline, as evidenced by the relative broadness of the peaks. Comparing these patterns against the PDF card 01-071-0393 of the Sb_2Te_3 material (which crystallises in the rhombohedral R3m space group), it appears that the preferred orientation of our thin film is along either (009) or (104) planes, as opposed to the (015) plane of the bulk material. The crystallisation temperature of Sb:Te materials has been reported to be near 100 °C for Sb_2Te increasing with Sb content to 250 °C for $Sb_{85}Ge_{15}$.[163] On the other hand, Fujimori *et al.* reported a crystallisation temperature ~110 °C for both Sb_2Te_3 and Sb_3Te_2.[202] It is possible that the activation energy of crystallisation for these compositions may be easier to overcome in the metastable materials deposited by co-evaporation of atoms in PVD.

The diffraction patterns of as-deposited GST225, GST124 and GST147 are also provided, for

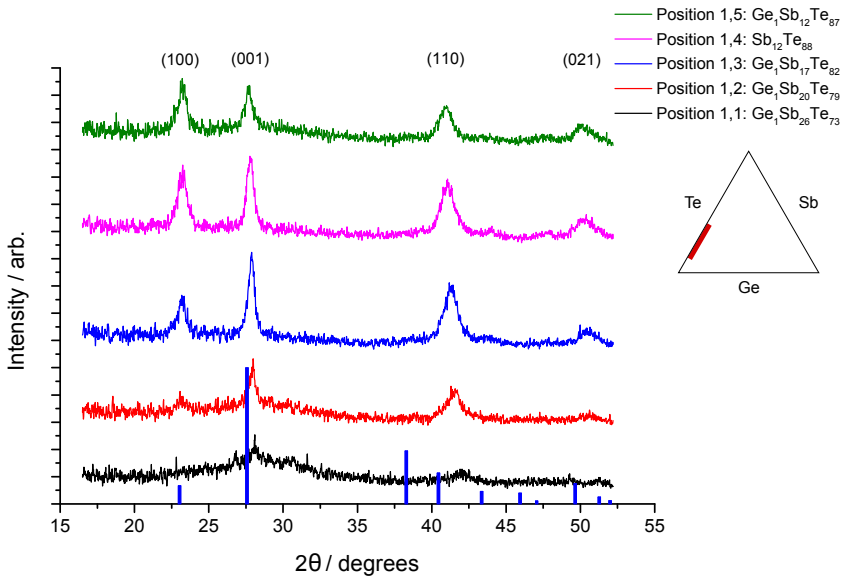

Figure 4.5: Diffraction patterns of selected compositions within the Te-rich, Ge-poor region of as-deposited sample #8296, with proposed peak assignments derived from the reference diffraction pattern for elemental Te (ICDD PDF 01-079-0736, blue vertical lines showing relative intensity). As the Te content of the film increases the predominant crystalline phase approached that of pure Te, which crystallises in the hexagonal $P3_121$ group. Ternary plot highlights the approximate location of the selected compositions within the ternary diagram of GST.

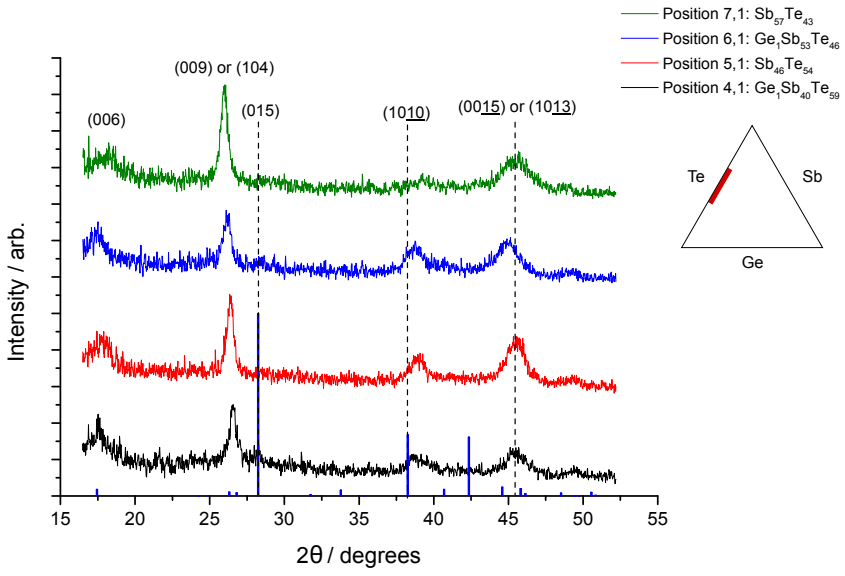

Figure 4.6: Diffraction patterns of selected compositions within the Sb_2Te_3–Sb_3Te_2 region of sample #8296, with proposed peak assignments derived from the reference diffraction pattern for Sb_2Te_3 (ICDD PDF 01-071-0393, blue vertical lines showing relative intensity). The Sb_2Te_3 material crystallises in the rhombohedral R3m space group. Ternary plot highlights the approximate location of the selected compositions within the ternary diagram of GST.

completeness, in Figure 4.7: No crystalline phases were observed. Materials throughout the rest of the sample follow a similar lack of long-range order and their diffraction patterns are therefore not shown individually.

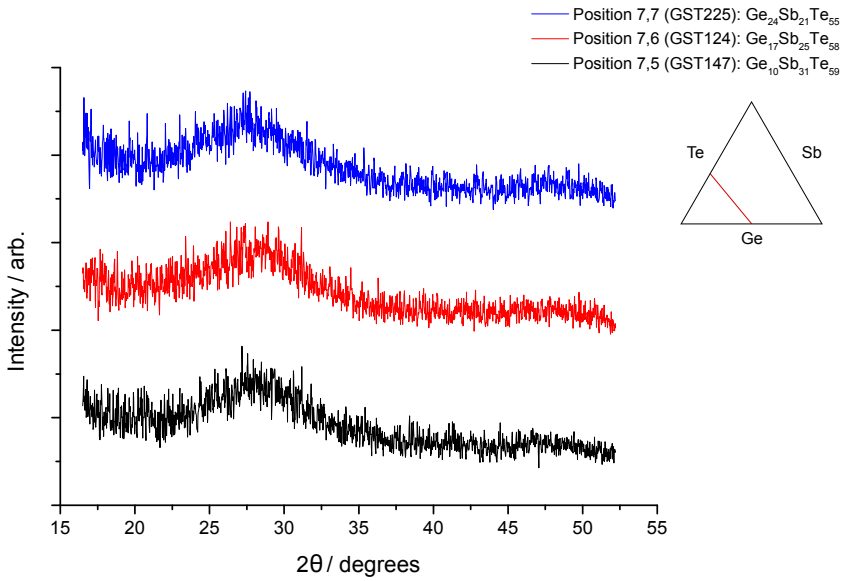

Figure 4.7: Diffraction patterns of GST147, GST124 and GST225 in as-deposited GST sample #8296. As expected, no diffraction peaks were observed. Ternary diagram highlights the approximate location of the GeTe–Sb_2Te_3 pseudobinary line along which these GST compositions can be found.

4.3.1.2 Raman Spectroscopy

Raman scattering measurements were performed on an as-deposited library on a silicon substrate (#8302). The measurements were performed using the apparatus described in section 3.2.2 covering a $100-250\,cm^{-1}$ Raman shift range collected over four 60 s acquisitions. A low laser power of 1% (0.25 mW) was used to prevent thermal annealing of the sample and a grating of 1800 grooves/mm was used.

A total of 196 Raman spectra were collected on sample #8302 which are all provided in Figure B.2 in the Appendix. In general the main features observed across the spectra are two distinct peaks: One centred at approximately $120\,cm^{-1}$, within a range of $100-135\,cm^{-1}$, and another with highest intensity observed at roughly $140\,cm^{-1}$ within a $135-180\,cm^{-1}$ range. These bands were defined in the Paradise software in order to calculate the frequency at which the local intensity maxima for each band were observed. It is important to remember, however, that an individual spectrum may show peaks within either one or both of the

bands. As result, it may be possible that a local maximum calculated by the software may not correspond to an actual peak in the spectrum. Figure 4.8 shows the Raman shift of the local maxima calculated for both bands across the GST ternary space.

For the 120 cm^{-1} band, the peaks shift to higher frequency with increasing Sb content, as elemental amorphous Sb only shows one broad band centred at 145 cm^{-1},[203] and therefore only the rising edge of the peak is seen within this band. With increasing Te content the peak is found at frequencies between 120 – 130 cm^{-1} which is close to the peak observed for amorphous elemental Te at 120 cm^{-1},[204] but also to A_1 modes of $GeTe_4$ tetrahedra observed on materials such as GST225 at 130 cm^{-1}.[205] Finally, with increasing Ge content the peaks are red shifted in a way similar to the Raman spectra of Ge-rich materials in the Ge:Te system,[206,207] which show a broad band that begins at its highest point near 70 cm^{-1} and extends to 300 cm^{-1}.

The peak shifts within the 140 cm^{-1} band show a different pattern where the trends in peak position are more scattered across the film. With increasing Te content the peak position gets closer to the second vibration of elemental Te at 146 cm^{-1}.[204] Sb-rich compositions have peak positions between 145 – 150 cm^{-1} corresponding to either strongly polarisable modes in $SbTe_3$ structures or to the amorphous elemental Sb broad peak at 145 cm^{-1}.[203] For Ge-rich compositions the expected peak near 150 cm^{-1} sometimes has lower intensity than Sb-related peaks that appear even at low Sb concentration, which leads to the scattered peak positions seen in that section of the film. The underlying trend, however, appears to be a blue shift of the peak as the Ge content increases.

Most of the spectra conform well to previous Raman studies of amorphous materials within the GST system. Figure 4.9 shows the spectra of two Sb-rich compositions with a broad peak between 120 – 180 cm^{-1}. This is in agreement with the results reported by Lannin and Rech-Esser, although they did not provide vibrational mode assignments.[203,208] Lannin, however, described the Sb spectrum as showing "non-molecular" qualities[203] due to the lack of clear polarisation modes, especially when compared to the spectrum of amorphous As which was reported to show both molecular and "non-molecular" qualities. The small shoulder that appears on the rising edge of the broad peak, near 120 cm^{-1}, may be due to the presence of $GeTe_4$ tetrahedra[205] as the material at these positions has a degree Ge and Te doping.

The spectra of Te-rich compositions are shown in Figure 4.10 is in good agreement with the

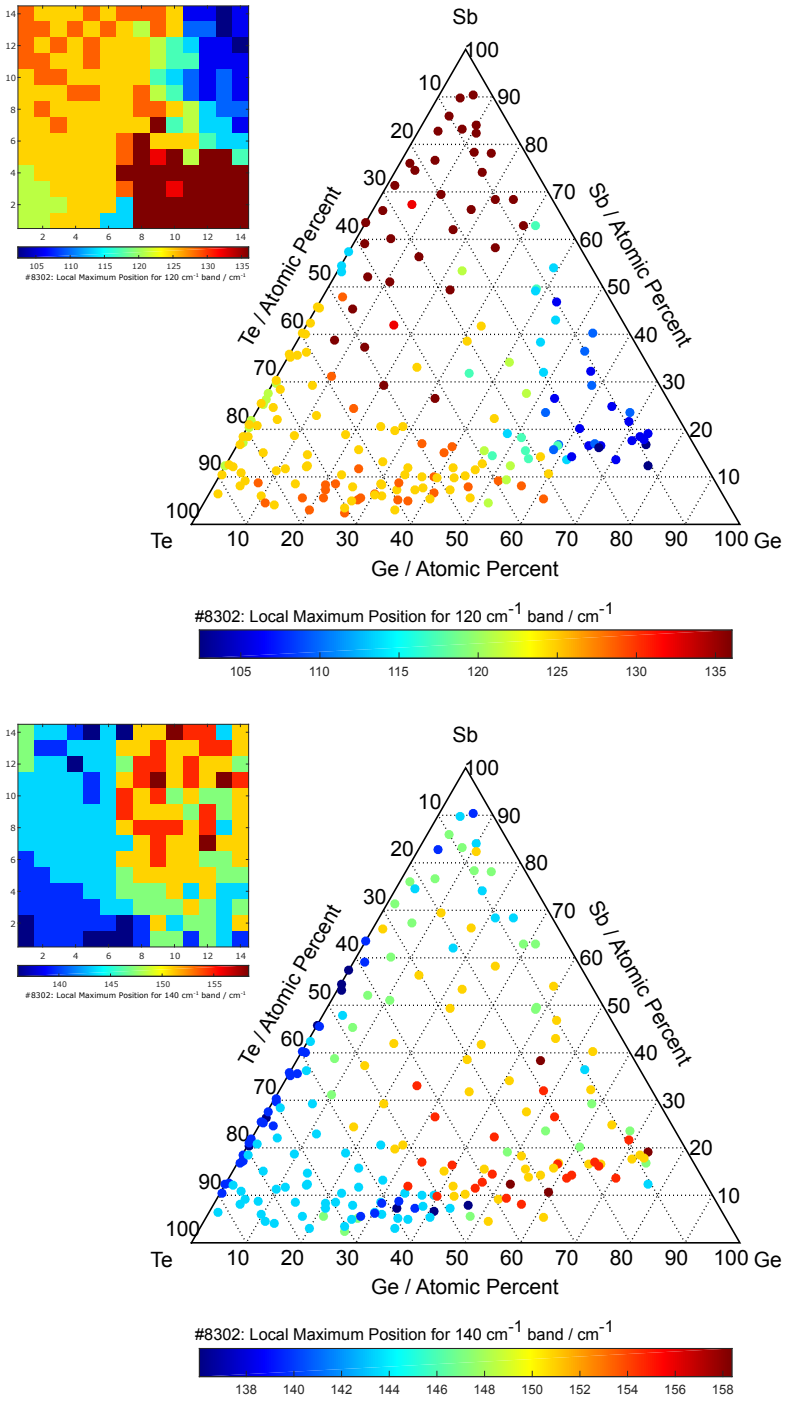

Figure 4.8: Raman shift of the local maxima calculated within the Raman bands centred at 120 cm^{-1} (top diagram) and 140 cm^{-1} (bottom diagram) across the GST ternary space for the as-deposited sample #8302. The square inset next to each ternary diagram shows the same information across the thin film: X-Y coordinates correspond to the position of each measurement point within the sample.

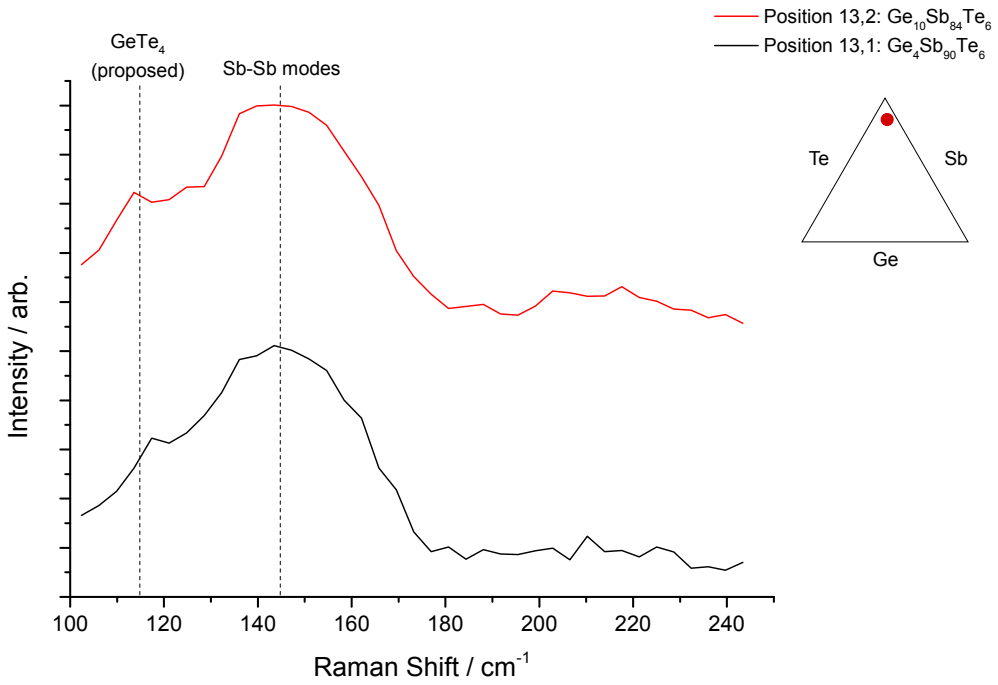

Figure 4.9: Raman spectra of selected Sb-rich compositions of the as-deposited GST sample #8302 with proposed mode assignments for the peaks found near 120 cm^{-1} and 145 cm^{-1}. Ternary plot highlights the approximate location of the selected compositions within the ternary diagram of GST.

results reported by Pine and Dresselhaus.[204] They assigned the 120 cm^{-1} peak to an A_1 mode and the 146 cm^{-1} peak to a doubly-degenerate E mode. This region of the sample showed some semicrystalline characteristics, as described in section 4.3.1.1. However, because the Raman peaks in amorphous and crystalline Te only differ in intensity (amorphous Te peaks are more intense) it would require the use of polarised Raman to assess the crystallinity of the material in our samples. The broad tail of the 146 cm^{-1} peak may be due to the existence of highly polarisable $SbTe_3$ pyramidal structures in the material. Modes belonging to $GeTe_4$ pyramids may also exist but would be masked within the much more intense $SbTe_3$ modes.

The Raman spectra of compositions close to the Ge:Te system are shown in Figure 4.11. For pure GeTe, the two reported peaks within our experimental range correspond to the A_1 mode of $GeTe_{4-n}Ge_n$ ($n = 1, 2$) corner-sharing tetrahedra at 126 cm^{-1} and the A_1 mode of edge-sharing $GeTe_4$ tetrahedra at 162 cm^{-1},[209] however the presence of defective octahedral Ge sites has not been ruled out.[205] The spectra for the Te-rich and Ge-rich compositions of the Ge:Te system broadly agree with those reported by Carria *et al.*,[206,207] although the presence of modes belonging to $SbTe_3$ pyramidal structures can also be observed near 145 cm^{-1}.

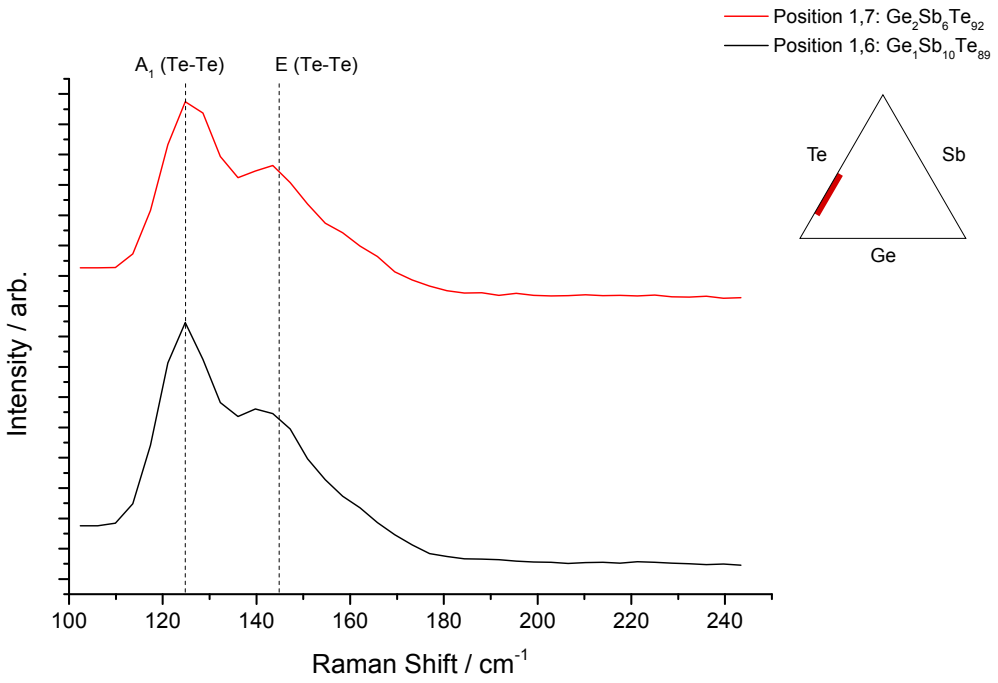

Figure 4.10: Raman spectra of selected Te-rich compositions of as-deposited GST sample #8302, with proposed vibrational mode assignments for the peaks found at 120 cm^{-1} (A_1) and 146 cm^{-1} (E). Ternary plot highlights the approximate location of the selected compositions within the ternary diagram of GST.

The Raman spectra of the Sb_2Te_3–Sb_3Te_2 region of sample cover some of the semicrystalline compositions described in section 4.3.1.1. These compositions include stoichiometric Sb_2Te_3, where it was found that the crystalline structure was approaching that of the rhombohedral R3m space group. The Raman spectrum of Sb_2Te_3 given in Figure 4.12 confirms the semicrystalline nature of the material, where the observed peaks are between those of amorphous and crystalline Sb_2Te_3. The broad band covering the 100 – 170 cm^{-1} range shows an intense peak near125 cm^{-1} similar to that of Te–Te A1 vibrations in pure Te (cf. Figure 4.11). The shoulder on the falling edge of the peak, near 145 cm^{-1}, would correspond to Sb–Te vibrations within amorphous $SbTe_3$ pyramidal sites. Finally, a second shoulder near 165 cm^{-1} may belong to an incipient $A_{1g}(2)$ mode in crystalline $SbTe_3$ pyramids.[210] This interpretation would explain the existence of the semicrystalline state through stabilisation by transient Te–Te bonds during the formation of the rhombohedral cell.

On the other hand, the spectrum of the Sb_2Te material resembles that of the amorphous Sb_2Te_3 material as given by Němec *et al.*[205] with a broad peak near 145 cm^{-1}. At the time of writing no reports have been found that attempt the Raman peak assignment of amorphous

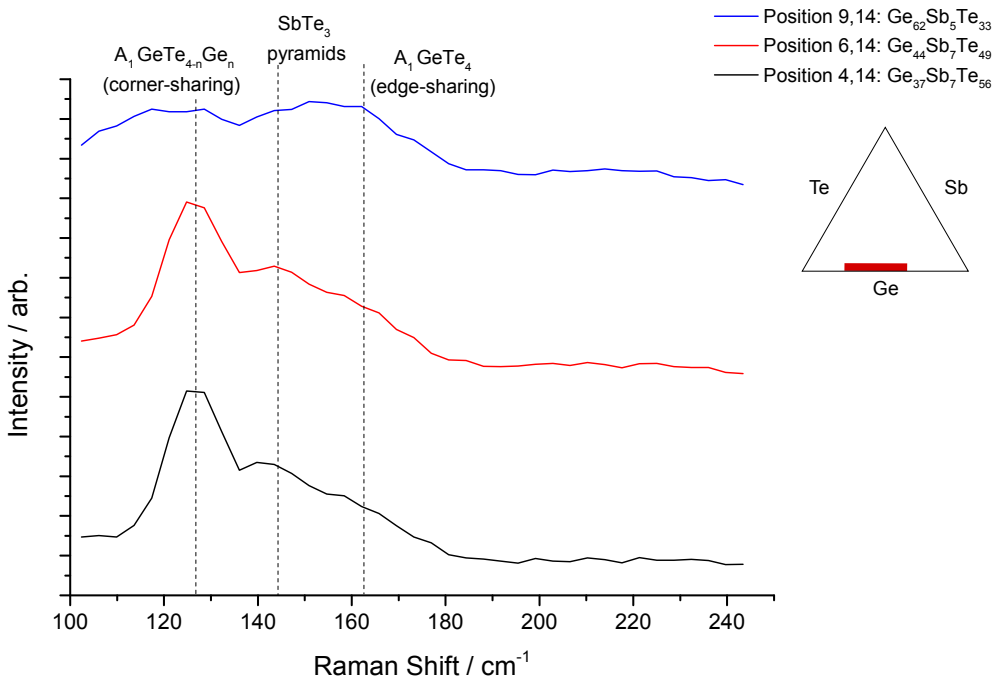

Figure 4.11: Raman spectra of selected compositions near the Ge_xTe_{1-x} system in as-deposited GST sample #8302. Highlighted are the vibrational modes at 126 cm^{-1}, and 162 cm^{-1} corresponding to A_1 modes of different types of Ge–Te tetrahedra. It is proposed that the mode seen near 145 cm^{-1} would belong to $SbTe_3$ pyramids that arise from the low levels of Sb doping in the material. Ternary plot highlights the approximate location of the selected compositions within the ternary diagram of GST.

Sb_2Te_3 to specific vibrational modes. Therefore, the current discussion this peak was assigned to Sb–Te stretches within $SbTe_3$ pyramidal sites, as proposed by Andrikopoulos *et al.* by comparison to the isomorphous (to Sb_2Te_3) Sb_2S_3 system.[102] However, Sosso *et al.* also present an argument derived from AIMD simulations that these vibrations could be due to Sb–Te bonds within defective octahedral structures.[211]

Having discussed the endpoint compositions of the GeTe–Sb_2Te_3 pseudobinary, it would not be out of place to assume that the Raman spectra of amorphous GST materials along this tie line would include some of the vibrational modes already discussed. Figure 4.13 shows the spectra of GST225, GST124 and GST147 where two distinct peaks can be observed at 129 cm^{-1} and 150 cm^{-1}. The 129 cm^{-1} peak has been assigned to A_1 modes of $GeTe_4$ tetrahedra[212,213] while studies on GeTe suggest this assignment can be further refined to $GeTe_{4-n}Ge_n$ ($n = 1, 2$) corner-sharing tetrahedra.[209] The intensity of this band would be expected to decrease with decreasing GeTe content in the material, a fact that is observed in the transition from GST225 to GST124. The broad peak centred at 150 cm^{-1} has previously

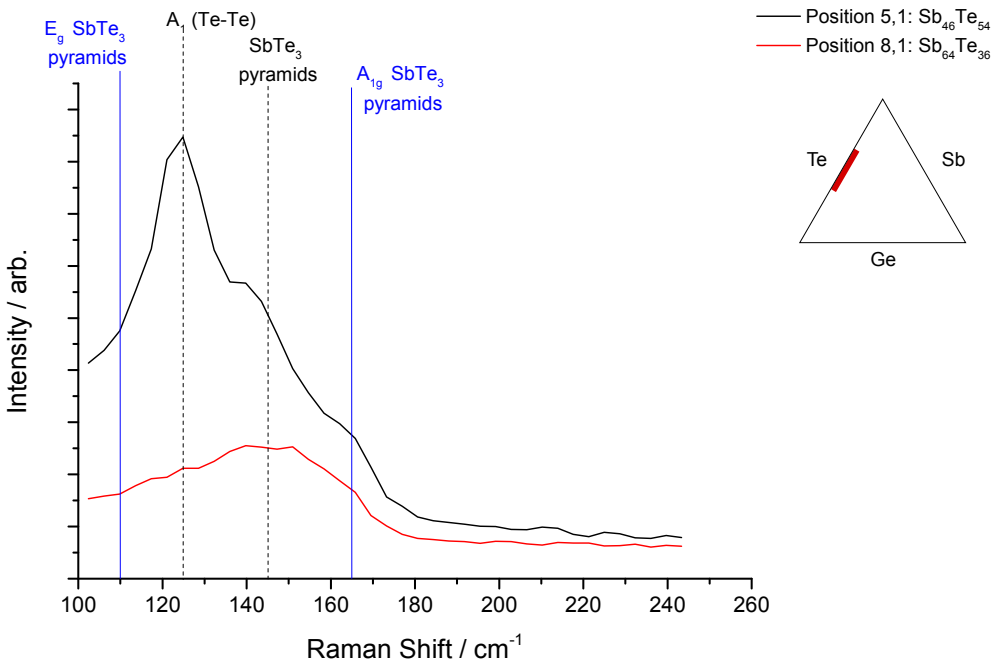

Figure 4.12: Raman spectra of selected compositions within the Sb_2Te_3–Sb_3Te_2 region of as-deposited GST sample #8302. Blue vertical lines show the position of vibrational modes in crystalline Sb_2Te_3 (110 cm^{-1} and 165 cm^{-1}). The dotted vertical lines show the proposed vibrational mode assignments in the experimental spectra. The top spectrum belongs to the semicrystalline Sb_2Te_3 material (as shown in Fig. 4.6) which appears to corroborate that the short-range order of the material within the sample is neither that of an amorphous or a fully crystalline species. The bottom spectrum belongs to a fully amorphous material close to the Sb_2Te stoichiometry. Ternary plot highlights the approximate location of the selected compositions within the ternary diagram of GST.

been assigned to Te–Te chains,[212] however experimental EXAFS[214] data and Monte Carlo simulations[90] have shown that homopolar Te–Te and Sb–Sb bonds are not significant in the amorphous structure of GST. Instead this band should be assigned to vibrations in $SbTe_3$ pyramids, with masked contributions from $GeTe_4$ tetrahedra (due to the lower intensity of these modes).[102,205] AIMD simulations by Sosso *et al.* instead propose that the vibrations on both bands should be assigned to defective octahedral Sb–Te structures, and that vibrations due to $GeTe_4$ tetrahedra would be found near 190 cm^{-1} masked by the more intense Sb–Te modes.[211] This interpretation, however, is not supported by our experimental data which show no distinguishable modes at 190 cm^{-1}.

DFT calculations have quantified the higher polarisability of the Sb–Te bonds relative to Ge–Te and Ge–Ge/Sb bonds leading to a more intense Raman response.[211] In addition, an argument has been presented by Andrikopoulos regarding the weakening of the Ge–Te

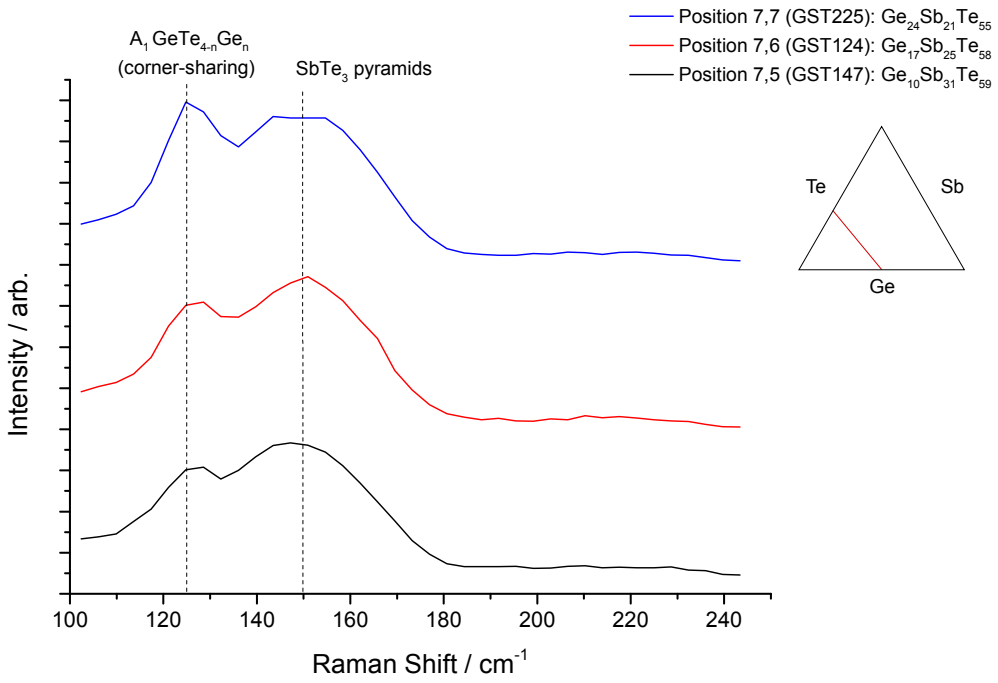

Figure 4.13: Raman spectra of GST225, GST124 and GST147 compositions of in as-deposited GST sample #8302. Highlighted are the proposed vibrational mode assignments for the peaks found at 129 cm^{-1} and 150 cm^{-1}. Ternary diagram highlights the approximate location of the $GeTe–Sb_2Te_3$ pseudobinary line along which these GST compositions can be found.

modes in presence of Sb–Te components by analogy to the (1-x)GeS_2–xSb_2S_3 system.[102] Here, the vibrations attributed to $GeS_{4-n}Ge_n$ ($n = 0, 1, 2, 3, 4$) have been reported to weaken in the presence of low concentrations of Sb_2S_3.[215] To test for this hypothesis, the logarithm of the intensity for each band shown in Figure 4.8 has been mapped across the GST ternary space in Figure 4.14.

Interestingly, the intensity of both bands decreases monotonically along the lines of increased material rigidity in the ternary space. This trend can be seen more easily in Figure 4.15 which plots the Raman peak intensity of the 120 cm^{-1} band along the GeSb–Te tie line. As the Te concentration drops across the ternary, the number of Ge–Ge/Sb bonds in the amorphous matrix increases and the Sb–Te modes would be expected to become less dominant. Moreover, from Figure 4.15 it would seem that this transition would begin at the intersection with the Ge_2Te_3–Sb_2Te_3 pseudobinary. However, closer inspection of the individual spectra from the more rigid region (i.e. increasingly Ge-rich and Te-poor) of the ternary space reveals that the 120 cm^{-1} band, containing Sb–Te modes, remains more intense than the Ge–Te modes. An example of this behaviour may be seen in Figure 4.11 for the Ge-rich material. These

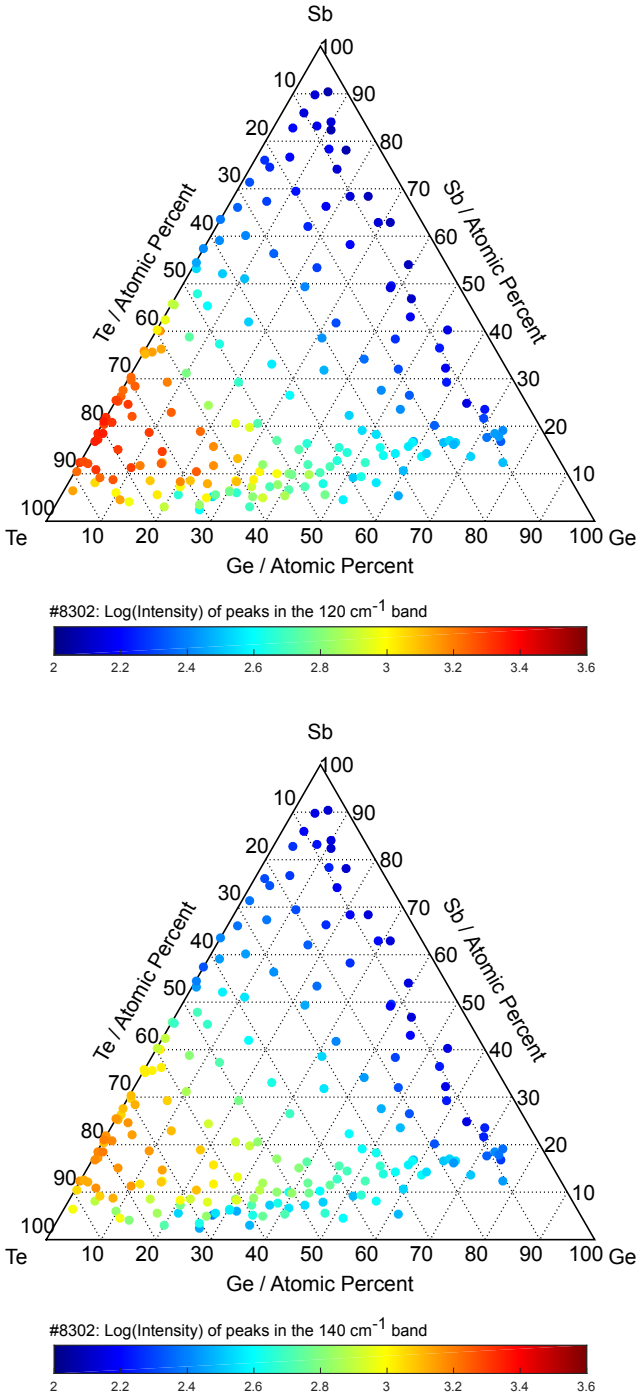

Figure 4.14: log(Intensity) of the peaks within the Raman bands identified in Figure 4.8 which are centred at 120 cm^{-1} (top) and 140 cm^{-1} (bottom) across as-deposited GST sample #8302.

modes remain clearly visible even at the lowest concentration of Sb+Te which was 23 at. %. Therefore it would not be unreasonable to assume that Sb–Te structures would have the effect of weakening the Raman response of Ge–Te structures within amorphous GST materials in a fashion similar to Sb–S structures in the GeSbS system, and that this effect becomes more pronounced as the material becomes more structurally constrained. The implication of this finding would be that Raman spectroscopy techniques should not be used in isolation to characterise the short-range order of amorphous chalcogenides containing Sb (and possibly As) and that the results thus obtained should compared to those obtained through other experimental techniques such as EXAFS.

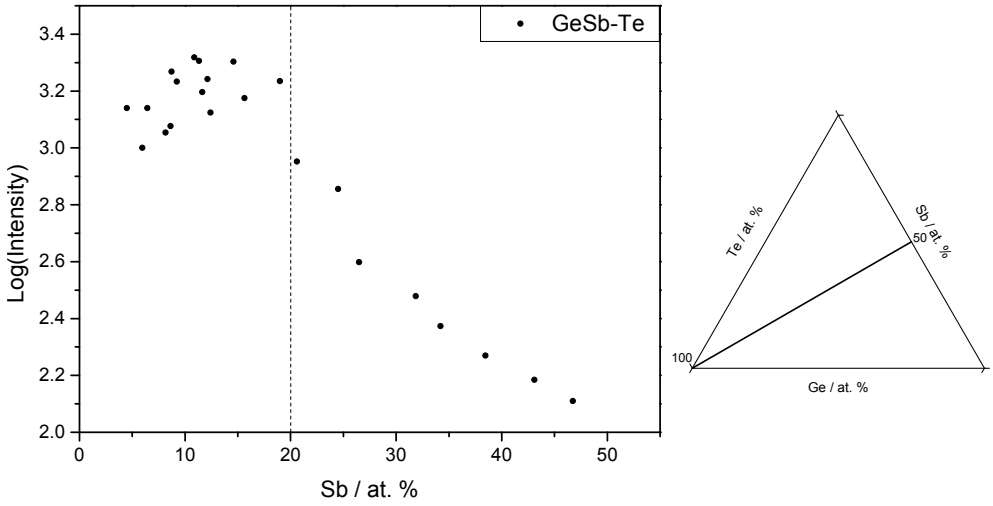

Figure 4.15: Logarithm of the maximum peak intensity within the 120 cm^{-1} Raman band along the GeSb–Te pseudobinary (within 5 at. %). The vertical dotted line shows the intersection with the Ge_2Te_3–Sb_2Te_3 tie line, at which point the intensity of the band begins to decrease. The ternary plot shows the position of the GeSb–Te pseudobinary within the GST ternary space.

4.3.2 GST Annealed at 200 °C

4.3.2.1 X-Ray Diffraction

Combinatorial libraries of GST of 214 ± 37 nm thickness were deposited on silicon nitride substrates for XRD analysis. After deposition a sample was annealed *in vacuo* for 20 min at 200 °C in the manipulator of growth chamber A (#8299). Collection of XRD patterns was performed as per the procedure described in section 3.2.1.

The 196 diffraction patterns of sample #8299 are all provided in Figure B.3 in the Appendix.

Most compositions showed crystalline phases with well-defined peaks with the exception of a Te-poor region (< 30 at. %) near the top right corner of the film, which can be identified in Figure 4.16. A pair of dark brown regions also appeared on the top left corner and lower left side of the film, and while analysis showed both of them contained crystalline phases, the origin of this colouration could not be satisfactorily explained.

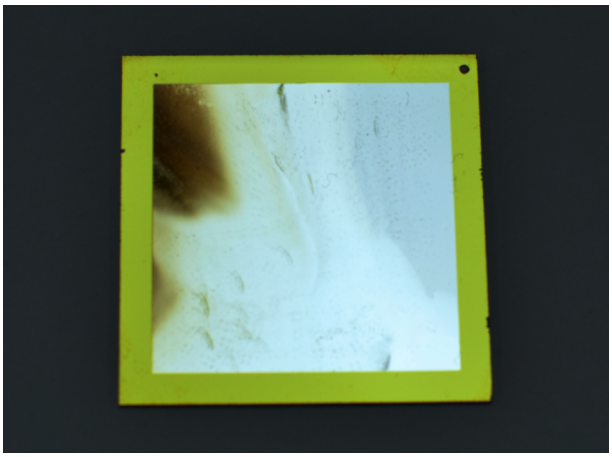

Figure 4.16: Photograph of a GST library annealed at 200 °C for 20 min (#8299) with compositional points shown in Figure 4.3. The Te-poor region that did not crystallise is the less reflective area on the top right corner of the sample.

Given the large compositional spread covered in our samples, the identification of phases in individual diffraction patterns can be an extended and difficult process. In combinatorial thin films with gradual compositional change, a mixture of phases will be found together with instances of preferential orientation that may lead to missing reflections. Moreover, planar stress in thin films may shift peak positions a few degrees relative to the reference powder samples. To help overcome these limitations a multivariate analysis algorithm has been used to model and analyse the annealed GST XRD data. This analysis produced five components which could be related to either one or two known structures each, thus creating a map of phases across the sample.

The multivariate analysis, as implemented in the Paradise software, required the reduction of the 2θ range of the patterns to $16° - 50°$ to remove any incomplete peaks near the edge of individual patterns that may confound the model. In addition, background correction of all 196 patterns using a single spline curve was performed. The number of components within the data was calculated with the Principal Component Analysis (PCA) algorithm from the TOMCAT toolbox in MatLAB.[216] The number of components was selected such

that the variance within the dataset would be maximised, while still producing components that could be interpreted using reference spectra. The five components determined by PCA were processed using the multivariate curve resolution-alternating least squares method produced by Jaumot *et al.*[217] Non-negativity constrains were placed so that the sum of phases thus calculated added up to 100% at each point. Limitations of this model arise from the shifting of peak positions across the sample due to the changing compositional gradient. Moreover, several phases may exhibit reflections at the same 2θ angle corresponding to different planes, but the model may interpret as belonging to the same phase. Therefore, care had to be exercised before the results of the model could be accepted as valid.

Component 1 of the PCA model is related to the amorphous phase of the film containing primarily compositions within the Te-poor region of the sample (< 30 at. % Te), which failed to crystallise at 200 °C, as shown in Figure 4.16. The diffraction patterns of two compositions within this component are shown in Figure 4.17, together with the concentration map of this phase across the film, expressed as a percentage of the sum of all Components.

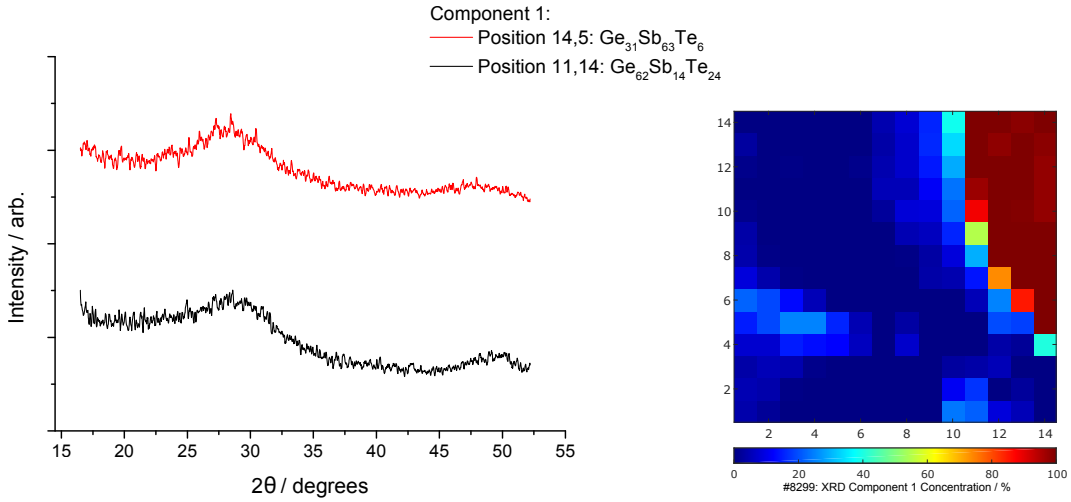

Figure 4.17: Diffraction patterns of two selected compositions within Component 1 of the PCA model of annealed GST sample #8299. These show that no crystallisation was achieved at the annealing temperature of 200 °C. The sample map to the right shows the concentration of Component 1 across the sample, given as a percentage of the sum of all five Components.

Two different hexagonal phases were contained within Component 2, which extended from the lower right portion of the sample towards the middle left. The lower region was composed primarily of hexagonal Sb_2Te-type materials crystallised in the hexagonal P3m1 space group, as per PDF 00-057-0492. The second group contained hexagonal phases of materials

found on GeTe–Sb_2Te_3 pseudobinary, such as GST225, which also crystallised in the P3m1 space group as per PDF 01-073-7758 (for GST225) and PDF 01-076-8867 (for GST147). While compositionally different, the reference diffraction patterns of both Sb_2Te and GST-type materials share several similarities in peak position and intensity, as may be seen in Figure 4.18.

Component 3, found primarily in the bottom left corner of the sample, covered Sb_2Te_3-type materials in the rhombohedral R3m space group, as per PDF 01-071-0393. In addition, this Component also contained a minority of Sb_2Te materials that crystallised in the hexagonal P3m1 space group, as per PDF 00-057-0492, similar to those found in Component 2. While these materials belong to physically distinct phases, the PCA model grouped them within the same Component due to the similarity of their diffraction patterns. This similarity may be seen in Figure 4.19, which shows selected diffraction patterns of both types of material within this component.

Two distinct phases were also found within Component 4, which extended from the top left corner towards the centre of the sample. The first one included GeTe-type materials that crystallised in the rhombohedral R3m space group, as per PDF 00-047-1079. The second phase includes materials that share the characteristic of having both Sb and Te content < 40 at. % and < 50 at. % respectively. It is proposed that, under our experimental annealing temperature, these materials crystallise in a cubic $Fm\bar{3}m$ space group similar to that of cubic GST225 as per PDF 01-073-7757. Figure 4.20 shows representative diffraction patterns of both types of material within this component and their proposed peak assignments.

Finally, Component 5 includes Sb-rich materials located in the bottom right corner of the sample. These crystallise in the rhombohedral R3m space group and possess a structure similar to that of elemental Sb as per PDF 00-035-0732. This component expands towards the middle region of the sample and might be indicative of Sb segregation as Sb atoms compete with Ge for spaces in the anion sublattice of GST. Figure 4.21 shows the location of this component within the sample together with diffractograms from representative compositions.

Careful observation of the Component concentration maps provided in Figures 4.17 to 4.21 will reveal a degree of overlap between neighbouring Components of the model. This may be expected, as the transition between phases would follow a gradual pattern analogous to the change in composition across the film. This observation is also consistent with Yamada's ob-

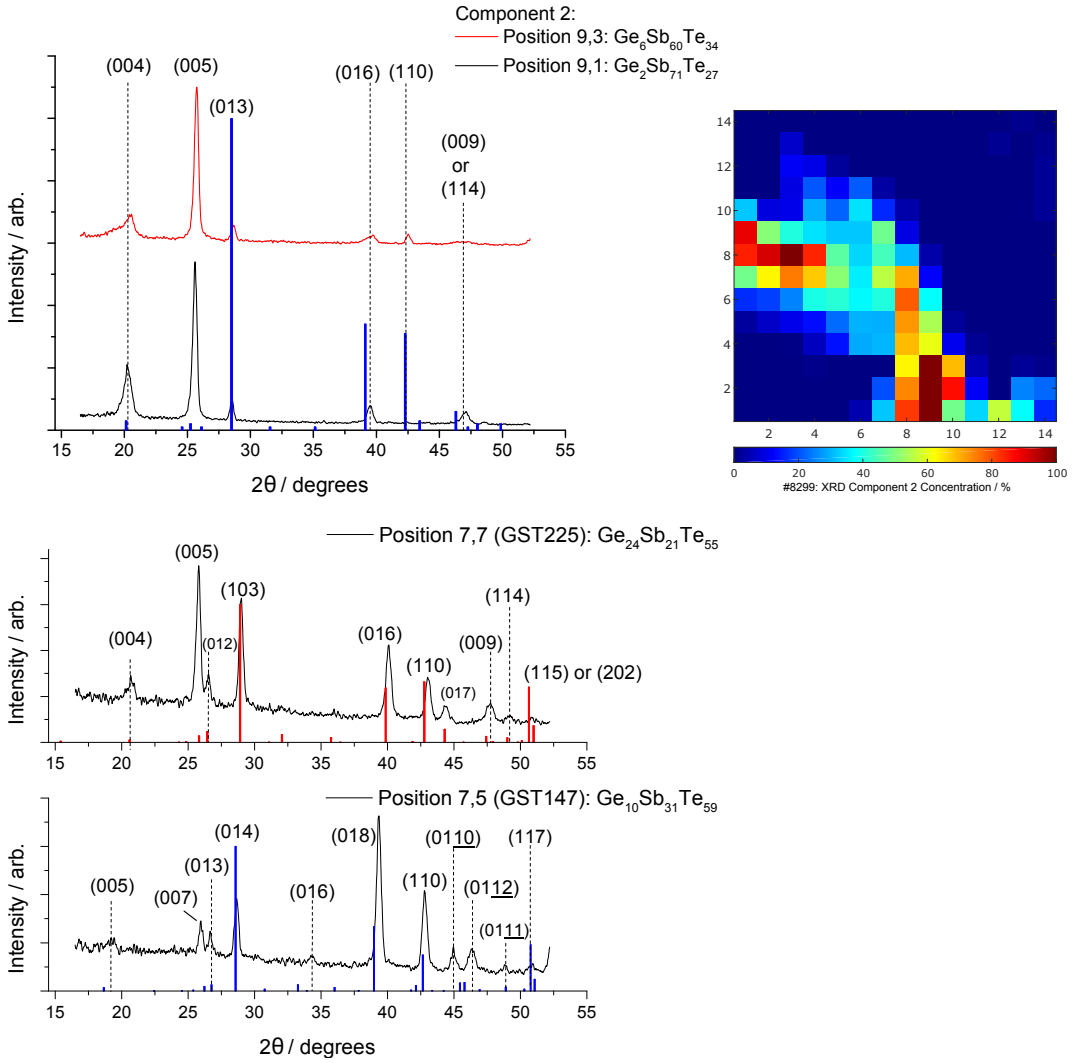

Figure 4.18: Diffraction patterns of three selected compositions within Component 2 of the PCA model of annealed GST sample #8299. The top graph shows a Sb_2Te-type material crystallised in the hexagonal P3m1 space group with proposed peak assignments (PDF 00-057-0492, blue vertical lines showing relative intensity), which shows that crystal alignment is along the (005) plane as opposed to the (013). The middle graph shows the diffraction pattern of GST225 which also crystallised in the P3m1 space group (PDF 01-073-7758 red vertical lines showing relative intensity). Similarly to the Sb_2Te-type material, alignment is along the (005) plane as opposed to the (013). Finally, the bottom pattern belongs to GST147 with proposed peak assignments (PDF 01-076-8867, blue vertical lines showing relative intensity). For this material, which crystallised in the P3m1 space group, alignment is along the (018) plane as opposed the (014). The sample map to the right shows the concentration of Component 2 across the sample, given as a percentage of the sum of all five Components.

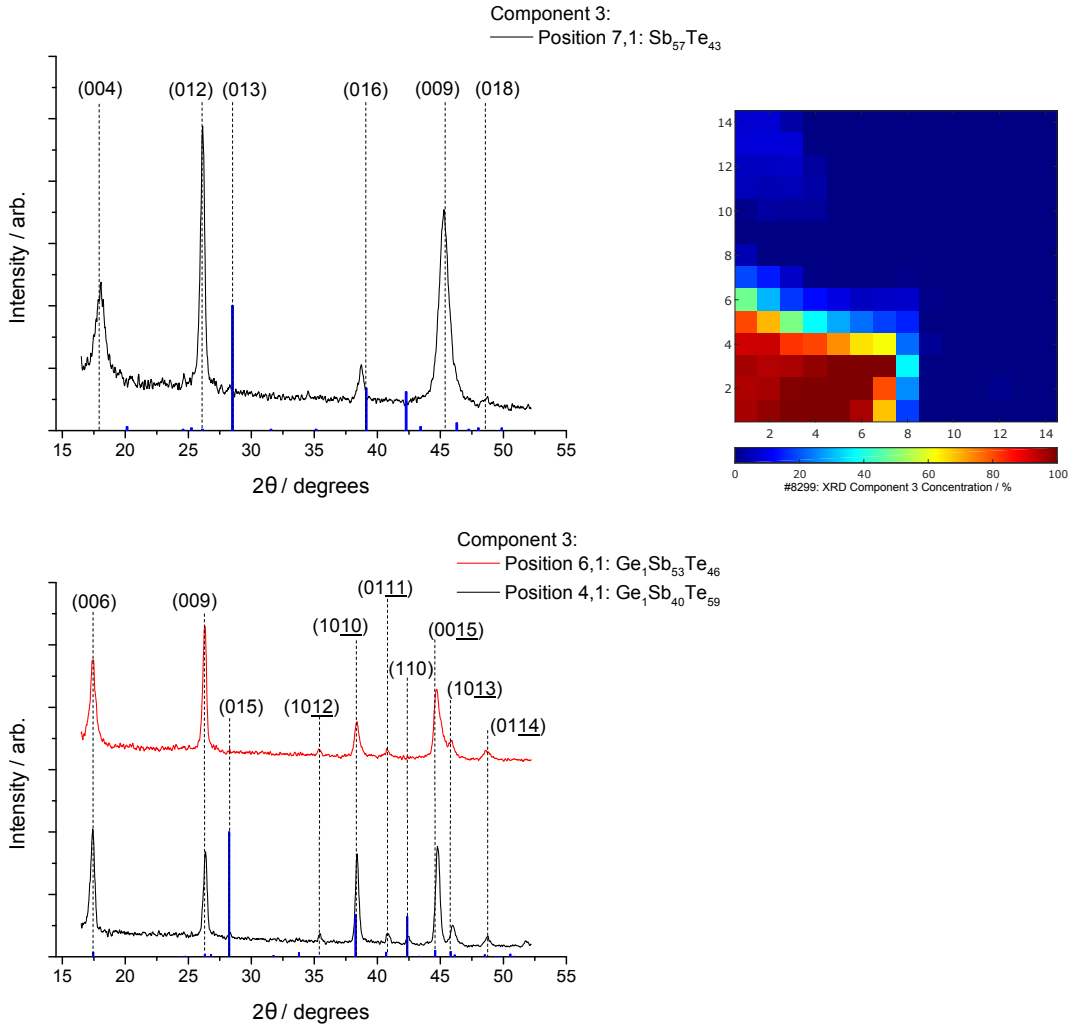

Figure 4.19: Diffraction patterns of three selected compositions within Component 3 of the PCA model of annealed GST sample #8299. The top graph shows a Sb_2Te-type material crystallised in the hexagonal P3m1 space group with proposed peak assignments (PDF 00-057-0492, blue vertical lines showing relative intensity), which shows that crystal alignment is along the (012) plane as opposed to the (013). The bottom graph shows a Sb_2Te_3-type material crystallised in the rhombohedral R3m space group also with peak assignments (PDF 01-071-0393, blue vertical lines), showing the material is aligned the (009) plane as opposed to the (015) plane. The sample map to the right shows the concentration of Component 3 across the sample, given as a percentage of the sum of all five Components.

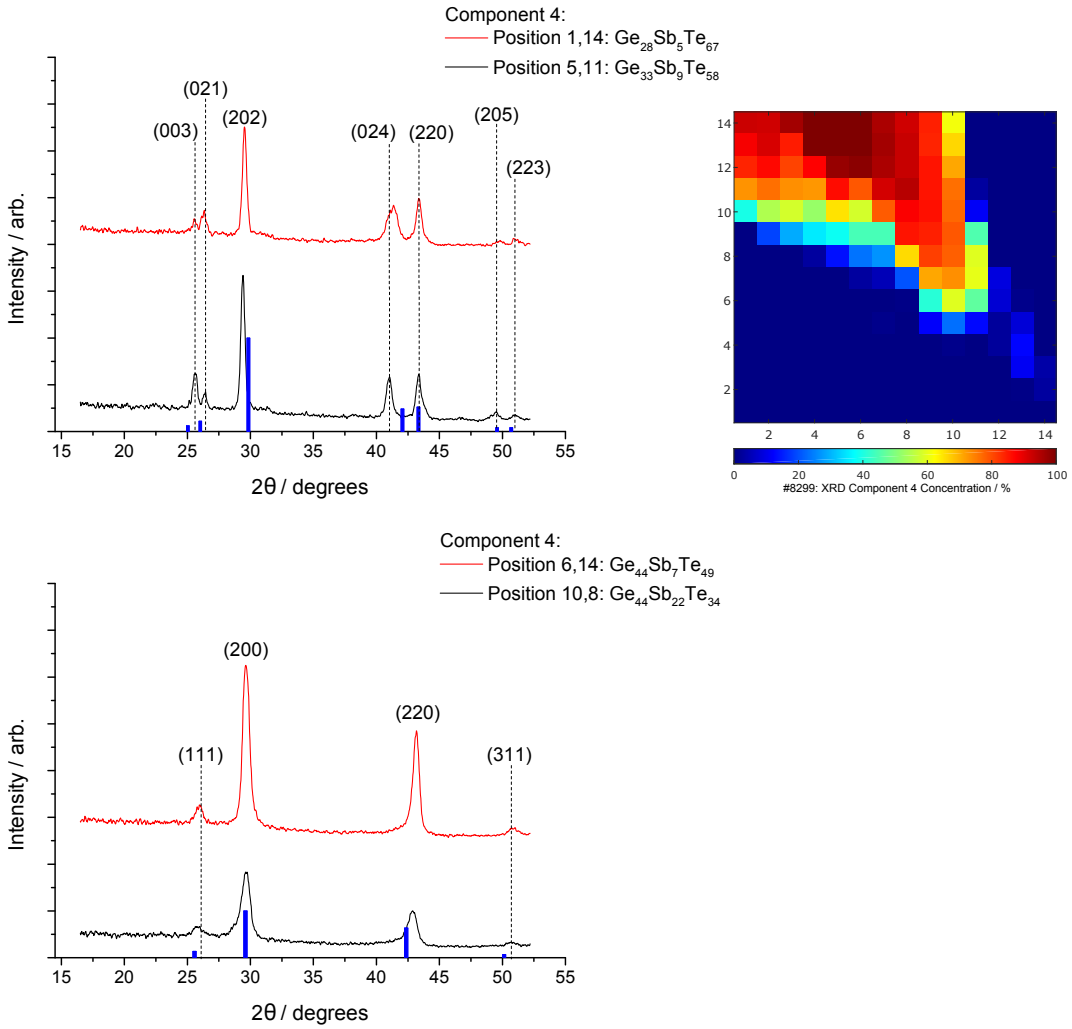

Figure 4.20: Diffraction patterns of four selected compositions within Component 4 of the PCA model of annealed GST sample #8299. The top graph shows a GeTe-type material crystallised in the rhombohedral R3m space group with proposed peak assignments (PDF 00-047-1079, blue vertical lines showing relative intensity), which shows that crystal alignment is along the (202) plane. The bottom graph shows a material crystallised in the cubic $Fm\bar{3}m$ space group also with peak assignments (PDF 01-073-7757, blue vertical lines), showing the material is aligned the (200) plane. The sample map to the right shows the concentration of Component 4 across the sample, given as a percentage of the sum of all five Components.

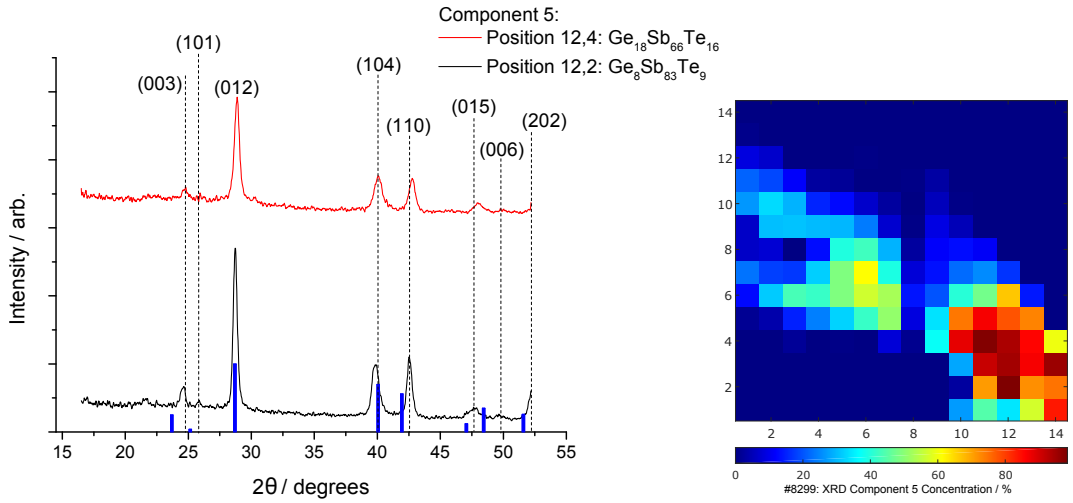

Figure 4.21: Diffraction patterns of two representative compositions within Component 5 of the PCA model of annealed GST sample #8299. The graph shows Sb-rich material crystallised in the rhombohedral R3m space group (PDF 00-035-0732, blue vertical lines showing relative intensity), which shows that crystal alignment is along the (012) plane, similar to the powdered reference sample. The sample map to the right shows the concentration of Component 5 across the sample, given as a percentage of the sum of all five Components.

servation of phase segregation outside of stoichiometric compositions, with multiple phases coexisting within the same compositional point in our combinatorial thin film library.[34]

The components from the PCA model were used to create a phase diagram of the GST system. To achieve this, the compositional points from Figure 4.3 were assigned to the Component with the highest concentration at each point. The result is shown in Figure 4.22, where individual phases within the same Component are also indicated. Following from the prior discussion, the five components of the PCA model contained a total of eight individual phases, most of which belonged to either the P3m1 or R3m crystallographic space groups. In addition, an amorphous phase and a cubic phase were also found. The map shows that at 200 °C materials along the GeTe–Sb_2Te_3 pseudobinary were already found in their high temperature hexagonal, phase (the first being a cubic phase, see Figure 2.10). It also became clear that materials having simultaneously high Ge and low Te content have higher crystallisation temperatures. No "pure" Te phases were observed, which may be due to the evaporation of excess Te during annealing, although no tests were performed to confirm this hypothesis.

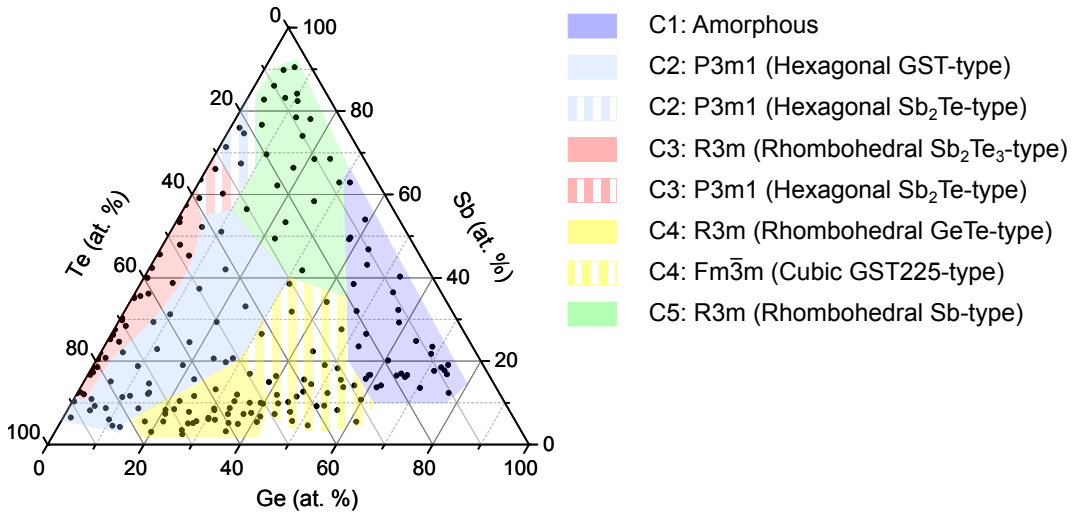

Figure 4.22: Proposed crystallographic phase map of GST annealed at 200 °C derived from the PCA model on the XRD dataset, described above. Each of the five components from the model is shaded with a different colour, while multiple phases within a single component are also highlighted. Legend shows the Component number (C1, C2, etc.) followed by the crystallographic space group and a description of the material type.

4.3.2.2 Raman Spectroscopy

Raman scattering measurements were performed on a library deposited on a silicon nitride substrate and annealed *in vacuo* for 20 min at 200 °C in the manipulator of growth chamber A (#8299). The measurements were performed using the apparatus described on section 3.2.2 covering a $100-250\,cm^{-1}$ Raman shift range collected over four 60 s acquisitions. A low laser power of 1% (0.25 mW) was used to prevent thermal annealing of the sample and a grating of 1800 grooves/mm was used.

The 196 Raman spectra that were collected on sample #8299 are all provided in Figure B.4 in the Appendix. The spectra confirmed the formation of multiple phases across the film, as observed through XRD in section 4.3.2.1. Each phase had its own distinctive set of vibrational bands and intensities and therefore band analysis, such as the one presented in Figure 4.8 for the as-deposited sample, would not be useful for the interpretation of this dataset. Rather, another multivariate PCA model was run on the annealed Raman dataset with identical constraints as those used for the XRD PCA model. The entire dataset was analysed between the $100\,cm^{-1}$ and $250\,cm^{-1}$ frequency, excluding "dead points" (i.e. points where the Raman spectrum was defective). It was determined that a five-component model would accurately

describe the local order across our combinatorial thin film library.

Component 1 corresponds to the modes present predominantly in GeTe-type materials with a peak near 125 cm^{-1}. The spectra for the compositions nearest the Ge:Te system, which are representative for this component, are shown in Figure 4.23. The spectra deviate significantly from those of the pure Ge_xTe_{1-x} compositions[207] due to the dominant Sb–Te modes arising from Sb doping. These materials show a peak at 125 cm^{-1} corresponding to a red shift of the 162 cm^{-1} peak, seen in amorphous GeTe, due to the reorganisation of the Ge–Te bonding environment from tetrahedral to octahedral.[209] However, the small shoulder near 180 cm^{-1} could be an $A_{1g}(2)$ mode of crystalline Sb_2Te_3 blue-shifted under compression from an enveloping GeTe matrix. In addition, the origin of the broad band running from 140 cm^{-1} to 180 cm^{-1} remains unexplained; while sharing similarities with the broad band of amorphous Ge:Te materials, XRD evidence showed that the annealed materials discussed in Figure 4.23 are in the crystalline state. In addition, due to the lack of undoped Ge:Te materials in our combinatorial libraries, it is not possible to fully assess the evolution of their local order with the current dataset.

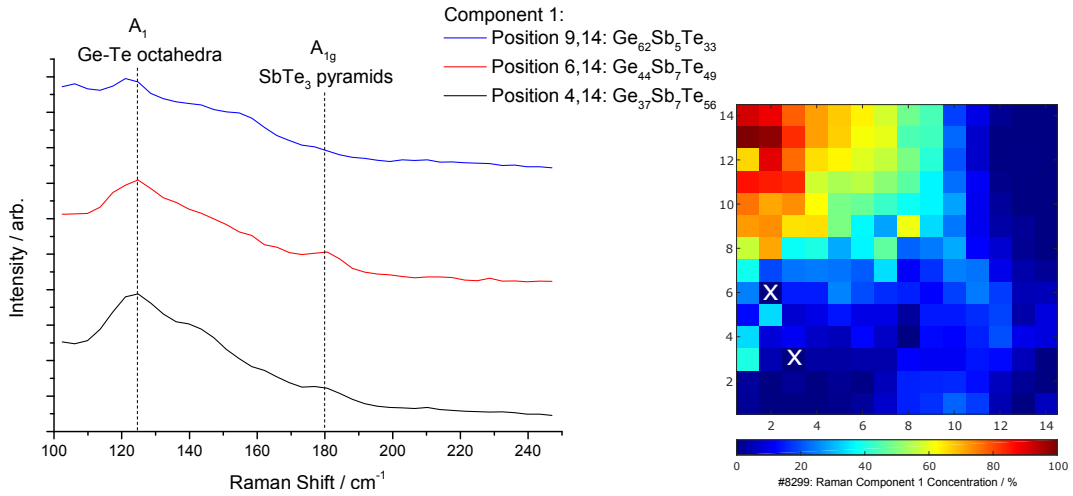

Figure 4.23: Raman spectra of selected compositions within Component 1 of the PCA model of annealed GST sample #8299 with proposed mode assignments for the peaks found near 125 cm^{-1} and 180 cm^{-1}. The spectra of within this component are related to Ge_xTe_{1-x}-type materials. The sample map to the right shows the concentration of Component 1 across the sample, given as a percentage of the sum of all five Components. White cross marks indicate a "dead point" not included in the analysis.

The compositions that were closer to elemental Sb are represented by Component 2. Representative Raman spectra of the Sb-rich region of the film, shown in Figure 4.24, feature

two peaks at 118 cm^{-1} and 150 cm^{-1}. In their study of high pressure modes of crystalline Sb, Wang *et al.* assigned these peaks to E_g and A_{1g} modes.[218] The E_g mode has blue shifted from its expected position at 110 cm^{-1} likely due to the presence of modes associated with Ge and Te impurities.

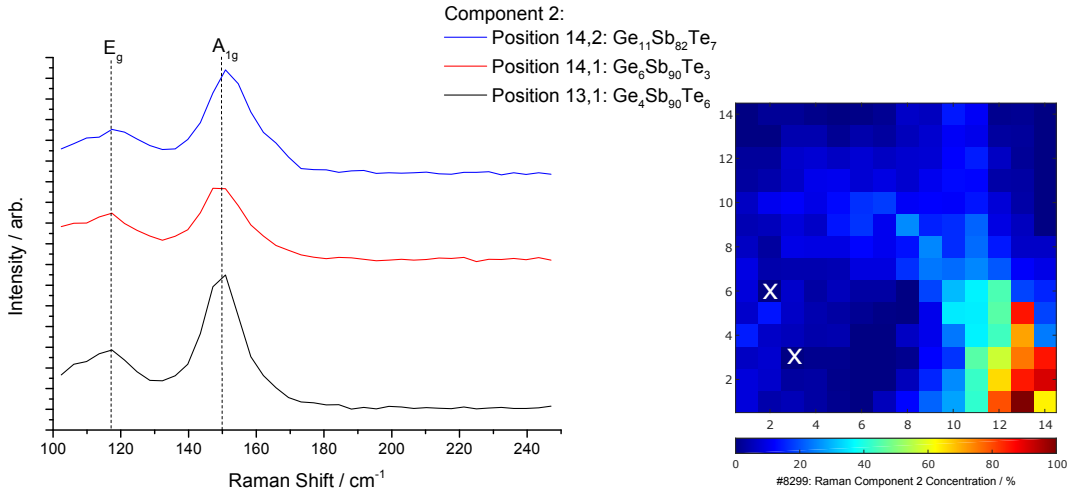

Figure 4.24: Raman spectra of selected compositions within Component 2 of the PCA model of annealed GST sample #8299 with proposed mode assignments for the peaks found near 118 cm^{-1} and 150 cm^{-1}. The spectra of within this component are related to Sb-type materials. The sample map to the right shows the concentration of Component 2 across the sample, given as a percentage of the sum of all five Components. White cross marks indicate a "dead point" not included in the analysis.

Sb_2Te_3 materials were modelled by Component 3 with peaks remarkably close to those of the pure crystalline material at 110 cm^{-1} and 165 cm^{-1}, consistent with $E_g(2)$ and $A_{1g}(2)$ modes of Sb_2Te_3 at 110 cm^{-1} and 165 cm^{-1} respectively.[210,219] Representative spectra for this component are shown in Figure 4.25. These show little shift in frequency despite the varying ratios of Sb:Te and low levels of Ge doping. However, they do show a marked drop in intensity with decreasing Te content. Neither of the modes has been assigned to specific structures within the material, although comparison to the amorphous spectra (Figure 4.12) reveals a split of the broad band at 145 cm^{-1} assigned to $SbTe_3$ pyramids. As such, these pyramids must evolve into different structures during crystallisation perhaps related to the (TeSb)Sb–Sb(TeSb) and (Te_2)Sb–Sb(Te_2) structures proposed by Liu for cubic GST materials for the 165 cm^{-1}.[220]

The spectra of the GST compositions along the Ge_2Te_3–Sb_2Te_3 pseudobinary were found within a single component (Component 4), unlike the case of the XRD PCA model were the diffraction patterns of these materials were split amongst those of the GeTe and Sb_2Te_3 components. The features of the crystalline Raman spectra of the compositions along the tie

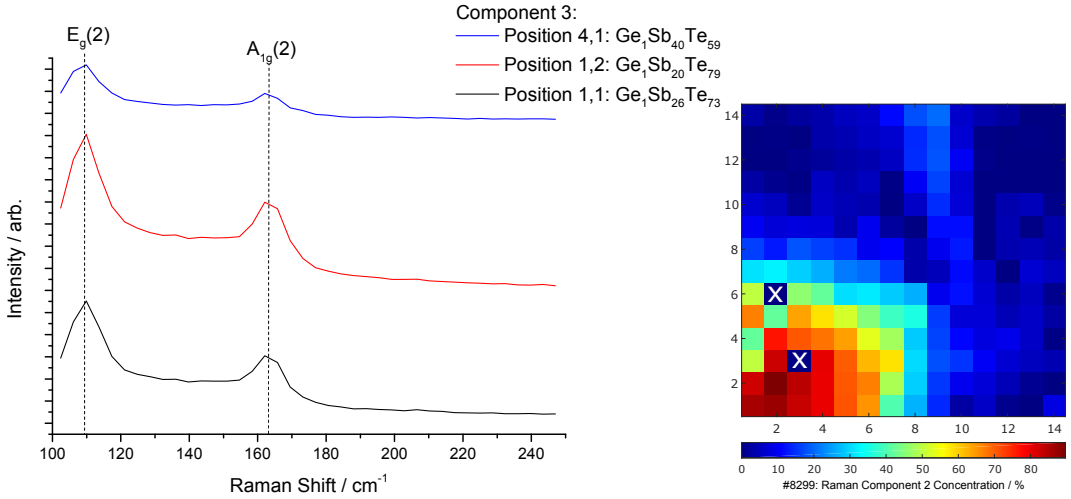

Figure 4.25: Raman spectra of selected compositions within Component 3 of the PCA model of annealed GST sample #8299 with proposed mode assignments for the peaks found near 110 cm^{-1} and 165 cm^{-1}. The spectra of within this component are related to Sb_2Te_3-type materials. The sample map to the right shows the concentration of Component 3 across the sample, given as a percentage of the sum of all five Components. White cross marks indicate a "dead point" not included in the analysis.

line possess bands that belong to both GeTe and Sb_2Te_3, as was the case with the amorphous materials. The spectra of GST225, GST124 and GST147 are shown in Figure 4.26. Both the GST124 and GST147 materials exhibit bands consistent with these materials found in the hexagonal crystal phase. The peak at 110 cm^{-1} corresponds to the $E_g(2)$ mode of Sb_2Te_3, probably with a contribution from the A_1 mode of Ge–Te octahedra which would cause the peak broadening. The peak at 170 cm^{-1} would belong to a blue-shifted $A_{1g}(2)$ mode of Sb_2Te_3, which would normally appear at 165 cm^{-1}, as described above. This shift has been reported to occur with increasing annealing temperature concurrently with a red-shift of the 110 cm^{-1} band.[220] As such, it is not clear why only the 165 cm^{-1} band would be shifted from its expected position. The spectrum of GST225 is more complex as it appears to have features of both cubic and hexagonal phases. This may be expected as GST225 has been reported to transition into the hexagonal phase at 250 °C,[221] whereas GST124 and GST147 have shown this transition at lower temperatures owing to their reduced GeTe content (Figure 2.10). For GST225 a band remained near 105 cm^{-1} likely belonging to residual $GeTe_4$ tetrahedra from the cubic phase.[220] As a consequence, the 110 cm^{-1} band for the $E_g(2)$ mode of Sb_2Te_3 appeared blue-shifted to 125 cm^{-1} due to the partial breakdown of $SbTe_3$ pyramids[205] and incipient formation of structures belonging to the crystalline modes of Sb_2Te_3. As a result, the broad band centred at 140 cm^{-1} could be treated as the vibrational mode of said residual

$SbTe_3$ pyramids. Finally, there is a blue-shifted $A_{1g}(2)$ mode of Sb–Sb bonds in (TeSb)Sb–Sb(TeSb) and $(Te_2)Sb–Sb(Te_2)$ as per Liu *et al.*[220] Therefore, while XRD data shows that the long range order of GST225 most closely resembles the hexagonal phase at 200 °C, the local order is likely conformed of a mixture of structures belonging to both the hexagonal and cubic phases.

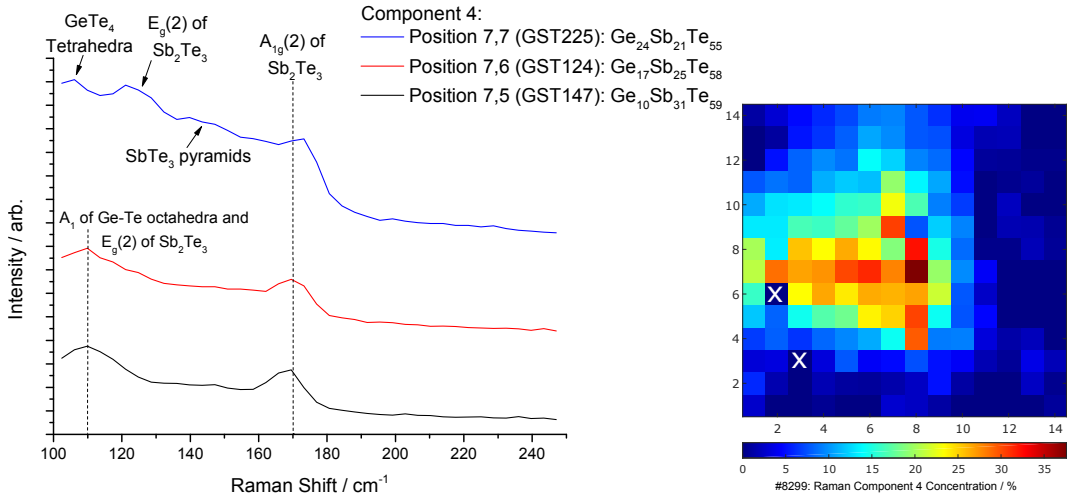

Figure 4.26: Raman spectra of selected compositions within Component 4 of the PCA model of annealed GST sample #8299 with proposed mode assignments. The spectra of within this component are related to materials along the Ge_2Te_3–Sb_2Te_3 pseudobinary. The sample map to the right shows the concentration of Component 4 across the sample, given as a percentage of the sum of all five Components. White cross marks indicate a "dead point" not included in the analysis.

Finally, the spectra found within Component 5 are a mixture of the uncrystallised Ge-rich materials and some of the highly Raman active modes of Sb–Te structures. XRD data showed these compositions did not crystallise upon annealing at 200 °C, which is confirmed through the Raman spectra which show that very little change in the local order took place. To demonstrate this, the spectra of both the as-deposited and annealed Ge-rich materials are shown in Figure 4.27. The main feature of the spectra is a broad band centred at approximately 150 cm^{-1} which is likely to belong to highly polarisable Sb-Te bonds in $SbTe_3$ pyramids, which despite their low concentration relative to Ge still possess very intense Raman modes.[102] The peak at 110 cm^{-1} and the broad band starting at 200 cm^{-1} may belong to acoustic modes of amorphous Ge.[222] The lack of modes related to crystalline Ge is to be expected as thin films of pure amorphous Ge only exhibit significant crystallisation at temperatures above 300 °C.[223] In section 4.4.1 the results of the HTOMPT experiments will show that materials that are both Te-poor and Ge-rich have the highest crystallisation temperatures of the entire

GST ternary space.

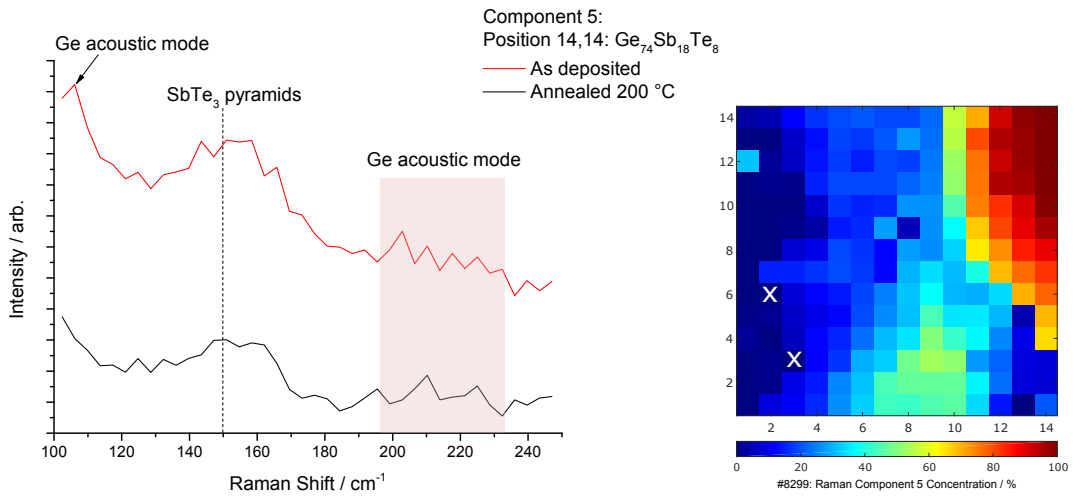

Figure 4.27: Raman spectra of a representative Ge-rich, Te-poor material within Component 5 of the PCA model. The spectra of both the as-deposited material (top, from sample #8302) and annealed material (bottom, from sample #8299) are shown, where it may be observed that little change in the local order took place in the material after annealing. Proposed mode assignments are provided for major features of the spectra. The sample map to the right shows the concentration of Component 5 across the sample, given as a percentage of the sum of all five Components. White cross marks indicate a "dead point" not included in the analysis.

The five components discussed above were mapped into the GST ternary space, as shown in Figure 4.28 using the same procedure employed to produce the XRD phase map (Figure 4.22). Within these components a total of six distinct phases were found, which could be mapped to those of the XRD model as per Table 4.2.

4.3.3 Discussion

The HT-PVD deposition method produced GST thin film combinatorial libraries with mean thickness of 214 ± 37 nm. Structurally, the as-deposited samples were found to be mostly amorphous with the exception of Te-rich compositions and materials within the Sb_2Te_3–Sb_3Te_2 region of the sample. These were found to be in a metastable semicrystalline state (Figures 4.5 and 4.6) that was also reflected in their local order configuration (Figure 4.12, for Sb_2Te_3–Sb_3Te_2). This is likely due to the low crystallisation temperature of these materials being thermodynamically easy to reach within the conditions used for the deposition of the combinatorial libraries. For the amorphous materials along the GeTe–Sb_2Te_3 pseudo-

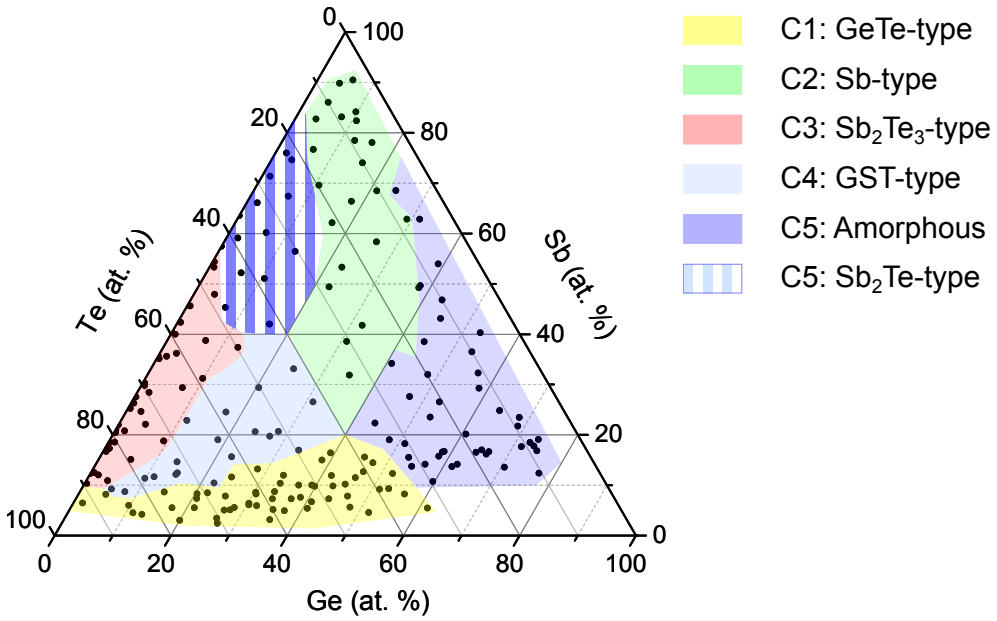

Figure 4.28: Proposed phase map of GST annealed at 200 °C derived from the PCA model on the Raman spectroscopy dataset, described above. Each of the five components from the model is shaded with a different colour, while multiple phases within a single component are also highlighted. Legend shows the Component number (C1, C2, etc.) followed by the proposed material type assignment.

Table 4.2: Mapping of PCA model components for both the Raman and XRD datasets to material types annealed at 200 °C within the Ge:Sb:Te compositional space.

Material Type	Raman Component	XRD Component
Ge:Te	1	4
Sb	2	5
Sb:Te	3 (Sb_2Te_3) and 5 (Sb_2Te)	2 (Sb_2Te) and 3 (Sb_2Te_3)
Ge:Sb:Te	4	2 (hexagonal GST)
Amorphous	5	1

binary, Raman evidence (Figure 4.13) is consistent with reports that support the presence of tetrahedral structures belonging to $GeTe_4$ in addition to $SbTe_3$ pyramids.[102,205,212,213] This interpretation is supported by the Raman spectra of materials near the Ge:Te system (Figure 4.11) and the available amorphous compositions on the Sb:Te system (Figure 4.12).

For materials along the GeTe–Sb_2Te_3 pseudobinary annealed at 200 °C, XRD evidence showed these materials had already crystallised in the hexagonal P3m1 space group (Figure 4.18) and therefore the cubic phases were generally not observed. The results of the Raman spectra of these materials (Figure 4.26) were also consistent with the formation of Ge–Te octahedra and (TeSb)Sb–Sb(TeSb) structures consistent with the formation of the hexagonal phase.[220,221] An exception was the GST225 spectrum which showed features consistent with both the cubic phase and hexagonal phase, suggesting that the material still had not fully transitioned between phases at this temperature.

A broader interpretation of the XRD and Raman datasets from the GST materials annealed at 200 °C was aided by a multivariate model using principal component analysis. Multiple iterations were run and it was determined that a model with five components approximated the data from each dataset more accurately. The components from the XRD model were described in Figures 4.17 to 4.21 and the Raman model components in Figures 4.23 to 4.26. Most of the material types mapped to a single component in each model (Table 4.2) with the exception of materials within the Sb:Te system, as these materials were found spread across two components in both models. In addition, traces of the $Fm\bar{3}m$ cubic phase of GST found in component 4 of the XRD model was found across four components in the Raman model (1, 2, 4 and 5). This could be interpreted as an indication that knowledge of local order of the material would not necessarily be a reliable predictor of its long range order.

Regardless, the similar compositions covered by both XRD and Raman PCA models may validate the assumption of there being multiple material types that exist in a continuum within the GST compositional space. These types would share structural motifs that would transition into those of the neighbouring materials as atomic ratios are changed. This would likely lead to the segregation of stoichiometric compounds and the coexistence of multiple phases within the same volume of material, as suggested by Yamada *et al.* in their original investigation of the GeTe–Sb_2Te_3 pseudobinary.[34] Therefore, it may be a good approximation to interpret the concentration of an individual PCA component at a given point of the sample as a measure of the degree of mixing between the different phases in the material.

Finally, there is no evidence that aging of the materials due to the lack of a protective capping layer may have affected the structural characterisation results in a significant manner, as the Raman spectra and XRD patterns lack distinctive features that may be attributed to oxygen incorporation into the GST matrix.[120,224]

4.4 Functional Characterisation

4.4.1 Crystallisation Temperature

The magnitude of reflectivity changes and the crystallisation temperature (T_x) derived from this information were determined using the HTOMPT technique described in section 3.3.2. The as-deposited sample #8294 was heated from room temperature to 330 °C at a rate of 5 °C min^{-1} under Ar flow. A 58×58 point grid was used to analyse this dataset, resulting in a pitch between points of 0.5 mm across the 29×29 mm sample, for a total of 3,364 data points. The compositional space shown in Figure 4.3 was interpolated to a matching 58×58 point array using a linear algorithm encoded in the Paradise software.

To facilitate the examination of the intensity versus temperature curves, a grid of only 14×14 points across the entire sample is provided in Figure B.5 in the Appendix. Figure 4.29 below shows a selection of the typical HTOMPT profiles obtained during the experiment. From these curves it can be seen that the reflectivity of the sample (measured as intensity) undergoes a sharp change near the crystallisation temperature of the material. In addition, some of the compositions began to exhibit a second increase in reflectivity near the endpoint of the experiment, which is suggestive of a second transition. GST compositions near the GeTe–Sb_2Te_3 pseudobinary are known to have two transitions, from the amorphous to cubic phase, and from cubic to hexagonal. Therefore the HTOMPT technique could, in principle, be used to study the second transition as well. However, due to the large variation between the magnitude and position of the second transition across the sample an algorithmic identification was proved to be unreliable.

Some observations relating XRD information presented in section 4.3.1 to the HTOMPT results can be made from Figure 4.29. The curve of point (13,13) in the Te-poor region of the film only showed a reflectivity change past 300 °C, far higher than the annealing temperature of 200 °C of sample #8299 where this region remained amorphous. Similarly, the curve of point

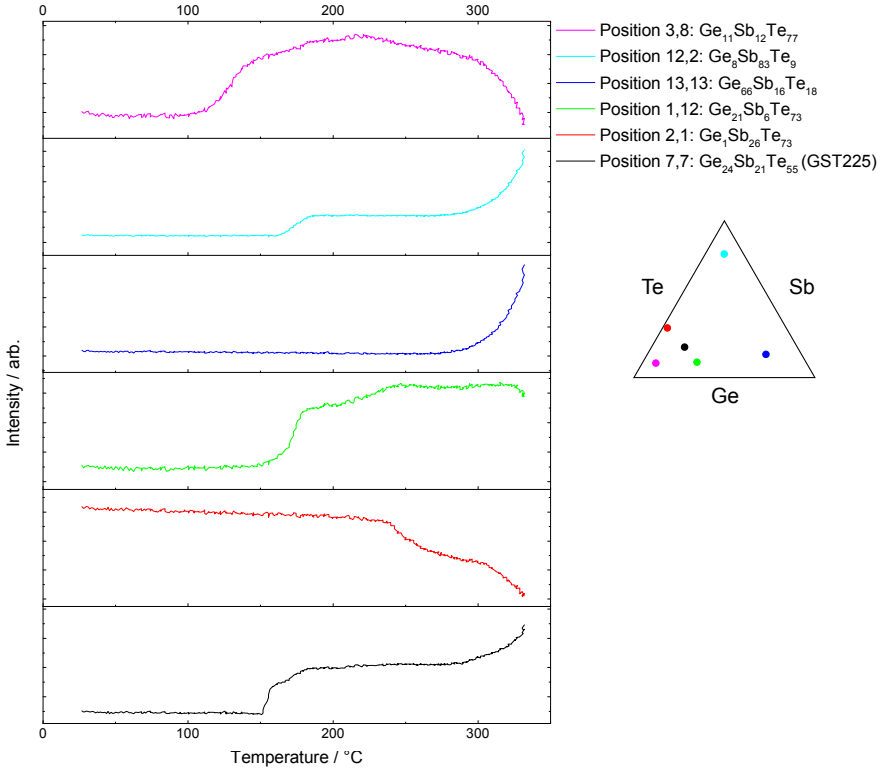

Figure 4.29: Selected HTOMPT curves for GST materials on sample #8294. Ternary diagram shows the location of each curve within the compositional space.

(2,1) is within the Sb_2Te_3–Sb_3Te_2 compositional region which was found to be semicrystalline in the as-deposited sample. While these materials fully crystallised after annealing (Figure 4.19) no increase in reflectivity was observed by 200 °C, which suggests that the transition in optical reflectivity could occur before full crystallisation of the material has taken place. Moreover, the reflectivity of the material began to decrease around 250 °C. A decrease in reflectivity at this temperature would likely be due to major structural rearrangements in the material, such as the decomposition of Sb–Te bonds or the beginning of the evaporation of Te off the film. At temperatures above 300 °C the decrease in reflectivity [as observed in the curves of points (3,8) and (2,1)] was correlated to the evaporation of Te off the film, which was deposited onto the surface of the HTOMPT heating chambers window.

The magnitude of the intensity change (ΔI) at a given temperature has been calculated as the reflectivity of a point at a given temperature minus the reflectivity of the material at the start of the experiment. As such, the entire dataset was normalised to the first frame collected during the test. Figure 4.30 shows the reflectivity change maps for sample #8294 at 200 °C and 330 °C. At the 200 °C cut-off the compositions with the largest reflectivity change were

near $Ge_{60}Te_{40}$–$Ge_{40}Te_{60}$ materials with Sb content < 10 at. %. The smallest changes were seen around the semicrystalline Sb_2Te_3–Sb_3Te_2 region, as well as a large compositional space delimited by the $Sb_{80}Te_{20}$–$Sb_{90}Ge_{10}$–$Ge_{70}Te_{30}$ lines, which contains the amorphous materials identified through XRD in sample #8299. These two regions are equivalent to components 3 and 1, respectively, of the XRD PCA model shown in Figure 4.22.

The calculated intensity change at the end of the experiment showed that materials with Sb content greater than 70 at. % had the largest ΔI. The smallest change was observed for materials with more than 80 at. % Te. Materials within the Sb_2Te_3–Sb_3Te_2 region showed a negative reflectivity change with respect to the room temperature reference. Therefore, materials showing this behaviour were excluded from the transition temperature calculation.

Figure 4.31 shows the ternary space plot of the first phase transition temperature, calculated between 50 °C and 330 °C, where the data have been resampled within 2 at. % composition. The smallest T_x was 73 °C for $Ge_1Sb_{34}Te_{65}$ and the largest 319 °C for $Ge_{61}Sb_{17}Te_{22}$. The overall trend appears to be along rigidity lines, with more rigid materials having a higher crystallisation temperature likely due to the more constrained environment found around Te atoms. The valley of low crystallisation proposed by Yamada[34] was observed within the compositional space delimited by the GeTe–Sb_2Te_3 and GeTe–SbTe pseudobinary lines. This is in contrast with the result obtained by Guerin *et al.* who observed said feature along the Ge_2Te_3–Sb_2Te_3 and GeTe–Sb_2Te_3 lines.[190] This discrepancy is highlighted in Table 4.3, which compares selected points both HT datasets with values from the literature.

The GeTe composition is generally reported to have the lowest crystallisation temperature within the Ge:Te system, while Guerin *et al.* reported similar temperatures for materials that were nearest to both $Ge_{40}Te_{60}$ and GeTe compositions. The results from the available HTOMPT data points closest to the GeTe system appear to agree with the trend observed in the literature (Table 4.4). However, differences in the actual value of the transition temperature are most likely due to the deposition method used to prepare the materials. Dieker and Wuttig reported changes of up to 22 °C in the crystallisation temperature of GST225 sputtered under different conditions, which they attributed to changes in the microstructure of the material.[225] Furthermore, the heating rate can also impact the crystallisation temperature of chalcogenide glasses, with a faster heating rates resulting in higher temperatures.[226,227] Finally, aging may lower T_x due to oxygen incorporation onto the first few layers of the material.[191] This may have affected the results obtained for GST415, GST325 and GST212 and other materials.

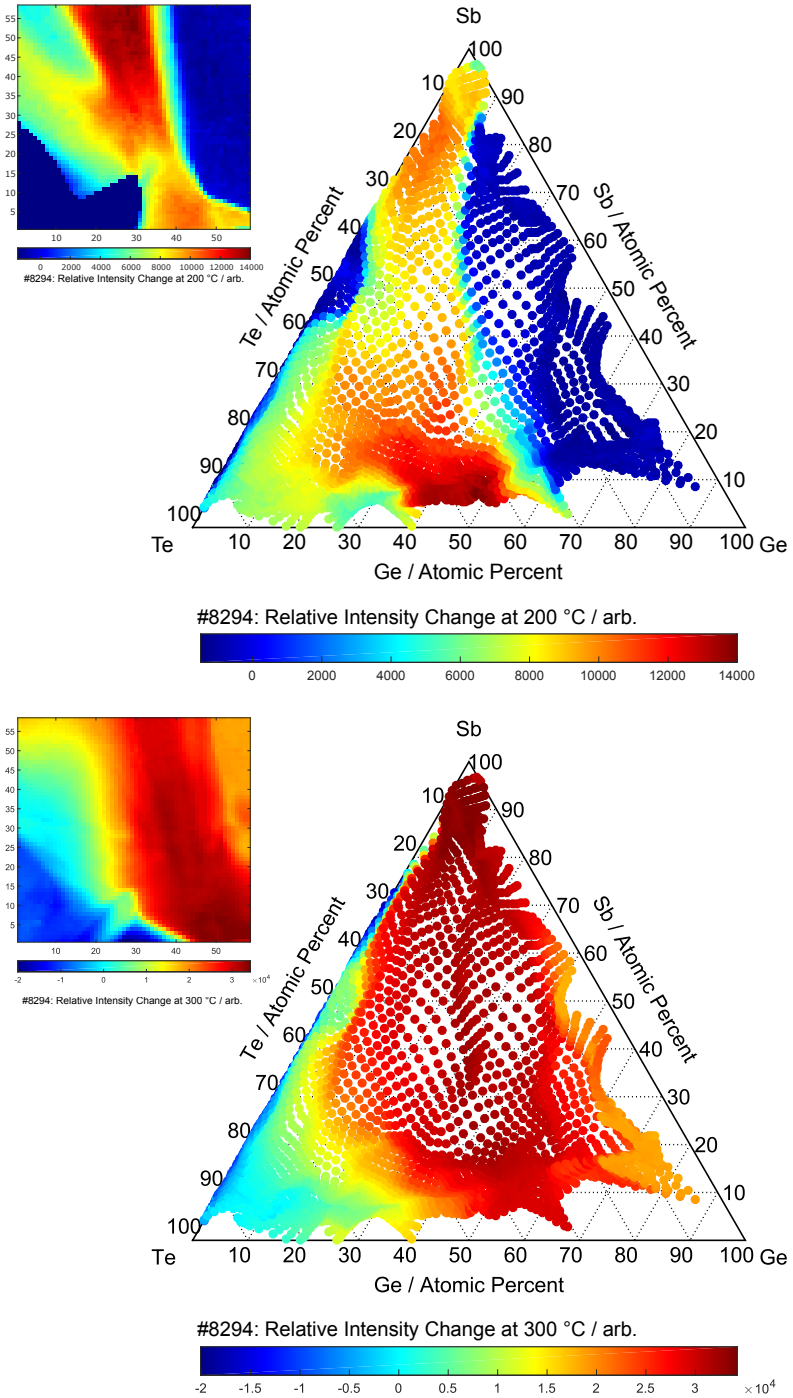

Figure 4.30: Intensity change (ΔI) of sample #8294 at 200 °C (top) and 330 °C (bottom) relative to the start of the HTOMPT experiment. Insets show the maps of ΔI across the sample.

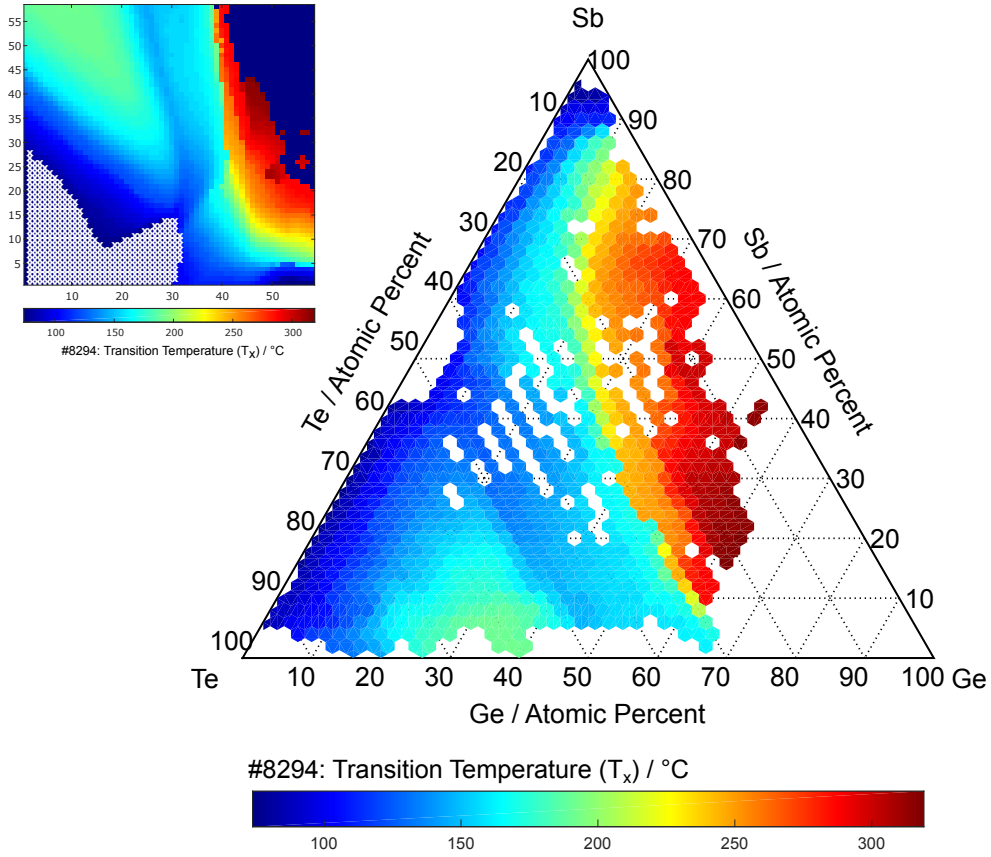

Figure 4.31: Temperature of the first phase transition (T_x) of the GST system as determined by HTOMPT experiment on sample #8294. Inset shows the map of transition temperatures across the sample, included the data points excluded from the analysis in the lower left corner of the sample. The dark blue region in the top right corner of the sample includes compositions for which the phase transition could not be calculated because their T_x fell outside the temperature range of the experiment. The white crosses in the inset represent "dead points" where the negative ΔI prevented the determination of the value of T_x. These points are not shown in the ternary diagram.

The trend of the transition temperature along pseudobinary lines is shown in Figures 4.32 and 4.33. Some scatter of the data points may be observed in the Sb-poor ends of the pseudobinary lines. This is due to the higher density of compositional points near the Ge:Te compositions which is an artefact of deposition (see section 4.2). In addition, the Sb-rich ends of the pseudobinaries, particularly those ending near the Sb_2Te_3, SbTe and $SbTe_4$ compositions have lower T_x values than reported in the literature. This is because some of these compositions were already in a metastable semicrystalline state after deposition, thus lowering the energy required to achieve the full crystallisation of the material.

Table 4.3: Crystallisation temperature (T_x) for selected compositions in the GST ternary space from sample #8294. Literature results provided for comparison.

Composition	Experimental (T_x / °C)	Literature (T_x / °C)	Citation
GST225	151	144	Guerin[190]
		138	Morales[228]
GST124	138	136	Guerin[190]
		131	Morales[228]
GST147	122	123	Guerin[190]
		110	Morales[228]
GST415	157	171	Guerin[190]
		152	Morales[228]
		168	Czubatyj[229]
GST325	142	172	Lu[230]
GST212	153	211	Cheng[93]
GST181	197	< 200	Song[231]
$Ge_{15}Sb_{85}$	247	250	Cabral[232]

Table 4.4: Comparison of reported crystallisation temperatures for selected compounds in the Ge:Te system. Experimental T_x values quote the closest compositions available within sample #8294.

Composition	Experimental (T_x / °C)	Guerin[190] (T_x / °C)	Carria[207] (T_x / °C)	Raoux[233] (T_x / °C)
$Ge_{40}Te_{60}$	191	145-161	244	230
GeTe	167	146-161	180	175
$Ge_{60}Te_{40}$	N/A	N/A	354	265

The T_x of the materials found within the $GeTe_4$–$SbTe_4$, Ge_2Te_3–Sb_2Te_3, GeTe–Sb_2Te_3 and GeTe–SbTe pseudobinaries all follow a similar pattern, with Sb-poor compositions having a higher crystallisation temperature than Sb-rich compositions. The T_x of compositions along the GeTe–Sb_2Te_3 tie line were found to be within the range of reported values, although slightly higher than those reported by Guerin *et al.* also using the HTOMPT method at a similar heating rate. This difference was more noticeable near the $20 - 25$ at. % Sb range, which includes the GST225 composition. Considering that Guerin *et al.* used a 120×120 point HTOMPT analysis grid on their thin films,[190] it is likely that their data have less variance than our 58×58 point dataset resulting in a smaller scatter of T_x values along the pseudobinary.

The GeTe–Sb line showed a rapid increase in T_x after its intersection with the GeSbTe pseudobinary. This increase peaked at $60 - 65$ at. % Sb at temperatures between 220 and 240 °C, although the scatter present in the data makes an accurate assessment difficult. Regardless, a similar trend was observed by Cheng *et al.* although for the compositions they investigated the temperature peak was found near 50 at. % Sb in between 253 °C and 274 °C.[93] However, there are large discrepancies between the values of T_x they reported for some compositions and our experimental values, in particular for GST212 as seen in Table 4.3. In their brief report they did not comment on the technique used to prepare these materials, so further assessment cannot be made in this basis. In addition, their method of determining T_x appears to have been by measuring the resistivity as a function of temperature, which is a common procedure, although this was not stated explicitly either.

The overall trend observed along the GeSb–Te line is of increasing transition temperature with increasing Sb content. However, the rate of increase reaches a local maximum between the Ge_2Te_3–Sb_2Te_3 and GeTe–Sb_2Te_3 lines ($20 - 22$ at. % Sb) and turns negative between GeTe–Sb_2Te_3 and GeTe–SbTe ($22 - 25$ at. % Sb). The value of T_x increases slowly right after the GeTe–SbTe line up until it intersects the GeTe–Sb pseudobinary at 33 at. %. At this point T_x increases rapidly with increasing Sb content.

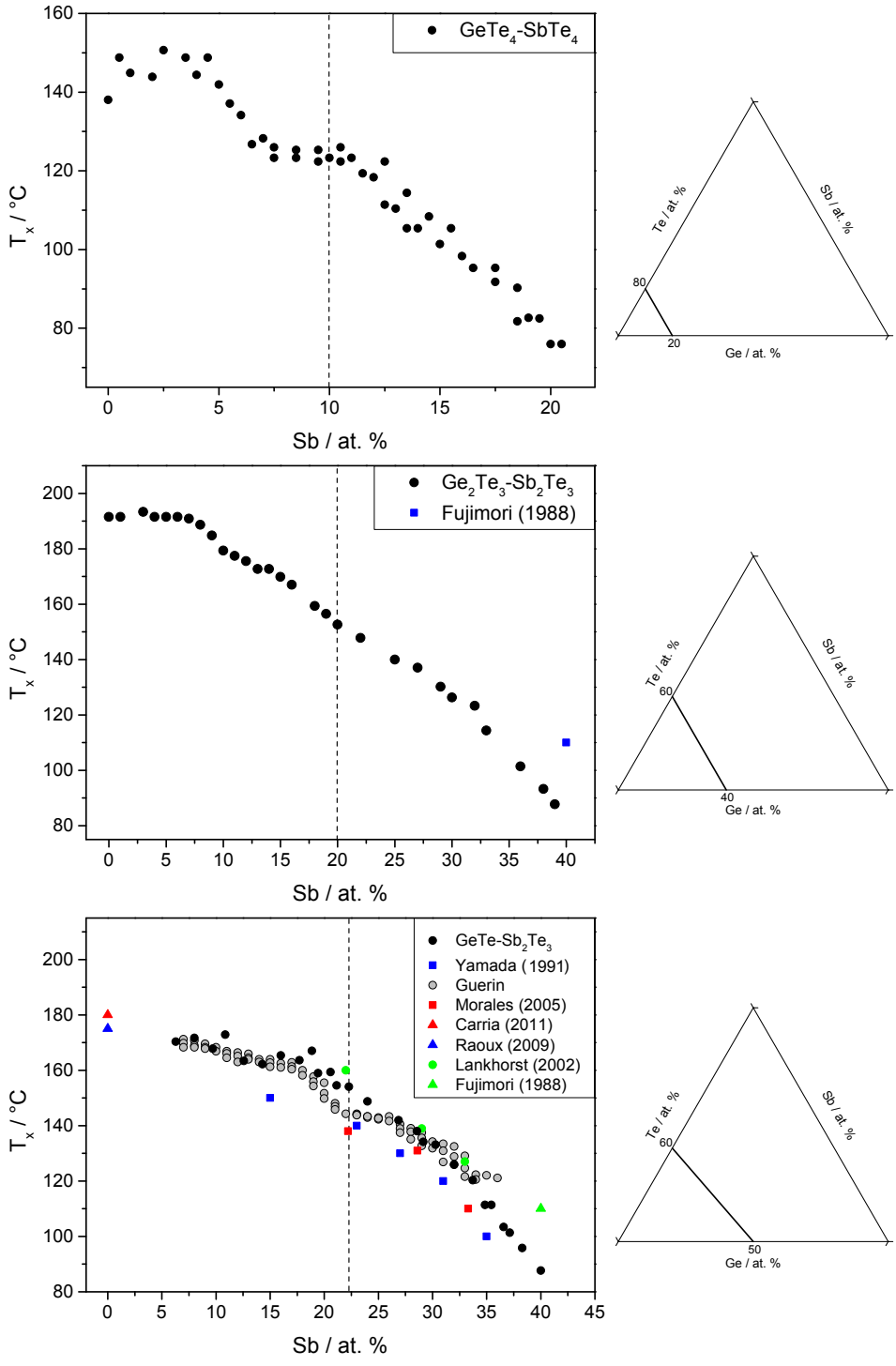

Figure 4.32: Transition temperature (T_x) as a function of Sb content for materials along the $GeTe_4$–$SbTe_4$, Ge_2Te_3–Sb_2Te_3 and GeTe–Sb_2Te_3 pseudobinaries as obtained during the HTOMPT experiment. Experimental results (black dots) are compared against the literature values.[34,147,190,202,207,228,233] Dotted lines indicate the intersection with other tie lines (see Figure 4.3). Ternary diagrams indicate the position of each pseudobinary within the GST ternary space.

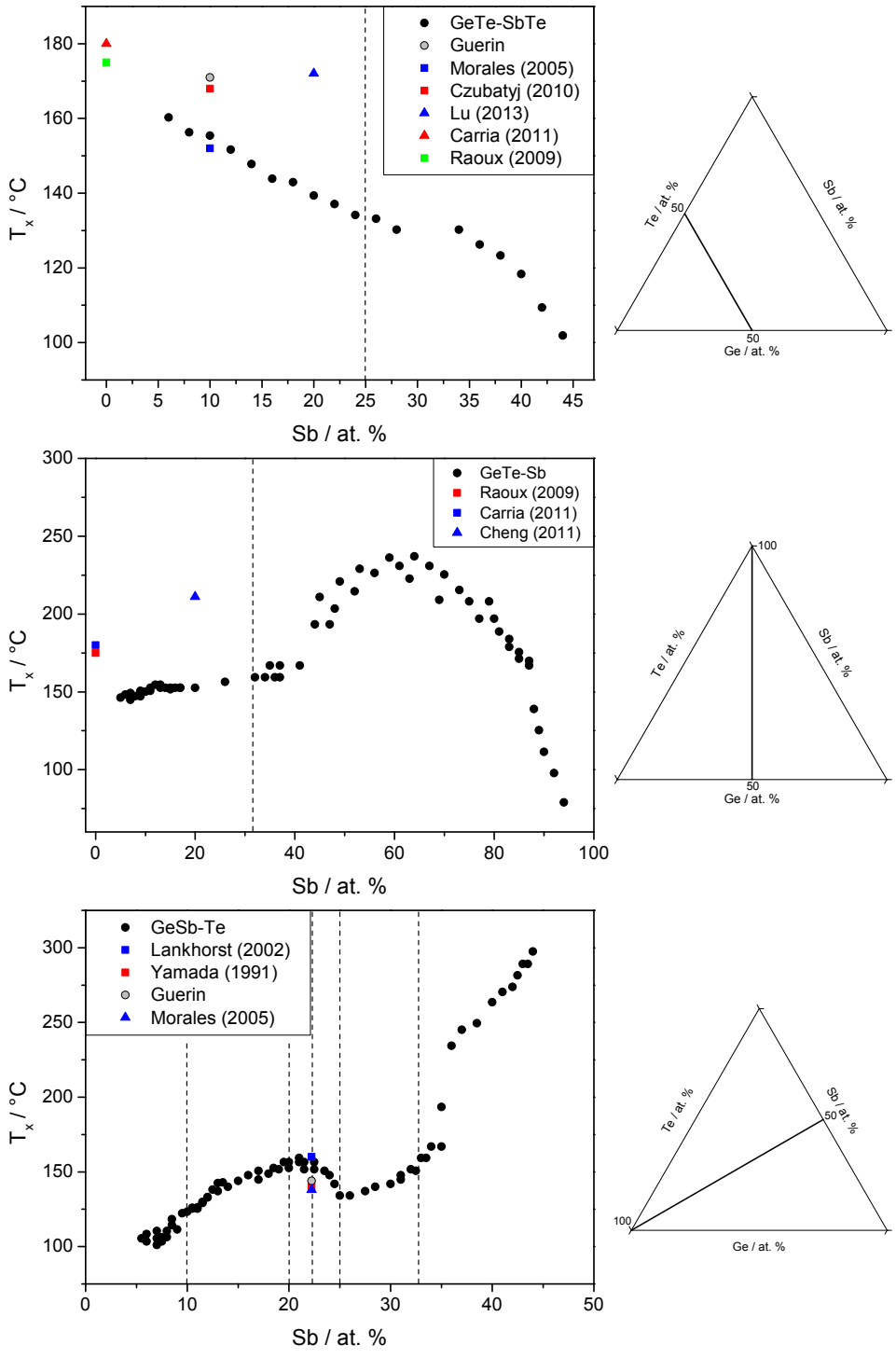

Figure 4.33: Transition temperature (T_x) as a function of Sb content for materials along the GeTe–SbTe, GeTe–Sb and GeSb–Te pseudobinaries as obtained during the HTOMPT experiment. Experimental results (black dots) are compared against the literature values.[34,93,147,190,207,228–230,233] Dotted lines indicate the intersection with other tie lines (see Figure 4.3). Ternary diagrams indicate the position of each pseudobinary within the GST ternary space.

4.4.2 Resistivity

The resistivity of samples #8296 and #8299 (214 ± 37 nm) thick, deposited on silicon nitride) was measured as per the procedure outlined in section 3.3.1. Due to large variations in resistivity Figure 4.34 shows the $log(\rho)$ maps for both samples after being corrected as per equation 3.3.

In the as-deposited sample #8296, the lowest resistivity was $8.1 \times 10^{-3}\,\Omega\,\text{cm}$ for $Sb_{45}Te_{55}$ while the highest resistivity was $1.8 \times 10^{5}\,\Omega\,\text{cm}$ for $Ge_{24}Sb_{13}Te_{63}$. The latter value is consistent with the observations of Guerin *et al.*,[190] although they did not observe semicrystalline regions in their amorphous films, so their low resistivity material was a Ge-rich composition ($Ge_{58}Sb_{26}Te_{16}$). The region of lowest resistivity correlated to the semicrystalline regions of Te-rich and Sb_2Te_3–Sb_3Te_2 materials identified through XRD. The highest resistivity was found within a region of approximately $GeTe_2$ compositional ratio.

For the material annealed at 200 °C the lowest resistivity was $1.8 \times 10^{-5}\,\Omega\,\text{cm}$ for $Sb_{61}Te_{39}$ and the highest $2.1 \times 10^{4}\,\Omega\,\text{cm}$ for $Ge_{58}Sb_{25}Te_{17}$. These values are only partially comparable with those reported by Guerin *et al.* Our $Sb_{61}Te_{39}$ material fell outside the compositional space of their samples, while $Ge_{58}Sb_{25}Te_{17}$ was found well within the high resistivity compositions reported at this annealing temperature. Some points in the sample could not be read by the 4PP due to either poor contact between probe and film, despite repeated attempts at measurement; these "dead points" appear crossed out in the insets of Figure 4.34. Regardless, resistivity trends were still observed. The region of highest resistivity correlated well with the amorphous Te-poor compositions (< 30 at. %) identified through XRD as Component 1.

Table 4.5 offers a comparison of the resistivity data for specific GST compositions with literature values. Some discrepancies have been observed from the reported values, in particular with the results post-anneal provided by Guerin *et al.* which were obtained on samples prepared with a similar HT deposition method. However, they did not report seeing semicrystalline regions across their as-deposited sample, suggesting that their deposition parameters may have influenced the structure of the materials in their films, such as the higher deposition rates used in our synthesis. The much lower resistivity of the annealed materials in sample #8299, compared to the literature values, may be due to the measurement technique typically employed in the reports whereby resistivity is measured throughout a heating cycle. Friedrich *et al.* found that the heating rate has an effect on the resistivity of GST225 measured using this

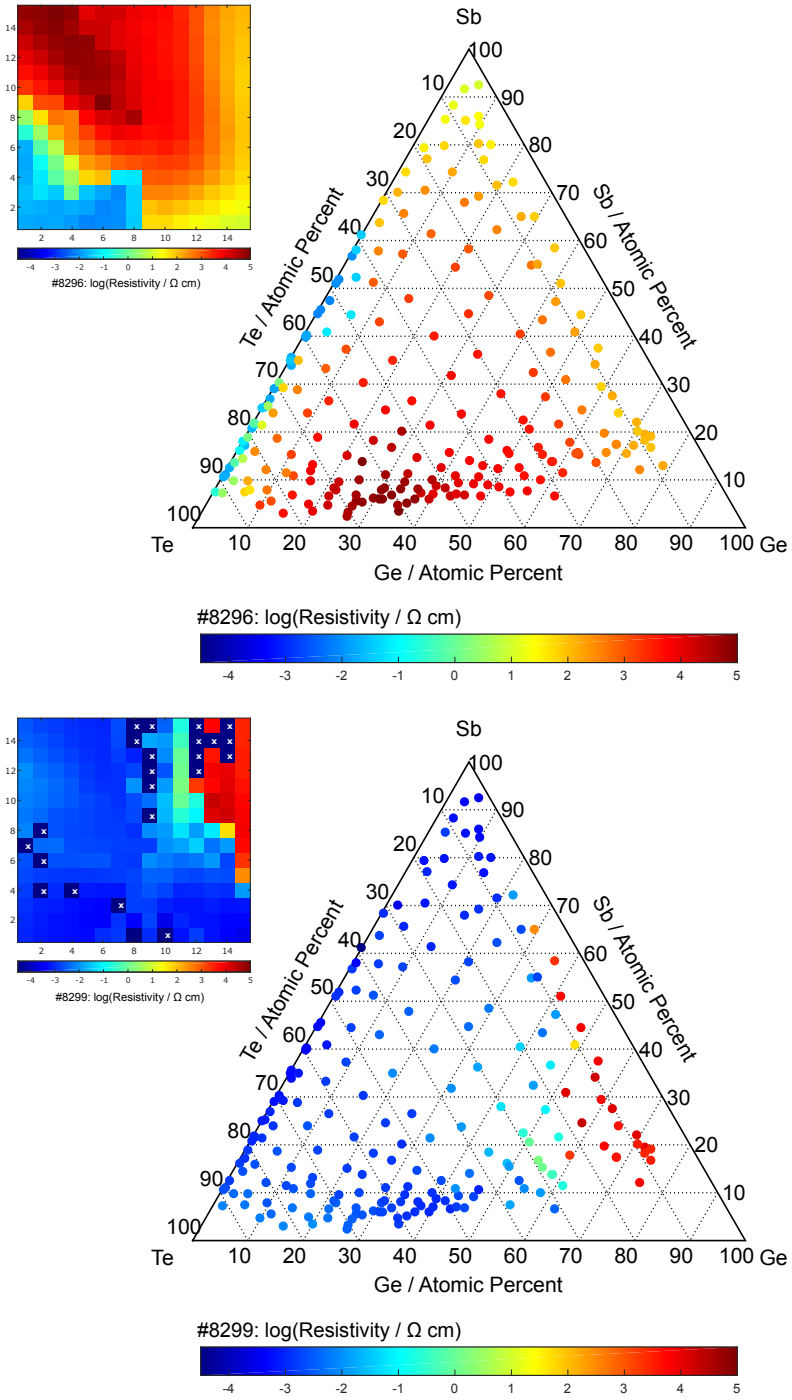

Figure 4.34: Resistivity maps, presented as $log(\rho)$, for as-deposited sample #8296 (top) and annealed sample #8299 (bottom) as determined using 4PP. The inset next to the ternary diagram shows the same information across the thin film: X-Y coordinates correspond to the position of each measurement point within the sample. Crossed out squares represent "dead points" where data could not be collected.

method, with faster rates resulting in a higher resistivity of the material, particularly near the transition temperature.[234] Furthermore, during this type of experiments the thickness of the thin film sample would not remain constant, therefore introducing uncertainty into the resistivity calculation from the measured sheet resistance. Higher resistivity may also be expected from aged materials due to oxide formation on the surface of the films. Finally, our results also follow the trend observed by Navarro *et al*. for Ge_xTe_{100-x} materials where the materials between the $GeTe_2$ and GeTe stoichiometries have the largest resistivity in the as-deposited films, which decreased with increasing Ge content.[199] The resistivity trends

Table 4.5: Resistivity data of selected GST compositions in the as-deposited (A) and crystalline (C) phases of samples #8296 and #8299. Data presented in Ω cm. Literature values provided for comparison.

Composition	Experimental (Ω cm)		Literature (Ω cm)		Citation
	A	**C**	**A**	**C**	
GST225	7.5×10^{3}	1.6×10^{-3}	2.4×10^{3}	1.2×10^{-1}	Guerin[190]
			1.5×10^{3}	1.0×10^{-3}	Vinod[221]
GST124	3.3×10^{3}	1.5×10^{-3}	1.6×10^{3}	9.7×10^{-3}	Guerin[190]
			2.6×10^{2}	2.5×10^{-2}	Morales[228]
GST147	7.7×10^{2}	1.7×10^{-3}	1.0×10^{3}	6.7×10^{-3}	Guerin[190]
			1.3×10^{2}	6.5×10^{-3}	Morales[228]
GST415	3.1×10^{4}	1.3×10^{-3}	1.9×10^{2}	1.2×10^{-1}	Guerin[190]
			1.6×10^{3}	5.0×10^{-3}	Czubatyj[229]
GST325	4.1×10^{4}	1.4×10^{-3}	1.0×10^{3}	1.0×10^{-1}	Lu[230]
GST212	6.3×10^{3}	2.4×10^{-2}	6.0×10^{3}	9.0×10^{-1}	Cheng[93]
Sb_2Te_3	1.5×10^{-2}	5.3×10^{-4}	2.4×10^{2}	3.8×10^{-3}	Das[235]
GeTe (nearest)	1.6×10^{4}	2.4×10^{-3}	1.0×10^{3}	8.0×10^{-2}	Navarro[199]
$GeTe_2$ *(nearest)*	7.8×10^{4}	2.0×10^{-3}	4.0×10^{5}	2.0×10^{2}	Navarro[199]
$Ge_{15}Sb_{85}$ *(nearest)*	3.5×10^{1}	6.8×10^{-4}	4.0×10^{0}	1.0×10^{-1}	Cabral[232]

along pseudobinary lines are shown in Figures 4.35 and 4.36 as a function of Sb content for both as-deposited and annealed materials. The resistivity of the Sb-poor compositions in the as-deposited sample was greater than those of the Sb-rich materials for all pseudobinaries except GeSb–Te. As the Figures show this trend is consistent with reports from the literature but may also be due in part to the semicrystalline Sb-rich compositions being less resistive. Along GeSb–Te the most resistive materials are found near the intersection with the Ge_2Te_3–Sb_2Te_3 tie line at 20 at. % Sb. For most lines our as-deposited experimental results were found within one order of magnitude of reported values, with the exception of the GeTe–SbTe line where the lack of literature reports makes more difficult to ascertain which set of data would be more accurate. On the other hand, our data along the GeTe–SbTe do not appear to be out of order compared to the rest of the as-deposited combinatorial library.

For the annealed sample the resistivity of most materials may be found within one order of magnitude along most pseudobinaries. Of note are the local maximum along the GeTe–Sb line around 20 at. % Sb, as well as the local minimum on the GeSb–Te line at the intersection with the Ge_2Te_3–Sb_2Te_3, GeTe–Sb_2Te_3 and GeTe–SbTe pseudobinaries (20 − 25 at. % Sb). In addition, for this pseudobinary the resistivity increases alongside the Sb content of the material, reaching a maximum around the materials that failed to crystallise at 200 °C.

4.4.2.1 Resistivity Contrast

The resistivity contrast $log(\Delta\rho)$ was calculated, using equation 3.5, for the GST materials for which data points were available in both the as-deposited and annealed samples. The result is shown in Figure 4.37. The smallest positive value of $log(\Delta\rho)$ was 0.6 found at composition $Ge_{49}Sb_{41}Te_{10}$ signifying little contrast between phases. The largest $log(\Delta\rho)$ was found at $Ge_{24}Sb_{14}Te_{62}$ with a value of 8.1. Negative $log(\Delta\rho)$ values were also calculated signifying that the as-deposited material was more conductive prior to annealing. Compositions that showed such behaviour were typically Te-poor and failed to crystallise during annealing. The lowest negative $log(\Delta\rho)$ was −1.9 for the composition $Ge_{56}Sb_{34}Te_{10}$.

Table 4.6 lists the $log(\Delta\rho)$ calculated from the values in Table 4.5. As discussed above, discrepancies with the literature may be a result of the methodology used to measure resistivity, as well as from the increased conductivity of the as-deposited semicrystalline materials.

Figures 4.38 and 4.39 show the trends of $log(\Delta\rho)$ across all pseudobinaries. The behaviour of

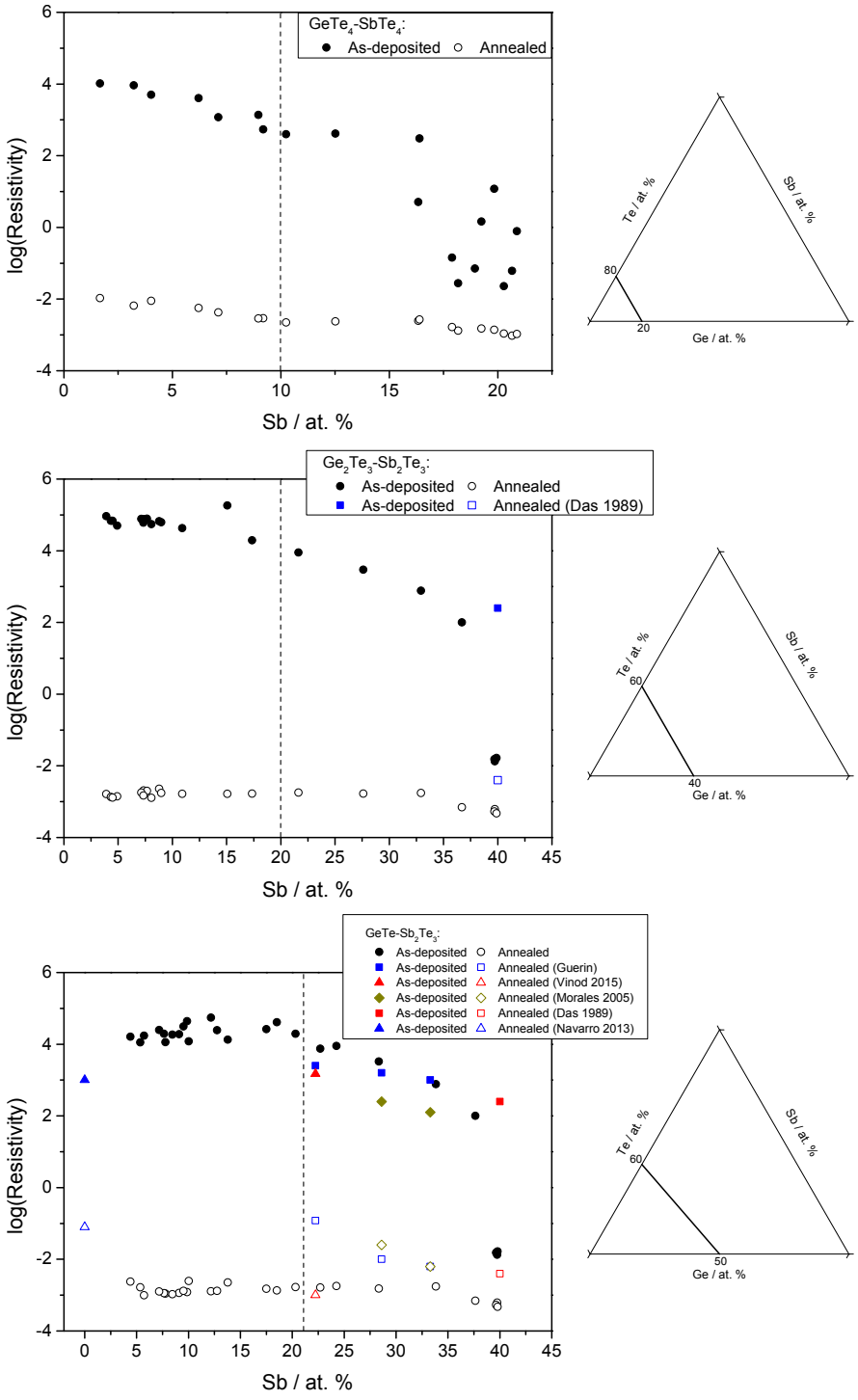

Figure 4.35: $log(\rho)$ as a function of Sb content for GST materials along the $GeTe_4$–$SbTe_4$, Ge_2Te_3–Sb_2Te_3 and GeTe–Sb_2Te_3 pseudobinaries as determined by 4PP. Experimental results are compared against the literature values.[190,199,221,228,235] Each plot compares the resistivity of the as-deposited (sample #8296, black dots) and annealed materials (sample #8299, 200 °C, white dots) along each line. Dotted lines indicate the intersection with other tie lines (see Figure 4.3). Ternary diagrams indicate the position of each pseudobinary within the GST ternary space.

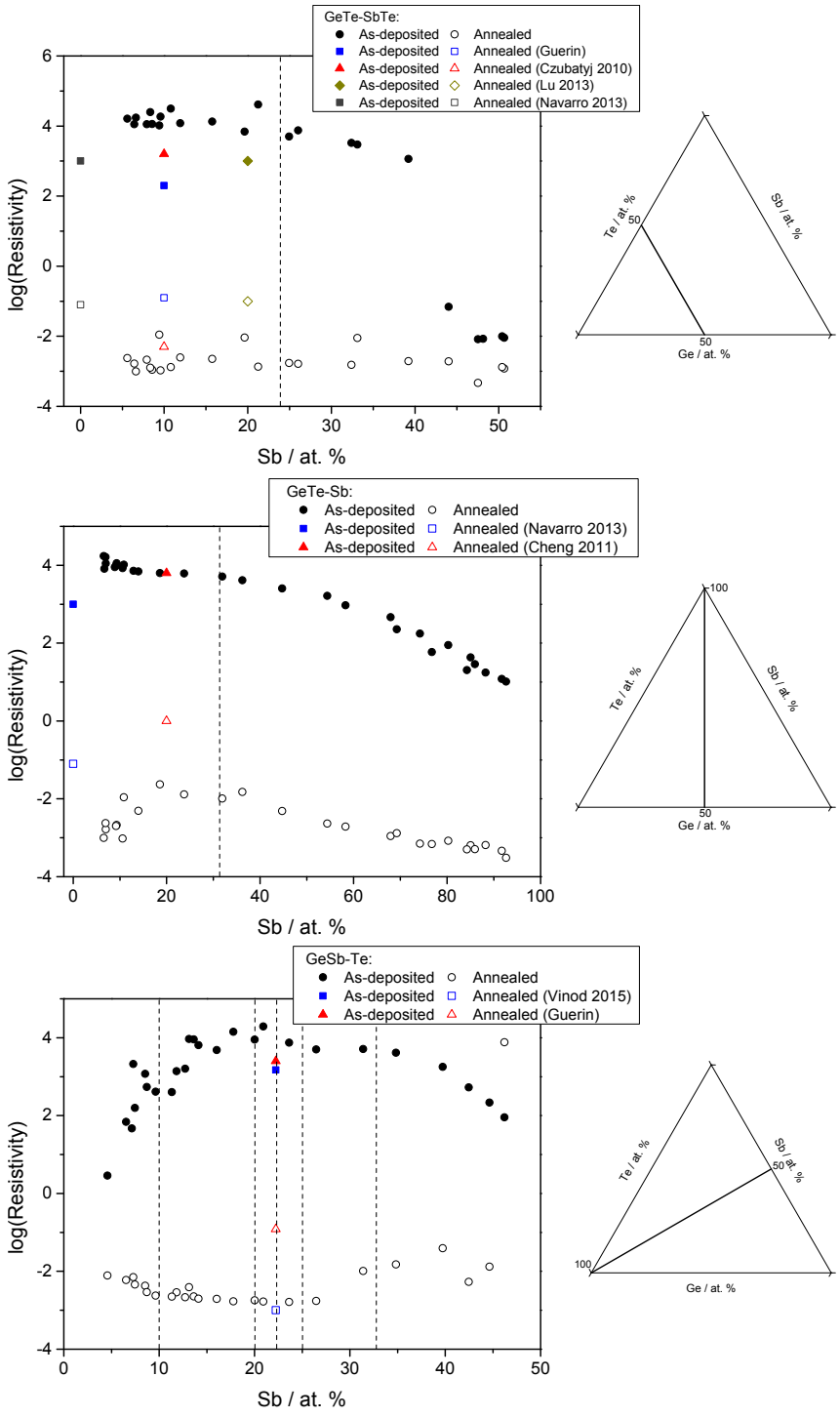

Figure 4.36: $log(\rho)$ as a function of Sb content for GST materials along the GeTe–SbTe, GeTe–Sb and GeSb–Te pseudobinaries as determined by 4PP. Experimental results are compared against the literature values.[93,190,199,221,229,230] Each plot compares the resistivity of the as-deposited (sample #8296, black dots) and annealed materials (sample #8299, 200 °C, white dots) along each line. Dotted lines indicate the intersection with other tie lines (see Figure 4.3). Ternary diagrams indicate the position of each pseudobinary within the GST ternary space.

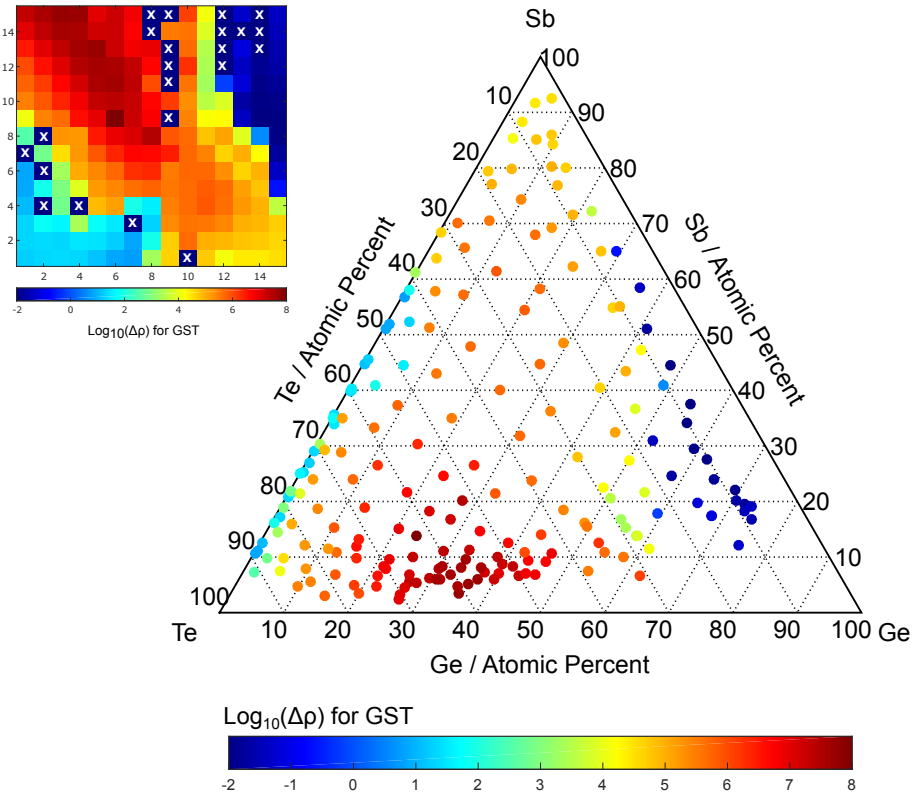

Figure 4.37: Map of the resistivity contrast, $log(\Delta\rho)$, between GST samples #8296 (as-deposited) and #8299 (annealed at 200 °C). Inset shows the distribution of this figure of merit across the thin film. The inset next to the ternary diagram shows the same information across the thin film: X-Y coordinates correspond to the position of each measurement point within the sample. Crossed out squares represent "dead points" where data could not be collected.

the GeSb–Te, which intersects all other tie lines, is the most notable. Its maximum resistivity contrast appears within the region where it intersects Ge_2Te_3–Sb_2Te_3 and GeTe–Sb_2Te_3 (20 – 22 at. % Sb) with $log(\Delta\rho) \cong 7$. Similarly, a local maximum along this pseudobinary was also seen at the 20 – 22 at. % Sb on the T_x trend line (Figure 4.33).

Compositions along the GeTe–Sb appear to have a consistent $log(\Delta\rho)$ within the range $4.5 < log(\Delta\rho) < 5.5$ past the GeTe composition. In particular, the local resistivity maximum seen in the annealed sample near 20 at. % Sb (Figure 4.33) turned out to be an inflection point in the plot, after which the value of $log(\Delta\rho)$ remained more or less constant up to 60 at. % Sb. The consistency of this parameter along this tie line could be exploited during the optimisation of other figures of merit of interest in PCRAM, such as switching speed.

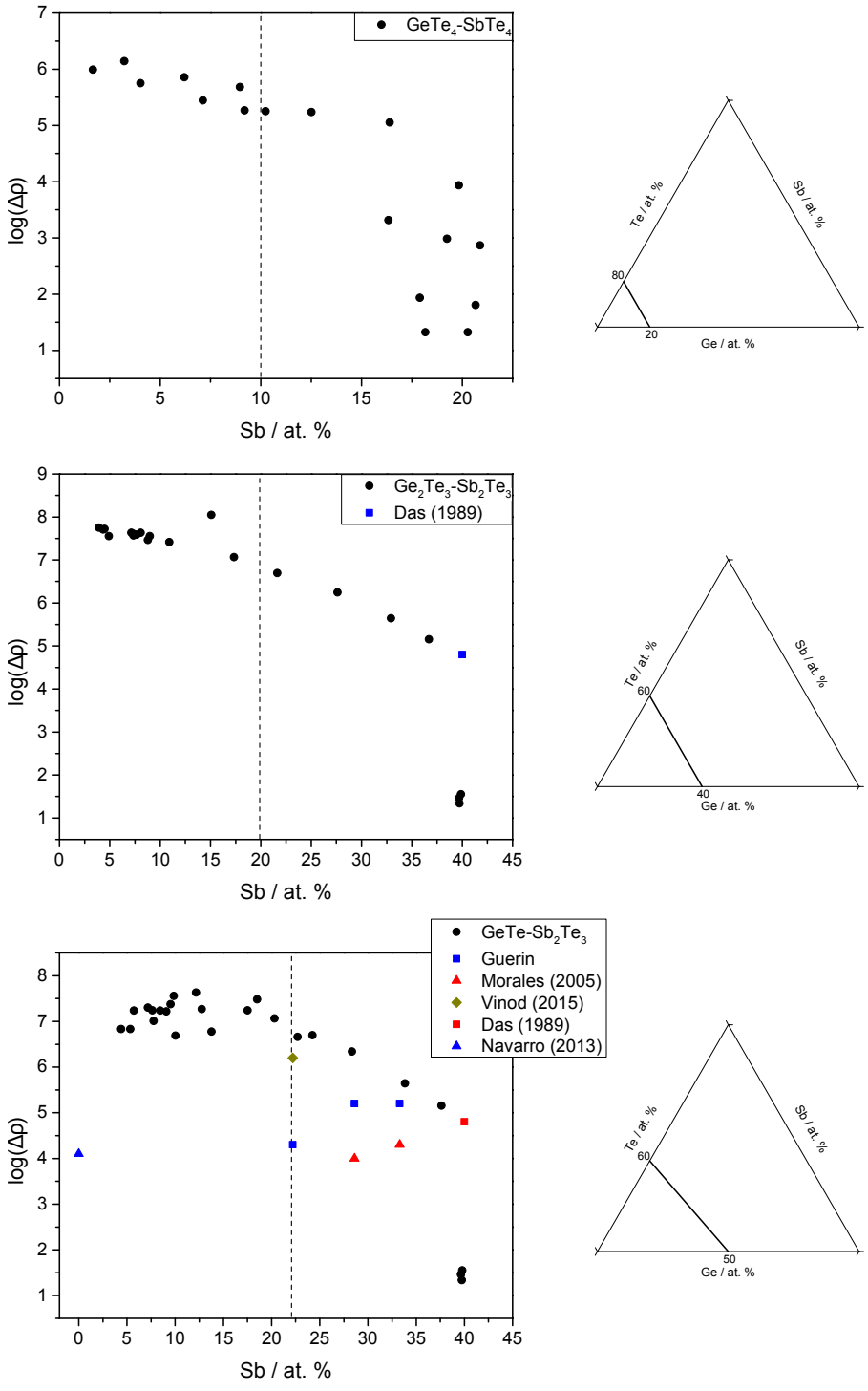

Figure 4.38: $log(\Delta\rho)$ as a function of Sb content for GST materials along the $GeTe_4$–$SbTe_4$, Ge_2Te_3–Sb_2Te_3 and GeTe–Sb_2Te_3 pseudobinaries. Experimental results (black dots) are compared against the literature values.[190,199,221,228,235] Ternary diagrams indicate the position of each pseudobinary within the GST ternary space.

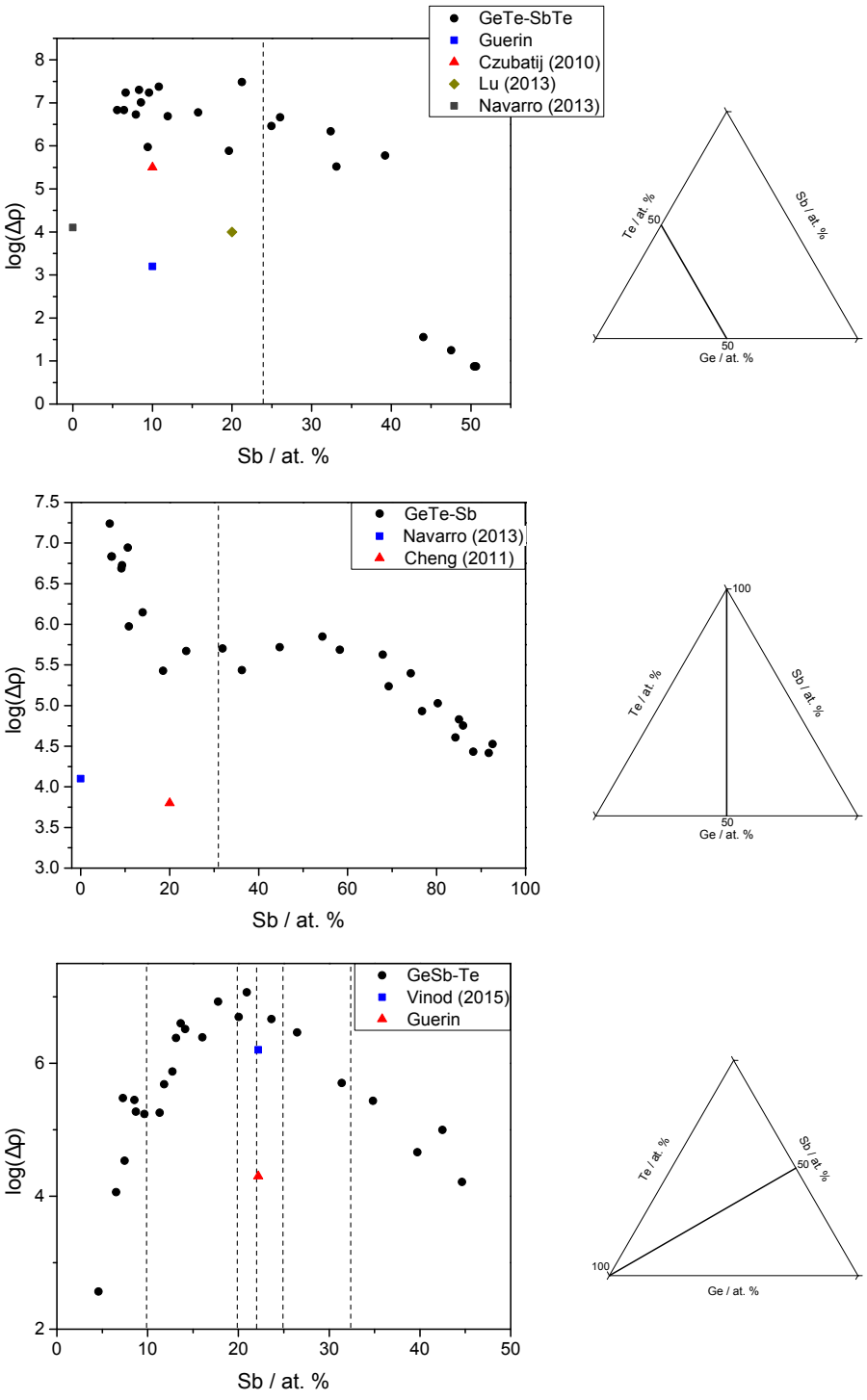

Figure 4.39: $log(\Delta\rho)$ as a function of Sb content for GST materials along the GeTe–SbTe, GeTe–Sb and GeSb–Te pseudobinaries. Experimental results (black dots) are compared against the literature values.[93,190,199,221,229,230] Ternary diagrams indicate the position of each pseudobinary within the GST ternary space.

Table 4.6: Resistivity contrast, $log(\Delta\rho)$, of selected GST compositions. Literature values provided for comparison.

Composition	Experimental $log(\Delta\rho)$	Literature $log(\Delta\rho)$	Citation
GST225	6.7	4.3	Guerin[190]
		6.2	Vinod[221]
GST124	6.3	5.2	Guerin[190]
		4.0	Morales[228]
GST147	5.7	5.2	Guerin[190]
		4.3	Morales[228]
GST415	7.4	3.2	Guerin[190]
		5.5	Czubatyj[229]
GST325	7.5	4.0	Lu[230]
GST212	5.4	3.8	Cheng[93]
Sb_2Te_3	1.5	4.8	Das[235]
GeTe (nearest)	6.8	4.1	Navarro[199]
$GeTe_2$ *(nearest)*	7.6	3.3	Navarro[199]
$Ge_{15}Sb_{85}$ *(nearest)*	4.7	1.6	Cabral[232]

4.4.3 Discussion

The functional characterisation of our combinatorial GST thin film libraries was done using the HTOMPT and 4PP techniques in order to determine their crystallisation temperature (T_x) and resistivity (ρ), respectively.

A ternary map of the crystallisation temperature of the GST system was given in Figure 4.31. The materials were found to crystallise within a 73 – 319 °C range, although towards the end of the HTOMPT experiment some Ge-rich materials still failed to crystallise. The resistivity of GST materials was shown in Figure 4.34 for both the as-deposited and annealed (200 °C) materials. The $log(\rho)$ ranges for the as-deposited and annealed samples were −2.1

to 5.3 and −4.7 to 4.3 respectively. In addition, the resistivity contrast between both phases was calculated and mapped into the GST ternary space in Figure 4.37. The resulting $log(\Delta\rho)$ values ranged from 0.6 to 8.1, although a few negative values were also obtained for some materials. These materials, characterised for their high Ge-content (> 50 at. %) and low Te-content (< 10 at. %) did not crystallise at 200 °C, and were found to be more conductive in the as-deposited state. It is possible that some structural rearrangement took place during annealing, like the formation of crystalline nuclei small enough not to be detected through XRD. These crystalline nuclei might increase resistivity due to their small grain size. However, examination of the Raman spectra of the materials within this region before and after annealing (Figure 4.27) did not provide enough evidence to either confirm or reject this hypothesis.

At first inspection there appears to be no further relationship between the results thus obtained and those obtained from structural characterisation (section 4.3). Of the six pseudobinary lines chosen for analysis,$GeTe_4$–$SbTe_4$, Ge_2Te_3–Sb_2Te_3, GeTe–Sb_2Te_3 and GeTe–SbTe did not provide any new insights into the function-structure relationship of GST materials. This may be a logical consequence of the relatively small number of functional tests performed on these materials. On the other hand, these pseudobinaries are physically close to each other and their path through the GST ternary space is short and covers some well-studied materials. Therefore, it should not be surprising to observe that the functional property trends along Ge_2Te_3–Sb_2Te_3, GeTe–Sb_2Te_3 and GeTe–SbTe happened to be very similar as shown in their pseudobinary plots of sections 4.4.1 and 4.4.2.

In contrast, the GeTe–Sb and GeSb–Te tie lines cover the longest possible paths across the GST ternary space from two different directions, increasing the probability to observe interesting trends. Specifically, Micoulaut *et al.* singled out the GeSb–Te pseudobinary as a good candidate to observe trends dependent on the structural rigidity of GST glasses be-cause the Te content of the materials decreases from 100 to 0 at. %.[88] On both T_x and $log(\rho)$ plots (Figures 4.33 and 4.36) the figures of merit increase monotonically until they reach a maximum near $20 - 22$ at. % Sb. Beyond this point the $log(\rho)$ of the as-deposited material decreased until the Te-content became exhausted. However, in the case of the T_x plot the crystallisation temperature decreased until 25 at. % Sb, at which point the Te-content of the material became 50 at. %. A more crowded environment around Te atoms would result in distorted bond lengths and therefore a more energetic glass. As discussed in section 2.4.3.1 these conditions

would favour crystallisation, hence the observed drop in T_x. Extending this interpretation, the local maximum at $20 - 22$ at. % Sb should be considered the compositional range at which the as-deposited glass would be at its lowest energy, thus increasing the resistivity of the material due to having fewer electrons being promoted to the conduction band. Beyond 25 at. % Sb, the Sb and Ge atoms of the cation sublattice dominate and begin to occupy the increasingly vacant anion sublattice formerly occupied by Te atoms. As the glass-forming properties of the material diminish due to Te loss, it becomes more rigid and more energy is required to crystallise it. At the same time, the imbalance of charge carriers due to excess Sb and Ge would reduce the resistivity of the as-deposited material as its structure begins to resemble more a GeSb alloy rather than a chalcogenide glass.

From the simulation results of Micoulaut[88] the rigidity of the materials along the GeTe–Sb pseudobinary would be expected to remain nearly constant. Therefore structural properties would be expected to have a greater impact than rigidity considerations in the functional properties of these materials. Figure 4.40a below shows the effect on T_x of the transition from a GST225-type material (which crystallises in the Fm$\bar{3}$m crystal group) to an Sb-type material (R3m space group). Similarly, Figure 4.40b the transition from a GeTe-type to an Sb-type local order was seen to have an effect on $log(\Delta\rho)$. While this analytical treatment may only be a qualitative approximation of the structure-function relationships within the GST ternary space, it would still be useful to inform decisions regarding the direction of future research. For example, it may be advantageous to restrict the optimisation of PCRAM materials to compositions known to crystallise in a specific space group (e.g. Fm$\bar{3}$m), in order to avoid epitaxial mismatch during manufacturing, and $log(\Delta\rho)$ within a given range (e.g. 5 to 6). Examination of the plots in Figure 4.40 shows that materials between $20 - 40$ at. % Sb along GeTe–Sb meet these requirements and also tend to crystallise within a narrow temperature range (150 °C). As a result of this process of elimination further characterisation may be performed on a smaller set of materials with the desired properties, thus helping to make the research and development cycle more efficient.

Regarding the Ge-rich GST212 "golden composition" studied by Cheng *et al.* (discussed in section 4.1)[93] it was possible to estimate a stoichiometric ratio, which we propose to be near $Ge_{51}Sb_{24}Te_{25}$, using our crystallisation and resistivity data. The "golden composition" had a T_x = 266 °C, a room temperature resistivity of 10 000 Ω m and a resistivity at 200 °C of 100 Ω m, resulting in $log(\Delta\rho) = 2$. Using the HTOMPT dataset T_x for $Ge_{51}Sb_{24}Te_{25}$ was found

to be 260 °C. The nearest composition, using the smaller resistivity dataset, was $Ge_{49}Sb_{22}Te_{29}$ with room temperature resistivity of 4217 Ω m and a resistivity at 200 °C of 0.3 Ω m, resulting in $log(\Delta\rho) = 4$. Sources of discrepancy between experimental and literature values have been addressed throughout the discussion in previous sections. In hindsight, given the number of compositions studied by Cheng *et al.* along the GeTe–Sb line, it may be obvious that the search of the "golden composition" for PCRAM applications could have been accelerated with the use of HT methods, while also achieving a similar degree of accuracy than more traditional experimental techniques.

From the previous discussion it may have become clear that the pseudobinary approach is a useful tool in the analysis of large compositional datasets such as those produced by HT methods. However, care must be exercised in the selection of said pseudobinaries so as to ensure that the data thus derived would be relevant to the task at hand.

4.5 Summary

The objective of the work carried out for this chapter was the synthesis and characterisation of combinatorial thin film libraries of GST. Synthesis was achieved using the HT-PVD system. Structural characterisation was done on both as-deposited and 200 °C-annealed samples using Raman spectroscopy and X-Ray diffraction. Primary functional characterisation involved the determination of resistivity and crystallisation temperature using the 4PP and HTOMPT techniques.

With the aid of a PCA model the results of the tests listed above identified five distinct clas-ses of materials within our thin film libraries. Table 4.2 summarised the structural characterisation findings of these models. The functional properties of our GST libraries appear to be in good agreement with published literature, especially around the popular GeTe–Sb_2Te_3 pseudobinary, although some disagreements were also observed around less well-studied regions of the ternary space. In addition, the unexpected semicrystallisation of some Sb:Te materials during deposition resulted in the determination of data that were not a true reflection of their known values from the literature.

The following significant results were obtained while working towards the primary objective of this chapter:

- The synthesis of the largest compositional space of GST materials reported to date, which included stoichiometric compositions such as GST225, GST124, GST147, GST212, GST325 and GST415.
- The first systematic examination of the short range order in both as-deposited and annealed GST materials via Raman spectroscopy.
- The use of a Principal Components Analysis models on XRD and Raman datasets to identify the constituent phases of annealed GST.
- Corroboration of the crystallisation temperature data obtained by Guerin *et al.* using the novel HTOMPT technique.
- The first systematic examination of functional properties across multiple pseudobinary lines, in particular GeTe–Sb and GeSb–Te.

It is hoped that our HT dataset will ameliorate the paucity of data beyond the GeTe–Sb_2Te_3 tie line and that any disagreements between our data and the literature will motivate further research into the Ge:Sb:Te system. It is expected that future use of the HT techniques demonstrated in this chapter will contribute not only towards the advance of PCRAM research, but also towards a better understanding of the fundamental properties of pure chalcogenide glasses.

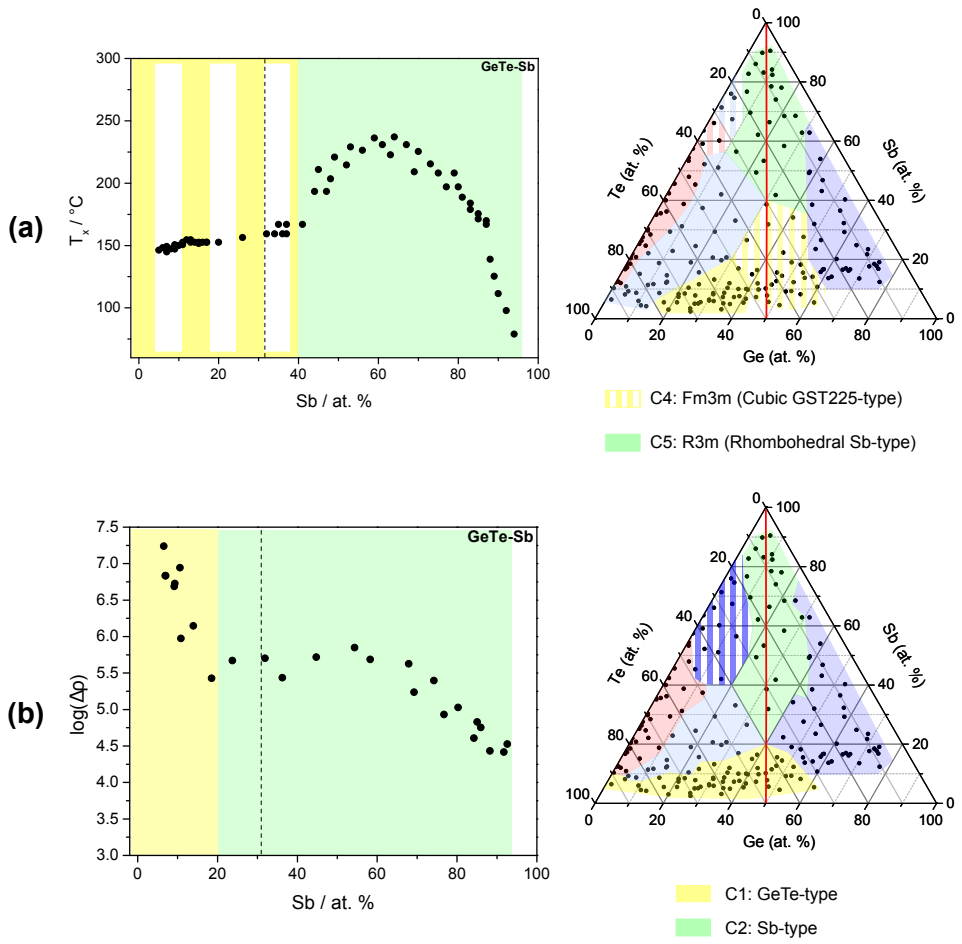

Figure 4.40: Qualitative effect analysis of the structure-function relationship of materials along the GeTe–Sb pseudobinary line of GST. (a) The plot of T_x along GeTe–Sb is shown alongside the phase map derived from the XRD PCA model (section4.3.2.1). Corresponding phases are shaded on the T_x plot, where the transition from GST225-type to Sb-type materials can be clearly seen at 40 at. %. (b) The $log(\Delta\rho)$ plot along the GeTe–Sb is shown alongside the phase map derived from the Raman PCA model (section 4.3.2.2). Corresponding phases are shaded, where the transition from GeTe-type to Sb-type materials can be seen at 20 at. % Sb.

Chapter 5

High-Throughput Deposition and Screening of N-GST

5.1 Introduction

In section 2.5.4 it was discussed that the effects of doping GST with N atoms resulted, amongst other effects, in higher crystallisation temperature, higher electrical resistivity, improved thermal stability and reduced PCRAM writing currents compared to the undoped material. However, most of the work on N-GST, has been carried out almost exclusively on the GST225 composition. It has only been recently that the effects of nitrogen doping on other GST compositions have been considered. Cheng *et al.* characterised sputtered GST325 thin films with increasing N doping levels up to a maximum 5 at. % N. They observed increased crystallisation temperature with increasing N content, peaking at 234 °C for the material containing 5 at. % N. Similar trends were reported during the determination of sheet resistance and optical band gap. They concluded that the formation of Ge nitrides, as evidenced by X-ray Photoelectron Spectroscopy (XPS) analysis, resulted in suppressed crystalline grain growth and was responsible for these observations.[236] They also tested a 2 at. % N-doped GST325 material for PCRAM performance and demonstrated improved data retention, thermal stability and power consumption compared to an equivalent device containing pure GST225.[237]

Osiac *et al.* doped a sputtered GST124 film with 1.8 and 3.7 at. % N for XRD analyses at different annealing temperatures and observed the suppression of hexagonal closed packed phases relative to undoped GST124. They also determined the phase transition temperature of the material doped at both 15 and 30 at. % N; a first transition was observed near 160 °C for both dopant levels, while a second transition was found at 180 °C and 190 °C respectively. They attributed the second transition to the formation of a state with mixed cubic and

hexagonal phases.[238]

Kim *et al.* doped GST147 using increasing N flow rates during the sputtering process. However they did not determine the precise dopant levels in their films. XRD studies on the materials annealed at 175 °C and 300 °C showed a suppression of crystallisation with increasing N content, as seen in other GST materials. They also reported an increase in transition temperature with increasing dopant levels.[239]

Given the promising properties of N-doped GST as a PCRAM material and the limited study of this system beyond the N-GST225 composition, our HT combinatorial methodology would be ideally positioned to explore the properties of materials in the wider N-GST compositional space.

5.2 Synthesis and Compositional Analysis by EDS

Combinatorial thin film libraries of GST materials were deposited in growth chamber A of the HT-PVD system described in section 3.1.1. Germanium (99.9999%, Alfa Aesar) was loaded onto e-gun 1, while antimony (99.9999%, Goodfellow) and tellurium (99.9999%, Alfa Aesar) were loaded into k-cells 1 and 3 respectively. The source geometry is shown in the left panel of Figure 5.1 and is similar to that used during the synthesis of GST materials depicted in Figure 4.1, including the use of the +60° angled wedge. The deposition parameters for these elements are provided in Table 5.1. In addition, a HD25 RF atom source (Oxford Applied Research), located at the position of k-cell 2 and aimed at sample substrate, was used to ionise a flow of molecular nitrogen gas during deposition (99.998%, oxygen-free, BOC) using 100 W of power. The nitrogen flow was controlled via a mass-flow controller and was set to 0.11 sccm resulting in 8.0×10^{-7} Torr partial pressure for the N_2 species and 2.0×10^{-8} Torr partial pressure for the monoatomic N species, as measured by the quadrupole mass spectrometer in the chamber. The incorporation of nitrogen into the films cannot be controlled in a combinatorial way by means of a wedge shutter. As the nitrogen plasma covers the sample substrate evenly, dopant levels will depend on the reactivity of the nitrogen with the composition of GST at any point in the library.

The growth chamber was baked at 150 °C for 50 hours. After this process the base pressure inside the chamber was 3.6×10^{-9} Torr. Samples were deposited as 28×28 mm continuous

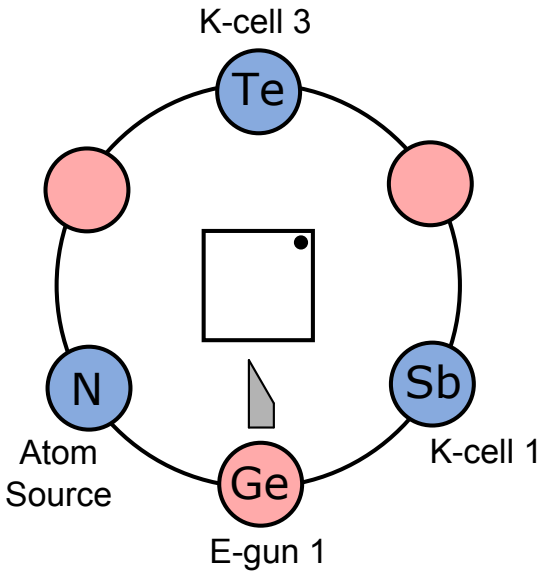

Figure 5.1: Top view of the source geometry for the HT deposition of N-GST, showing the physical location of the elemental sources and the position of the sample in relation to them. Also depicted is the angled wedge on e-gun 1.

Table 5.1: Deposition parameters for the synthesis of N-GST libraries.

Element	**Source**	**Rate**	**Temperature / °C**	**Wedge / mm**
Germanium	e-gun	0.5 Å s^{-1}	–	17.0, +60°
Antimony	K-cell	–	610	29.3
Tellurium	K-cell	–	410	22.0
Nitrogen	RF Atom	0.11 sccm, 100 W	–	–

films on a variety of substrates (Table 3.1) supplied by NOVA electronics. Before deposition, substrates were cleaned in an ultrasonic bath for 15 min in a 3 : 1 solution of isopropanol and deionised water. The clean substrates were dried under a flow of Ar (99.999%, BOC).

The deposition time varied according to the desired thickness of the films. An AFM measurement showed that the mean thickness of a sample deposited over 30 min was 82 ± 3 nm, and that a sample deposited over 55 min had a mean thickness of 149 ± 13 nm. This information was used to construct a calibration curve for the deposition of films of different thicknesses.

The aim for the synthesis of N-GST materials was to synthesise a small compositional space primarily centred at the section of the GeTe–Sb_2Te_3 pseudobinary containing the GST124,

GST147 and GST225 compositions. A plasma atom source has been used to incorporate reactive atomic nitrogen in the GST thin film library. This method has been applied previously in the synthesis of oxynitrides in perovskite materials[186] and nitrides.[240]

A series of HT EDS measurements was done on sample #7739 at an accelerating voltage of 12 kV. The measurements covered a 14×14 point grid, with a pitch between points of 1.867 mm. Figure 5.2 shows the atomic percent per element at each measurement point across the sample, where it is possible to inspect the deposition gradient for each element. Determination of N content in combinatorial libraries synthesised using our HT-PVD technique was done using EDS fitted with a state of the art silicon drift detector. Given the low concentration of N across the film relative to the GST elements, further refinement of the dopant content of the films was performed using the LayerProbe software supplied by Oxford Instruments. The software used the experimental EDS spectra collected during the 14×14 macros to model and quantify N levels in the samples. The objective was to dope the GST material with less than 10 at. % N as these levels have been reported to produce materials with the best PCRAM performance.[145] At this point it is important to remark that no detectable doping of the GST films was observed when molecular N_2 was used while the atom source was off at partial pressures as high as 1.0×10^{-6} Torr. Therefore, it may be inferred that during depositions that make no use of the atom source the conditions are not met to overcome the potential energy barrier required to break the N–N triple bond that would allow individual N atoms to adsorb onto the thin film.

The compositional gradients of Ge, Sb and Te on the N-GST sample are similar to those observed in GST (cf. Figure 4.2). Nitrogen doping was not homogeneous across the sample, and roughly followed the same concentration profile as Sb. Under the non-equilibrium conditions of the deposition process, this may be indicative of the greater thermodynamic stability of the Sb–N bond. Looking at the bond dissociation energies of the elements in the N-GST system (Table 5.2) it is clear that, apart from the N–N bond, the Sb–N bond is the most energetic and therefore has a deeper energy well than the Ge–N and Te–N bonds. Therefore, it may be expected that Sb–N bonds would have longer lifetimes during the deposition process and this would be reflected in the elemental composition after the sample has reached thermal equilibrium at the end of the process.

Quantification of nitrogen in the GST matrix is not a straightforward process, and several methods have been reported in the literature for this purpose. Techniques such as secondary

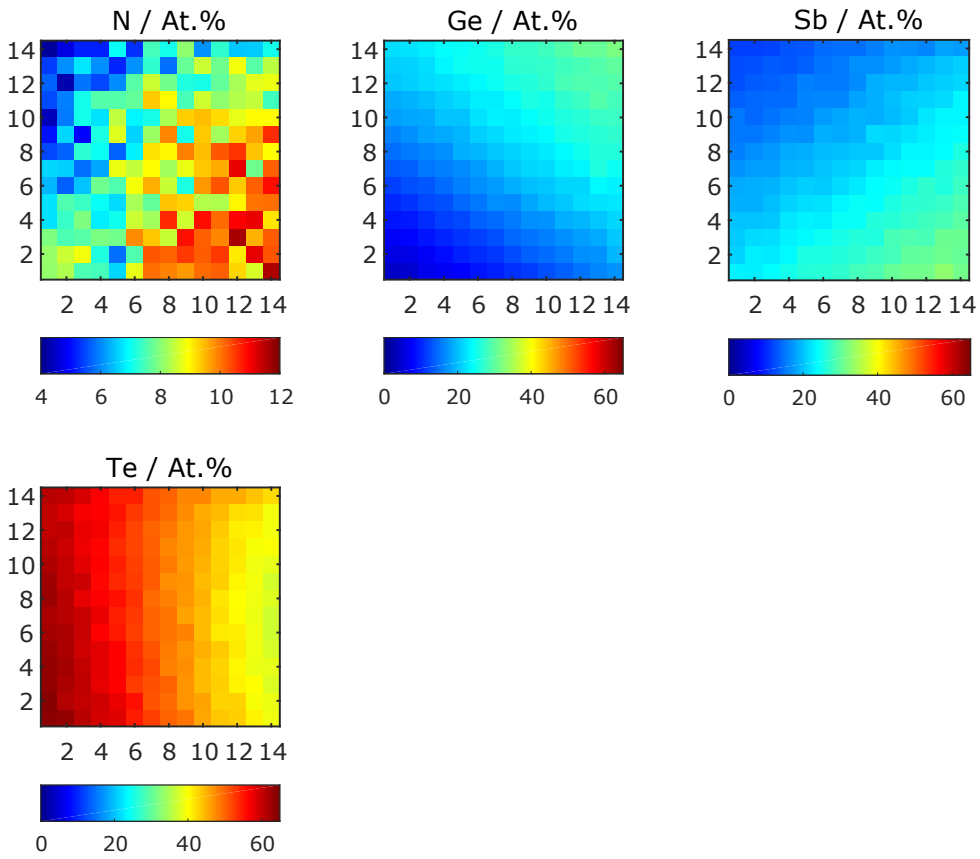

Figure 5.2: Composition gradients for each element in the combinatorial N-GST samples. The composition of each element is given in atomic percent, as determined by EDS (for GST) and EDS+LayerProbe (for N). The X-Y coordinates correspond to the position of each measurement point within the sample.

ion mass spectrometry (SIMS)[138] or inductively coupled plasma mass spectrometry (ICPMS) are qualitative unless a high-quality standard is used for quantification. XPS[119,237] has also been used for N determination and, while a highly sensitive technique, it is limited to elemental quantification on the surface of the sample unless coupled with depth profiling techniques[145] or synchrotron radiation.[241] In the case of N-GST materials, it is possible for XPS to underestimate the amount of N in the sample as it is mainly a surface probing technique. High-energy ion scattering (HEIS) spectrometry has been used to quantify N doping in N-GST, but the technique is not able to resolve Sb:Te ratios and a full quantification of the system had to be coupled with particle induced X-ray emission (PIXE),[145,242] or X-ray fluorescence.[139] Electron probe microanalysis (EPMA),[121] EDS[243] and X-ray fluorescence[244] techniques have all been used on their own to quantify the totality of the elements in N-

SbTe and N-GST systems, although the limitations of techniques based on the detection of characteristic X-rays have been covered in section 3.1.3. Given the benefits and drawbacks of each technique, as well as instrumental availability, it is not surprising that some groups have opted to report N content of their N-GST materials as a function of the N_2 gas rate used during sputtering,[236,239,245] or as a function of the ion implantation dose.[246]

Table 5.2: Bond dissociation energy (BDE) of the elements bonded with N in the N-GST. No data was found for the Te–N bond owing to the explosive nature of tellurium nitride.[247] Therefore, an estimate of this bond's energy was calculated using a simple linear regression, least squares fit, of the energies of the group 16 elements (also given).

Bond	**BDE** (kJ mol^{-1})
N–N[248]	945
Sb–N[248]	301
Ge–N[249]	257
Te–N	*242*
Se–N[248]	381
S–N[248]	464
O–N[248]	631

Figure 5.3 shows the location of all 196 points within the ternary compositional space of GST. This Figure also highlights the three pseudobinary lines that were used in the analysis of the data: Ge_2Te_3–Sb_2Te_3, GeTe–Sb_2Te_3 and GeTe–SbTe. Nitrogen content at each point has been colour mapped into the ternary diagram. The atomic percent range for each element was found to be: Ge (4 – 32 at. %), Sb (12 – 33 at. %), Te (37 – 64 at. %) and N (4 – 12 at. %). The rate of change in concentration for each element was ~1 at. % mm^{-1} (for Te) and ~0.8 at. % mm^{-1} for Ge and Sb. A list of compositions at each point quoted with their 95% confidence levels is given in Appendix A. Finally, the range of N doping for selected stoichiometric GST compositions are listed in Table 5.3.

5.3 Structural Characterisation

In this section the structural characterisation of the GST thin film combinatorial libraries obtained in section 5.2 will be discussed. The methods described in section 3.2 were used to

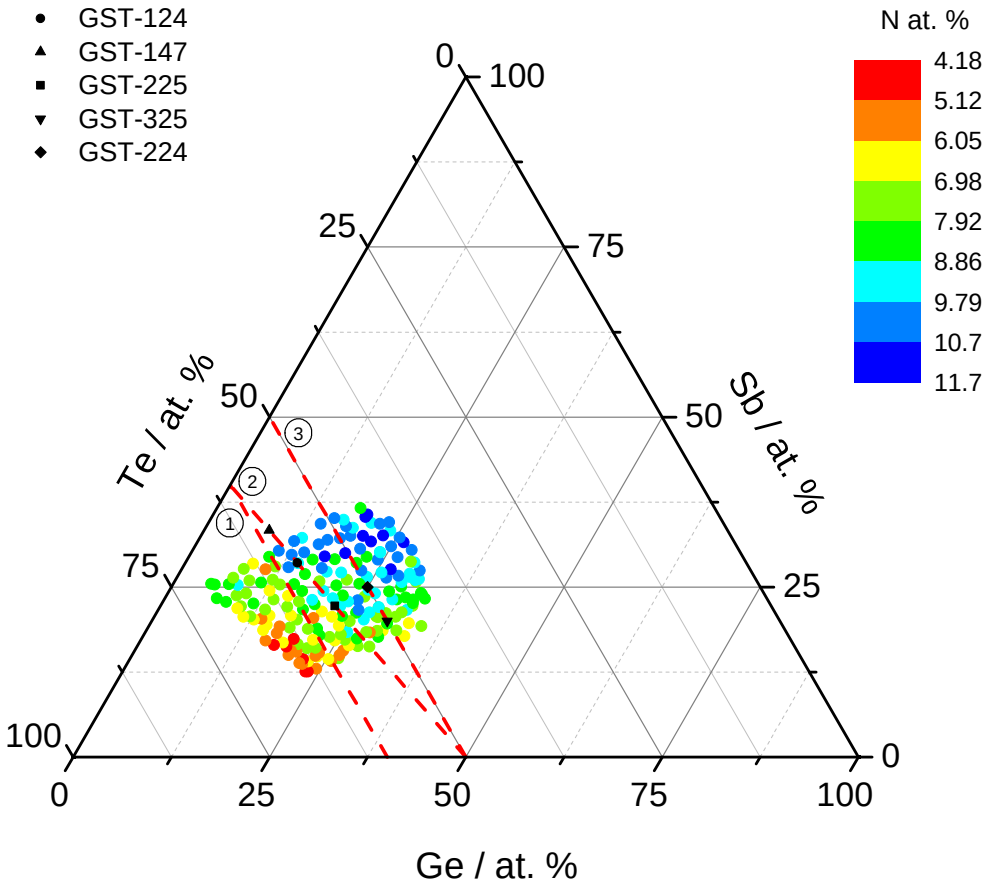

Figure 5.3: Ternary space coverage of deposited combinatorial libraries of N-GST. Dots show the composition of all 196 points measured by EDS in sample #7739. The colour map at each point shows the N doping levels. Also highlighted are the locations of some compositions of interest (in black) as well as the following pseudobinary lines: (1) Ge_2Te_3–Sb_2Te_3; (2) GeTe–Sb_2Te_3; (3) GeTe–SbTe. GST147 fell outside the compositional range of the film.

Table 5.3: Nitrogen doping range for selected GST compositions.

Composition	**N doping range** (at. %)
GST225	8.0 ± 1.3
GST124	9.1 ± 1.3
GST325	7.3 ± 1.4
GST224	8.3 ± 1.2

characterise N-GST libraries in both their as-deposited condition and after *in vacuo* annealing at 300 °C for 20 min in the manipulator of growth chamber A. XRD was used to characterise the long-range order of the materials, whereas Raman spectroscopy was used to determine their short-range order. Analysis of the as-deposited samples will be presented first and will be followed by the discussion of the annealed materials. XRD patterns will be compared against literature reports as no ICDD PDF reference cards were found for N-GST materials in the available databases. In addition, a very limited number of reports have been found that examine the Raman spectra of N-GST, however analysis can still be made by comparing the data to that of undoped GST. No evidence of film aging due to oxygen incorporation into the films was seen during analysis.

5.3.1 As-deposited N-GST

5.3.1.1 X-Ray Diffraction

A combinatorial library of N-GST of 149 ± 13 nm thickness was deposited on a silicon nitride substrate for XRD analysis. Collection of the XRD patterns was performed as per the procedure described in section 3.2.1. A total of 196 XRD patterns were collected for sample #7754 and are all provided in Figure B.6 in the Appendix: None of which showed evidence of crystalline phases. A photograph of the sample is shown in Figure 5.4 and shows no distinct features on the film which could be associated with a crystalline region, while Figure 5.5 shows a selection of XRD patterns from different points across the sample.

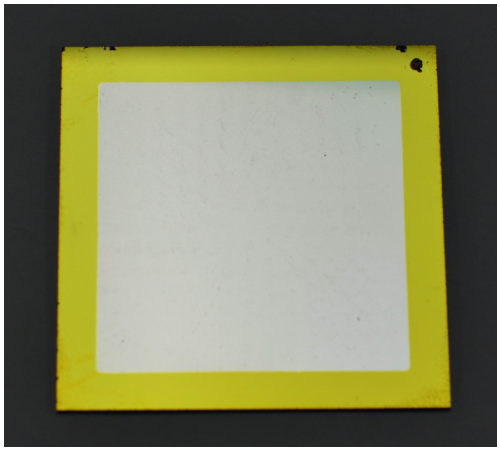

Figure 5.4: Photograph of an as-deposited N-GST library (#7754) with compositional points shown in Figure 5.3.

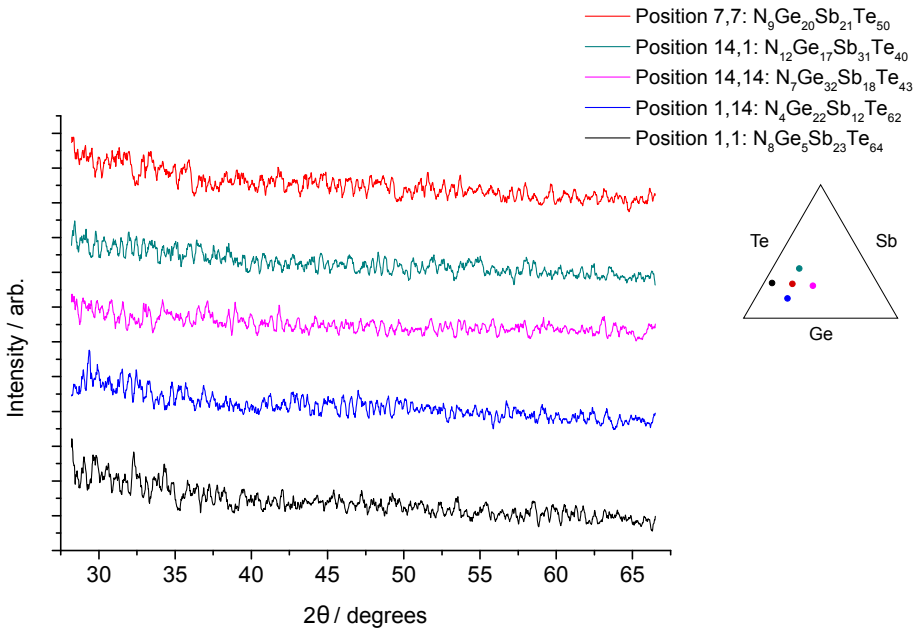

Figure 5.5: Selected diffraction patterns of N-doped GST compositions from as-deposited sample #7754. Ternary plot highlights the approximate location of the selected compositions within the ternary diagram of GST.

5.3.1.2 Raman Spectroscopy

Raman scattering measurements were performed on an as-deposited library on a silicon nitride substrate (#7754). The measurements were performed using the apparatus described on section 3.2.2 covering a $100 - 250\,\mathrm{cm}^{-1}$ Raman shift range collected over four 60 s acquisitions. A low laser power of 1% (0.25 mW) was used to prevent thermal annealing of the sample and a grating of 1800 grooves/mm was used.

A total of 196 Raman spectra were collected on sample #7754 are provided in Figure B.7 in the Appendix. The most dominant feature across all spectra is the wide band peaking at $150\,\mathrm{cm}^{-1}$. The location of this band is consistent across the entire sample within $\pm 5\,\mathrm{cm}^{-1}$, as shown in Figure 5.6. In addition, a small shoulder is observed in some compositions near the $125\,\mathrm{cm}^{-1}$ frequency, and its presence seems to be contingent on there being a Ge concentration higher than 20 at. %.

Since the combinatorial library of sample #7754 is centred at the part of the GeTe–Sb_2Te_3 pseudobinary containing the GST124 and GST225 compositions, it is expected that the Raman spectra of N-GST would show features present in those of the undoped materials. This is largely what is observed. The reduction and eventual disappearance of the $125\,\mathrm{cm}^{-1}$ band

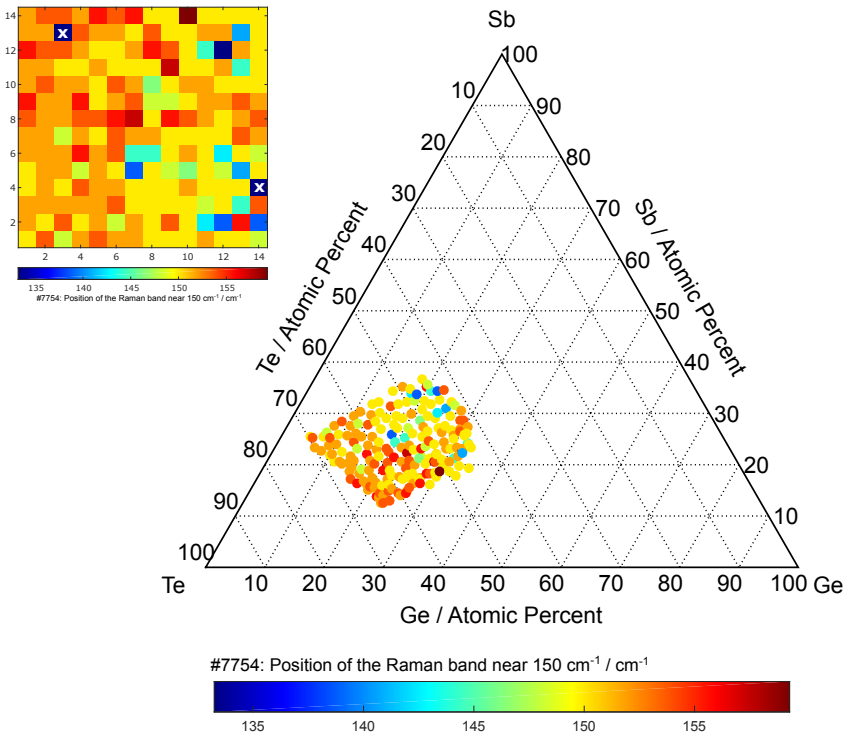

Figure 5.6: Position (in cm^{-1}) of the Raman band centred at 150 cm^{-1} of as-deposited N-GST sample #7754. Cross marks represent "dead points" in the sample. The inset next to the ternary diagram shows the same information across the thin film: X-Y coordinates correspond to the position of each measurement point within the sample. White cross marks indicate a "dead point" not included in the analysis.

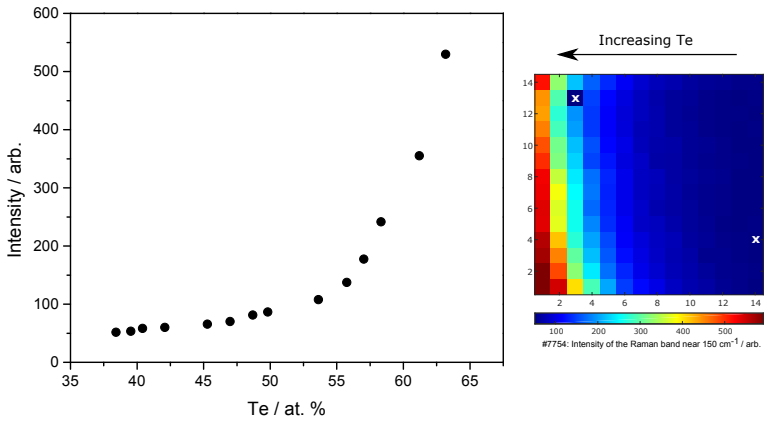

Figure 5.7: Maximum Intensity of the Raman band peaking at 150 cm^{-1} of as-deposited N-GST sample #7754 as a function of Te composition. Plot data points were taken from row 8 of the sample map (shown right). Increased intensity may be due to the formation of $SbTe_3$ pyramids within the material, which have intense Raman modes.[211] Cross marks represent "dead points" in the sample not included in the analysis.

would be consistent with the removal of Ge atoms from $GeTe_4$ corner-sharing tetrahedra for the formation of Ge–N bonds. This conclusion would be supported by XAS[241] and XPS[250] data which saw a prevalence of tetrahedral Ge. The 150 cm^{-1} band would belong to Sb–Te stretches within $SbTe_3$ pyramids, by analogy to the GST system (section 4.3.1.2). An interesting feature of this band is that its maximum intensity increases with increasing Te content, regardless of the level of N doping as shown in Figure 5.7. This may be indicative of an increased number of Te atoms in the amorphous matrix becoming available for bonding with primarily Sb atoms. The formation of structures containing only Te–Te bonds would be ruled out due to the lack of an intense band that would be expected to appear near 125 cm^{-1} for the Te-rich compositions, as demonstrated in Figure 5.8. Examples of the intense Te–Te modes just referred to may be seen in Figures 4.10 and 4.12.

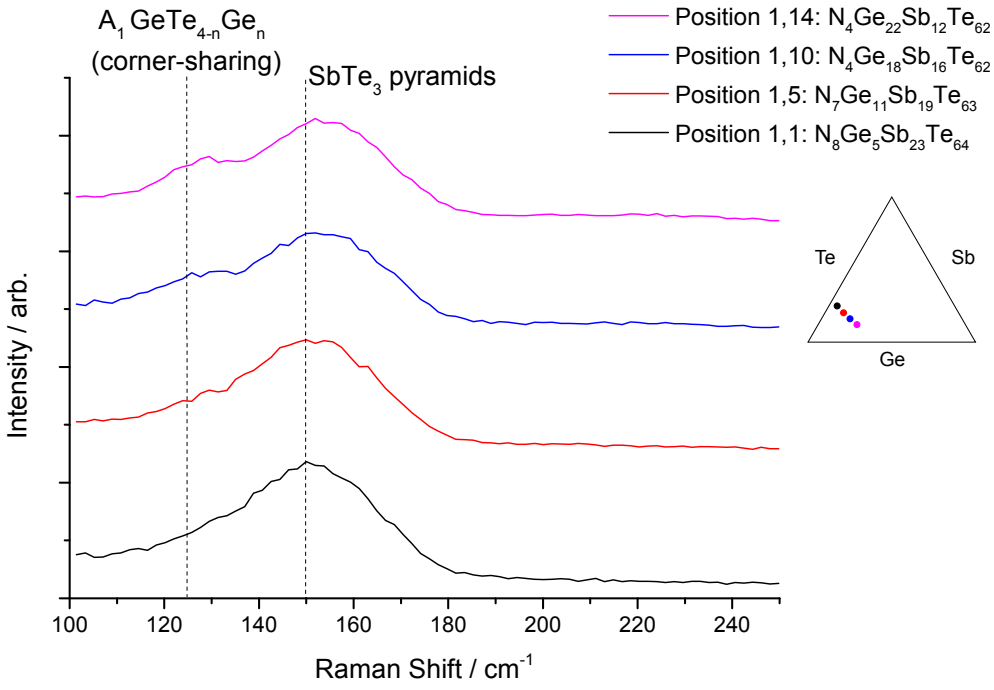

Figure 5.8: Raman spectra of Te-rich compositions within the N-GST system of as-deposited sample #7754 with proposed mode assignments for the peaks found near 125 cm^{-1} and 150 cm^{-1}. The intensity of the A_1 $GeTe_{4-n}Ge_n$ modes increases with increasing Ge content and reduced N content. The position of the Sb–Te mode appears to blue shift which may be due to the strain relaxation in the film as the N content also drops. Ternary plot highlights the approximate location of the selected compositions within the ternary diagram of GST.

Figure 5.9 compares the spectra of compositions GST124, GST225 and GST325 at approximately 8 at. % N doping and assigns the vibrational modes based on the pure amorphous

GST spectra (Figure 4.13). For all compositions the intensity of the A_1 mode of $GeTe_{4-n}Ge_n$ ($n = 1, 2$) corner-sharing tetrahedra is significantly lower than that of the Sb–Te bond stretches, however this difference is more marked for the GST124 composition as it inherently has less GeTe content. Conversely, for GST225 and GST325 the A_1 mode is of slightly higher intensity due to the higher GeTe content.

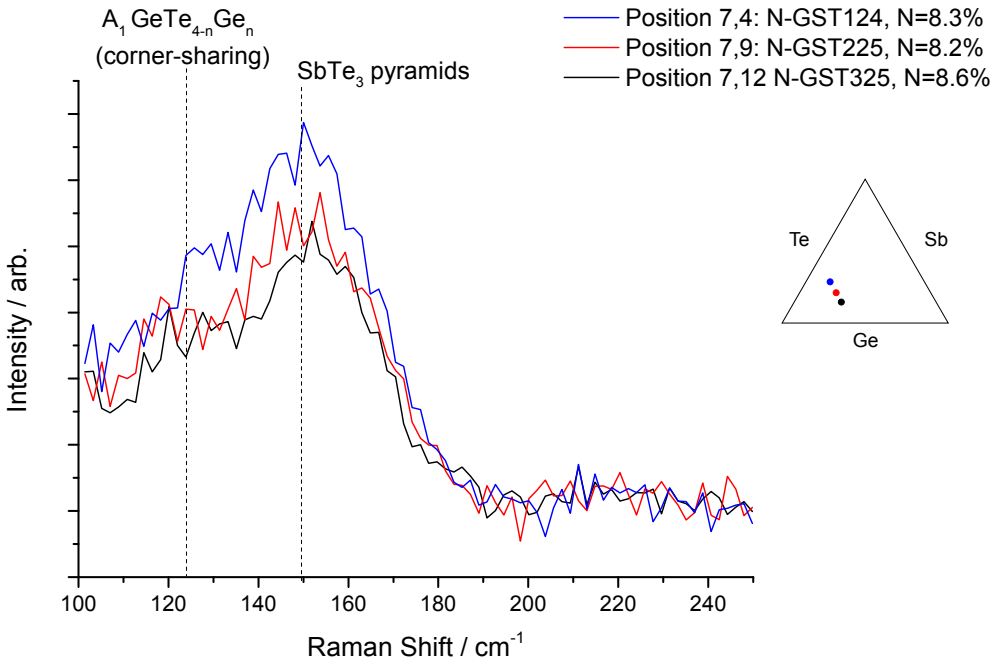

Figure 5.9: Raman spectra of GST124, GST225 and GST325 at ~8 at. % N doping for as-deposited N-GST sample #7754. Proposed mode assignments for the peaks found near 125 cm^{-1} and 150 cm^{-1} are also given. Ternary plot highlights the approximate location of the selected compositions within the ternary diagram of GST.

5.3.2 N-GST Annealed at 300 °C

5.3.2.1 X-Ray Diffraction

A combinatorial library of N-GST of 149 ± 13 nm thickness was deposited on a silicon nitride substrate for XRD analysis. Collection of the XRD patterns was performed as per the procedure described in section 3.2.1. The 196 diffraction patterns of sample #7760 are provided in Figure B.8 in the Appendix. After annealing to 300 °C the film, pictured in Figure 5.10, did not look substantially different from the as-deposited sample.

Because of the poor definition of the diffraction patterns due in part to the relatively low

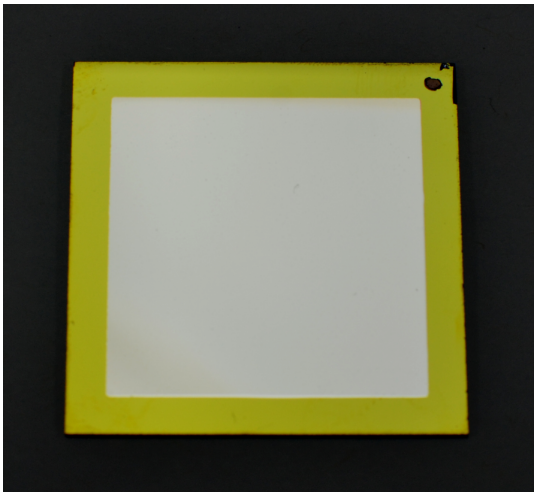

Figure 5.10: Photograph of an N-GST library annealed at 300 °C for 20 min (#7760) with compositional points shown in Figure 5.3.

annealing temperature chosen for this experiment, and also to the grain refinement caused by the precipitation of nitrides at grain boundaries, it was not possible to run a PCA model in this sample. Instead, the trend in peak position and intensity of the better resolved reflection at $2\theta = 42°$ was studied. This is shown in Figure 5.11. The position of the peak can consistently be located within $2\theta = 42.8° \pm 0.6°$. The intensity increases with the Ge content of the film, which may be an indication of the increased concentration of Ge–N precipitates along grain boundaries.

Figure 5.12 shows the diffraction patterns of some selected stoichiometric N-GST materials together with peak assignments. For the N-GST materials reported in the literature the diffraction peaks appearing at $2\theta = 28°$ and 42° correspond to cubic planes (200) and (220) respectively.[121,146,236,238] After annealing to temperatures higher than 250 – 300 °C the 42° reflection belongs to a hexagonal (100) plane instead.[121,139,146] The formation of exclusively hexagonal planes takes place at annealing temperatures exceeding 400 °C. A peak near $2\theta = 36°$ has been reported to belong to a hexagonal (106) plane in N-GST124 at 15 at. % N.[238] However, since this reflection can be observed all across sample #7760 it is more likely to belong to a residual hexagonal (015) phase of undoped GST. This is because the incorporation of nitrogen into the GST matrix is an energetically unfavourable process and as a result it tends to precipitate at grain boundaries.[121] Depending on how far the material is in the crystallisation process, the remaining peaks at $2\theta = 51°$ and 53° may belong to either hexagonal N-GST phases (201) and (112) or cubic N-GST phases (311) and (222).[121,139]

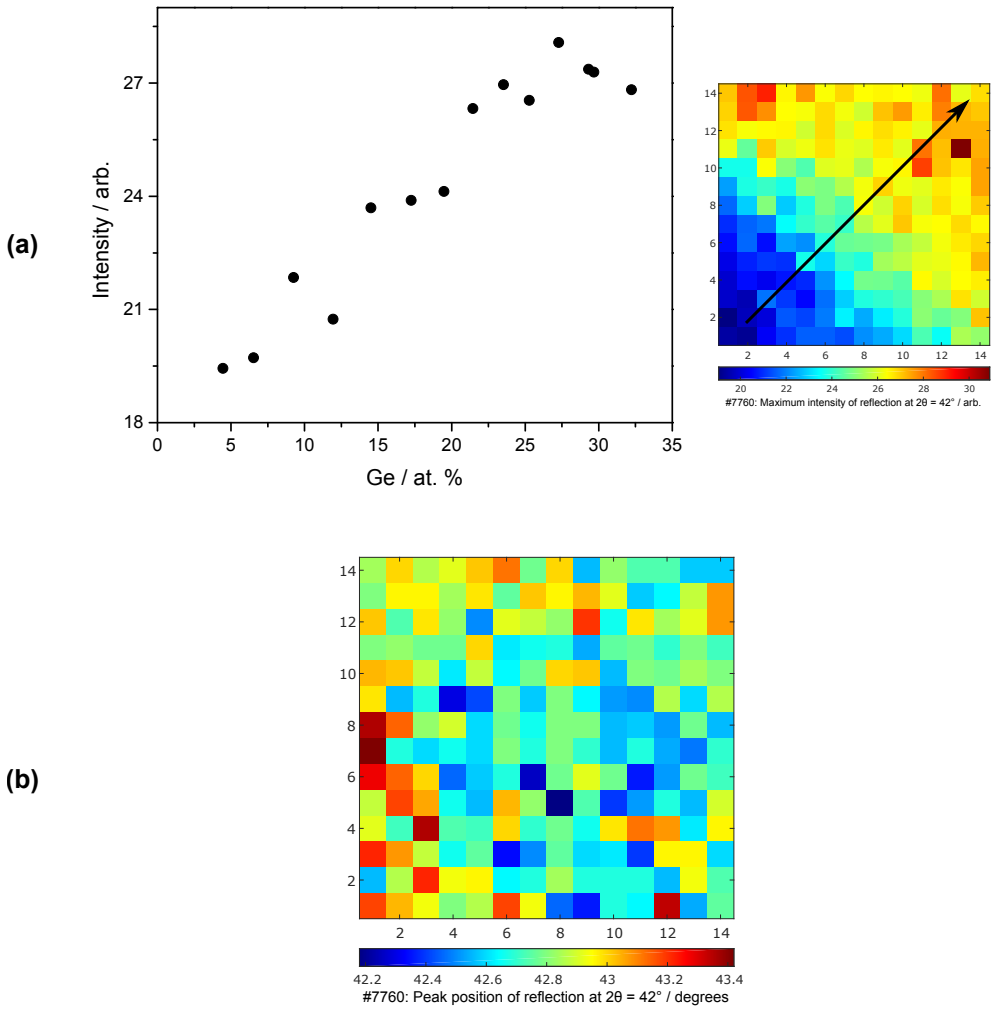

Figure 5.11: (a) Maximum intensity of the reflection at $2\theta = 42.8°$ as a function of Ge composition for the N-GST library of sample #7760 annealed at 300 °C. Data points were taken from a diagonal across the sample map (shown right) from coordinates (1,1) through (14,14). Arrow indicates the direction of increasing Ge concentration across the film. (b) Sample map showing the position across the film of the peak centred at $2\theta = 42.8°$.

Finally, the reflection near $2\theta = 58°$ has been assigned to a hexagonal N-GST (202) plane.[139] It can thus be concluded that the combinatorial library annealed at 300 °C contains a mixture of cubic and hexagonal N-GST phases together with undoped hexagonal GST phases. All diffraction patterns in the sample show some degree of crystallisation, and the low intensity and general broadness of the peaks are in agreement with those reported in the literature for dopant levels up to 30 at. % N and annealing temperatures between 250 – 300 °C.[121,139,146] Broad diffraction peaks are consistent with small grain sizes in the material, which have been reported for N-GST before.[140]

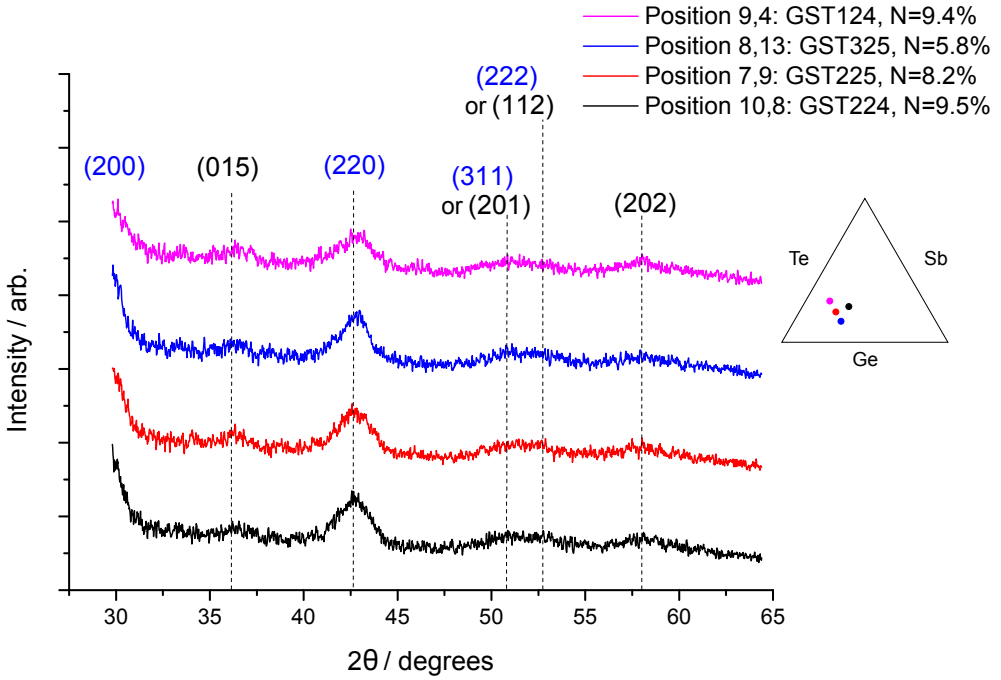

Figure 5.12: Selected diffraction patterns of N-doped GST compositions from sample #7760 after annealing to 300 °C. Proposed peak assignments are shown for cubic (blue) and hexagonal (black) phases. Ternary plot highlights the approximate location of the selected compositions within the ternary diagram of GST.

The diffraction patterns in the Ge-poor region of sample #7760, shown in Figure 5.13, further reinforce the notion of mixed phases within the film. Yin *et al.* reported that N-doped Sb_2Te_3 materials annealed at 290 °C can exist as a mixture of separate hexagonal Te and orthorhombic Sb–N phases.[251] Our XRD patterns more closely resemble those with the highest N content as prepared by Yin *et al.* although some shift in peak position was observed, likely due to the presence of Ge atoms as dopants which would introduce distortions into the N-SbTe lattice.

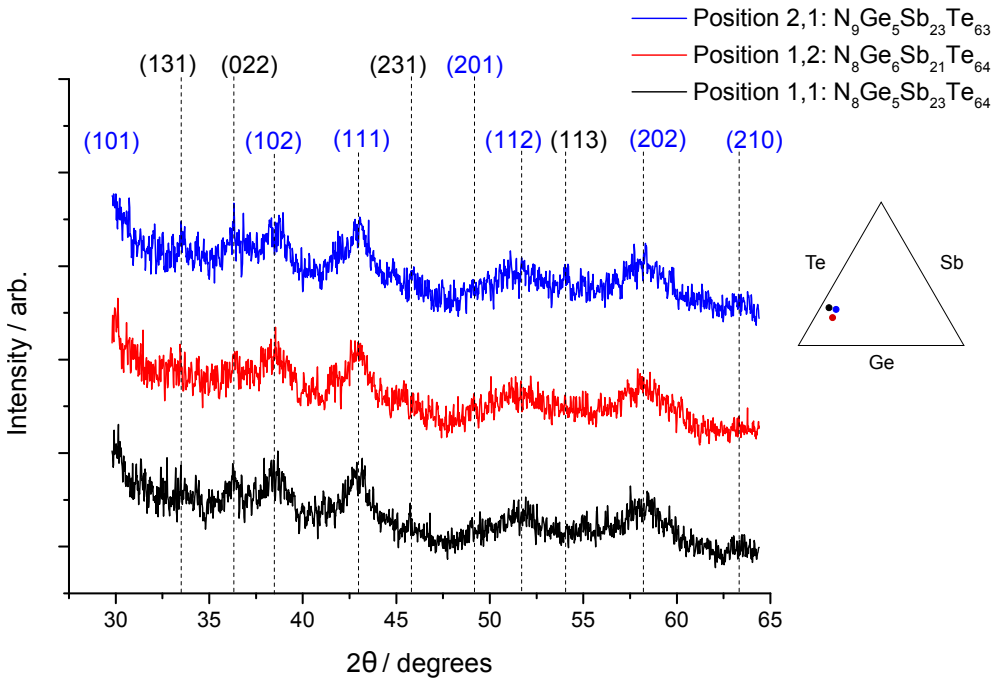

Figure 5.13: Selected diffraction patterns of N-doped, Ge-poor, N-GST compositions in sample #7760 after annealing to 300 °C, peak assignments follow Yin *et al.*[251] and correspond to hexagonal Te (blue) and orthorhombic Sb–N (black) phases. Ternary plot highlights the approximate location of the selected compositions within the ternary diagram of GST.

5.3.2.2 Raman Spectroscopy

Raman scattering measurements were performed on a library deposited on a silicon nitride substrate and annealed *in vacuo* for 20 min at 300 °C in the manipulator of growth chamber A (#7760). The measurements were performed using the apparatus described in section 3.2.2 covering a 100 – 250 cm^{-1} range collected over four 60 s acquisitions and a grating of 1800 grooves/mm. A low laser power of 1% (0.25 mW) prevented thermal annealing of the sample during the experiment.

The 196 Raman spectra were collected on sample #7760 are provided in Figure B.9 in the Appendix. The sample presents two vibrational bands centred at 110 cm^{-1} and 150 cm^{-1}. The spectra match qualitatively those obtained by Liu *et al.* for ion-implanted N-GST225 where they reported nitrogen content in relation to implanted ion dose,[246] which also resemble the Raman spectra of cubic undoped GST.[205,211] Liu *et al.* also observed the 110 cm^{-1} band blue shifts and the 150 cm^{-1} band red shifts with increasing nitrogen content. However this trend was not observed on either band for compositions within sample #7760, which may be

due to the relatively narrow N doping range. Figure 5.14 shows the positions of the Raman bands in the sample. Both bands have a variation in position of $\pm 5\,\mathrm{cm}^{-1}$. Liu *et al.* assigned the $110\,\mathrm{cm}^{-1}$ band to $GeTe_4$ vibrations which likely originate from an A_1 mode of α-GeTe,[252] by analogy to the hexagonal GST system. They ascribed the $150\,\mathrm{cm}^{-1}$ band to unassigned Sb–Sb vibrations within (Te_2)Sb-Sb(Te_2) or (SbTe)Sb–Sb(SbTe) substructures following their previous work on the crystalline GST system.[220] These structures would be an evolution of the $SbTe_3$ pyramids identified in the as-deposited sample (Figure 5.8).

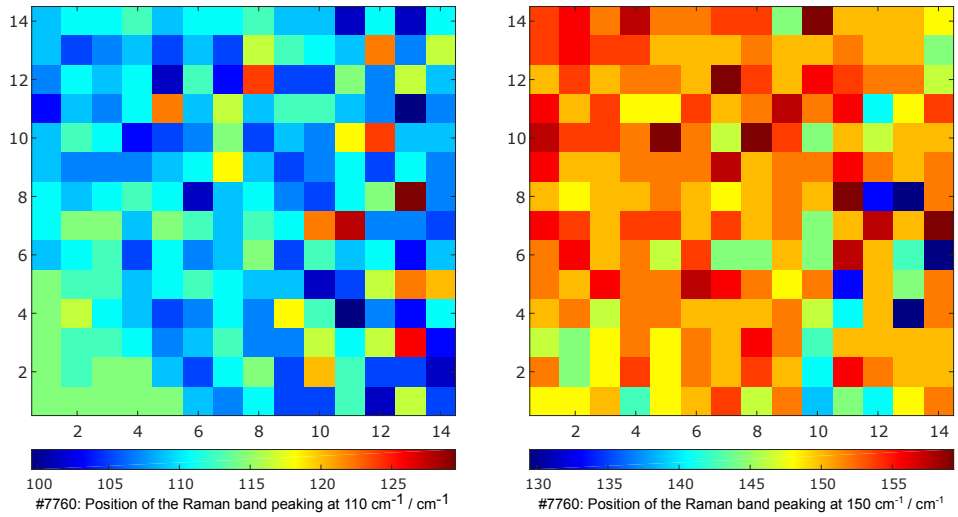

Figure 5.14: Position of the peaks within the observed Raman bands centred at $110\,\mathrm{cm}^{-1}$ (left) and $150\,\mathrm{cm}^{-1}$ (right) for N-GST sample #7760 after annealing to 300 °C.

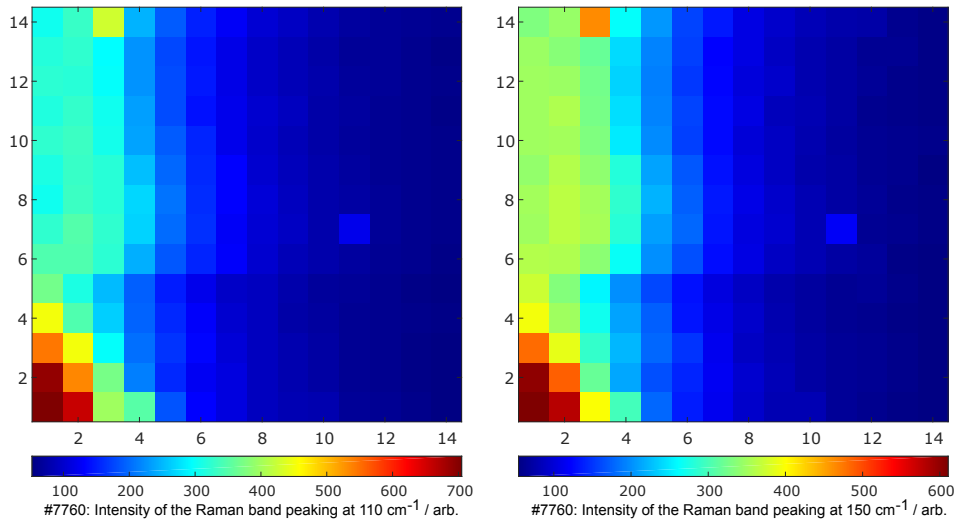

Figure 5.15: Maximum intensity of the Raman bands peaking at $110\,\mathrm{cm}^{-1}$ (left) and $150\,\mathrm{cm}^{-1}$ (right) for N-GST sample #7760 after annealing to 300 °C.

The intensity of both bands, shown in Figure 5.15, follows a similar pattern to that seen in the

as-deposited sample (Figure 5.7) with greater intensity at higher Te content independent of N doping. However, unlike the amorphous phase the annealed material had significant Te–Te bond formation in the Ge-poor corner of the sample. At these compositions the 110 cm^{-1} band is blue shifted to a consistent 115 cm^{-1} frequency, as may be appreciated on the left panel of Figure 5.14, due to the presence of a relatively intense peak within the band. As demonstrated in Figure 5.16 said 115 cm^{-1} peak disappears with increased Ge concentration. This is suggestive of Te–Te bond formation through a segregated Te phase, given that the A_1 mode of pure crystalline Te is expected to appear at 120 cm^{-1},[204] with the red shift being due to strain induced by surrounding nitride structures. The XRD data for this region of N-Sb_2Te_3-type materials (Figure 5.13) provides further evidence of Te–Te bond formation through phase segregation. Finally, a small peak at 165 cm^{-1} has been assigned to the A_{1g} mode of Sb_2Te_3 by analogy to the undoped system (Figure 4.25).[219] This mode becomes less intense and ultimately disappears as the Ge content of the materials increases.

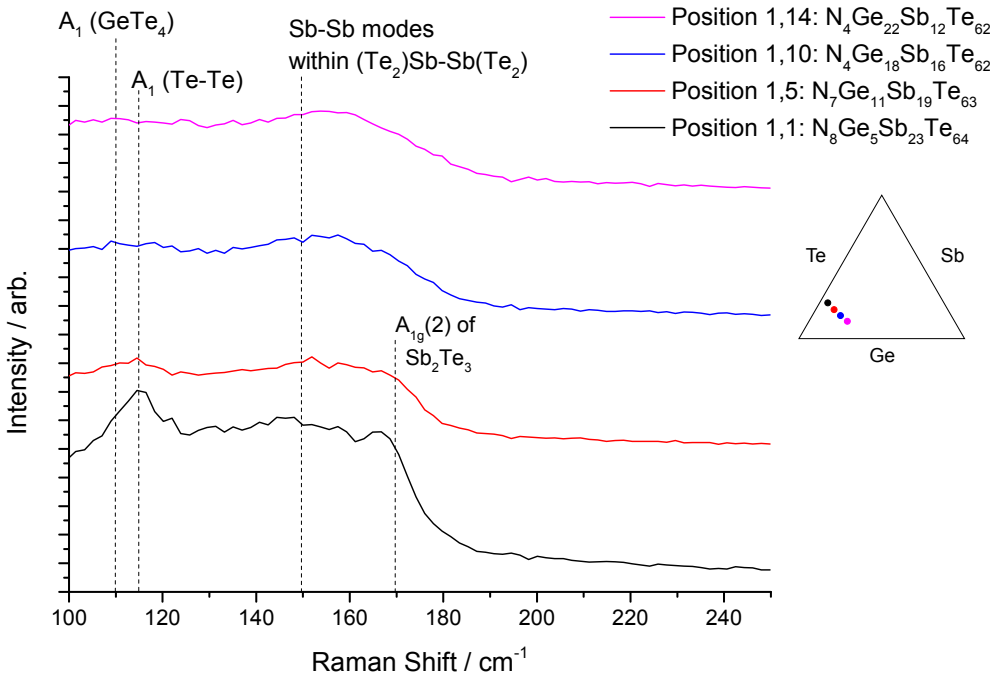

Figure 5.16: Raman spectra of Te-rich compositions within the N-GST system of sample #7760 after annealing to 300 °C. The intensity of the Te–Te modes at 115 cm^{-1} and Sb_2Te_3 modes at 165 cm^{-1} decreases with increasing Ge content. The $GeTe_4$ peak at 110 cm^{-1} becomes more important relative to the Sb–Sb modes at 150 cm^{-1} as the Ge content increases. Ternary plot highlights the approximate location of the selected compositions within the ternary diagram of GST.

The spectra of the crystalline compositions GST124, GST225 and GST325 at approximately

8 at. % N are given in Figure 5.17. The $GeTe_4$ band at 110 cm^{-1} has become more intense, relative to the amorphous state, a behaviour that is also observed in cubic undoped GST.[211] This behaviour is consistent with the XRD data presented in Figure 5.12 that showed these compositions exist as a mixture of cubic and hexagonal N-GST phases. This suggests that the atomic order at the local level remains closer to the cubic phase than the hexagonal. While it is clear that Ge nitrides remain an important component of the material, simulations have shown that N–Ge–Te bonds with long lifetimes also form during the crystallisation of N-GST.[144] Moreover, this band becomes better defined with increased N content.[246] Thus it would not be surprising if further structural studies revealed the formation of some type of highly polarisable structure containing N–Ge–Te (such as N_xGeTe_{4-x}) as the primary contributor to the intensity of this band. Alternatively, this mode could belong to an E_{2g} vibration of β-Ge_3N_4,[253] although the noticeable dip in the spectra around 130 cm^{-1} where an intense E_{1g} band would be expected does not support this interpretation. The Sb–Sb band at 150 cm^{-1} also becomes better resolved with increasing N doping. Substitutions of Te with N within the (Te_2)Sb–Sb(Te_2) or (SbTe)Sb–Sb(SbTe) substructures proposed by Liu would also significantly change the environment around the Sb–Sb bonds. These Te substitutions in both bands are supported by AIMD simulations that suggest that the most favourable place for N insertion would be Te vacancies.[143]

5.3.3 Discussion

The HT-PVD deposition method produced N-GST thin film combinatorial libraries with mean thickness of 149 ± 13 nm. Structurally, the as-deposited N-GST libraries were found to be amorphous across the entire sample. This was demonstrated through XRD measurements (Figure 5.5) where none of the collected patterns showed any diffraction peaks. N-GST libraries annealed at 300 °C showed evidence of crystallinity across all points as evidenced by XRD (Figures 5.7 and 5.8).

The Raman spectra of N-doped GST225 materials were similar to those of the as-deposited undoped GST (Figure 5.18). The most notable difference was the decrease in intensity of the peak associated with $GeTe_4$-type structures, while Raman spectra of the annealed materials showed vibrational modes similar to those observed in undoped cubic GST.[211]

Raman vibrational modes belonging to $GeTe_4$-type structures that exist in undoped GST

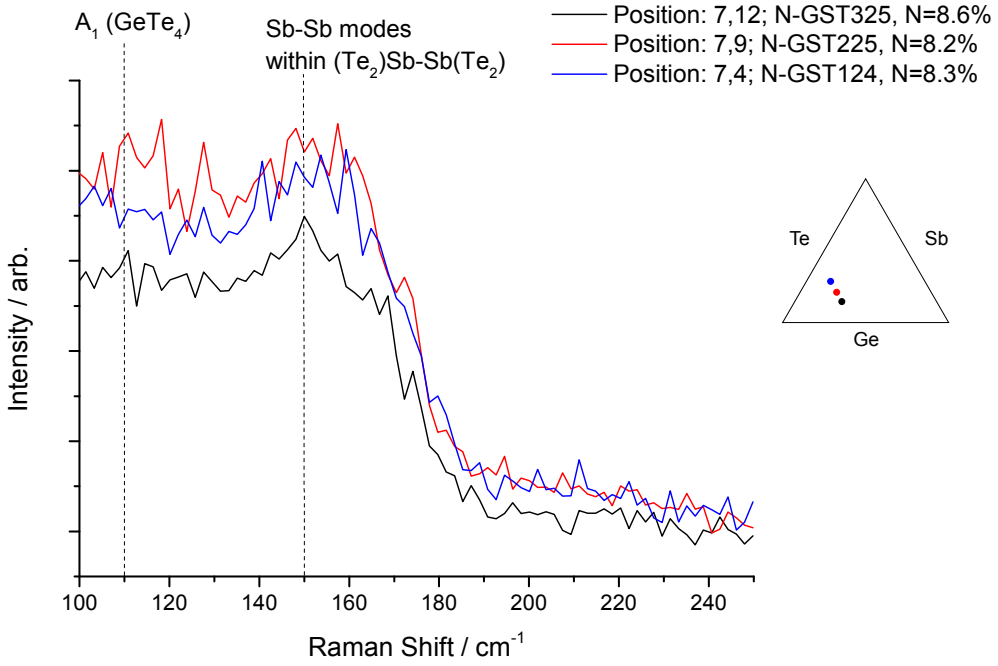

Figure 5.17: Raman spectra of GST124, GST225 and GST325 at ~8 at. % N doping for N-GST sample #7760 after annealing to 300 °C. Proposed mode assignments for the peaks found near 110 cm^{-1} and 150 cm^{-1} are also given. Ternary plot highlights the approximate location of the selected compositions within the ternary diagram of GST.

may have been supressed due to the formation of Ge–N bonds within the doped material. Evidence for the formation of Ge–N bonds (belonging to Ge_3N_4) originates from XAS,[241] XPS[250] and NEXAFS[141] data. However, XRD measurements have not been able to detect distinct Ge–N phases, either because the precipitates do not crystallise or, if they do, due to their small concentration relative to the rest of the N-GST system.[139] Both our XRD and Raman measurements failed to detect any Ge_3N_4 within the measured experimental ranges. While a single vibrational mode of β-Ge_3N_4 might have been detected near the 110 cm^{-1} frequency in the crystalline sample, the lack visible vibrational modes at higher frequencies within the experimental range discourages this interpretation. On the other hand, γ-Ge_3N_4 has been reported to have strong Raman vibrational modes at frequencies higher than the range used in our experiments[254] and might still be detected that way.

The structural analysis of both as-deposited and crystalline libraries revealed that two distinct classes of materials may be found within the films. The first class is related to typical N-GST-type materials, such as N-GST225, and covered the majority of the film (Figure 5.12). The second class was restricted to the Ge-poor section of the film and included composi-

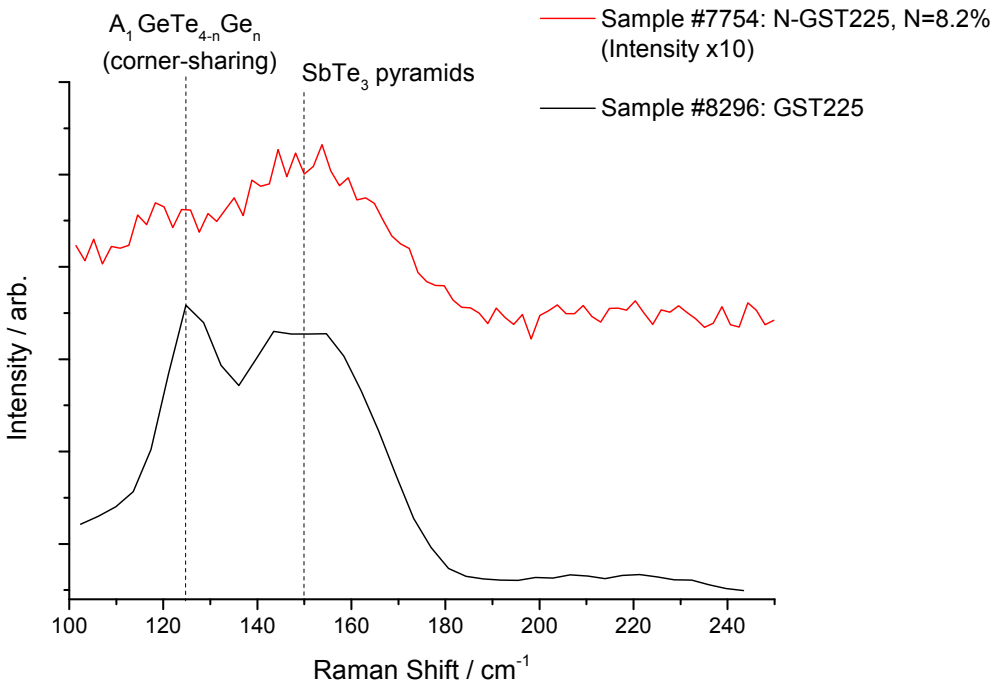

Figure 5.18: Comparison of the Raman spectra of as-deposited N-GST255 (N = 8.2 at. %, from sample #7754) and as-deposited GST225 (from sample #8296). The intensity of the N-GST225 spectrum has been multiplied by 10 in order to facilitate this comparison. Proposed peak assignments are provided following the discussion in sections 4.3.1.2 and 5.3.1.2.

tions with structure similar to N-Sb_2Te_3-type materials (Figure 5.13). XRD analysis of the crystalline films revealed both classes of N-doped materials exist as a mixture of phases. For N-GST-type materials cubic and hexagonal phases were identified, whereas hexagonal Te and orthorhombic Sb–N phases were found in N-Sb_2Te_3-type materials. The specific space group of these phases could not be assigned with the available experimental data. Moreover, reports in the literature only determine the crystal system of the material after the calculation of lattice parameters. In consequence these phases have been discussed in terms of the crystal systems to which they belong.

Figure 5.19 compares the diffraction patterns of N-doped and undoped GST225 materials from samples #7760 and #8299 respectively. Despite the different annealing temperatures, the contrast between the two materials is evident. After annealing to 200 °C, GST225 crystallised into the hexagonal P3m1 phase. N-GST225 materials with a doping range of 8.0 ± 1.3 at. % N, annealed at 300 °C, crystallised as a mixture of hexagonal and cubic phases. This is in agreement with reports of higher crystallisation temperature of the N-doped GST for which temperatures in excess of 350 °C are required to fully crystallise the material into the

hexagonal phase (at N-doping levels < 10 at. %).[139,140,146]

Finally, AFM surface scans show evidence of grain refinement in 9 at. % N-doped GST225 (sample #7760) with an average crystallite size of < 20 nm (Figure 5.20). On the other hand, undoped GST225 (sample #8299) was found to have an average crystallite size of ~2 µm. The measured crystallite size was found to be in good agreement with the literature for both systems. Kim *et al.* prepared N-GST225, 5.4 at. % N, and reported a crystallite size of ~5 nm after annealing to 300 °C.[244] For undoped GST225, Jeong *et al.* observed large crystallites (> 1 µm) on sputtered films annealed at 145 °C, which were similar in shape and size to those observed in Figure 5.20.[255]

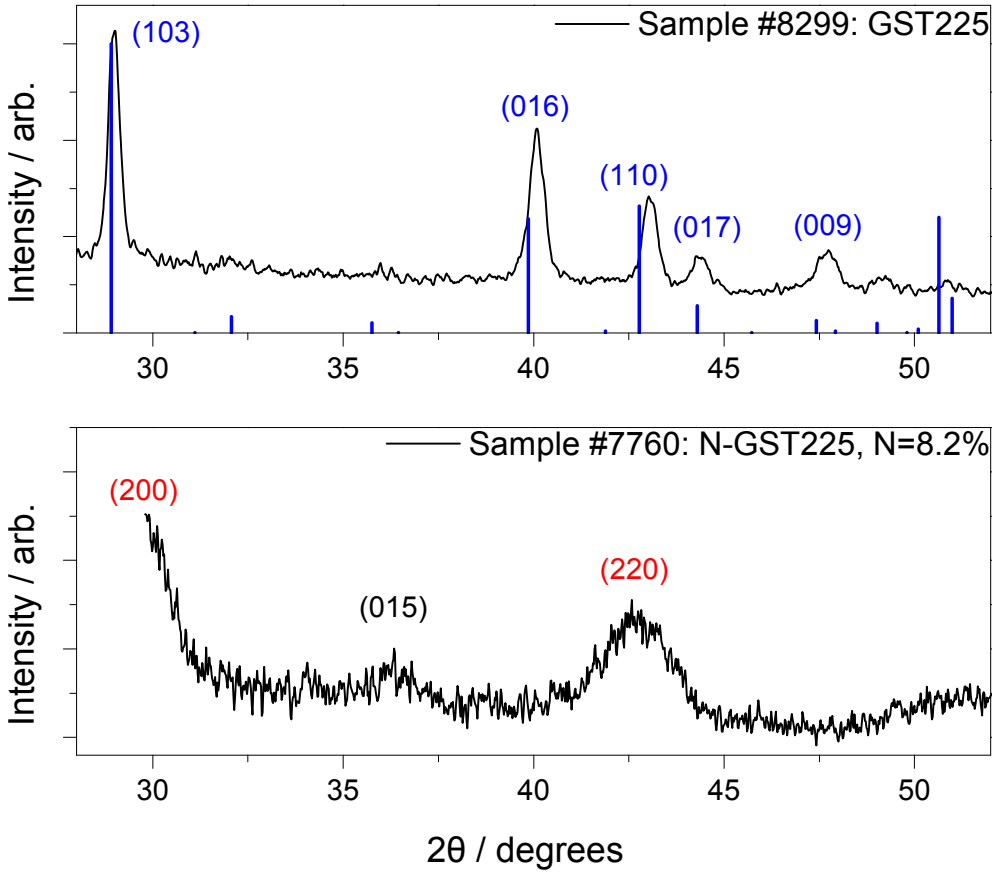

Figure 5.19: Comparison of diffraction patterns of GST225 (from sample #8299 annealed at 200 °C, top) and N-GST225 doped at 8.2 at. % N (from sample #7760 annealed at 300 °C, bottom). GST was found to crystallise in the hexagonal P3m1 phase (PDF 01-073-7758, blue vertical lines) while N-GST was found as mixture of cubic (red labels) and hexagonal phases (black label).[121,139] No ICDD PDF patterns for N-GST were found in the available databases.

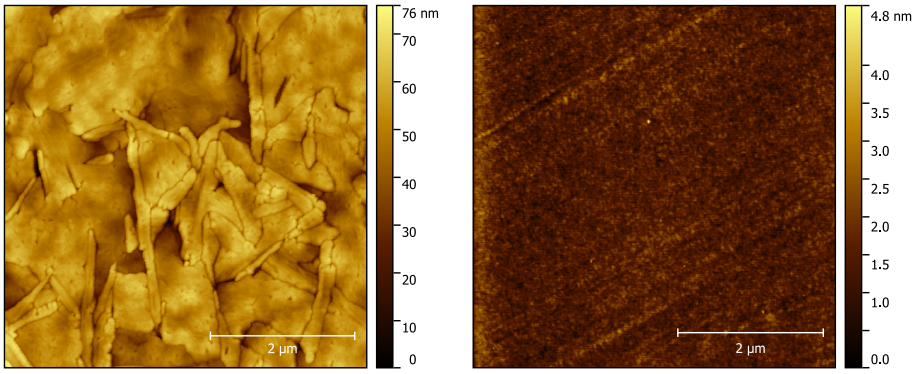

Figure 5.20: Tapping mode AFM scans over a 25 µm^2 area comparing the surface of combinatorial thin film libraries of GST and N-GST. Scale bar represents a length of 2 µm. (a) Scan of sample #8299 (GST annealed at 200 °C) over the area corresponding to the GST225 composition showing large, flake-like crystallites of ~2 µm mean diameter; (b) Scan of sample #7760 (N-GST annealed at 300 °C) over the area corresponding to N-GST225 (N = 9 at. %) showing much smaller crystallites less than 20 nm in diameter.

5.4 Functional Characterisation

5.4.1 Crystallisation Temperature

The magnitude of reflectivity changes and the crystallisation temperature (T_x) derived from them were measured using the HTOMPT technique described in section 3.3.2. The as-deposited N-GST sample #7750 was heated from room temperature to 475 °C at a rate of 10 °C min^{-1} under Ar flow. The HTOMPT analysis for this sample was performed on a 14 × 14 matrix, as used for the other characterisation techniques.

All 196 intensity versus temperature curves collected in this measurement are shown in Figure B.10 in the Appendix. Figure 5.21 below shows a selection of the typical HTOMPT profiles obtained during the experiment. Unlike the sharp intensity transitions observed for most undoped GST compositions (Figure 4.29) detection of the first phase transition on N-GST using this technique is more subtle; some transitions either take place over an extended temperature range or their relative intensity change is small. The usefulness of the HTOMPT technique for the detection of a second transition in N-GST is debatable, as no reports were found that suggest a reflectivity change concomitant with the phase change. Moreover, the typical resistivity method for determining phase transition temperatures also encounters

difficulty with this transition, particularly at higher N concentrations.[145,236,238,246,251] As such, for the purpose of this analysis only the first phase transition is reported.

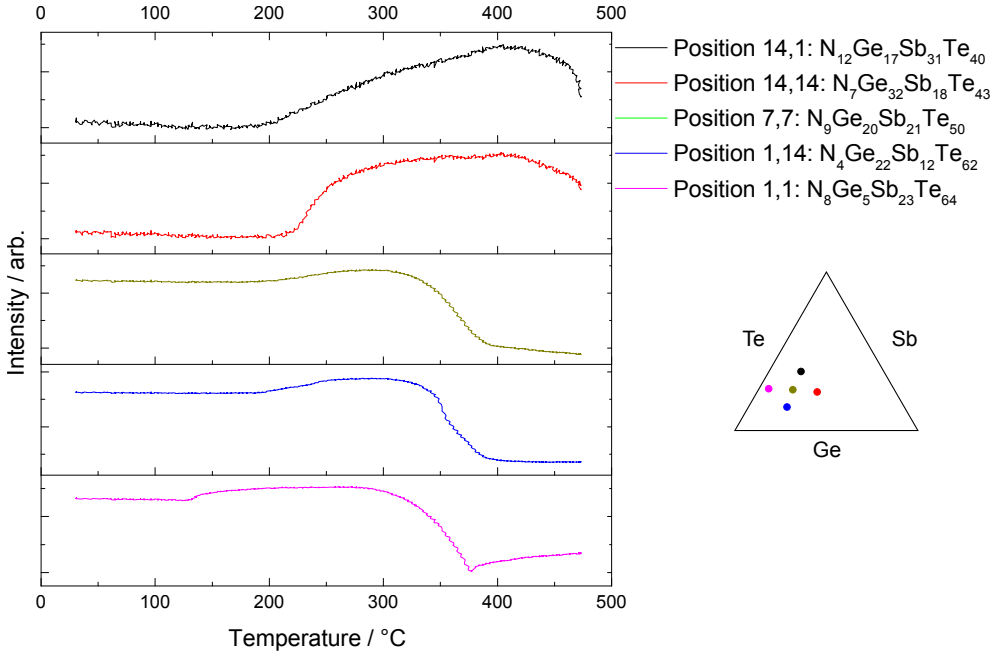

Figure 5.21: Selected HTOMPT curves for N-GST materials on sample #7750. Ternary diagram shows the location of each curve within the compositional space.

Maps of the intensity change (ΔI) at 200 °C, 300 °C and 400 °Crelative to the intensity at the start of the experiment are shown in Figure 5.22. At 200 °C the N-Sb_2Te_3-type materials and neighbouring compositions exhibit the largest intensity change, while intensity the rest of the film that contains N-GST-type materials has not changed substantially. At 300 °C some compositions along an imaginary "boundary" separating the N-Sb_2Te_3 and N-GST-type materials show negative intensity change. The intensity of the rest of the film has increased relative to 200 °C, with the largest change observed for Ge-rich compositions. Finally, at 400 °C the intensity change shows is directly related to the Te content of the material, as materials with more Te show the largest intensity drop and the intensity change in Te-poor materials continues to increase. In addition, some compositions along the valley appear to have a lower intensity change than neighbouring materials. This is probably associated with the small increase in reflectivity after 350 °C observed in these materials, of which position (1,1) in Figure 5.21 is an example.

The first phase transition temperature (T_x) of the N-GST system is shown as a ternary space plot in Figure 5.23. The composition with lowest transition temperature was $N_8Ge_5Sb_{23}Te_{64}$

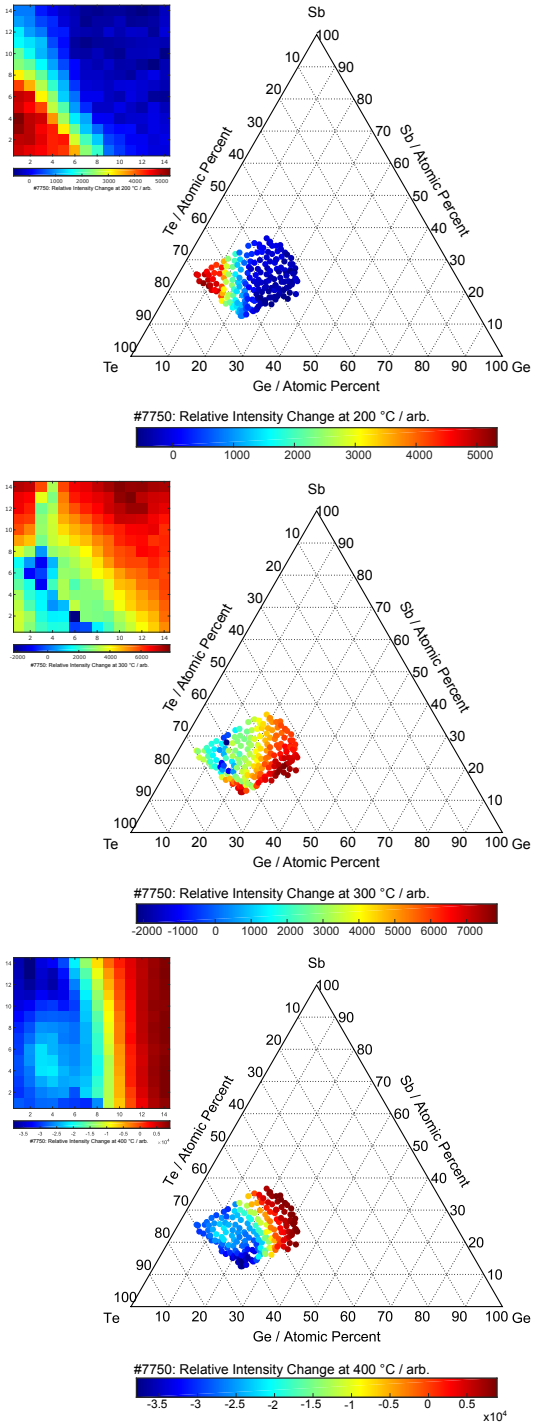

Figure 5.22: Intensity change (ΔI) of N-GST sample #7750 at 200 °C (top), 300 °C (middle) and 400 °C (bottom) relative to the intensity at the start of the HTOMPT experiment. Insets show the maps of ΔI across the sample.

which crystallised at 138 °C. The highest transition temperature was 254 °C for the composition $N_6Ge_{20}Sb_{14}Te_{60}$. The region with the lowest transition temperatures corresponds to the N-Sb_2Te_3 type materials. Compositions within the "boundary" region mentioned above, which contain 10 at. % to 15 at. % Ge, showed transition temperatures between 160 °C and 190 °C. In addition, several compositions across the sample had transition temperatures near 250 °C: Amongst them are materials near the centre of the sample similar to $N_9Ge_{17}Sb_{26}Te_{48}$ and others on the Te-poor side of the sample with compositions like $N_{11}Ge_{24}Sb_{28}Te_{37}$. All of these materials appear to have in common a N content > 8 at. %.

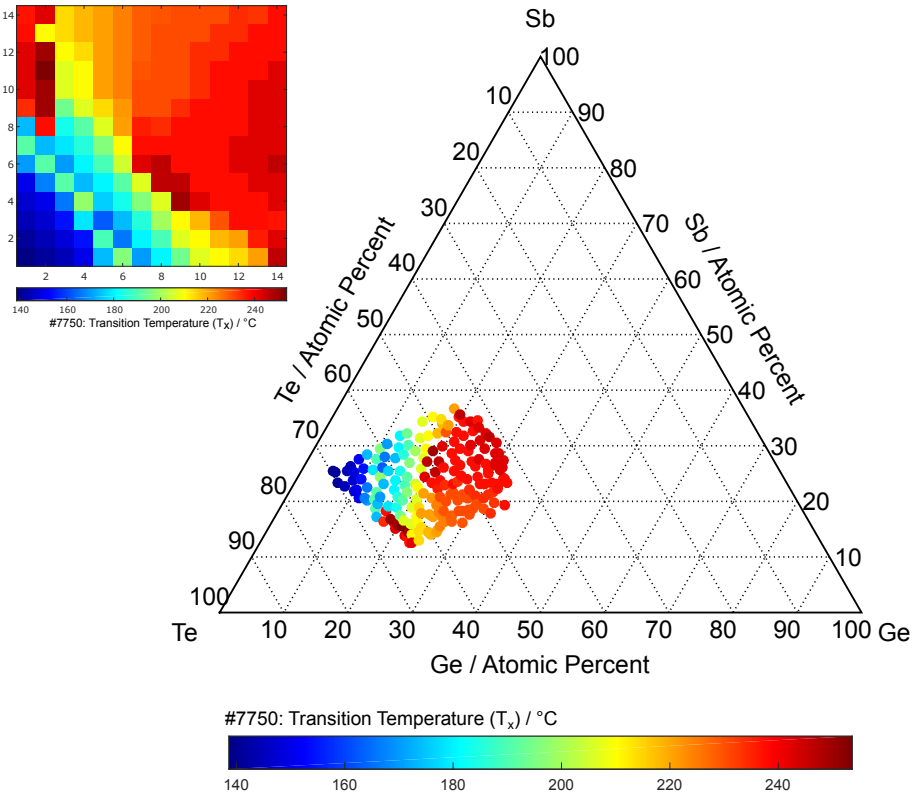

Figure 5.23: Temperature of the first phase transition (T_x) of the N-GST system as determined by the HTOMPT experiment on sample #7750. Inset shows the map of transition temperatures across the sample.

The trend of the transition temperature along pseudobinary lines is shown in Figure 5.24 as a function of Sb content. The overall trend along the Ge_2Te_3–Sb_2Te_3 and GeTe–Sb_2Te_3 lines is of decreasing T_x with increasing Sb content. The outlying points along the GeTe–Sb_2Te_3 pseudobinary that show an increase in T_x were found to belong to N-GST225 materials. For the GeTe–SbTe pseudobinary there is a steady increase in T_x with Sb content, however at

~30 at. % Sb it decreases sharply by about 25 °C.

Figure 5.24 also compares the transition temperature against the data collected for undoped GST (section 4.4.1). As expected, T_x is higher in the N-doped materials along all three pseudobinaries. The average difference in T_x between doped and undoped materials varied between pseudobinaries: Along Ge_2Te_3–Sb_2Te_3 the T_x of doped materials was 47 °C higher than undoped GST. This difference increased to 64 °C for materials on the GeTe–Sb_2Te_3 line and 97 °C for those on GeTe–SbTe. The increased T_x in doped materials is due to the high number of N atoms in sp^2 and sp^3 geometries, which have been shown to frustrate the crystallisation process by interrupting nucleation.[144] This would have the effect of requiring higher annealing temperatures to overcome the energy barrier for nucleation and achieve crystallisation.

The effect of N doping on the crystallisation temperature was analysed on the stoichiometric compositions GST225, GST124, GST325 and GST224. The results are shown in Figure 5.25 and compared with literature values if available. The transition temperature of N-GST225 increases with added N content, while the opposite occurs for N-GST124. These results are consistent with literature reports.[121,139,141,145,238] The decrease in T_x observed in the N-GST124 compositions is not well understood, but may be due to segregation of Sb_2Te_3 arising from the preferential binding of N to Ge. This would limit the formation of Ge–Te bonds, which tend to increase T_x within GST. This argument was used to explain a similar drop in T_x with increased doping which was observed by Jang *et al.* in the O-doped GST system.[256]

The crystallisation temperatures of both GST compositions with no intrinsic vacancies (GST325 and GST224) show little variation with N-doping and may be assumed to be equal within experimental error, as all the T_x values shown in Figure 5.25 can be found within 4 °C of each other. This observation, however, contradicts the observations by Cheng *et al.* for the N-GST325 system who reported a higher T_x with increasing N content.[236]

However, direct comparison of T_x obtained through HTOMPT with reported literature values is complicated by the fact that multiple techniques have been used to determine it. The two most common techniques are the resistivity method and differential scanning calorimetry. In addition, the reflectivity method using an IR camera during annealing, as used by Kölpin *et al.* appears to underestimate T_x consistently across all the compositions they studied.[121]

The most reliable values appear to be those determined by Raoux using two different tech-

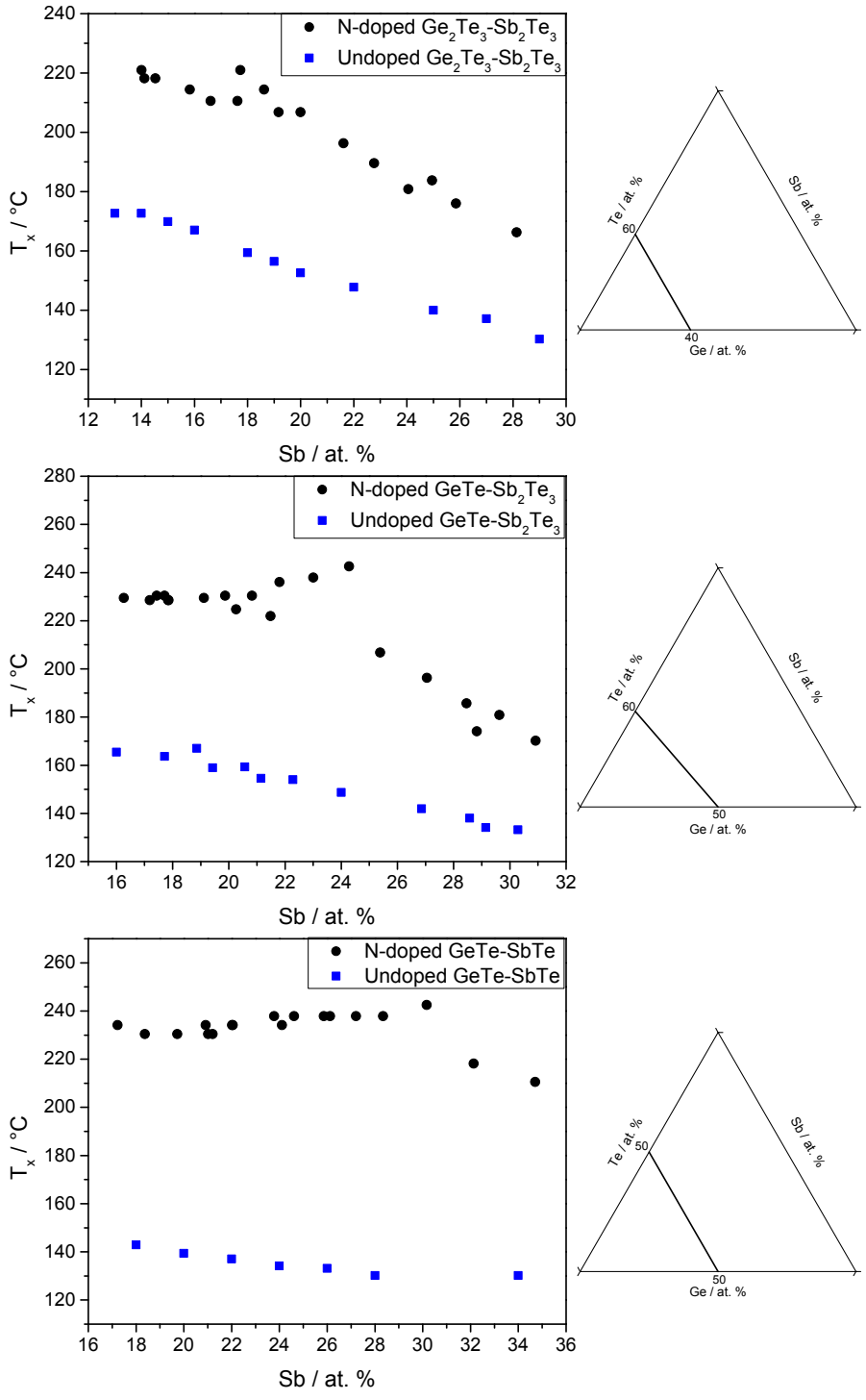

Figure 5.24: Transition temperature (T_x) as a function of Sb content for N-GST materials along the Ge_2Te_3–Sb_2Te_3, GeTe–Sb_2Te_3 and GeTe–SbTe pseudobinaries as obtained using the HTOMPT technique. Experimental results (black dots) are compared against T_x values of the corresponding undoped GST compositions (blue squares, data from section 4.4.1). Ternary diagrams indicate the position of each pseudobinary within the GST ternary space, omitting N content.

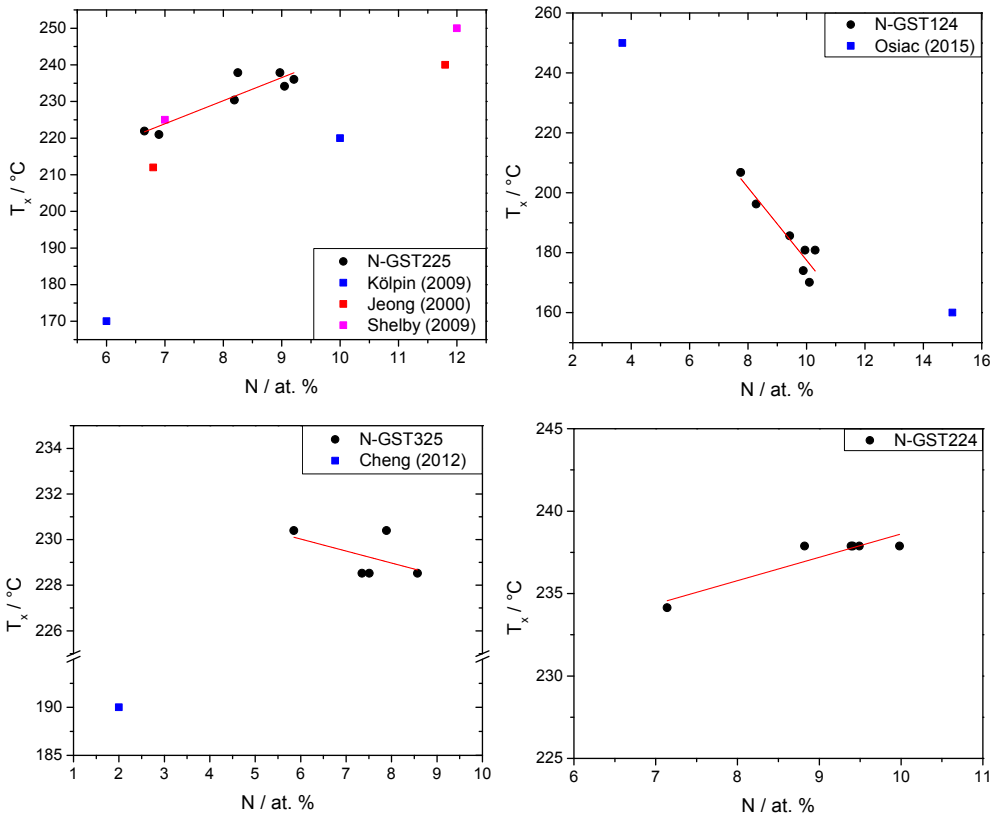

Figure 5.25: Transition temperature (T_x) of selected N-doped GST materials as a function of nitrogen content, as determined using the HTOMPT technique. The plots for N-GST225, N-GST124 and N-GST325 also include literature values (see Table 5.4). A linear regression fit was used for all data sets.

niques (resistivity and time-resolved XRD) for GST225 doped with 7 at. % N as they are consistent with each other.[145,242] Table 5.4 compares these literature values (including those used in Figure 5.25) against our experimental results. Overall, our experimental data for the N-GST225 system appears to be in best agreement with the results reported by Shelby, while the N-GST124 dataset follows the general trend seen in Osiac *et al.* There are not enough reports available for the N-GST325 and N-GST224 materials to evaluate the accuracy of our data.

Table 5.4: Crystallisation temperatures (T_x) for selected compositions in the N-GST system for materials within sample #7750. Literature references are also provided for comparison. For the N-GST124, N-GST325 and N-Sb_2Te_3 compositions the comparison is made against the closest reported values.

Composition	Experimental (T_x / °C)	Literature (T_x / °C)	Citation	N % in Citation
GST225, N = 6.7 at. %	222	170	Kölpin[121]	6.0 at. %
		212	Jeong[139]	6.8 at. %
GST225, N = 6.9 at. %	221	225	Shelby[145]	7.0 at. %
		227	Raoux[242]	7.0 at. %
GST225, N = 9.2 at. %	236	220	Kölpin[121]	10.0 at. %
		240	Jeong[139]	11.8 at. %
		250	Shelby[145]	12.0 at. %
GST124, N = 10.3 at. %	181	160	Osiac[238]	15.0 at. %
		250		3.7 at. %
GST325, N = 5.9 at. %	230	220	Cheng[236]	"2N" material
		190	Cheng[237]	2.0 at. %
$N_8Ge_5Sb_{23}Te_{64}$	138	175	Yin[251]	Sb_2Te_3 "N1"

5.4.2 Resistivity

The resistivity of samples #7754 (as-deposited N-GST) and #7760 (N-GST annealed at 300 °C) was measured as per the procedure outlined in section 3.3.1. Both samples were deposited

on silicon nitride substrates. The thickness of the film was found to be 149 ± 13 nm. Due to large variations in resistivity within the combinatorial libraries Figure 5.26 shows the $log(\rho)$ maps for both samples after being corrected as per equation 3.3.

The resistivity map of sample #7754 shows a region of high resistivity that has been purposely encircled. The sheet resistance of the compositions within was found to be higher than the measurement limit of the 4PP instrument ($8 \times 10^9\,\Omega$/square). This instrumental limit was used to calculate the resistivity of these compositions, and therefore must be considered as a *minimum* resistivity value for these materials in their as-deposited state. In addition, resistivity could not be measured at few points at the corner of both samples due to bad contact of the probe with the thin film.

The composition $N_8Ge_6Sb_{21}Te_{65}$ had the lowest resistivity at $9.7 \times 10^1\,\Omega$ cm, while the highest resistivity was for composition $N_8Ge_{17}Sb_{19}Te_{56}$ at $4.9 \times 10^4\,\Omega$ cm (excluding materials within the encircled region of Figure 5.26). For the materials annealed at 300 °C on sample #7760 the lowest resistivity was found at composition $N_8Ge_4Sb_{24}Te_{64}$ with a value of $8.0 \times 10^{-2}\,\Omega$ cm. The material with composition $N_7Ge_{13}Sb_{23}Te_{57}$ had the highest resistivity at $2.0 \times 10^1\,\Omega$ cm.

On both samples the region with lowest resistivity in the film corresponds with the Ge-poor, N-Sb_2Te_3-type materials described throughout section 5.3. The highest measured resistivity for both samples was found at compositions with GST proportions of approximately $Ge_1Sb_{2-n}Te_{4-n}$ ($n = 0, 1$). However, the compositions whose resistivity exceeded the instrumental limit would be expected to have the highest resistivity of all in the as-deposited library. These compositions are characterised by having approximately > 20 at. % Ge and < 20 at. % Sb and include the N-GST325 stoichiometry.

The resistivity trends along pseudobinary lines are shown in Figure 5.27 as function of Sb content for both as-deposited and annealed materials. The as-deposited resistivity plots along Ge_2Te_3–Sb_2Te_3 and GeTe–Sb_2Te_3 include some of the materials exceeding the 4PP instrument's measurement limit. The overall trend in resistivity of the as-deposited material tends to decrease with increasing Sb content in all pseudobinaries. This may be an indication of Ge exhaustion through nitridation and the formation of segregated Sb_2Te_3 phases.

For the as-deposited sample, the highest resistivity materials along the Ge_2Te_3–Sb_2Te_3 pseudobinary were found near the $N_8Ge_{17}Sb_{19}Te_{56}$ composition. These were also the most resistive points in the entire sample, excluding the instrument-limited measurements. The

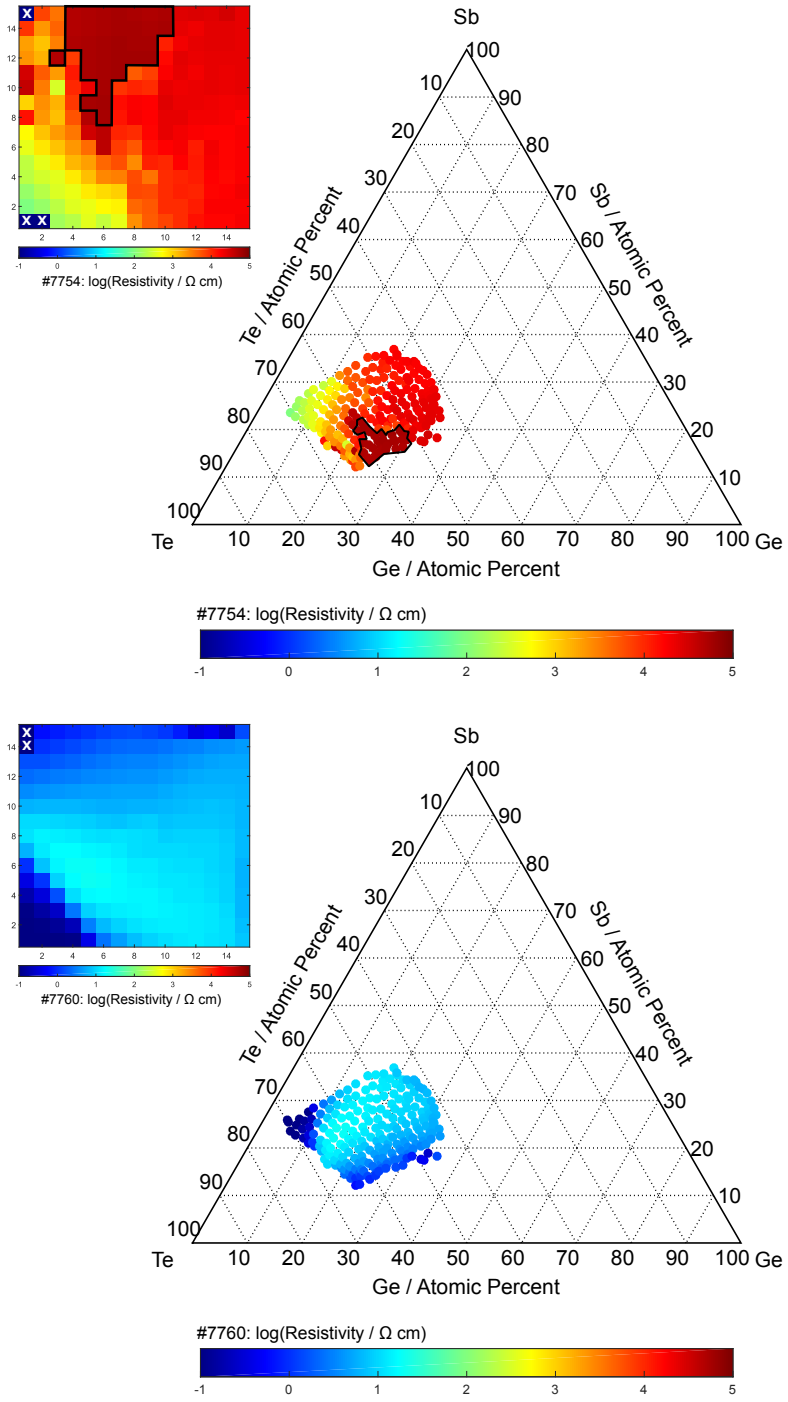

Figure 5.26: Resistivity maps, presented as $log(\rho)$, for as-deposited sample #7754 (top) and annealed sample #7760 (bottom) as determined using 4PP. The inset next to the ternary diagram shows the same information across the thin film: X-Y coordinates correspond to the position of each measurement point within the sample. Crossed out squares represent "dead points" where data could not be collected. The compositions enclosed within the black boundary in the as-deposited sample were more resistive than the instrumental limit of the experiment.

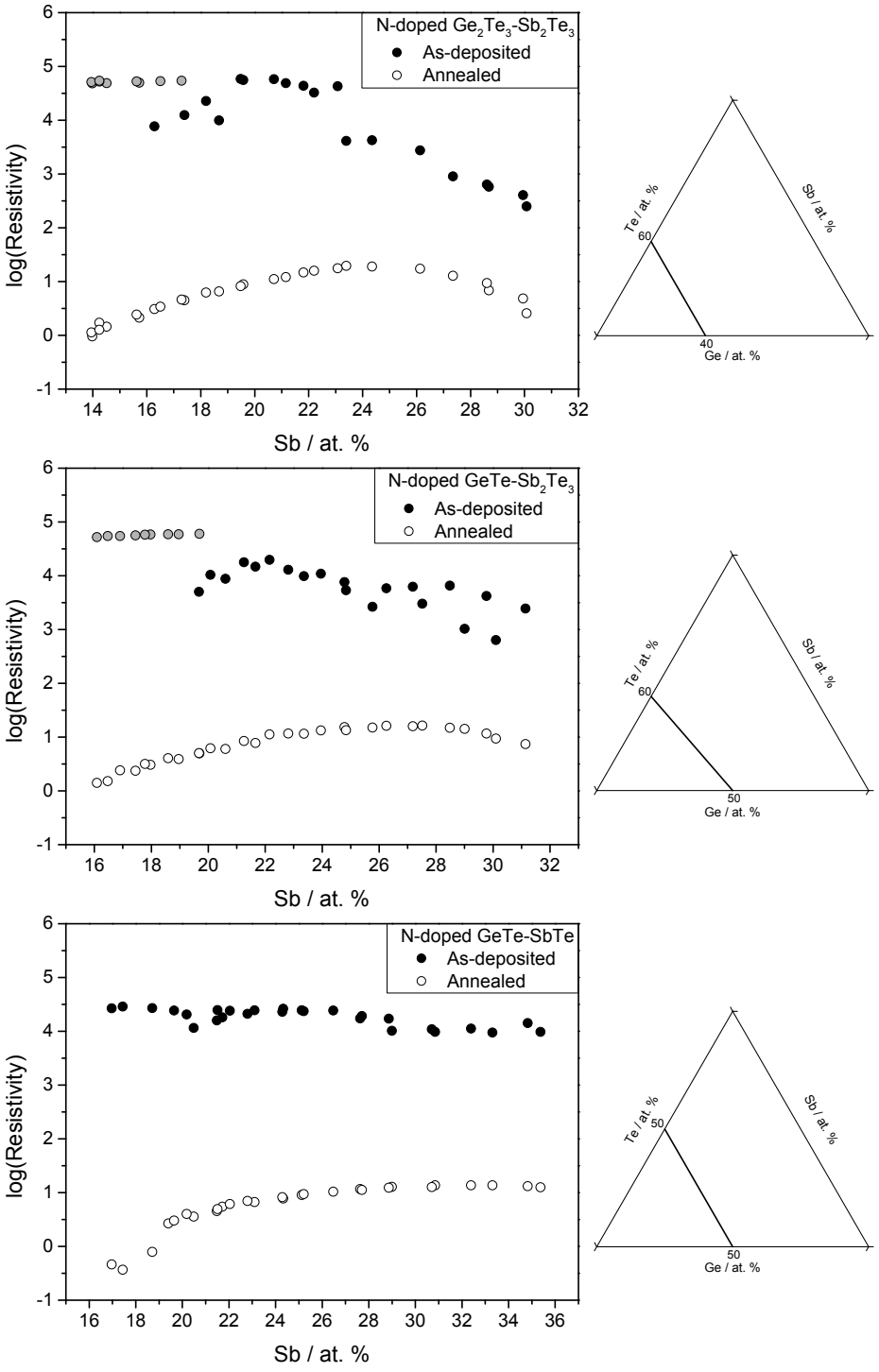

Figure 5.27: $log(\rho)$ as a function of Sb content for N-GST materials along the Ge_2Te_3–Sb_2Te_3, GeTe–Sb_2Te_3 and GeTe–SbTe pseudobinaries as determined by 4PP. Each plot compares the resistivity of the as-deposited (sample #7754, black dots) and annealed materials (sample #7760, 300 °C, white dots) along each line. The grey dots highlight the compositions whose resistivity exceeded the instrumental limit. Ternary diagrams indicate the position of each pseudobinary within the GST ternary space, omitting N content.

drop in resistivity near 23 at. % Sb fell within the boundary between N-GST and N-Sb_2Te_3-type materials. This boundary may also be observed at around 25 at. % Sb in the GeTe–Sb_2Te_3 tie line. The resistivity of the all compositions along the GeTe–SbTe line were found within the same order of magnitude, while the resistivity range of the materials along both Ge_2Te_3–Sb_2Te_3 and GeTe–Sb_2Te_3 lines spanned two orders of magnitude.

On the other hand, the resistivity of the materials annealed at 300 °C showed a maximum near 24 at. % Sb for the Ge_2Te_3–Sb_2Te_3 line and 27 at. % Sb for GeTe–Sb_2Te_3. These maxima were noted to be near the N-GST to N-Sb_2Te_3 boundary zone. At higher Sb content the resistivity along both lines began a downward trend. In addition, the resistivity trend along GeTe–SbTe appeared to approach asymptotically a value of $log(\rho) = 1.1$ with increasing Sb content.

Figure 5.28 compares the resistivity of N-doped and undoped GST materials along the GeTe–Sb_2Te_3 pseudobinary. The as-deposited materials in both systems had resistivity values within the same order of magnitude. This is in agreement with the early observations of Mott and Kolomiets related to the lack of sensitivity to doping of amorphous chalcogenide glasses (section 2.4.3).[74,78] The GST materials annealed at 200 °C were three to four orders of magnitude less resistive than the corresponding N-GST compositions annealed at 300 °C. This observation was also found to be in good agreement with previous reports.[116,141,146]

The effect of N doping on individual GST compositions is shown in Figure 5.29 for both as-deposited and annealed GST225, GST124 and GST224 materials. Each composition showed a different behaviour with increased dopant levels. The resistivity of both amorphous and annealed N-GST225 increased with increased N content, which is consistent with other reports in the literature.[141,145] On the other hand, the resistivity of N-GST124 was approximately constant regardless of doping in the annealed material, but decreased in the as-deposited state. On N-GST224 materials the resistivity appeared to be constant in both the as-deposited and annealed materials, although the doping range was the smallest of all three materials (1.2 at. % N). Table 5.5 lists the resistivity values of N-GST compositions for which there are comparable literature values. Only a few selected compositions are shown due to the scarcity of N-GST resistivity data in the literature. Our experimental values for as-deposited materials were within the same order of magnitude as those reported in the literature. However, for the annealed materials our resistivity values tend to be higher. This discrepancy may be a consequence of different experimental setups: Resistivity measurements in the literature are

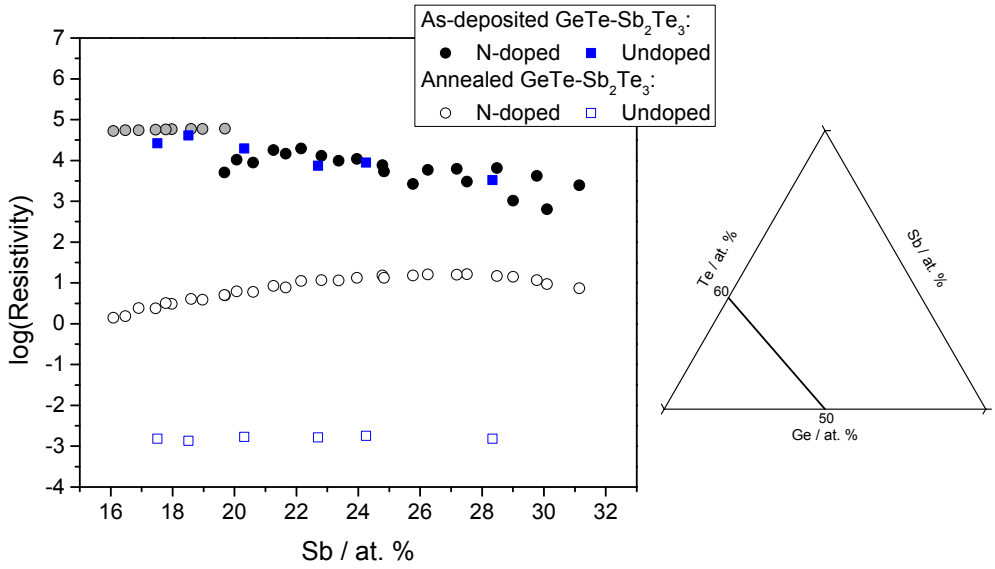

Figure 5.28: $log(\rho)$ as a function of Sb content for N-GST materials GeTe–Sb_2Te_3 pseudobinary as determined by 4PP. N-GST results (black dots) are compared against resistivity values of the corresponding undoped GST compositions (blue squares, data from section 4.4.2), for both annealed and as-deposited materials. The grey dots highlight the N-GST compositions whose resistivity exceeded the instrumental limit. Ternary diagram indicates the position of the pseudobinary within the GST ternary space, omitting N content.

done as R vs. T curves as the sample is slowly heated up, whereas in our setup the measurement takes place after the sample has been allowed to cool down to room temperature. It is a well-known phenomenon that the resistivity of semiconductors decreases with increasing temperature.[194] Therefore, it would follow that the resistivity measurement of a material at 300 °C should be lower than the measurement performed on the same material at room temperature.

5.4.2.1 Resistivity Contrast

The resistivity contrast $log(\Delta\rho)$ was calculated, using equation 3.5, for the GST materials for which data points were available in both the as-deposited and annealed samples. The result is shown in Figure 5.30. The largest measured $log(\Delta\rho)$ value was 5.0 for the $N_6Ge_{31}Sb_{18}Te_{44}$ material and surrounding compositions on the Ge-rich corner of the sample. Materials with resistivity higher than the instrumental limit are expected to have $log(\Delta\rho) > 4.5$. The composition $N_6Ge_{19}Sb_{16}Te_{60}$ had the lowest value for $log(\Delta\rho)$ at 1.7. While overall $log(\Delta\rho)$ becomes larger with increasing Ge content, there appears to be a "valley" of low contrast

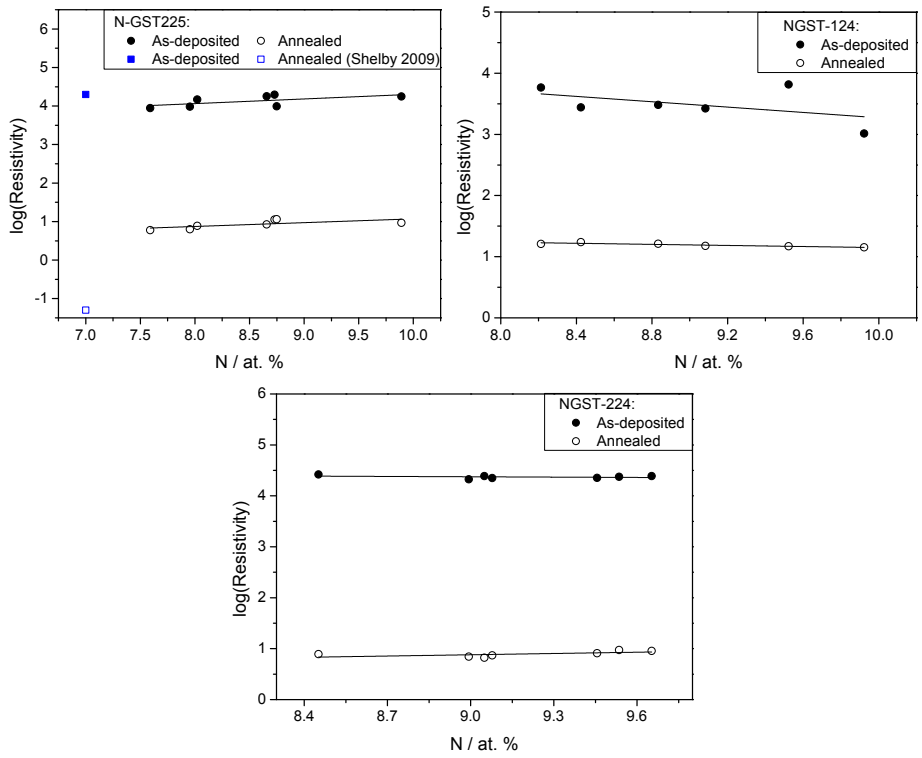

Figure 5.29: $log(\rho)$ of selected N-doped GST materials as a function of nitrogen content, as determined by 4PP. Each plot compares the resistivity of the as-deposited (black dots) and annealed materials (300 °C, white dots). The plot of N-GST225 also includes literature values (see Table 5.5). A linear regression fit was used for all data sets.

Table 5.5: Resistivity data of selected N-GST compositions in the as-deposited (A) and crystalline (C) phases of samples #7754 and #7760. Data presented in Ω cm. Closest available literature values provided for comparison.

Composition	**Experimental (Ω cm)**		**Literature (Ω cm)**		**Citation**
	A	**C**	**A**	**C**	
GST225, N = 7.6 at. %	8,800	6.0	20,000	0.1	Shelby,[145] N = 7.0 at. %
GST225, N = 9.8 at. %	18,000	9.2			
GST124, N = 9.9 at. %	1,000	14.0	3,000	0.6	Osiac,[238] N = 15 at. %
GST325, N = 7.9 at. %	N/A	4.0	100,000	4.0	Cheng,[236] "5N"
$Ge_4Sb_{24}Te_{64}$, *N = 8.0* at. %	96	0.1	100	0.1	Yin,[251] Sb_2Te_3 "N1"

between 10 – 15 at. % Ge. This valley may be a transition zone between stoichiometric N-GST materials and the N-Sb_2Te_3-type materials identified through XRD and Raman in section 5.3.

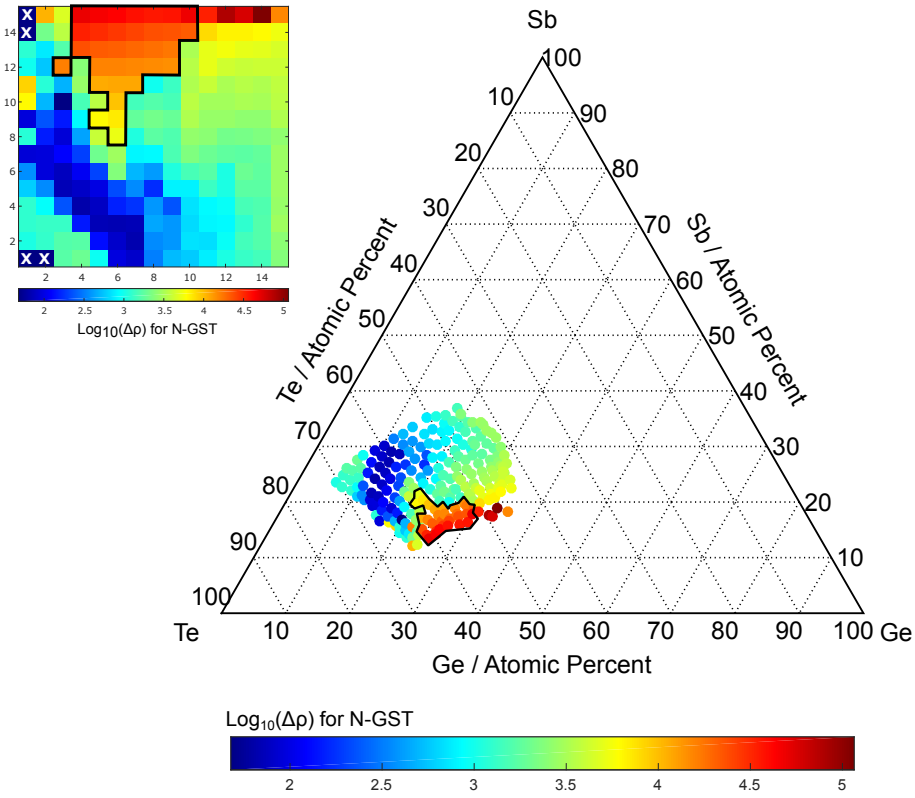

Figure 5.30: Map of the resistivity contrast, $log(\Delta\rho)$, between N-GST samples #7754 (as-deposited) and #7760 (annealed at 300 °C). Inset shows the distribution of this figure of merit across the thin film. The inset next to the ternary diagram shows the same information across the thin film: X-Y coordinates correspond to the position of each measurement point within the sample. Crossed out squares represent "dead points" where data could not be collected. The compositions enclosed within the black boundary correspond to compositions that were more resistive in the as-deposited phase than the instrumental limit of the experiment.

The trend in $log(\Delta\rho)$ for each pseudobinary has been calculated and is shown in Figure 5.31. Under the assumption that a value of $log(\Delta\rho) \geq 3$ would be a high enough resistivity contrast for PCRAM applications, then compositions with low Sb content before the N-GST to N-Sb_2Te_3 transition zone would be good candidates along the Ge_2Te_3–Sb_2Te_3 and GeTe–Sb_2Te_3 lines. These transitions would be located near 23 at. % Sb for the Ge_2Te_3–Sb_2Te_3 line and 25 at. % Sb for GeTe–Sb_2Te_3. The GeTe–SbTe line shows an interesting drop in $log(\Delta\rho)$ near 20 at. % Sb, although $log(\Delta\rho)$ only drops below 3 at 30 at. % Sb. Therefore, materials

rich in the Ge:Te component of the N-GST system along these three pseudobinaries have the highest resistivity contrast, which is also consistent with the results presented in section 4.4.2.1 for the undoped GST system.

Table 5.6: Resistivity contrast, $log(\Delta\rho)$, of selected N-GST compositions. Closest available literature values provided for comparison.

Composition	**Experimental** $log(\Delta\rho)$	**Literature** $log(\Delta\rho)$	**Citation**
GST225, N = 7.6 at. %	3.2	5.6	Shelby,[145] N = 7 at. %
GST225, N = 9.8 at. %	3.3		
GST124, N = 9.9 at. %	1.8	3.7	Osiac,[238] N = 15 at. %
GST325, N = 7.9 at. %	N/A	4.4	Cheng,[236] "5N"
$Ge_4Sb_{24}Te_{64}$, *N = 8.0* at. %	3.0	3.2	Yin,[251] Sb_2Te_3 "N1"

Figure 5.31 also shows the $log(\Delta\rho)$ values of the corresponding compositions along all three pseudobinaries from the undoped GST system. All the N-GST materials are shown to have lower $log(\Delta\rho)$ than undoped GST, which is a natural consequence of the higher resistivity of annealed N-GST. In general, the average difference in $log(\Delta\rho)$ between both systems was found to be ~3.3 orders of magnitude, with extreme values between 2 and 5. The resistivity contrast for both systems also tends to decrease with increasing Sb content.

The resistivity contrast as a function of N content for the doped compositions GST225, GST224 and GST124 is shown in Figure 5.32. Overall, N-GST224 materials have the highest contrast at ~3.5, followed by N-GST225 (~3.25) and finally N-GST124 (< 2.5). The value of $log(\Delta\rho)$ decreased with increasing N-doping for both N-GST124 and N-GST224. For N-GST225 $log(\Delta\rho)$ increased with increasing N content.

Finally, Table 5.6 lists the $log(\Delta\rho)$ values of the selected N-GST compositions given in Table 5.5. As discussed in the previous section, discrepancies between our values and those from the literature may be a result of the experimental method used to measure resistivity.

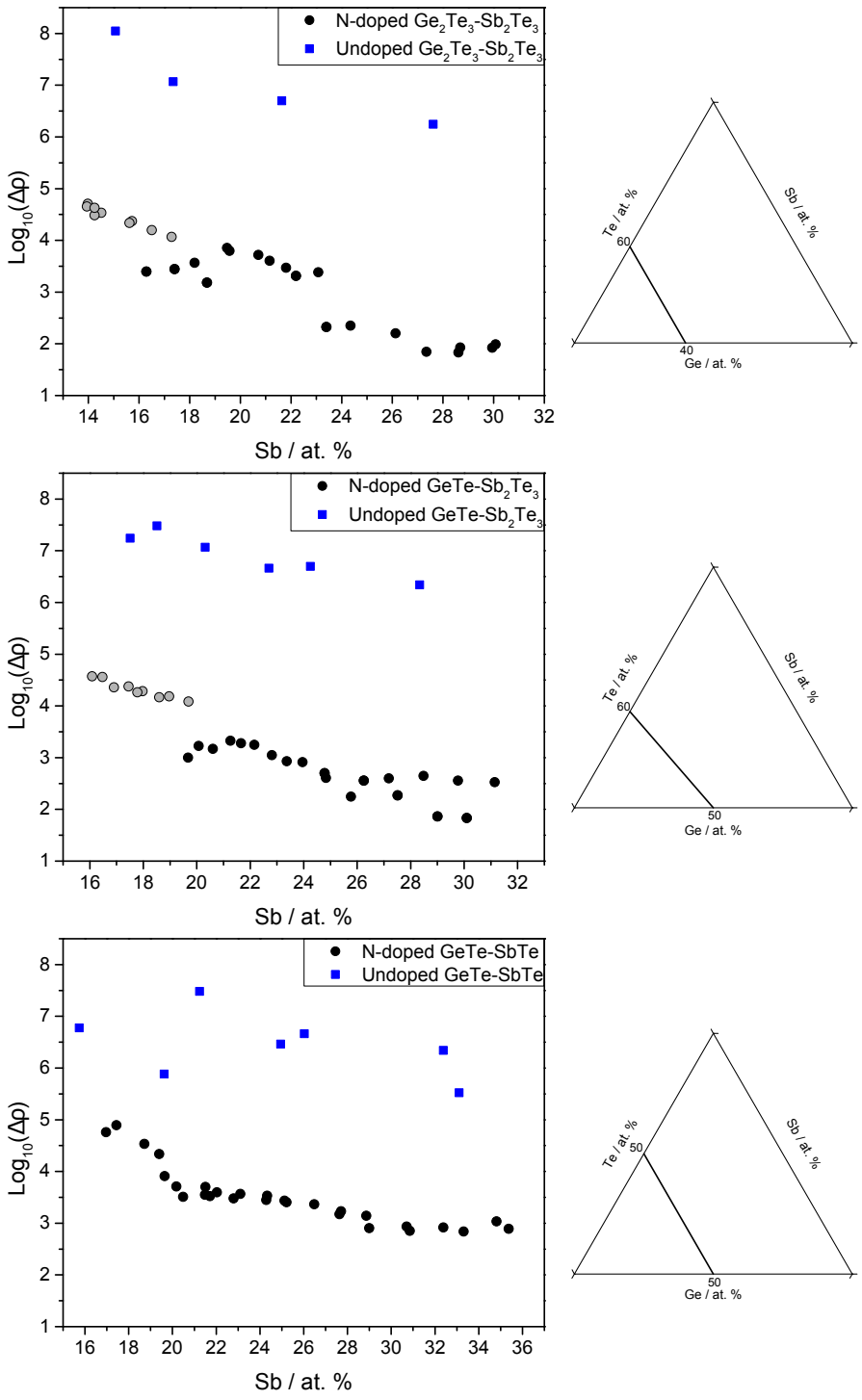

Figure 5.31: Trend of the resistivity contrast, $log(\Delta\rho)$, as a function of Sb content for N-GST materials along the Ge_2Te_3–Sb_2Te_3, GeTe–Sb_2Te_3 and GeTe–SbTe pseudobinaries. Each plot compares the resistivity of the N-doped material (black dots) and the undoped material (blue squares) along each line. The grey dots highlight the compositions whose resistivity exceeded the instrumental limit. Ternary diagrams indicate the position of each pseudobinary within the GST ternary space, omitting N content.

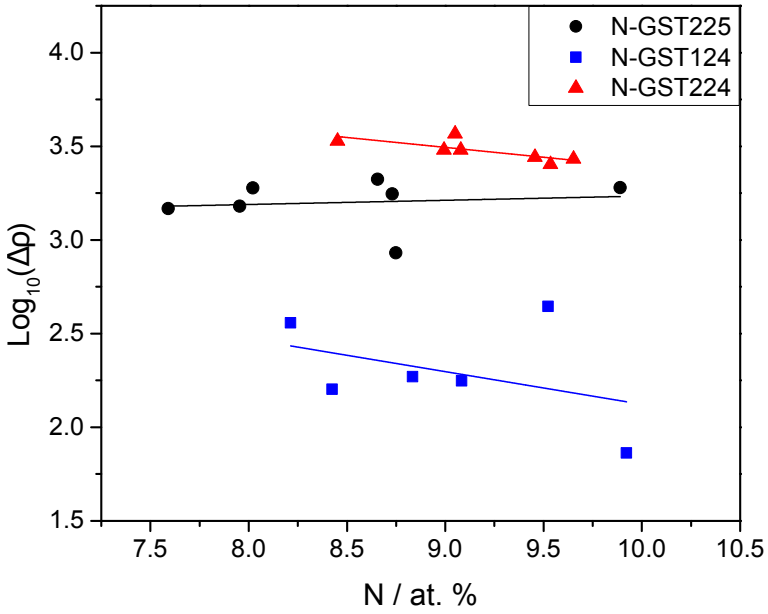

Figure 5.32: Trend of the resistivity contrast, $log(\Delta\rho)$, of selected N-doped GST materials as a function of nitrogen content, as determined by 4PP. A linear regression fit was used for all data sets.

5.4.3 Discussion

The functional characterisation of our combinatorial N-GST thin film libraries was done using the HTOMPT and 4PP techniques in order to determine their crystallisation temperature (T_x) and resistivity (ρ), respectively. The results thus obtained are consistent with those obtained from structural characterisation (section 5.3) regarding the existence of two distinct classes of materials: N-GST and N-Sb_2Te_3-type materials. No evidence of film aging due to oxygen incorporation into the films was seen during analysis.

The crystallisation temperature of N-GST has been shown as a ternary map in Figure 5.23. Overall, the T_x of the N-doped materials is higher than the corresponding undoped materials (Figure 5.24). This effect was attributed to the influence of sp^2 and sp^3 hybridised N atoms which inhibit the formation of nucleation sites in the amorphous matrix of the material, therefore requiring higher temperatures to achieve crystallisation. N-Sb_2Te_3 had crystallisation temperatures within a range of 140 – 170 °C, while N-GST materials had higher T_x within a range of ~170 – 250 °C.

The resistivity of N-GST materials was shown in Figure 5.26 for both the as-deposited and annealed (300 °C) materials. The as-deposited N-GST showed similar resistivity values as GST, while the doped materials annealed at 300 °C where more resistive than the undoped

materials (Figure 5.28). N-Sb_2Te_3-type materials were less resistive than N-GST materials in both the as-deposited and annealed states, while the resistivity contrast range was one order of magnitude narrower in N-Sb_2Te_3 materials (Table 5.7).

While the increase in crystallisation temperature of N-GST materials has already been accounted for through the number of N atoms in sp^2 and sp^3 geometries inhibiting crystallisation, the effect of doping in the electrical resistivity remains to be discussed. The conductivity in the amorphous, insulating phase of GST is typically modelled with the Poole-Frenkel effect, although other mechanisms have been proposed.[110] Electrons are trapped within localised states in the material and may move into the conduction band due to random thermal fluctuations. Once there they can briefly travel across the amorphous matrix before relaxing into a different localised state. Pirovano[83] proposed that the existence of lone pair chalcogenides (the dangling bonds discussed in section 2.4) particularly around Te atoms, results in localised states close to the edge of the valence band. Interaction of these lone pairs with the amorphous matrix sets up a range of states of varying charge configurations and bond strengths, which have the effect of giving the amorphous material low carrier mobility. When doping amorphous GST with a low concentration of N the number of lone pairs would be expected to remain unchanged as N tends not to form bonds with Te[143,250] and therefore the resistivity of both amorphous GST and N-GST should be approximately equal (Figure 5.28).

In the crystalline cubic phase the conductivity properties of the material change and are closer to those of a semiconductor[246] and are the result of competing effects. It has been shown that the crystallisation process itself increases the concentration of charge carriers in the material.[141] This is due to increased hole concentration arising from occupied N_{Te} sites.[143] Moreover, the defects in the crystal structure introduced by the occupation of interstitial sites

Table 5.7: Resistivity range, given as $log(\rho)$, of the N-GST and N-Sb_2Te_3 classes of materials found in samples #7754 (as-deposited) and #7760 (annealed). The range of resistivity contrast, $log(\Delta\rho)$, is also provided.

Material Class	**As-deposited** $log(\rho/\Omega\,\mathrm{cm})$	**Annealed** 300 °C $log(\rho/\Omega\,\mathrm{cm})$	**Resistivity Contrast** $log(\Delta\rho)$
N-GST	3 to 5	0 to 1	2 to 5
N-Sb_2Te_3	2 to 3	−1 to 0	2 to 4

in the cubic lattice should also increase the number of charge carriers.[246] Both effects would reduce the resistivity of the material. On the other hand, the addition of N also has the effect of suppressing the crystallisation of the material thus reducing the number of charge carriers. Grain size refinement (Figure 5.20) due to the formation of Ge_3N_4 envelopes increases the surface area of the grain boundaries with the concomitant increase in the number of charge traps. Moreover, Ge_3N_4 itself is insulating although current tunnelling might be possible if the nitride envelope is thin enough. The outcome of these competing effects in N-GST results in a material where the cubic phase is more conductive than the amorphous phase, but is less conductive than undoped GST, leading to the smaller resistivity contrast of N-GST relative to GST (Figure 5.31).

5.5 Summary

The objective of the work carried out for this chapter was the synthesis and characterisation of combinatorial thin film libraries of N-doped GST. Synthesis was achieved using the HT-PVD system. Structural characterisation was done on both as-deposited and 300 °C-annealed samples using Raman spectroscopy and X-Ray diffraction. Primary functional characterisation involved the determination of resistivity and crystallisation temperature using the 4PP and HTOMPT techniques.

The results of the tests described above identified two distinct classes of materials within our thin film libraries. The first class had properties related to N-doped GST materials, while the second class was related to N-doped Sb_2Te_3 materials. Table 5.8 summarises the characterisation findings from this chapter as they relate to these materials. The functional properties of the N-GST-type materials appear to be better suited to PCRAM applications than those of the N-Sb_2Te_3 materials, particularly for high-temperature applications such as automotive memory.

In addition to the above, the following significant results were obtained while working towards the primary objective of this chapter:

- The synthesis of the largest compositional space of N-doped GST materials reported to date, which included stoichiometric compositions such as GST225, GST325, GST124 and GST224 with a range dopant levels.

- The first systematic examination of the short range order of both as-deposited and annealed N-GST materials via Raman spectroscopy.
- The first systematic examination of the long range order of annealed N-GST materials via X-Ray diffraction.
- The first high-throughput determination of crystallisation temperature of N-GST materials using the novel HTOMPT technique.
- The first determination of the resistivity of N-GST materials using a high-throughput 4PP technique.
- The first systematic comparison of the functional properties between N-doped and undoped GST materials along the Ge_2Te_3–Sb_2Te_3, GeTe–Sb_2Te_3 and GeTe–SbTe pseudo-binary lines.

It is expected that future use of the HT techniques demonstrated in this chapter will contribute towards the advance of PCRAM research by facilitating the rapid synthesis and characterisation of doped chalcogenide glass systems and allowing their comparison with their corresponding undoped systems.

Table 5.8: Summary of the characterisation results of the N-GST and N-Sb_2Te_3 classes of materials obtained in this chapter.

Property	**N-GST materials**	**N-Sb_2Te_3 materials**
Crystal system (at 300 °C*)*	Cubic + hexagonal	Hexagonal + orthorhombic
T_x	170 to 250	140 to 170
$log(\rho)$, *as-deposited*	3 to 5	2 to 3
$log(\rho)$, *at* 300 °C	0 to 1	−1 to 0
$log(\Delta\rho)$	2 to 5	2 to 4

Chapter 6

PCRAM Microelectrode Parametric Testing System

6.1 Introduction to PCRAM Devices

The architecture of an array of memory cells of any type is comprised of an address decoder and a read-write unit. The address decoder connects to the memory cells via a circuit known as the *word line*, while the read-write unit is connected via a *bit line*. The word and bit lines form a matrix with intersections at individual memory cells, where each cell accounts for a single bit of memory. An access device, known as the cell selector, is either a transistor or diode that is used to address the cell only if both the bit line and word line connecting to it are active. In a PCRAM cell, the word line acts as an anode, supplying a voltage bias across the access device which acts as a gate for the cell, whereas the bit line acts as a 0 V rail.

Programming of a PCRAM cell operates by the scheme of pulses presented in Figure 2.3. The cell is designed so that the only current path through the device passes through a small aperture. By reducing the size of this aperture it is possible to reduce the volume of PCM used to fill it. This has the effect of reducing the power requirements of the cell. As a result, a smaller access device may be used to deliver power to switch the cell from the SET state to the RESET state and vice versa. Therefore, the overall volume of the cell is reduced resulting in increased memory density.

PCRAM cells may be classified into two types depending on how the heating current is delivered to the PCM: Contact-minimised and volume-minimised. A schematic for each type is shown in Figure 6.1. In contact-minimised cells a very narrow cylindrical electrode, typically made of TiN[44] and known as the bottom contact electrode (BCE), confines the current to an already crystallised thin film of PCM. In the RESET state the BCE forms an amorphous dome of material, resembling the cap of a mushroom, which plugs the current

path within the cell and accounts for its high resistance. In the SET state this dome of material is recrystallised and the path of the current is unhindered resulting in low resistance. Contact-minimised cells are also referred to as "mushroom cells" in the literature. These cells have the advantage of minimising heat loss therefore reducing thermal cross talk between neighbouring cells.

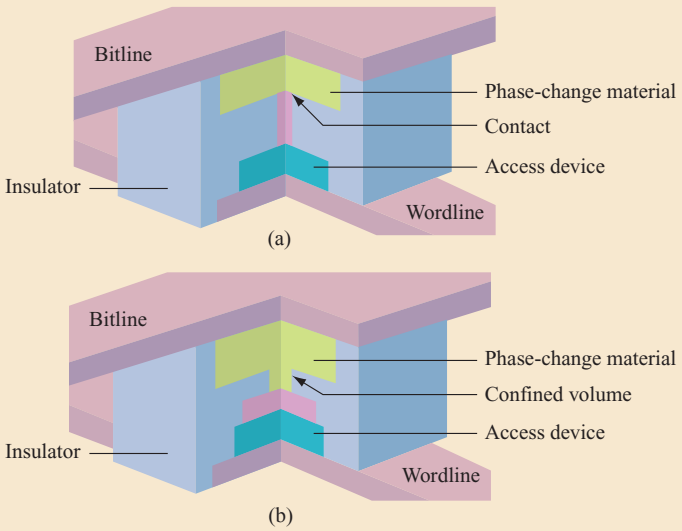

Figure 6.1: Schematic of the two main types of PCRAM cell. (a) Shows a mushroom-type, contact minimized cell. (b) Depicts a pore-type, volume-minimised cell. The insulator material is typically Si_3N_4 chosen for its high thermal insulation and dielectric properties. "Contact" refers to the BCE. The access device can be fabricated out of a variety of materials and diode configurations, as summarised in Table 3 of Wong *et al.*[44] Figure adapted from Raoux *et al.*[257]

In volume-minimised cells the size of the PCM volume is reduced as much as possible. A typical design of this kind of cell has a narrow pillar of PCM sandwiched between two electrodes. This pillar creates a high current density that heats the material and effects the phase change. Therefore, the BCE can be much larger in volume-minimised cells compared to the mushroom cells. An alternative design confines the volume of PCM to be switched within a pore sandwiched between a film of PCM and the BCE, as seen in Figure 6.1 (b). Regardless of the design, volume-minimised cells have the advantage superior scaling characteristics compared to mushroom cells, while offering the possibility of reduced RESET currents and increased endurance.[257]

Either type of cell requires the fabrication, through photolithography, of critical features smaller than size of the chosen process node. For contact-minimised cells this feature would be the diameter of the BCE, while in volume-minimised cells it would be the confined volume

of PCM. Nanofabrication of such small features in high yield and low variability introduces significant manufacturing challenges that remain under investigation.[258] To overcome them several cell designs have been put forward that iterate over the two basic types presented above. Discussion of these designs is beyond the scope of this thesis and has been done in detail elsewhere.[44]

6.2 PCRAM Tests Using c-AFM

The mode of operation of conventional AFM modes was described in section 3.2.3. Under optimal conditions AFM can resolve surface structures with resolution as low as 1 nm, orders of magnitude greater than the resolving power achieved in optical microscopes. By its nature the technique is non-destructive and surface sensitive. It also provides localised information as opposed to averaging over an area, as in the case of XRD or XPS. The technique has been developed beyond physical surface analysis to electrical characterisation, in a technique called conductive AFM (c-AFM). By using a conductive cantilever connected to a voltage source, the resulting current can be recorded as the sample is being scanned in contact mode, thus generating a conductivity map of the surface. Some AFM instruments are also capable of delivering voltage pulses that can be used to emulate the SET and RESET pulses necessary to switch PCRAM devices.

Conductive AFM has been used to perform parametric tests on specially prepared PCRAM cells. The advantages of this method arise from the small contact area of the AFM tip, which can be made small enough to mimic the device dimensions of PCRAM cells. By doing this, it would be possible to avoid interfacial issues between the tip and crystallites or grain boundaries on the material, thus ensuring that the contact area remained constant throughout the tests. Finally, modern AFM instruments allow the user to program automatic measurement routines which are enabled by a sample stage controlled by stepper motors, thus allowing for the possibility of parametric tests in HT.

The first use of c-AFM to electrically switch an amorphous layer of GST was reported by Kado and Tohda in 1995.[259] They deposited a 200 nm layer of Pt on a Si substrate to function as a BCE. Then, a 20 nm continuous film of GST124 was deposited on top of the Pt. An AFM pyramidal Si_3N_4 tip was custom-coated with a 100 nm layer of Au in order to enhance its conductivity. They we able to crystallise areas of the film leaving mark sizes ranging from

10 nm to 70 nm diameter using 5 ms pulses of 3 V amplitude, although they did not report attempts to reamorphitise the material.

Gidon *et al.* deposited 10 nm-thick GST255 amorphous, continuous films on a 10 nm-thick amorphous carbon layer as BCE. Additionally, a 2 nm-thick amorphous carbon capping layer was deposited on the GST film. A pyramidal AFM tip made of n-doped Si and custom coated with a 25 nm W_2C conductive layer was used for the experiments. Using this setup they were able to crystallise the PCM layer using 3 µs pulse of 6.5 V amplitude, leaving a mark size of 15 nm. However, they failed to switch back to the amorphous state with pulses as high as 9 V. As a result, it was suggested this technique would be useful for write-once electrical probe storage.

Lee *et al.* used nanoimprint lithography to create arrays of GST225[260] and AIST pillars.[261] For the AIST arrays the pillars had a 200 nm diameter and 15 nm thickness; the BCE was a 100 nm Pt layer and a 10 nm-thick TiN top electrode was also used. The GST pillars were 100 nm thick and 130 nm to 400 nm wide, while the BCE was made of a 100 nm Mo layer with a top electrode of 10 nm-thick Cr. A Pt-coated c-AFM tip was used to perform parametric tests on both types of pillars. On the GST system, RESET pulses of 5 ns and 2 V were achieved, while SET pulses were 100 ns long and 1.3 V in amplitude.

Yang *et al.* prepared 50 nm-thick GST225 films on a 20 nm Au BCE.[262] No capping layer was used while a c-AFM tip coated in Pt/Ir alloy was used for the measurements. They determined a V_{th} of 1.51 V for the material and concluded that threshold switching was a result of the formation of conducting filaments along the material, which is consistent with the original observations of Sie in As:Te:Ge.[25,27]

Similar filament formation was observed by Pandian *et al.*[263] on Sb-rich, amorphous GST225 films of either 20 or 40 nm thickness deposited on a 100 nm-thick Mo BCE. However, they proposed that the conducting filaments would be primarily composed of the excess Sb precipitated at the GST grain boundaries. V_{th} for these Sb-rich GST materials was reported to be higher than 4 V. They used a Si c-AFM tip coated in Pt/Ir alloy for their measurements.

The review of the literature just presented has demonstrated the feasibility of using the tip of an AFM instrument as a microelectrode to perform PCRAM parametric tests on a variety of test structures. However, the use of c-AFM for this purpose is typically limited by the range of both current and voltage it can sense and output (normally ±10 nA and ±10 V). Therefore,

an external signal generator must be used if greater currents and voltages are desired. The discussion in the following sections will describe the testing system developed with the goal to overcome this limitation, which integrates a Keysight 5600LS AFM with a Keysight B1500A semiconductor device analyser described in sections 3.2.3 and 3.3.3 respectively.

6.3 The Integrated Microelectrode Testing System

6.3.1 Purpose and Components

The Integrated Microelectrode Testing System (IMTS) was developed as a parametric testing platform to analyse the combinatorial thin film libraries produced by HT-PVD. The system was designed to carry out experiments to determine the power of SET and RESET pulses in addition of threshold field strength (derived from V_{th}) of PCRAM test structures. Moreover, the system would ideally be able to perform other DC tests such as parametric tests on Resistive RAM devices. This required passing high-frequency voltage pulses and running I-V sweeps in DC mode. The summarised requirements of the instrument for testing GST-derived phase-change memory are as follows:

- Record the I-V response curves of a test device, accurately and reproducibly, at ranges that may exceed ±10 V.
- Deliver high-frequency (nanosecond) voltage pulses of consistent amplitude and duration.
- Position the microelectrode quickly and accurately on the surface of the device under test (DUT).
- Have the capability to setup and run automated high-throughput measurements.

The development and evaluation of such a system is described presently. The system integrates a Keysight 5600LS AFM as a microelectrode and a Keysight B1500A Semiconductor Analyser as a signal source and measurement device. The aim was to connect these two instruments together as per the conceptual diagram shown in Figure 6.2.

The B1500A uses two source/monitor units (SMUs) as signal relays, as described in section 3.3.3. These are units housing a voltage source, current source, voltmeter and ammeter such that any relation of current and voltage can be measured (see circuit diagram in Figure

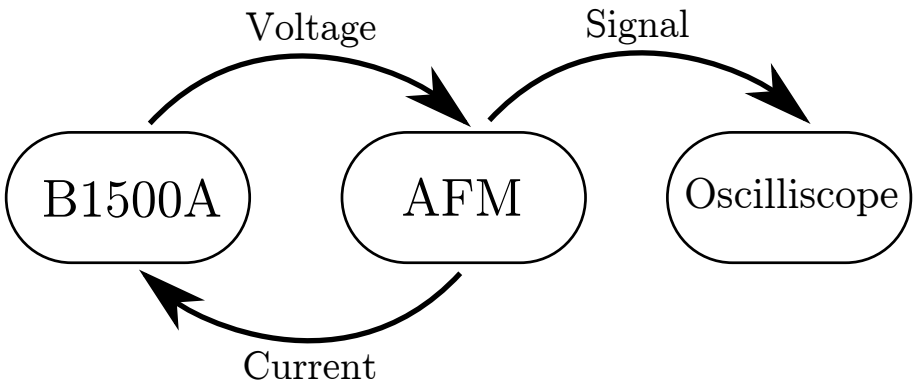

Figure 6.2: Conceptual diagram of the IMTS: The B1500A feeds a voltage to the AFM, which is passed across the tip to the DUT, and reads the current in the circuit. A GHz oscilloscope is used to monitor high-frequency signals. Figure prepared in collaboration with Ron Leizrowice.

3.14). They use triaxial cables as interconnects which are constructed as shown in Figure 6.3. The cable incorporates two layers of shielding that are held at a ground potential in order to insulate against electromagnetic interference and reduce leakage current. This is advantageous as nanosecond pulses behave like radio frequency signals and a long cable may act as an antenna, modulating the pulse and thus distorting the original waveform. By fixing the cable shielding at ground potential any induced signal would be dissipated to earth.

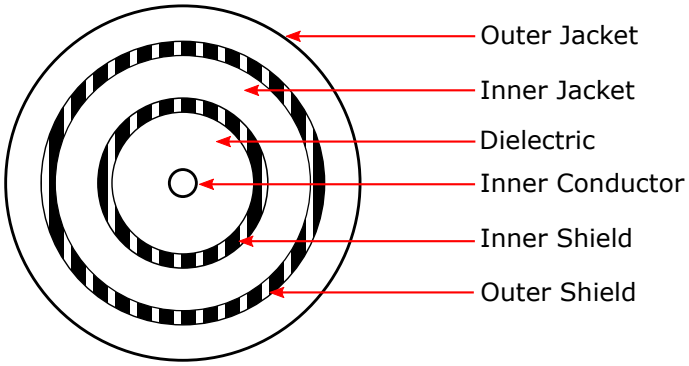

Figure 6.3: Cross section diagram of a triaxial cable. The "inner conductor" is connected to the output of the SMU and carries the signal. The "outer shield" is held at ground potential along with the "inner shield".

The signal connection between the B1500A and the AFM is achieved through a custom-made cable, pictured in Figure 6.4. One end of this cable has a female triaxial connector where the SMU signal can be connected into. The other end of the cable has two Micro DB9 connectors that plug into the AFM electronics (Figure 6.4a) and the AFM scanning head (Figure 6.4b)

respectively. The signal from the B1500A travels through the inner conductor of the triaxial cable, which is then linked to one of the pins within the Micro DB9 portion of the cable that connects to the AFM scanning head. The signal then travels through the scanning head and into the AFM tip, which then makes contact with the sample. A disadvantage of this setup is that the double shielding of the triaxial cable is lost in the conversion to the Micro DB9 connector, which only has a single layer of shielding. The effect of this loss was noticeable during the impedance matching between instruments and will be discussed in section 6.3.3.

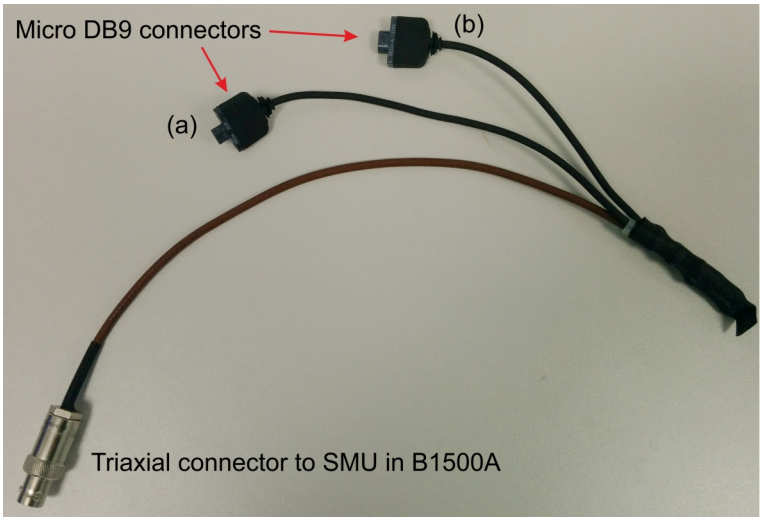

Figure 6.4: Photograph of the adaptor cable that transmits the signal from the B1500A instrument to the AFM. The cable from the SMU connects into the female triaxial connector. The Micro DB9 connector (a) plugs into the AFM electronics. Connector (b) plugs into the AFM scanning head and delivers the signal from the SMU to the AFM tip.

6.3.2 AFM Conductive Tip Selection

For conventional AFM surface scanning modes, the tip material must be hard with a low elastic modulus so as not to deform when interacting with a surface. As a result Si, Si_3N_4 or borosilicate tips are commonly used. However, these are wide band gap insulators and are unsuitable for electrical measurements. Typical commercially available c-AFM tips are made of n-doped Si coated with 10 nm-thick Pt/Ir alloy to enhance conductivity. These tips are designed for the low currents measured in c-AFM (~10 nA) which are inadequate for PCRAM parametric measurements. In order to carry out memory testing the AFM tip must have the following properties:

- Be conductive with negligible resistance that remains unchanged over time or with repeated usage.
- Provides a stable I-V response for up to 100 µA current compliance.
- Must be able to withstand repeated measurements without degrading.

Bespoke AFM tips that meet these requirements have been described in the review offered in section 6.2. In addition, Bhaskaran and coworkers have developed a SiO_2-encapsulated, n-doped Si/Pt tip that has been reported to operate under 200 µA currents and have good resistance to wear.[264,265] These tips just recently became available from a commercial supplier (NanoWorld AG, under their Nanosensors brand) so their compatibility with our setup was not tested. Alternatively, conducting diamond tips have proven useful in similar electrical AFM measurements.[266] Instead, three conductive tips were chosen and tested in the Integrated Microelectrode Testing System. SEM images of each tip are provided in Figure 6.5.

1. An all-metallic, Pt tip of 20 nm radius supplied by Rocky Mountain Nanotechnology in the United States. Model 12Pt400A, 0.3 N m^{-1}, 4.5 kHz.
2. An n-doped Si tip of 20 nm radius coated with a 10 nm-thick Pt/Ir alloy supplied by Keysight Technologies. Model N9540-60002, 0.35 N m^{-1}, 32 kHz.
3. An n-doped Si "plateau" blunt tip with a tip radius of 1.5 µm. These tips were coated with a custom 100 nm Pt/Ir alloy to enhance conductivity and were supplied by AppNano. Model ACT-PTU-PtIr, 45 N m^{-1}, 300 kHz.

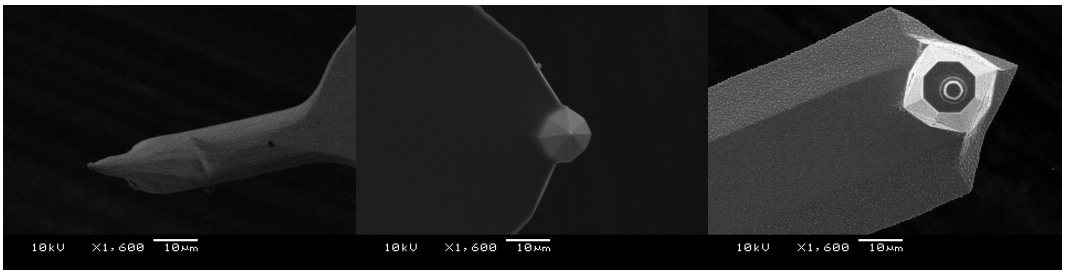

Figure 6.5: SEM scans taken at 10 kV and 1600x magnification of the three c-AFM tips tested in the Integrated Microelectrode Testing System. Left frame shows the the Rocky Mountain all-metallic Pt tip. Centre frame shows the Keysight n-doped Si tip with 10 nm Pt/Ir conductive coating. Finally, the right frame shows the AppNano "plateau" n-doped Si tip with custom 100 nm Pt/Ir coating. Scale bar for all three frames =10 µm.

In order to evaluate their performance an I-V sweep between 0 V to 1 V 0 to 1 V (and back) was run on a clean platinised silicon substrate (SSTOP which has a 100 nm Pt layer that was used as BCE in this setup) at increasing current compliance. The results of these I-V scans are shown in Figure 6.6. The Keysight tip performed well under currents up to 1 mA compliance but failed at 2 mA and higher currents. This was likely due to the small contact area of the tip leading to overheating under high current, resulting in the loss of the tip's conductive coating.

The all-metallic Pt Rocky Mountain tips showed signs of instability in the forward scan at 60 mA compliance, which then completely failed in the return scan. This tip also failed to operate at currents higher than 60 mA. It is possible that the Joule heating generated by these higher currents passing through the tip (which is essentially a very thin Pt wire) was high enough to increase the resistance of the circuit leading to a breakdown of the field at the tip.

Finally, the AppNano tip performed with complete linearity for forward and return sweeps up to 100 mA compliance. The SEM image in Figure 6.5 (right frame) shows the contact area of the tip is a plateau of ~3 µm diameter. It was expected that the increased contact area and thicker conductive coating (100 nm) would diminish tip heating which may increase the durability of the tip. For this reason the AppNano tips were chosen as the microelectrode for further tests in the IMTS. It was determined that the force applied by the tip on the sample, using a 0.3 V setpoint for the AFM piezoelectric scanner, was 6.8 nN.

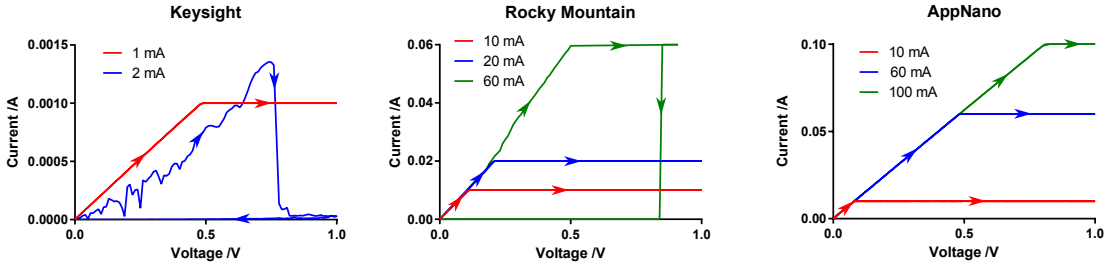

Figure 6.6: I-V sweeps of the three tested tips at increasing current compliance settings on a clean SSTOP substrate. The sweeps ran from 0 – 1 V in the forward scan immediately followed by a 1 – 0 V return scan. Where not indicated by arrows, the return sweeps followed the same path as the forward sweeps.

6.3.3 Voltage Pulse Calibration

Passing a DC signal through a triaxial cable is trivial as the duty cycle is 0 and therefore not subject to jitter. However, nanosecond pulses may act as radio frequency and therefore would be sensitive to interference. For example, consider one half cycle of a sinusoidal curve with a base-width (τ) of 50 ns; the effective frequency (f) would be:

$$\frac{1}{2\tau} = f = 10\,\text{MHz} \tag{6.1}$$

Similarly, an equivalent square wave of 50 ns width (i.e. a pulse) would behave as a 10 MHz signal through the triaxial cable and would become sensitive to impedance mismatch between components of the circuit (e.g. the AFM and the B1500A in this case). As well as the characteristic resistance for the cable there is also parasitic capacitance and inductance which gives rise to the following three impedance (Z) relations:

Resistive impedance: $Z_R = R$

Inductive impedance: $Z_L = j2\pi fL$

Capacitive impedance: $Z_C = \frac{1}{j2\pi fC}$

where L is inductance, C is capacitance and j is a phase correction factor. Collectively these relations result in variable impedance for the circuit, which is dependent on the frequency of the transmitted pulse. This makes it difficult to match the impedance for the cables and source (Z_S) and the tested material (Z_M). A mismatch can result in reflectance of the signal ($\bar{R}$), reducing the transmittance ($\bar{T}$) by an equivalent amount as described by the following relations:[267]

$$\bar{T} = \frac{2Z_M}{Z_M + Z_S} \tag{6.2}$$

$$\bar{R} = \frac{Z_M - Z_S}{Z_M + Z_S} \tag{6.3}$$

$\bar{T}$ can be maximised by holding Z_M at the same value as Z_S (such that $\bar{R} = 0$) but the variable resistance (R) of the sample makes this impossible. Since the output impedance of the B1500A was fixed at 50 Ω (by the resistor built in between the inner conductor and the jacket of the triaxial cables) a 50 Ω resistor in parallel with the signal line to fix Z_R between both instruments produced the best results. Correction of Z_L and Z_C was not attempted, but they may be addressed with more substantial modifications to the circuit.

Another issue identified with the circuit setup originated at the connection from the triaxial cable to the AFM circuitry (through the adapter cable shown in Figure 6.4) which terminated the shielding and left the potential to float between the two cables, thus creating a ground loop. The AFM circuitry also used a different earth (which originated in the steel sample stage) than the B1500A. Finally, an oscilloscope (Tektronix TDS 684B) was connected to the mains earth. The mismatch of all these ground lines introduced significant interference to the signal. In order to address this issue all three earths were linked and a conductive bridge between the jackets of the cables before and after the DUT, was introduced. The final circuit design is shown in Figure 6.7.

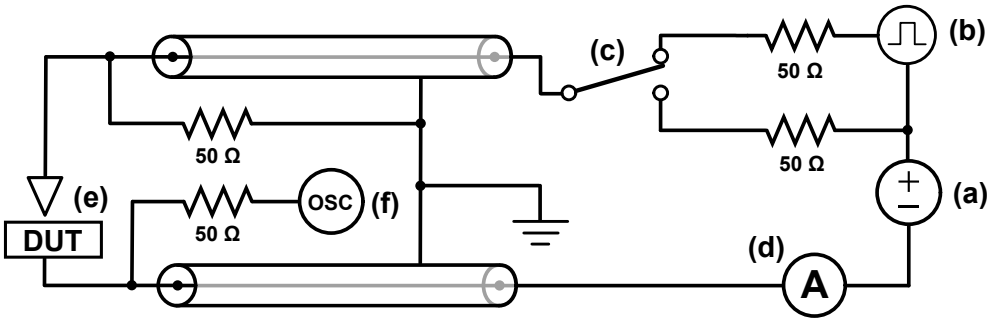

Figure 6.7: Circuit diagram of the Integrated Microelectrode Testing System. (a) Voltage source (an SMU) for I-V tests; (b) single pulse generator unit (SPGU) for voltage pulses; (c) relay switch to switch automatically between I-V sweep measurements and voltage pulses; (d) ammeter to measure current during I-V sweeps, located within the SMU; (e) the device under test (e.g. a combinatorial GST sample) in contact with the AFM tip (triangle); (f) external oscilloscope. Components (a), (b), (c) and (d) are part of the B1500A Semiconductor Analyser. Component (e) is part of the 5600LS AFM. Figure prepared in collaboration with Ron Leizrowice.

In combination these changes produced the best possible signal output. Using an SSTOP wafer as a high conductivity surface to test the setup, trial pulses were compared before and after modifications, as shown in Figure 6.8.

This setup still did not produce a perfectly faithful representation of the programmed pulses but within the limitations of the system it was considered adequate. A variety of different pulse widths were trialled and below ~75 ns the impact of the impedance as a function of frequency heavily distorted the measured waveforms, as shown in Figure 6.9. It may be observed that as the frequency of the pulse increases the influence of Z_L and Z_C become more prominent and the reflectance of the signal increases. As a result the distortion of the waveform becomes more pronounced. Within the limitations of the system this distortion of

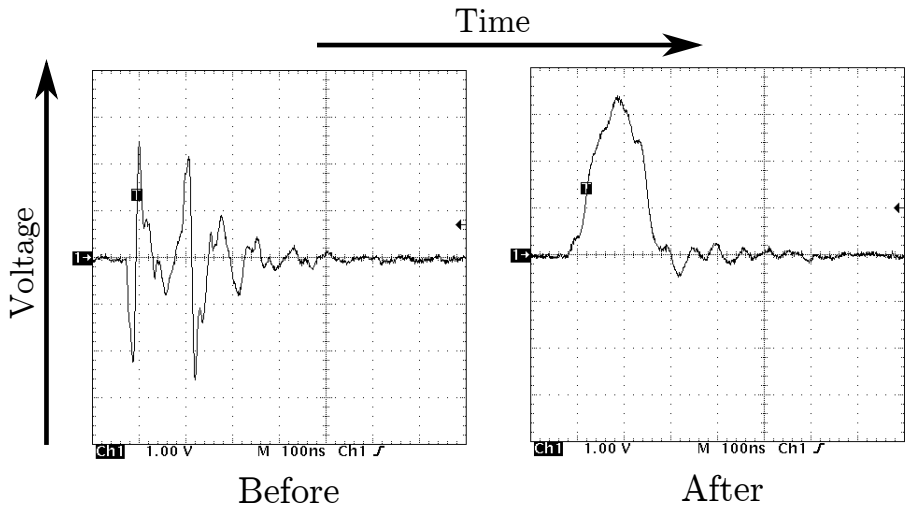

Figure 6.8: Oscilloscope trace of a programmed 200 ns wide, 3 V pulse before impedance matching (left frame) and after (right frame). On each frame the horizontal scale is 100 ns in the x-axis and 1 V in the y-axis. Figure prepared in collaboration with Ron Leizrowice.

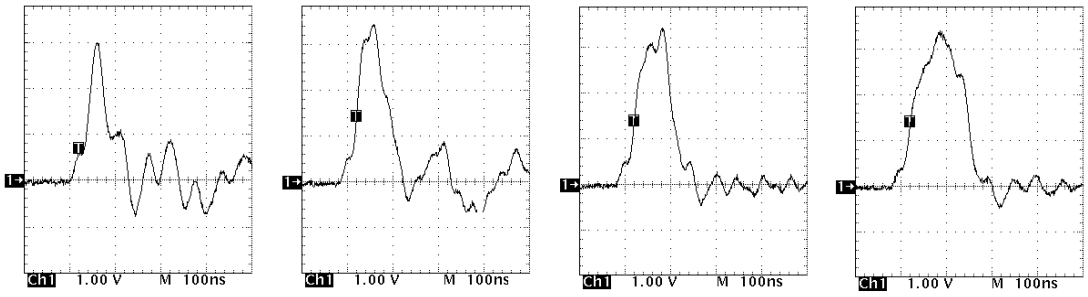

Figure 6.9: Oscilloscope traces of 3 V amplitude pulses of increasing width, respectively: 50 ns, 150 ns, 200 ns and 250 ns. On each frame the horizontal scale is 100 ns in the x-axis and 1 V in the y-axis. The "ringing" effect observed at the peak of the pulse is an artifact of the mismatch between the high impedance probe of the oscilloscope (10 MΩ) and the lower impedance of the Integrated Microelectrode Testing System (50 Ω). The impedance mismatch due to Z_L and Z_C is more clearly observed as the ringing immediately after the pulse.

the waveform was considered an acceptable compromise since it would be sufficient to carry out voltage pulse experiments as there is evidence in the literature of amorphization with pulses as long as 128 ns on GeTe devices.[268]

6.3.4 I-V Sweep Testing

In section 6.3.2 it was demonstrated that a bias could be applied to a conductive wafer in order produce a stable current and that AppNano tip yielded the best ohmic response. It was

subsequently necessary to verify that this could be used to carry out threshold switching measurements of PCRAM test structures. A 50 nm-thick reference sample of amorphous GST225 was deposited at room temperature via sputtering on an SSTOP substrate under the following conditions: Base pressure 10^{-8} Torr; Ar process gas (20 – 70 sccm flow rate); DC bias 233 V; forward power 35 W. The GST225 target was supplied by Testbourne Ltd. No capping layer was deposited on top of the GST225 film. The resulting structure is shown in Figure 6.10.

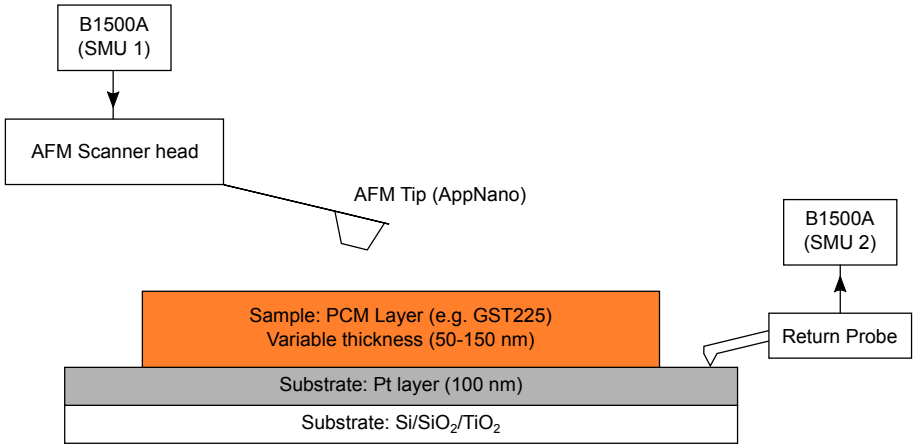

Figure 6.10: Typical PCRAM test structure deposited on an SSTOP substrate. The PCM layer may either be a single composition thin film (such as GST225) or a combinatorial thin film library. Diagram and structures are not to scale.

An I-V sweep from 0 – 2 V and back was performed on the sample using a 25 mA current compliance. The result is shown in Figure 6.11a. The curve initially follows the high resistance load line characteristic of the amorphous phase of PCMs until V_{th} had been reached at 1.82 V. Current continued to rise up to the specified compliance, which was chosen to preserve to preserve the AFM tip. On the return sweep the current is compliance limited until it reaches a voltage for which (according to its resistance) current drops below 25 mA to follow a low resistance load line. Replotting this I-V sweep on a log_{10} axis (Figure6.11b) enables analysis of the pre-V_{th} region, which illustrates the nature current-response in the amorphous conductivity regime. Note that between 0.25 V and V_{th} the curve in Figure 6.11b is linear. Since this plotted on a log_{10} axis, this indicates that it is following an exponential curve on a linear axis (see section 2.5.3 for discussion and Figure 2.13 therein). In addition, using this representation the magnitude of resistance contrast between the two phases may be more easily observed, it being approximately three orders of magnitude at 0.5 V.

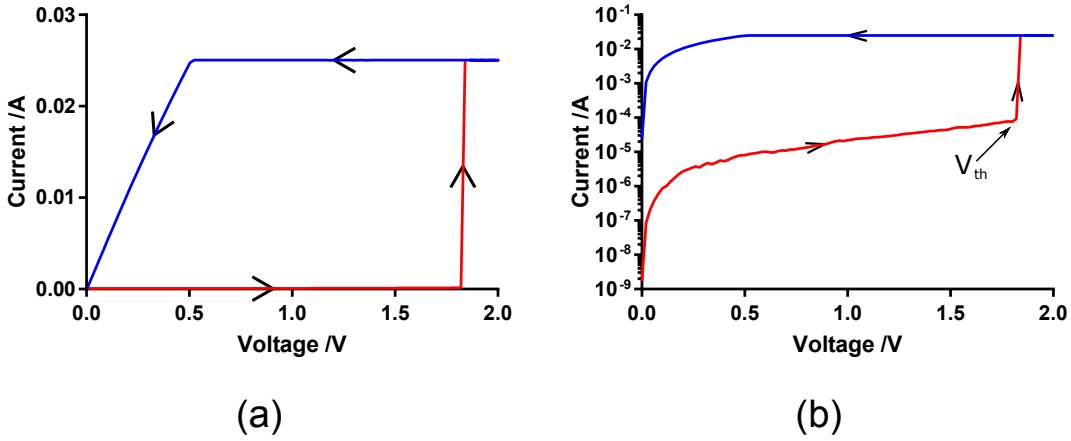

Figure 6.11: (a) I-V sweep showing both the forward (red line) and reverse (blue line) scans between a 0 V to 2 V range on an amorphous GST225 sample. The current compliance was set to 25 mA. Threshold switching (V_{th}) is observed at 1.82 V. (b) The same I-V sweep is replotted using a log_{10} scale for the y-axis. Figure prepared in collaboration with Ron Leizrowice.

The V_{th} of 1.82 V observed on our GST225 reference sample is slightly higher than that reported by Yang *et al.* (1.51 V) where they used c-AFM on a PCRAM test structure that contained a GST225 layer of comparable thickness.[262] The disagreement between both values may be due to the different materials used as electrodes on both experiments (Pt vs. Au) which result in a different contact resistance between them and the GST225 layer. A further source of discrepancy may be found in the different methods used to deposit the GST layers (sputtering vs. electron beam evaporation) possibly leading to different local order within the amorphous materials. Regardless, the fact that threshold switching was observed on a GST sample using the IMTS within a voltage range comparable to those found in the literature validates its use in further investigations of V_{th} in combinatorial thin film libraries of PCMs.

6.3.5 Threshold Voltage Measurement Optimisation

During the setup of the IMTS it was observed that the value of V_{th} measured on the reference GST225 sample was not constant and seemed dependent on the parameters of the I-V sweep. In order to achieve a consistent and reproducible V_{th} value these parameters were investigated systematically.

I-V sweeps can be programmed on the B1500A to be run under two modes: Continuous and pulsed, illustrated as plots of voltage against time in Figure 6.12. On a continuous mode I-V the voltage is supplied to the DUT as a staircase-like waveform where the height of each step

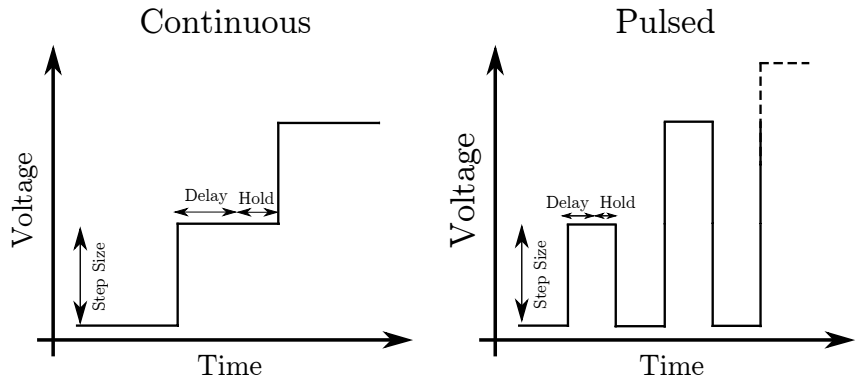

Figure 6.12: Waveforms of the two I-V sweep modes available in the B1500A. Continuous sweeps sustain the output voltage between steps, while pulsed sweeps return to a baseline voltage between steps. The step size represents the voltage difference between each data point. *Delay* is the time the SMU sustains the bias before carrying out the current measurement and the *Hold* is the period over which the analyser collects and integrates the current response of the DUT. Figure prepared in collaboration with Ron Leizrowice.

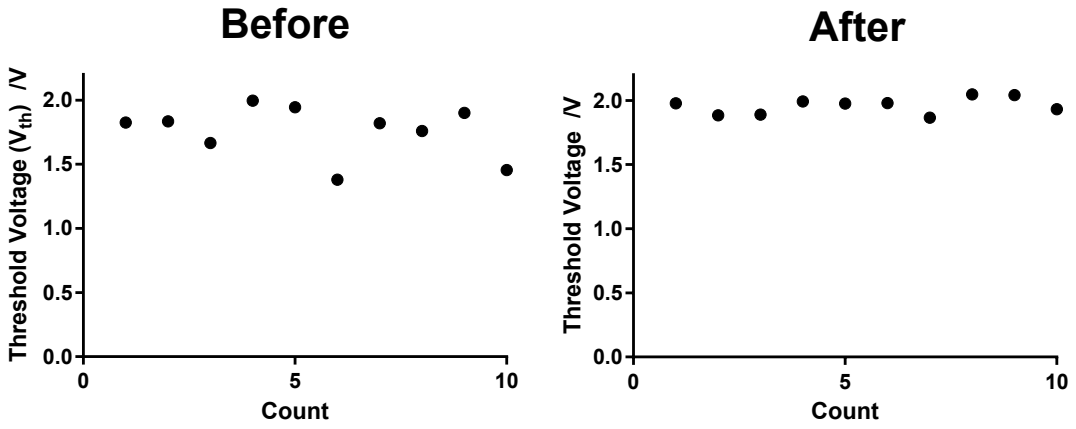

Figure 6.13: V_{th} of the reference GST225 sample as determined through continuous I-V sweeps (a) and pulsed I-V sweeps (b) over ten consecutive measurements. Sweep settings: (a) 1 mV step size, 1 ms delay, 250 µs hold; (b) 0.5 mV step size, 25 ms total pulse width (1 ms delay), 0 V baseline between pulses. Figure prepared in collaboration with Ron Leizrowice.

(the step size, in V) is configurable by the user. The length of the step is defined as the sum of two additional parameters, the delay and hold times, which are also user-defined. The delay is the time during which the SMU applies a bias to the DUT before a measurement is made. This ensures the SMU has had enough time to provide stable outputs after increasing the bias while moving to a new step. The hold time is the period over which the current output of the DUT is collected and integrated by the B1500A.

A pulsed mode I-V requires the voltage to be supplied in pulses of a given width. The delay and hold times are defined at the peak of the pulse. After the pulse is completed the SMU returns to a baseline voltage before moving on to the next pulse. The SMUs installed in the B1500A can output pulses with a minimum width of 500 µs. Pulsed I-V sweeps reduce device self-heating during testing as the sample is under bias for a shorter time and, as consequence, may overestimate the value of V_{th} of a device. However, they only record current in 5 µA steps and thus there is a loss of resolution in the current measurement.

Figure 6.13 shows ten successive measurements of V_{th} performed on the reference GST225 sample using both continuous and pulsed I-V sweeps, after optimal parameters were determined for each mode. For continuous I-V sweeps the mean value of V_{th} was found to be 1.76 ± 0.15V (at a 95% confidence interval). Mean V_{th} for pulsed I-V sweeps was 1.96 ± 0.05V (95% confidence). Therefore, it was concluded that pulsed I-V sweeps produced the most precise set of values of V_{th} for our device configuration. The higher V_{th} obtained through pulsed sweeps highlights the reduced device heating during this type of measurement, as V_{th} is known to increase with decreasing cell temperature.[269] As such, this method was deemed accurate for the determination of V_{th} in combinatorial thin film libraries of GST and N-GST.

6.3.6 Final Instrument Setup

The final setup of the IMTS as used for the experiments described in the following sections is shown in Figures 6.14 and 6.15.

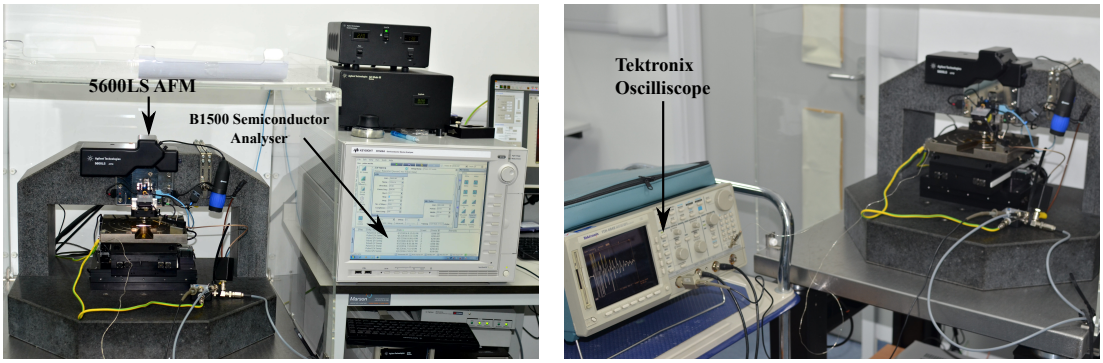

Figure 6.14: Overview of the experimental setup. Left frame shows the 5600LS AFM and the B1500A Semiconductor Device Analyser together with miscellaneous AFM components (unlabelled). The right frame again shows the 5600LS AFM together with the Tektronix Oscilloscope. Figure prepared in collaboration with Ron Leizrowice.

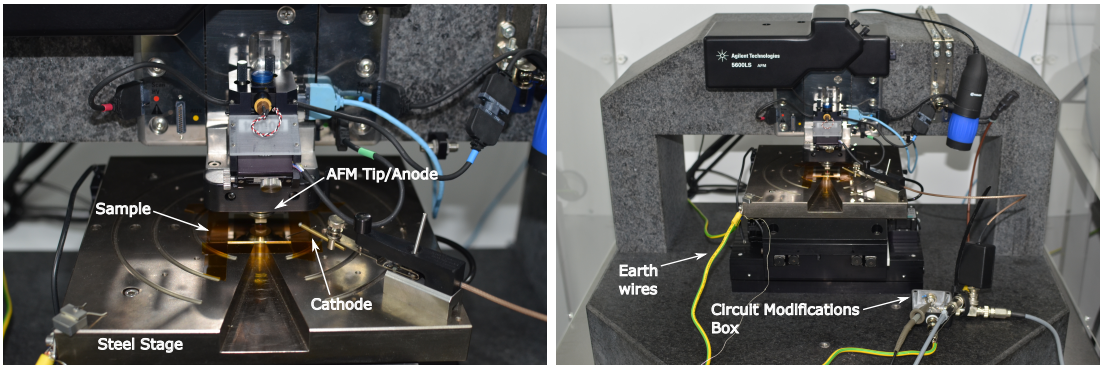

Figure 6.15: Close-up of the individual components within the AFM enclosure. The left frame shows the AFM sample stage (with sample). The probe labelled "cathode" connects to the Pt BCE and is wired to the triaxial line that returns the signal to the B1500A. The right frame shows the position of the various earth wires. The box labelled "circuit modifications" contains the 50 Ω resistor found in parallel with the signal line (described in section 6.3.3). This box also provides an anchor point for the high impedance probe that connects the oscilloscope to the experimental system. Figure prepared in collaboration with Ron Leizrowice.

6.4 Results and Discussion

6.4.1 Evaluation of the Amorphous Conduction Mechanism

The data obtained with the IMTS on the I-V response of our PCRAM devices created an opportunity to investigate the conductivity behaviour prior to threshold switching. To this end, a conduction mechanism based on Poole-Frenkel effect[270] for the intermediate field region of the I-V curve (see Figure 2.13) was derived in collaboration with Ron Leizrowice and verified against experimental data. Poole-Frenkel theory assigns charge carriers as trapped in lattice defects; hence, conduction in the amorphous state was modelled by considering charge carriers in a coulombic potential well, which experience a force (F) from an applied field (E)

$$\overrightarrow{F} = q\overrightarrow{E} \tag{6.4}$$

where q is the elementary charge. The work done on the carrier is defined as

$$\overrightarrow{W} = \overrightarrow{F}d \tag{6.5}$$

where d is the distance travelled by carrier before escaping the potential well. Each trapped carrier experiences a Coulombic potential U that is induced by the ion it creates when removed from the well:

$$U(x) = \frac{q^2}{\epsilon x} \tag{6.6}$$

where $\epsilon = 4\pi\varepsilon_r\varepsilon_0$ (which we define as a polarisability factor, with ε_r being the dielectric constant of the material and ε_0 the vacuum permittivity) and x is the carrier displacement. For a distance r_0, $\frac{dU}{dx} = 0$, which represents the maximum height of the barrier (U_0) as shown in Figure 6.16.

Under an applied electric field the height of the barrier is lowered by ΔU. Alternatively, ΔU may be considered as the potential of the carrier being raised. The work necessary to move the carrier out the potential well then becomes:

$$W = -(U_0 - \Delta U) \tag{6.7}$$

By substituting equations 6.4, 6.5, 6.6, Equation 6.7 may be redefined as:

$$\Delta U = \frac{q^2}{\epsilon r_0} + r_0 qE \tag{6.8}$$

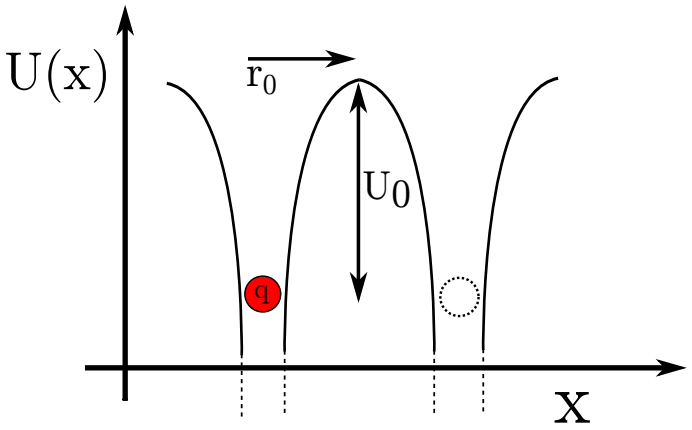

Figure 6.16: Diagram of a charge carrier (q) in a defect state with a potential barrier U_0 needed to reach the next defect. r_0 is the displacement necessary for the carrier to reach U_0 and move on to the next potential well. Figure prepared in collaboration with Ron Leizrowice.

Considering the ion left behind by the carrier at the initial well at position r_0 as $qE = \frac{q^2}{\epsilon r_0^2}$. This expression can be rearranged into:

$$r_0 = \sqrt{\frac{q}{\epsilon E}} \tag{6.9}$$

Hence:

$$\Delta U = 2qEr_0 = 2\sqrt{\frac{q^3 E}{\epsilon}} \tag{6.10}$$

Covalently-bonded chalcogenide semiconductors such as GST show temperature-activated electrical conductivity[271] (σ) of the form:

$$\sigma = \sigma_0 e^{\frac{E_a}{kT}} \tag{6.11}$$

The barrier height (U_0) can be equated to the activation energy (E_a) to transport the carrier out of the well. As such, σ can be restated as

$$\sigma = \sigma_0 e^{-\frac{U_0 - \Delta U}{kT}} \tag{6.12}$$

Using Ohm's law and the result in Equation 6.10, it is now possible to write an expression for the amorphous conductivity of GST in the region of the I-V sweep prior to threshold switching:

$$I = I_0 V e^{\Gamma\sqrt{E}} \tag{6.13}$$

Where:

$$I_0 = \frac{A}{\mathcal{L}}\sigma_0 e^{\frac{-U_0}{kT}} \tag{6.14}$$

And:

$$\Gamma = \frac{1}{kT}\sqrt{\frac{q^3}{\pi\varepsilon_r\varepsilon_0}} \tag{6.15}$$

A is the area of the electrode in the device (in this case, the AFM tip) and $\mathcal{L}$ is the thickness of the PCM layer. The I_0 term contains information about the resistance of the device and the thermally promoted exchange current. The Γ term is defined as a scaling factor of the electric field strength and describes the responsiveness of the material to the applied field. This term contains only fundamental physical constants with the exception of ε_r, the dielectric constant, which is an intrinsic property of the material.

In order to test the validity of this conduction mechanism Equation 6.13 can be linearised in the form

$$ln\frac{I}{V} = \Gamma\sqrt{E} + ln(I_0) \tag{6.16}$$

such that a plot of $ln(I/V)$ against $\sqrt{E}$ results in a linear function of gradient Γ. This result can then be verified by solving for ε_r and comparing the result against experimental data.

$$\varepsilon_r = \left(\frac{2\Gamma kT\sqrt{\pi\varepsilon_0}}{q^{3/2}}\right)^2 \tag{6.17}$$

The pre-threshold region of a typical continuous I-V sweep run on a 50 nm-thick reference sample of GST225 is shown in the left frame of Figure 6.17. The data from the intermediate field region of the I-V curve has been linearised using Equation 6.16 within a V range of 0.1 V to 0.7 V and is also shown on the right frame of Figure 6.17.

It may be seen that the model provides a good fit of the experimental data. Using the gradient of the linearised plot in Figure 6.17 into Equation 6.17, and $T = 300$ K a value of $\varepsilon_r = 16.6$ was obtained for GST225. Prokhorov *et al.* reported a ε_r for GST225 determined using impedance spectroscopy of 16 ± 2[272] and 16.5 ± 1.7[273] on a separate measurement. The agreement of this result with the literature suggests that our defect-limited model may be useful in describing the amorphous conduction behaviour of covalently-bonded chalcogenide glasses similar to GST225. However, this model is limited to the intermediate field region of the I-V curve in devices with dimensions similar to our own where the data has been collected at room temperature. It has been shown, for example, that for thin devices (<30 nm thick) conduction

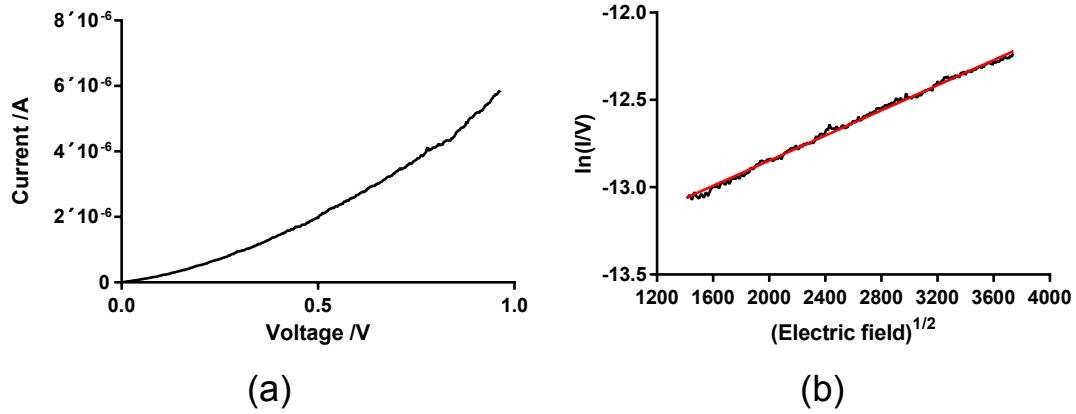

Figure 6.17: Pre-threshold switch region of a continuous I-V sweep performed on a sputtered reference sample of GST225. Sweep settings: 1 mV step size, 1 ms delay, 250 µs hold. Left frame: I-V sweep data as collected by the instrument. Right frame: linearised data as per Equation 6.16 (within the 0.1–0.7 V range); the red line is a linear regression fit of the experimental data. Figure prepared in collaboration with Ron Leizrowice.

models based on optimum channel field emission or percolation conduction may be more appropriate.[110] The main advantage of our model compared to other proposed conduction mechanisms (such as those discussed by Nardone *et al.* in their comprehensive review[110]) is the possibility to compare results obtained from the I-V data through the determination of ε_r of the material by other experimental means. Moreover, the ability to measure the dielectric constant of amorphous chalcogenides using I-V sweeps may be of use on its own in situations where other experimental methods would not be available.

6.4.2 Threshold Voltage Measurements in Combinatorial Libraries

With the current-voltage scans calibrated and optimised for V_{th} measurements as per section 6.3.5, measurements performed on as-deposited combinatorial thin film libraries of GST and N-GST deposited on SSTOP substrates to form test structures akin to the one introduced in Figure 6.10. Threshold voltage was measured using pulsed I-V sweeps with the following settings: 0.5 mV step size, 25 ms total pulse width, 1 ms delay and 0 V baseline between pulses. The tests were carried on a 14×14 grid similar to those used for the characterisation techniques discussed in Chapter 3. The average over three measurements near the same spot (~5 µm apart, so that compositional changes due to gradient could be considered negligible) has been presented as the final V_{th} value for a given composition.

Due to the nature of the HT-PVD deposition process, our thin film libraries tend to not have an even thickness across the sample. Given that the thickness of the sample is known to have an effect in the measured value of V_{th},[43,44] this variable must be taken into account in order to directly compare the collected data across compositions. To achieve this, the strength of the electric field across the sample was calculated using the following formula:

$$E_{th} = \frac{V_{th}}{l} \tag{6.18}$$

Where E_{th} is the threshold field strength across the device and l is the film thickness in µm.

6.4.2.1 GST Combinatorial Libraries

Sample #8298 was deposited on a SSTOP substrate with the same compositional spread as that shown in Figure 4.3. The length of the deposition was controlled as to produce a thin film with a mean thickness of 50 nm, although the thickness ranged from 17 nm to 51 nm. A map of the interpolated thickness across sample #8298 is shown in Figure 6.18. These thicknesses were used to calculate E_{th} from the experimentally measured V_{th}. The threshold voltage for all compositions is shown in Figure 6.19. The lowest value of V_{th} was 0.8 V for the composition $Ge_1Sb_{12}Te_{87}$, while the highest was 4.5 V for $Ge_{46}Sb_8Te_{46}$. However the data, as seen in the inset of Figure 6.19, show a banded pattern across neighbouring rows which follows the horizontal raster pattern used to collect the I-V sweeps. This pattern may be considered an experimental artefact, possibly related to the integrity of the conductive coating of the AFM tip which was observed to degrade after extended use (~100 I-V sweeps). Whenever possible, the AFM tip would be replaced at the beginning of a row in order to keep the results for that row of materials consistent.

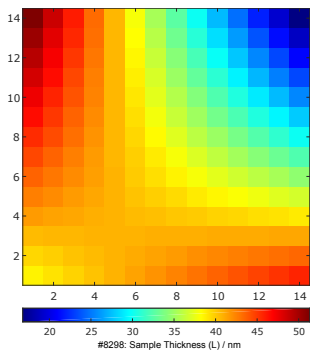

Figure 6.18: Linear interpolation map of AFM-determined film thickness (l/nm) of GST sample #8298.

The results of the threshold field calculation using the datasets from Figures 6.18 and 6.19 are shown in Figure 6.20. The smallest threshold field was 18.9 V µm^{-1} for the composition $Ge_1Sb_{12}Te_{87}$ while the largest was 170 V µm^{-1} for $Ge_{77}Sb_{12}Te_{11}$. Overall, the smallest fields were seen in compositions where Te was the predominant element (>80 at. % Te), which are found within the flexible region of the amorphous glass ternary, as per Figure 2.8. On the other hand, Ge-rich compositions (>70 at. % Ge) required the largest fields to switch and would be amongst the most rigid materials within the GST ternary space following Micoulaut *et al.*[88] Rigid glasses in the GST space would have a large average coordination number (see section 2.4.3.1) increasing the number of carrier traps in the material and lowering its conductivity. As a result, higher voltages would be necessary to supply the required energy to promote carrier mobility and fill the traps.[47] Once all trap sites have been filled, the lifetime of the charge carriers in the material would increase and threshold switching would be able to take place. It would follow that for more flexible materials the number of carrier traps would also be lower, therefore requiring a lower voltage to achieve threshold switching.

A better understanding of the data may be obtained by examining the trends in E_{th} as a function of Sb-content along the pseudobinary lines studied in Chapter 4. These are shown in Figures 6.21 and 6.22. A large degree of scatter in the data may be observed in these plots due to the experimental artefacts described earlier in this section. However, our results appear to be in good agreement with literature values for similar devices, particularly along the GeTe–Sb_2Te_3 line for which more data points are available. It may be of interest to note the low variability in E_{th} (near 50 V µm^{-1}) along the Ge_2Te_3–Sb_2Te_3, GeTe–Sb_2Te_3 and GeTe–SbTe pseudobinaries, for materials in between the binary compositions, which may be a consequence of these materials having similar structural environments (as suggested by the as-deposited Raman data in section 4.3.1.2) resulting in similar carrier trap densities. Moreover, the overall trend in E_{th} follows that of crystallisation temperature (T_x) for these same pseudobinaries (section 4.4.1 and Figures therein) where compositions near GeTe have the highest E_{th} values and those near Sb_2Te_3 the lowest. This is not unexpected as V_{th} for GST materials has been shown to be directly proportional to the square of the activation energy of crystallisation.[274] This relationship may be clearer in the trend of E_{th} along GeSb–Te (bottom of Figure 6.22) which follows closely the trend of its corresponding T_x plot (bottom of Figure 4.33) despite the experimental artefacts in the V_{th} measurement.

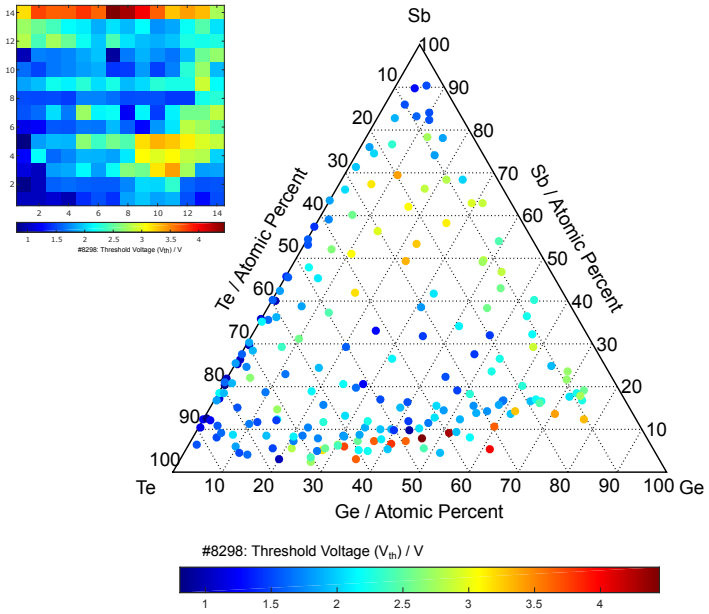

Figure 6.19: Experimental threshold voltage (V_{th}) values for different GST compositions across sample #8298 obtained through pulsed I-V sweeps using the Integrated Microelectrode Testing System apparatus. The inset next to the ternary diagram shows the same information across the thin film: X-Y coordinates correspond to the position of each measurement point within the sample.

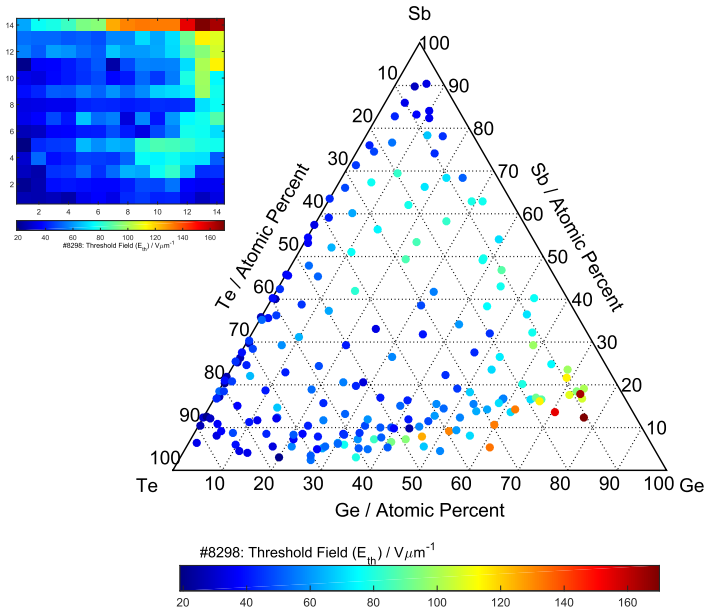

Figure 6.20: Calculated threshold field (E_{th}) values for different GST compositions across sample #8298 obtained through pulsed I-V sweeps using the Integrated Microelectrode Testing System apparatus. The inset next to the ternary diagram shows the same information across the thin film: X-Y coordinates correspond to the position of each measurement point within the sample.

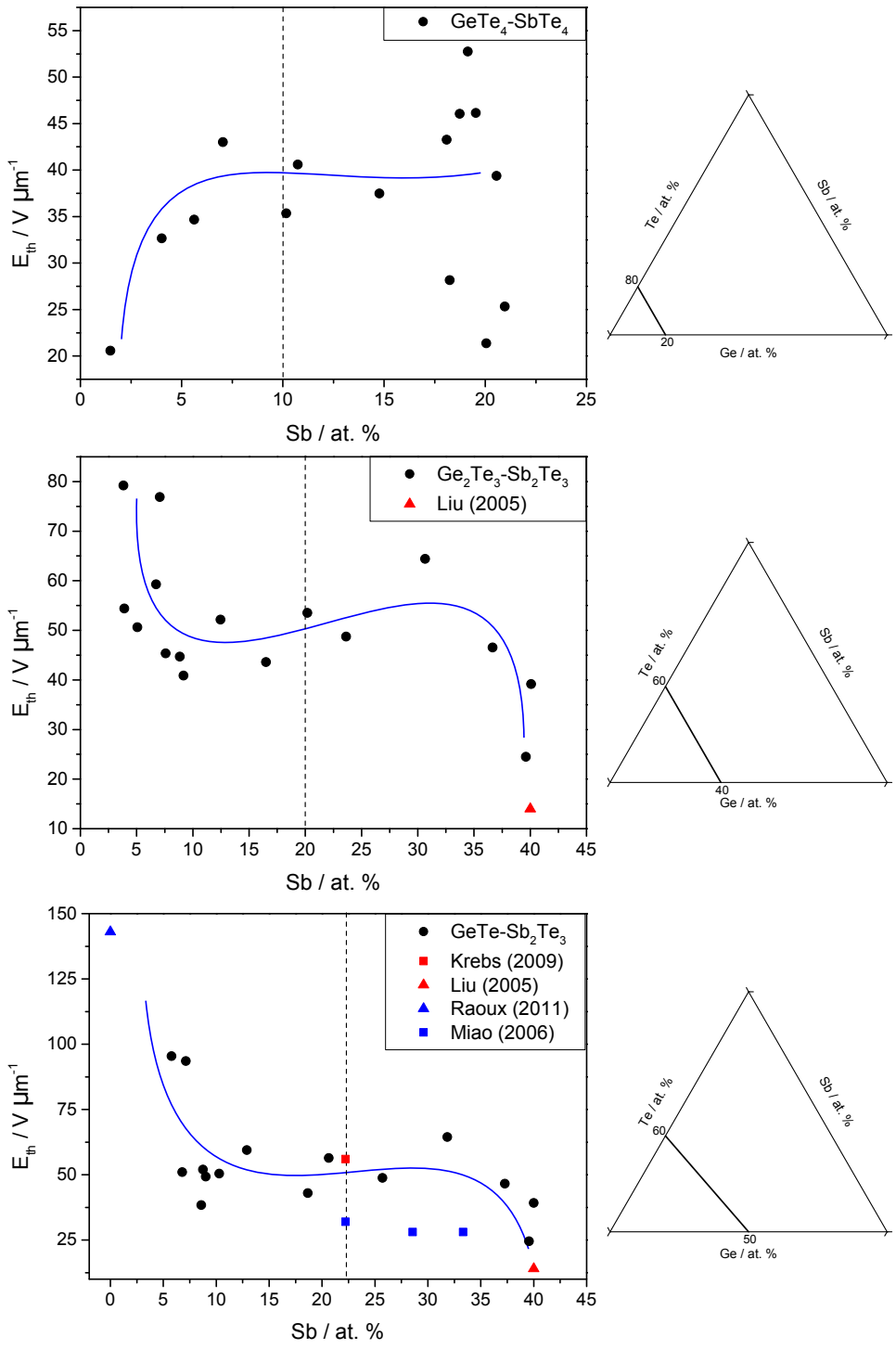

Figure 6.21: Threshold field (E_{th}) as a function of Sb content for materials along the $GeTe_4$–$SbTe_4$, Ge_2Te_3–Sb_2Te_3 and GeTe–Sb_2Te_3 pseudobinaries as obtained using the Integrated Microelectrode Testing System apparatus. Experimental results (black dots) are compared against the literature values where data are available from comparable thin film devices.[43,269,275,276] Blue trend lines included to guide the eye. Dotted lines indicate the intersection with other tie lines (see Figure 4.3). Ternary diagrams indicate the position of each pseudobinary within the GST space.

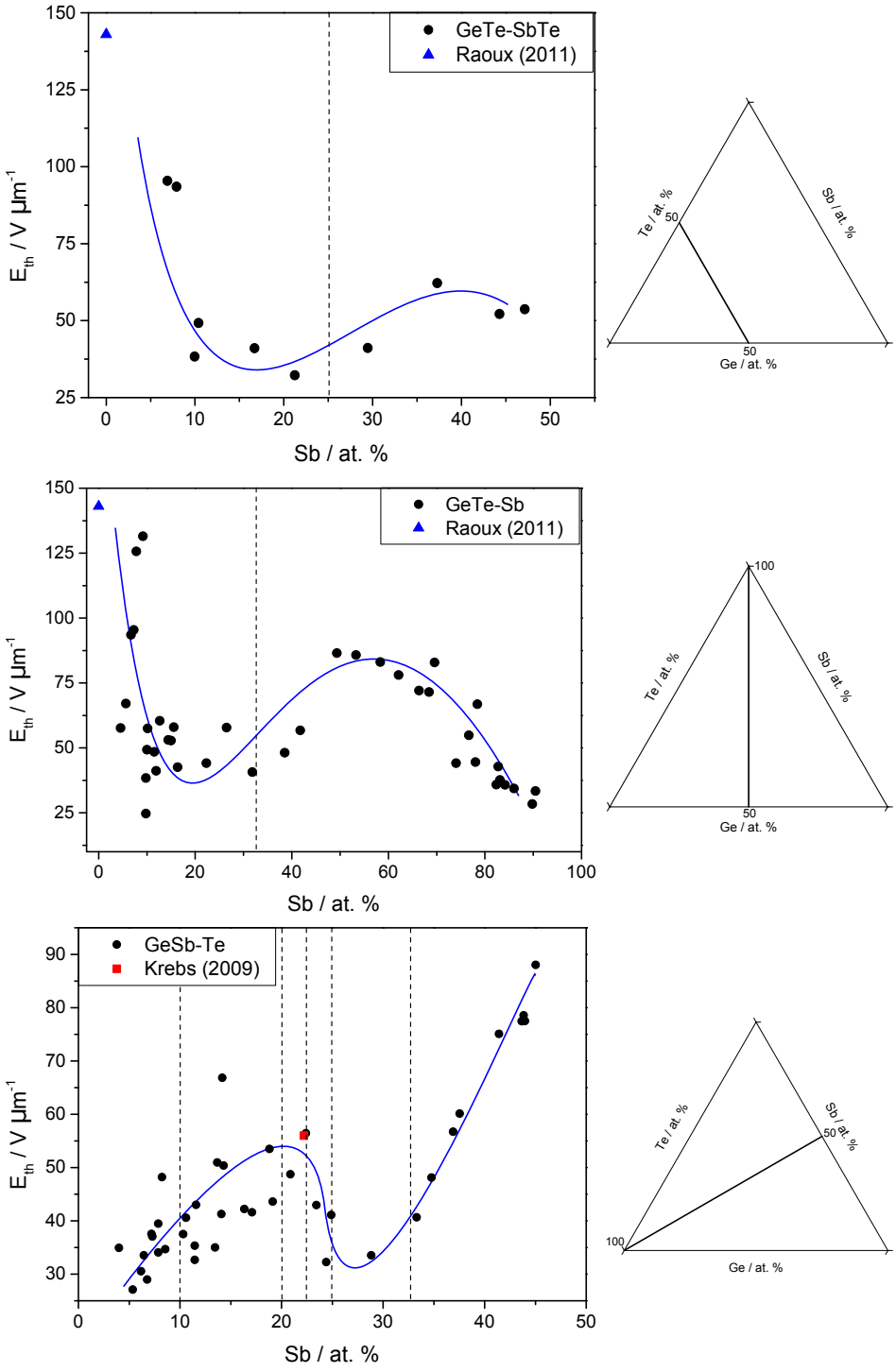

Figure 6.22: Threshold field (E_{th}) as a function of Sb content for materials along the GeTe–SbTe, GeTe–Sb and GeSb–Te pseudobinaries as obtained using the Integrated Microelectrode Testing System apparatus. Experimental results (black dots) are compared against the literature values where data are available from comparable thin film devices.[43,276] Blue trend lines included to guide the eye. Dotted lines indicate the intersection with other tie lines (see Figure 4.3). Ternary diagrams indicate the position of each pseudobinary within the GST space.

6.4.2.2 N-GST Combinatorial Libraries

Sample #7758 was deposited on a SSTOP substrate with the same compositional spread as that shown in Figure 5.3. The length of the deposition was controlled as to produce a thin film with a mean thickness of 150 nm, while the thickness ranged from 146 nm to 153 nm which reflects the smaller compositional space of this library compared to the full GST library of section 6.4.2.1. A map of the interpolated thickness across sample #7758 is shown in Figure 6.23. These thicknesses were used to calculate E_{th} from the experimentally measured V_{th}. The threshold voltage for all compositions is shown in Figure 6.24. The lowest value of V_{th} was 1.2 V for the composition $N_6Ge_{12}Sb_{19}Te_{63}$, while the highest was 7.1 V for $N_9Ge_{17}Sb_{33}Te_{41}$. As was the case with the GST data discussed in the previous section, the V_{th} dataset for N-GST also shows experimental artefacts from the collection method, as seen in the inset of Figure 6.24. In addition, there were six compositions where it was not possible to switch the material and are crossed out as "dead points".

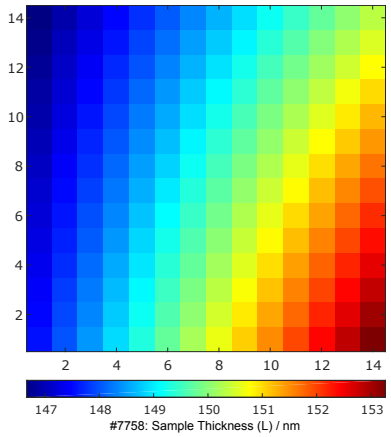

Figure 6.23: Linear interpolation map of AFM-determined film thickness (l / nm) for N-GST sample #7758.

The results of the threshold field calculation using the datasets from Figures 6.23 and 6.24 are shown in Figure 6.25. The smallest threshold field was 8.2 V µm^{-1} for the composition $N_6Ge_{12}Sb_{19}Te_{63}$ while the largest was 47 V µm^{-1} for $N_{10}Ge_{13}Sb_{31}Te_{46}$. The data showed that N-doped GST materials require a lower field to switch than the equivalent undoped compositions, in agreement with published results for dopant levels <10 at. % N.[146,277] This phenomenon has also been observed in N-doped Sb_2Te_3 and Sb_2Te materials.[243,251,278] Lai *et al.* described two mechanisms for this occurrence: First, they proposed that N doping would increase the load resistance of the device during the I-V sweep resulting in a lower current

necessary to effect Joule heating. Alternatively, they also proposed that nitrides found at the grain boundaries of the material would decrease its thermal conductivity, suppressing heat diffusion and confining it to a small programming volume increasing the efficiency of the memory cell.[146] Finally, while not covered in our compositional space, it may be of interest to note that there are contradictory reports as to the effect of N doping in the E_{th} of GeTe materials. Raoux *et al.* measured a large increase in E_{th} at 10 at. % N relative to undoped GeTe,[276] while Fantini *et al.* reported a small decrease in E_{th} between 2 and 4 at. % N.[279]

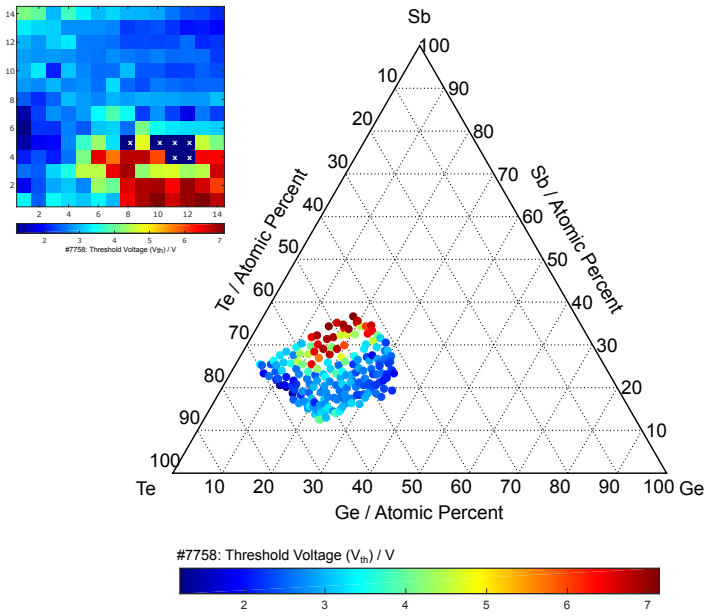

Figure 6.24: Experimental threshold voltage (V_{th}) values for different N-GST compositions across sample #7758 obtained through pulsed I-V sweeps using the Integrated Microelectrode Testing System apparatus. The inset next to the ternary diagram shows the same information across the thin film: X-Y coordinates correspond to the position of each measurement point within the sample.

The trend in E_{th} along the three pseudobinary lines investigated in Chapter 5 is shown in Figure 6.26. The E_{th} values calculated in the previous section for the corresponding undoped GST compositions are also included. It may be apparent that N-GST compositions require lower electric fields than GST to achieve threshold switching. This is one of the properties that make N-GST an attractive material for PCRAM applications as it would lead to reduced power consumption in memory devices.[116]

In addition, the E_{th} trends shown in Figure 6.26 are not directly proportional to the crystallisation temperature of N-GST, as was the case for some of the GST materials discussed in

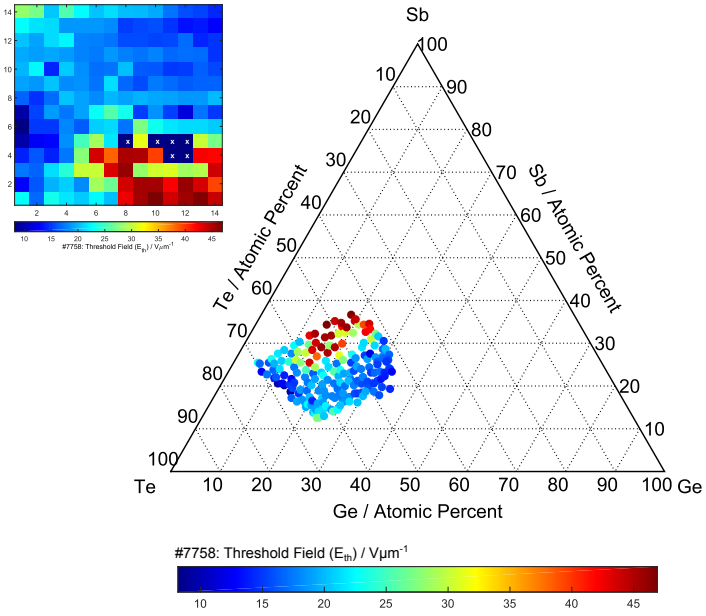

Figure 6.25: Experimental threshold field (E_{th}) values for different N-GST compositions across sample #7758 obtained through pulsed I-V sweeps using the Integrated Microelectrode Testing System apparatus. The inset next to the ternary diagram shows the same information across the thin film: X-Y coordinates correspond to the position of each measurement point within the sample.

section 6.4.2.1. In fact they appear to follow the opposite trend (cf. Figure 5.24). The preferential binding of N to Ge[141] and subsequent precipitation of Ge_3N_4 along grain boundaries[138] may be used together with Lai's arguments outlined above to explain this behaviour. Materials with a higher Ge content achieve lower E_{th} due to a greater concentration of Ge_3N_4 making the cell more thermally efficient. This may not be the case in materials with higher Sb content, which have a lower Ge_3N_4 concentration and would require higher voltages to switch.

Finally, the change in E_{th} as a function of increasing at. % N is given for the GST225, GST224, GST325 and GST124 compositions in Figure 6.27. There is large degree of scatter in the data likely due to the uncertainty introduced by the IMTS instrumentation. The lack of comparable experimental data in the literature hinders the positive identification of any likely trends. Only for the most commonly studied N-GST225 material are there relevant studies that may be used as markers for this purpose: Lai *et al.*[146] measured an $E_{th} = 8.5\,\mathrm{V\,\mu m^{-1}}$ for a material with $0.8 <$ at. $\%N < 1.3$, whereas Raoux *et al.*[276] found $E_{th} = 70\,\mathrm{V\,\mu m^{-1}}$ for a material with 10 at. % N. Taking these values together in consideration the results in Figure

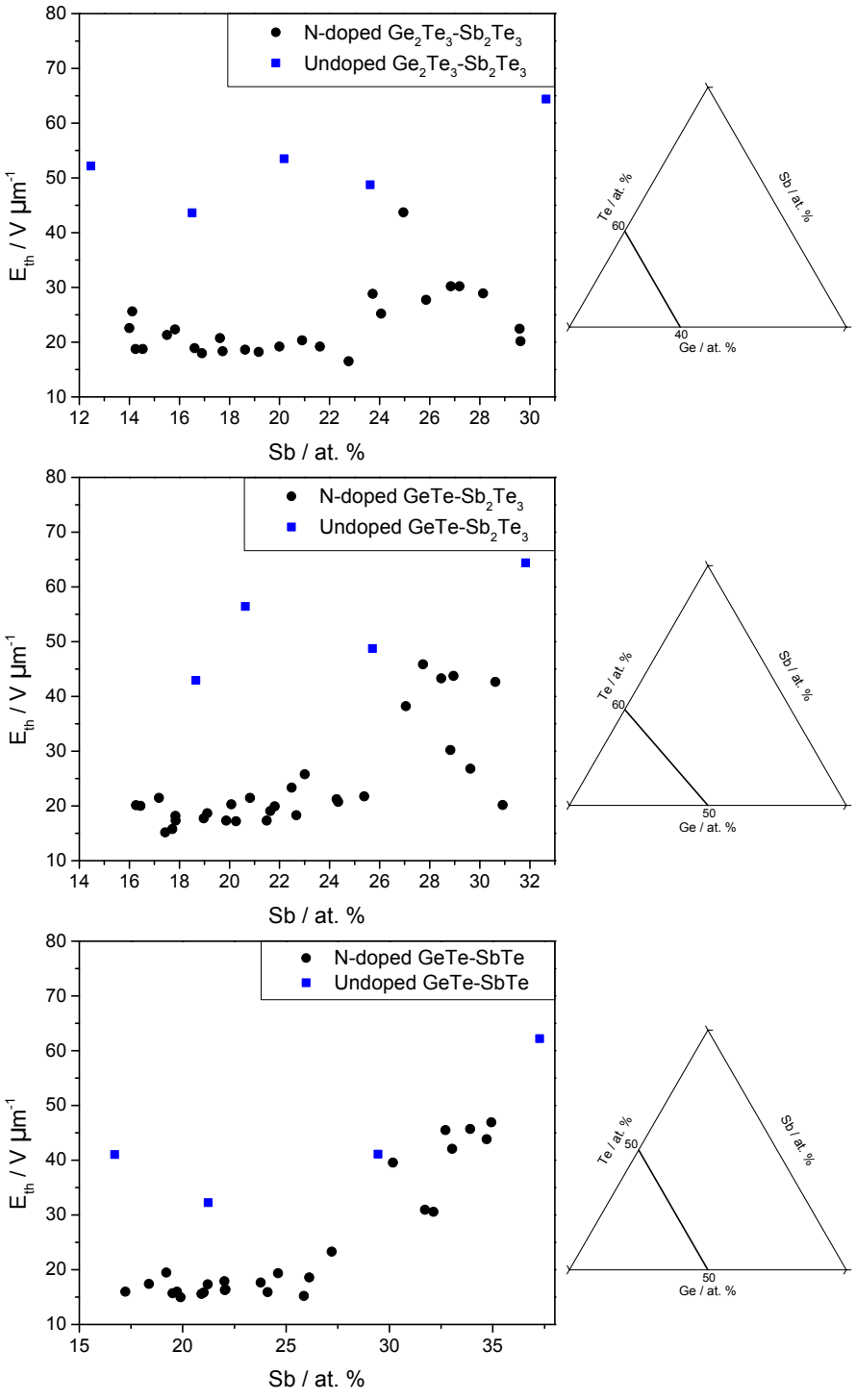

Figure 6.26: Threshold field (E_{th}) as a function of Sb content for N-GST materials along the Ge_2Te_3–Sb_2Te_3, GeTe–Sb_2Te_3 and GeTe–SbTe pseudobinaries as obtained using the Integrated Microelectrode Testing System apparatus. Experimental results (black dots) are compared against E_{th} values of the corresponding undoped GST compositions (blue squares, data from section 6.4.2.1). Ternary diagrams indicate the position of each pseudobinary within the GST ternary space, omitting N content.

6.27 it may be concluded that for the N-GST225 compositions E_{th} is directly proportional to N-content. The data are suggestive of a similar conclusion for the N-GST224 materials, while no firm determination could be made for the N-GST325 compositions. However, it could be hypothesised that E_{th} would decrease with increased doping due to the greater availability of N atoms to form nitrides. The N-GST124 material, being relatively Ge-poor and possessing a high percentage of structural vacancies compared to the other compositions in this figure, generally requires the largest fields to switch. However, whether the variability seen in its dataset is real or a result of instrumental error cannot be determined conclusively.

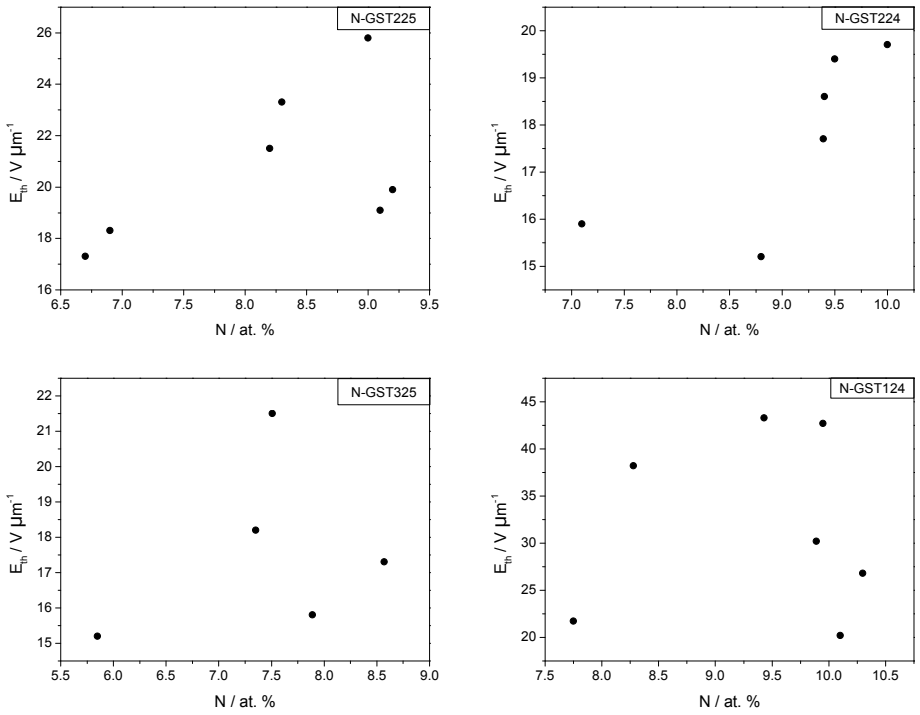

Figure 6.27: Threshold field (E_{th}) as a function of N content for selected N-GST materials as determined using the Integrated Microelectrode Testing System apparatus.

6.5 Summary

The primary objective of the work carried out for the completion of this chapter was the characterisation of secondary functional properties, relevant to PCRAM, of our combinatorial chalcogenide libraries. To this end, the Integrated Microelectrode Testing System was developed as a parametric testing platform for PCRAM devices built upon our combinatorial thin film libraries.

The following significant results were obtained while working towards this objective:

- The development of the IMTS itself. This system enables the use of the full power and operational capabilities of the B1500A semiconductor analyser while achieving high levels of accuracy in addressing combinatorial libraries through the use of the AFM tip and stage. This work also involved the optimisation of the operational parameters to perform I-V sweeps using the IMTS.
- First experimental determination of V_{th} and E_{th} for the vast majority of the Ge:Sb:Te compositional space in a single experiment. The Interpretation of these results using the pseudobinary line approach and extending it to lines beyond the traditional GeTe–Sb_2Te_3.
- First experimental determination of V_{th} and E_{th} for compositions, other than GST225, within the N-doped Ge:Sb:Te compositional space.
- Interpretation of the V_{th} and E_{th} results using the pseudobinary line approach and extending it to lines beyond GeTe–Sb_2Te_3. Notable stoichiometric compositions include N-GST325, N-GST224 and N-GST124 at varying dopant levels.
- Derivation of a model that enabled the determination of the dielectric constant (ε_r) of GST225 using pre-threshold data collected during a continuous I-V sweep.

It is expected that these advances will contribute towards the development of PCRAM technology by allowing reliable parametric characterisation of chalcogenide materials found in HT combinatorial libraries. Using these results in conjunction with primary characterisation data (Chapters 4 and 5) should enable a much more rapid selection of PCRAM materials tailored to a specific application. The IMTS supports characterisation of memory types that require only two SMUs to operate, such as Resistive RAM, and therefore may be a useful tool in other areas of NVM research.

Chapter 7

Conclusions and Further Work

7.1 Conclusions

The principal aim pursued within this research project has been to achieve a greater understanding between the structural and functional properties of chalcogenide materials for PCRAM applications. To this end, two material systems were synthesised in the form of thin film combinatorial libraries using high-throughput methods: Ge:Sb:Te and N-doped Ge:Sb:Te. By studying these systems and comparing our results with previously published data it has been possible to validate the use of high-throughput synthesis and screening methodologies in PCRAM research.

Original contributions of this work to the fields of chalcogenide glass chemistry and phase change materials are listed in the following sections. These are directly linked to the project aims discussed in Chapter 1.

7.1.1 Characterisation of GST Combinatorial Libraries (Chapter 4)

The main objectives of this Chapter were the synthesis and primary characterisation of combinatorial thin film libraries of GST. Synthesis was achieved using the HT-PVD system. Structural characterisation was done using Raman spectroscopy and X-Ray diffraction techniques, while primary functional characterisation involved the determination of resistivity and crystallisation temperature using the 4PP and HTOMPT instruments. The following lists the original contributions of this work towards the fields of PCRAM research:

- The synthesis of the largest compositional space of GST materials reported to date, which included stoichiometric compositions such as GST225, GST124, GST147, GST212, GST325 and GST415.

- The first systematic examination of the short range order in both as-deposited and annealed GST materials via Raman spectroscopy.
- The use of Principal Components Analysis models on XRD and Raman datasets to identify the constituent phases of annealed GST across the ternary space.
- Corroboration of the crystallisation temperature data obtained by Guerin *et al.* using the novel HTOMPT technique.
- The first systematic examination of functional properties across multiple pseudobinary lines, in particular GeTe–Sb and GeSb–Te.

7.1.2 Characterisation of N-GST Combinatorial Libraries (Chapter 5)

The main objectives of this Chapter were the synthesis and primary characterisation of combinatorial thin film libraries of N-doped GST. The same HT methods and techniques used in the completion of the objectives of Chapter 4 were also used for the completion of this work. The following are the major contributions of this Chapter to the field of doped chalcogenide glasses:

- The synthesis of the largest compositional space of N-doped GST materials reported to date, which included stoichiometric compositions such as GST225, GST325, GST124 and GST224 with a range dopant levels.
- The first systematic examination of the short range order in both as-deposited and annealed N-GST materials via Raman spectroscopy.
- The first systematic examination of the long range order of annealed N-GST materials via X-Ray diffraction.
- The first high-throughput determination of crystallisation temperature of N-GST materials using the novel HTOMPT technique.
- The first reported determination of the resistivity of N-GST materials using a high-throughput 4PP technique.
- The first systematic comparison of the functional properties between N-doped and undoped GST materials along the Ge_2Te_3–Sb_2Te_3, GeTe–Sb_2Te_3 and GeTe–SbTe pseudobinary lines.

7.1.3 Characterisation of PCRAM Properties of GST and NGST (Chapter 6)

The objective to characterise the properties relevant to PCRAM of our combinatorial GST and N-GST libraries was carried out after the completion of their primary characterisation in Chapters 4 and 5. To this end, the Integrated Microelectrode Testing System (IMTS) was developed as a parametric testing platform for PCRAM devices built upon our combinatorial thin film libraries. While working towards this objective the following significant results were obtained:

- The development of the IMTS itself. This system enables the use of the full power and operational capabilities of the B1500A semiconductor analyser while achieving high levels of accuracy in addressing combinatorial libraries through the use of the AFM tip and stage.
- First experimental determination of threshold voltage (V_{th}) and threshold field (E_{th}) for the vast majority of the Ge:Sb:Te compositional space in a single experiment.
- First experimental determination of V_{th} and E_{th} for compositions other than GST225, within the N-doped Ge:Sb:Te compositional space.
- Interpretation of the V_{th} and E_{th} results using the pseudobinary line approach and extending it to lines beyond the traditional GeTe–Sb_2Te_3.
- Derivation of a model that enabled the determination of the dielectric constant (ε_r) of GST225 using pre-threshold data collected during a continuous I-V sweep.

7.2 Material Recommendations for Further Study

As discussed in Chapter 1, the motivation for the use of high-throughput, combinatorial methods was the acceleration of material synthesis and characterisation. Having demonstrated the effectiveness of these methods in the study of phase-change materials, it would not be out of place to recommend some of the compositions covered in this thesis for further study in the applications for which chalcogenides have proven useful so far.

The phase-change material requirements for NAND Flash replacement memories have been extensively covered in Chapter 2. In Chapter 4, a "golden" Ge:Sb:Te composition identified by Cheng *et al.* was discussed and potentially identified as $Ge_{51}Sb_{24}Te_{25}$ ($T_x = 260$ °C, $log(\Delta\rho) =$

4, $E_{th} = 60\,\mathrm{V\,\mu m^{-1}}$). Another material studied in this thesis which showed similar properties was $Ge_{20}Sb_{60}Te_{20}$ ($T_x = 230\,^{\circ}\mathrm{C}$, $log(\Delta\rho) = 4.5$, $E_{th} = 70\,\mathrm{V\,\mu m^{-1}}$) which may be useful in PCRAM cell designs where the entire volume is switched, thus avoiding the issue of Sb segregation after repeated cycling. Alternatively, $N_9Ge_{17}Sb_{26}Te_{48}$ ($T_x = 250\,^{\circ}\mathrm{C}$, $log(\Delta\rho) = 3$, $E_{th} = 32\,\mathrm{V\,\mu m^{-1}}$) could be considered for designs where power consumption may be an issue.

The specific case of PCRAM used in high-temperature environments (such as automotive applications) requires materials with $T_x > 125\,^{\circ}\mathrm{C}$.[280] For this purpose the known properties of the "golden composition" make it a good material choice. Additionally, materials with a $Ge_{40}Te_{60}$ ratio and no more than 10 at. % Sb also showed high T_x (near 200 °C) and $log(\Delta\rho) = 7$ that would minimise resistance drift issues and their E_{th} of $60\,\mathrm{V\,\mu m^{-1}}$ is similar to that of the golden composition. A viable N-GST composition ($N_7Ge_7Sb_{26}Te_{60}$, $T_x = 200\,^{\circ}\mathrm{C}$, $log(\Delta\rho) = 4.5$, $E_{th} = 27\,\mathrm{V\,\mu m^{-1}}$) was also identified as a potential low-power alternative.

Phase-change materials have been used as components of arithmetic processors and neuromorphic networks.[281,282] The material requirements for these applications for low power consumption (low E_{th}) and the capacity to retain multiple intermediate metastable estates between the amorphous and crystalline phases [high $log(\Delta\rho)$], amongst others. Materials satisfying these two requirements are $Ge_{40}Sb_{20}Te_{40}$ ($T_x = 150\,^{\circ}\mathrm{C}$, $log(\Delta\rho) = 5.5$, $E_{th} = 37\,\mathrm{V\,\mu m^{-1}}$) and $N_9Ge_{17}Sb_{26}Te_{48}$ ($T_x = 220\,^{\circ}\mathrm{C}$, $log(\Delta\rho) = 3$, $E_{th} = 45\,\mathrm{V\,\mu m^{-1}}$).

The final application that will be considered in this discussion is that of flexible displays made of PCM pixels. The materials used in this application require a very high optical contrast between phases.[41] While this specific figure of merit was not explicitly explored in this thesis, the intensity correction calculation performed for the HTOMPT experiment (ΔI, section 3.3.2) could serve as a surrogate indicator. Examination of Figure 4.30 reveals an area delimited by 5 at. % to 15 at. % Sb and 40 at. % to 50 at. % Ge that contains GST materials with ΔI of up to four orders of magnitude after annealing to 200 °C. The N-GST materials studied were deemed to have a low ΔI for this application (three orders of magnitude, at most) and therefore no recommendations are offered.

The main advantage of the high-throughput methodology introduced in this thesis is its ability to deliver enough data so that it is possible to make an informed decision as to which part of the available chemical space should be explored further for a given application.

Therefore, it is important remember that the material suggestions just given must be taken as the starting point for application-specific screening, since it is likely that the compositions listed above will be modified as materials are optimised for specific use cases and device configurations.

7.3 Further Work

This thesis has demonstrated the power and utility of high-throughput, combinatorial methodologies in the synthesis of chalcogenide glasses. As a result, it should be possible to use them to prepare any number of chalcogenide glass systems not only for PCRAM characterisation, but also for the novel applications detailed at the end of section 2.3.1.

The GST and N-GST glasses prepared for this thesis were characterised using established a number of HT screening techniques and the newly developed IMTS described in Chapter 6. While the IMTS has proven a useful tool for characterising some phase-change memory properties of our materials during the course of design and experimentation it became clear that there was still room for further development.

One of the issues of the IMTS was the complexity of the circuit between the B1500A and the AFM introduced by the use of the adaptor cable pictured in Figure 6.4, which was required in order to deliver the signal to the AFM tip. The adaptor cable connected to the AFM scanning head, whose internal circuit design was not provided by Keysight Technologies. This introduced uncertainty as to the possible sources of interference within the instrument, which affected the reproducibility of our PCRAM pulse tests. In order to overcome this limitation it is proposed that the tip holder of Keysight's scanning microwave microscope technology (SMM) compatible with our 5600LS AFM. This tip holder (known as a "nosecone" in Keysight terminology, part number N9546B) is capable of transmitting signals with a frequency range of 1−20 GHz.[283] This range would be ideal for nanosecond pulse tests on PCRAM devices. In addition, the SMM nosecone has with a high-frequency SMA cable connection (50 Ω impedance) built-in that serves to deliver the signal directly to AFM tip, thus bypassing the scanning head electronics. Implementation of this nosecone into the IMTS would only require the use to a simple SMA to triaxial adaptor (available commercially) immediately reducing circuit complexity. However, the SMM nosecone does not accommodate AFM tips supported on chips of standard dimensions meaning, for example, that the AppNano tip

could not be used. Therefore, a commercial supplier would need to be found capable of producing tips of the desired electrical characteristics and dimensions.

The IMTS could be further improved by replacing the original stainless steel AFM stage with a custom made, electrically insulating stage for sample positioning. The original stage was found to be a source of interference during measurements because it was not designed for sensitive electrical switching experiments. Figure 7.1 shows the photograph a prototype aluminium stage with a Macor ceramic inset intended to hold the sample during measurement. This prototype also has a built-in triax connector and pin to make contact with the sample substrate. Preliminary testing showed good performance of this stage during I-V sweeps, however during pulse tests it was not possible to reamorphitise our reference GST225 sample, a process that had been possible on the regular AFM stage. It has been surmised that the stainless steel stage was functioning as a heat sink during the pulse experiments, and that this effect had been lost due to the low thermal conductivity of the Macor ceramic in the new stage. Therefore, further refinement of the stage design would be required before full implementation into the IMTS.

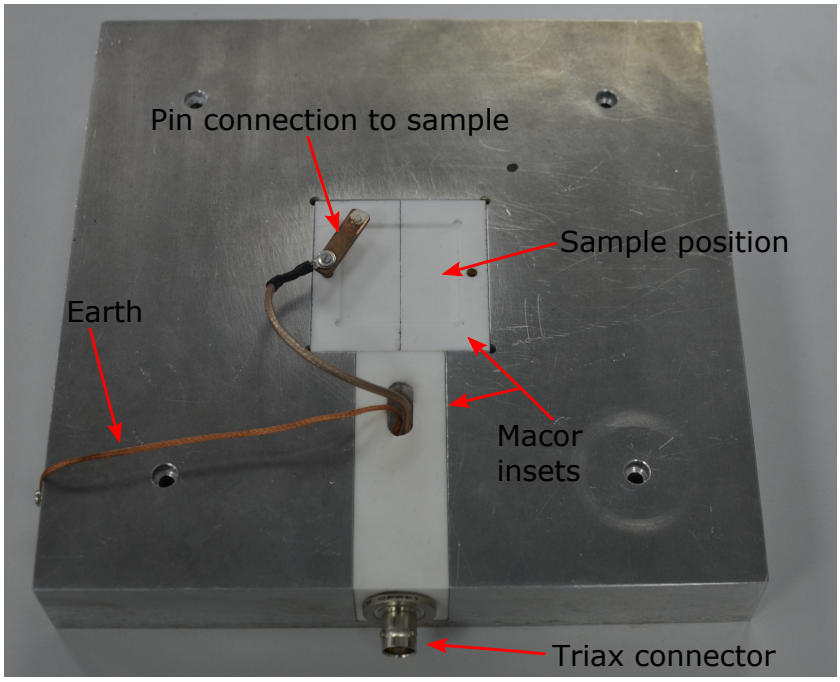

Figure 7.1: Prototype AFM stage for use with the IMTS. Labels indicate relevant components.

PCRAM tests using the IMTS were carried out on samples that consisted of continuous thin film combinatorial libraries deposited on SSTOP substrates as shown in Figure 6.10. However this type of test structures may not be ideal due to the likelihood of current leakage across

the film. In order to avoid this issue the possibility to create chalcogenide pillar structures, similar to those used by Lee *et al.*[260,261] (section 6.2), was explored using our HT-PVD system. This may be achieved using masks in contact with the sample substrate during the deposition process. Typical masks used in our HT-PVD process are made of machined stainless steel and are ~0.5 mm-thick. Using these masks, the smallest feature size through which material may be reliably deposited is a circle of 250 µm in diameter. In order to achieve a smaller feature size, a contact mask with patterns etched on a silicon nitride membrane has been developed in a process described in Appendix C. Using these newly developed masks a 10 µm diameter feature resulted in circles of 15 ± 2 µm diameter deposited through the membrane (Figure 7.2) arising from the "shadowing" effect normally observed during deposition.[284] Due to the small size and distance of these features, multiple micro-devices could be fabricated in a HT, combinatorial way with minimal compositional change between them. In addition, the silicon nitride contact masks are strong enough to be used multiple times under UHV and may be used in a process where a sample may need to be moved between chambers (e.g. from chamber A to the sputter chamber in order to deposit a capping layer). The fabrication of these micro-devices would enable more vigorous statistical testing of memory materials on the IMTS.

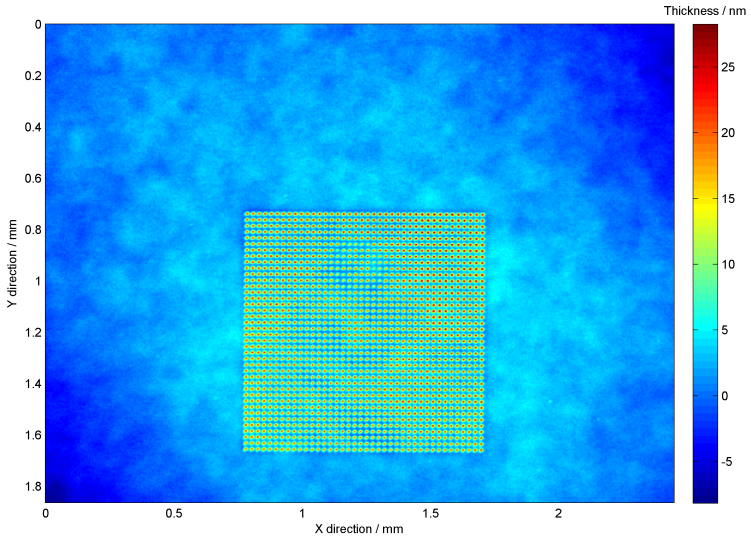

Figure 7.2: Optical profilometry image of an array of Cu pillars deposited via sputtering using a silicon nitride membrane contact mask. The pillars, which had a mean diameter of 15 ± 2 µm, were deposited through etched circles in the membrane 10 µm in diameter. The dimensions of the array are < 1.2 mm on each side. Image courtesy of Rob Noble at Ilika plc.

Richard Feynman in his famous 1959 talk *There's Plenty of Room at the Bottom* to the American Physical Society wondered about the possibility of storing large amounts of data in a small physical volume.[285] Today the challenge is not so much in achieving high-density storage, but to make said storage more efficient, durable and ultimately cheaper. It is my conviction that high-throughput methodologies can speed up the discovery process of materials useful not only in PCRAM devices, but also for future non-volatile memory technologies like ReRAM.

Appendices

Appendix A

Combinatorial Library Compositions

Table A.1: Mean composition and 95% confidence level of GST combinatorial libraries used in Chapter 4.

Point #	Ge / at. %		Sb / at. %		Te / at. %	
	Mean	Error	Mean	Error	Mean	Error
1	73.6	15.4	17.8	0.4	8.6	15.3
2	77.1	18.0	12.4	19.2	10.5	4.2
3	70.6	1.5	13.6	2.3	15.8	2.3
4	62.2	13.4	14.2	10.6	23.6	5.6
5	59.7	5.6	10.7	4.9	29.6	5.2
6	61.5	12.6	5.4	1.4	33.1	12.5
7	51.3	4.8	9.2	5.3	39.5	6.9
8	46.5	7.2	7.8	9.0	45.7	4.9
9	43.5	11.5	7.3	15.0	49.2	4.7
10	40.9	4.9	6.7	12.7	52.4	8.2
11	37.1	9.3	7.3	1.5	55.7	9.0
12	35.5	5.9	3.1	1.5	61.4	5.1
13	31.8	6.3	5.9	3.4	62.3	4.6
14	27.7	4.8	5.1	2.6	67.2	3.1
15	26.8	0.4	2.4	2.4	70.8	2.0
16	28.1	4.2	5.6	2.4	66.3	5.6
17	30.4	4.1	6.1	6.8	63.5	10.9
18	35.0	1.9	5.2	0.8	59.8	2.5
19	38.5	0.5	7.6	2.2	53.9	2.6
20	39.2	8.9	10.0	5.8	50.7	3.3

Continued on next page...

Point #	Ge / at. %		Sb / at. %		Te / at. %	
	Mean	Error	Mean	Error	Mean	Error
21	44.9	11.2	10.2	7.5	44.9	4.0
22	51.8	13.0	4.6	9.9	43.7	8.4
23	56.1	25.4	8.2	15.8	35.7	12.5
24	56.6	8.0	14.2	10.5	29.2	5.0
25	58.2	6.1	15.7	5.1	26.1	8.3
26	65.0	8.3	17.0	5.6	18.0	5.8
27	66.2	10.4	16.2	4.4	17.7	9.1
28	71.5	24.0	17.7	16.6	10.9	7.7
29	74.5	12.0	16.8	12.6	8.6	6.2
30	72.6	13.8	18.5	7.5	8.9	6.4
31	66.4	23.6	16.6	12.7	17.0	11.1
32	61.5	17.4	13.7	12.2	24.8	5.7
33	54.6	3.9	13.7	2.1	31.7	3.3
34	52.9	15.9	9.3	11.3	37.8	5.8
35	46.8	9.5	12.7	12.4	40.6	3.6
36	48.0	6.0	5.6	4.7	46.4	3.6
37	40.8	9.6	5.4	6.2	53.8	9.0
38	37.1	1.9	4.9	1.5	58.0	3.4
39	33.8	3.3	7.3	8.3	58.8	5.1
40	30.2	3.7	6.4	7.9	63.4	10.6
41	26.2	4.5	3.4	6.5	70.4	2.5
42	21.3	1.6	5.5	6.6	73.2	6.6
43	20.0	4.3	3.0	7.6	77.0	11.8
44	20.8	6.1	7.4	5.0	71.8	1.5
45	26.6	0.3	5.0	9.1	68.3	8.8
46	30.3	1.0	8.6	3.8	61.1	3.7
47	33.5	10.4	8.7	11.1	57.8	3.7
48	37.0	9.1	10.0	2.1	53.0	8.3
49	43.0	0.5	9.8	2.4	47.2	2.1
50	46.0	7.7	11.5	0.4	42.5	7.7

Continued on next page...

Point #	Ge / at. %		Sb / at. %		Te / at. %	
	Mean	Error	Mean	Error	Mean	Error
51	52.0	4.3	12.3	0.8	35.7	4.9
52	53.2	4.6	15.5	2.3	31.3	4.2
53	58.4	13.4	16.6	8.5	25.0	5.0
54	64.3	12.1	16.5	7.0	19.2	6.0
55	73.7	18.7	19.1	3.5	7.3	15.6
56	68.8	5.5	21.7	7.0	9.4	6.3
57	64.2	5.7	24.8	5.3	11.0	4.2
58	68.2	4.9	23.5	4.7	8.3	2.9
59	60.7	13.6	20.2	9.1	19.1	8.1
60	58.7	6.6	16.7	7.9	24.6	7.0
61	48.1	3.9	19.0	4.9	32.9	2.0
62	47.5	13.2	14.4	13.4	38.0	8.6
63	41.7	6.1	11.9	1.5	46.4	6.5
64	39.9	6.5	9.8	10.2	50.3	8.9
65	33.7	6.0	10.3	5.4	56.0	2.1
66	30.5	2.6	8.2	7.9	61.2	8.9
67	25.5	4.9	7.8	7.3	66.7	11.4
68	22.1	0.7	8.5	7.6	69.5	8.3
69	17.4	3.5	5.5	8.2	77.1	6.6
70	12.9	1.6	4.2	5.5	82.9	7.1
71	9.8	0.8	6.0	4.4	84.3	4.5
72	14.5	3.3	8.6	3.1	76.8	0.8
73	14.9	3.4	12.4	8.0	72.6	10.6
74	20.4	5.4	8.3	6.7	71.4	1.4
75	24.6	1.9	11.6	4.8	63.7	5.6
76	28.3	7.6	13.2	6.9	58.5	5.0
77	33.4	2.8	12.0	10.6	54.6	7.8
78	38.5	7.6	15.0	13.8	46.5	6.3
79	45.6	4.1	15.6	5.8	38.9	1.7
80	51.1	4.6	18.3	13.2	30.6	9.3

Continued on next page...

Point #	Ge / at. %		Sb / at. %		Te / at. %	
	Mean	Error	Mean	Error	Mean	Error
81	52.8	6.4	23.5	4.2	23.7	3.9
82	53.0	8.4	26.5	6.4	20.5	3.7
83	58.4	15.9	29.3	15.3	12.4	5.5
84	56.8	6.0	32.3	4.2	11.0	6.0
85	53.1	6.1	40.3	2.3	6.6	8.4
86	53.5	5.7	36.5	5.4	10.0	9.5
87	48.2	7.6	32.0	6.2	19.8	6.7
88	47.3	14.3	27.6	9.2	25.1	8.9
89	44.0	9.3	22.3	10.2	33.7	4.9
90	39.3	6.0	16.4	1.9	44.3	7.2
91	33.5	5.9	17.0	4.4	49.5	3.1
92	27.2	1.3	19.7	6.1	53.1	4.8
93	22.6	8.0	15.6	1.4	61.7	6.8
94	22.2	10.0	10.4	9.6	67.3	2.4
95	14.8	4.9	12.1	4.7	73.1	0.6
96	11.3	3.9	11.6	9.4	77.1	12.7
97	11.2	2.5	4.5	3.8	84.2	6.2
98	4.7	3.0	8.2	5.3	87.1	3.4
99	1.6	3.7	6.4	9.3	92.0	11.2
100	5.2	6.3	9.2	8.2	85.6	3.8
101	7.8	6.0	8.7	14.1	83.5	9.8
102	9.9	3.0	11.3	8.2	78.8	6.6
103	13.8	3.4	14.6	1.0	71.6	4.4
104	18.6	1.7	19.0	11.7	62.4	13.4
105	24.2	9.6	20.6	14.7	55.2	6.2
106	28.2	4.4	20.6	3.9	51.2	1.0
107	31.2	2.6	26.5	2.3	42.3	4.8
108	34.8	6.7	31.9	3.7	33.4	4.4
109	40.9	12.6	34.2	5.8	24.9	7.0
110	44.4	9.8	38.5	4.4	17.2	6.0

Continued on next page...

Point #	Ge / at. %		Sb / at. %		Te / at. %	
	Mean	Error	Mean	Error	Mean	Error
111	44.9	2.3	43.1	2.3	12.0	3.6
112	43.3	5.5	46.8	1.8	10.0	3.8
113	39.0	7.0	54.0	9.7	7.0	9.5
114	38.1	1.3	49.2	5.5	12.7	6.1
115	38.1	1.4	49.6	7.3	12.3	8.6
116	32.0	11.5	41.8	1.9	26.2	10.9
117	31.0	2.0	38.6	1.9	30.5	1.0
118	24.6	5.6	33.1	3.6	42.3	6.6
119	20.5	3.3	29.4	6.0	50.2	3.4
120	17.3	6.7	24.5	10.7	58.2	5.3
121	11.4	1.6	22.8	4.1	65.8	3.9
122	9.4	4.2	18.8	8.7	71.8	9.4
123	5.6	4.8	15.1	11.0	79.3	8.8
124	3.7	2.7	10.9	4.4	85.4	7.1
125	1.5	3.3	12.0	13.0	86.5	10.3
126	0.4	0.8	10.3	2.6	89.3	3.3
127	0.6	0.3	12.5	2.5	86.9	2.4
128	0.5	1.5	16.7	1.5	82.8	3.0
129	1.1	2.5	18.6	2.2	80.4	4.8
130	1.7	5.4	20.8	4.0	77.5	9.1
131	4.6	6.0	22.1	7.9	73.3	10.1
132	7.3	3.1	29.4	6.5	63.3	6.6
133	9.9	4.5	31.2	2.0	58.9	2.7
134	12.8	5.3	37.4	9.9	49.8	8.7
135	16.0	4.4	42.0	13.8	42.1	9.8
136	22.6	3.7	49.4	7.0	28.1	5.1
137	22.8	4.1	53.3	3.0	23.9	3.3
138	26.2	2.1	58.3	2.2	15.4	3.2
139	29.2	5.3	62.8	9.6	8.0	5.4
140	31.4	8.7	62.8	7.3	5.8	8.7

Continued on next page...

Point #	Ge / at. %		Sb / at. %		Te / at. %	
	Mean	Error	Mean	Error	Mean	Error
141	24.5	6.7	68.5	5.7	7.0	11.6
142	21.2	2.2	68.5	5.5	10.4	3.8
143	17.9	5.4	66.4	6.8	15.8	7.0
144	16.7	9.1	62.1	17.0	21.2	7.9
145	13.2	6.4	56.4	11.0	30.4	4.8
146	10.6	4.0	51.0	11.5	38.4	9.3
147	6.7	5.1	45.3	6.8	48.0	8.6
148	6.6	6.7	38.8	9.5	54.6	6.4
149	2.9	0.6	36.2	7.6	60.9	7.2
150	2.0	6.0	28.4	3.5	69.5	7.6
151	2.6	3.3	24.6	9.1	72.8	11.8
152	0.0	0.0	21.1	3.9	78.9	3.9
153	0.2	0.7	18.5	8.3	81.3	8.4
154	0.0	0.0	12.3	8.2	87.7	8.2
155	0.8	2.8	17.3	2.6	81.9	3.7
156	0.0	0.0	21.9	8.2	78.1	8.2
157	0.0	0.0	25.5	4.3	74.5	4.3
158	0.3	1.5	30.3	0.7	69.3	2.1
159	0.5	1.9	35.1	8.2	64.5	6.9
160	0.5	2.3	42.3	6.8	57.1	5.3
161	3.6	1.0	47.9	6.5	48.5	6.6
162	6.0	2.3	52.2	6.9	41.8	4.8
163	6.3	1.3	60.1	6.8	33.5	5.7
164	6.5	2.6	67.4	8.3	26.1	8.0
165	10.7	1.1	69.6	3.7	19.8	2.9
166	12.4	5.0	78.4	2.0	9.1	4.1
167	16.0	0.9	74.0	11.6	10.0	10.6
168	15.6	2.4	78.0	8.2	6.4	6.9
169	10.8	3.5	82.4	8.0	6.9	4.6
170	9.8	5.7	84.2	10.2	6.1	5.9

Continued on next page...

Point #	Ge / at. %		Sb / at. %		Te / at. %	
	Mean	Error	Mean	Error	Mean	Error
171	7.8	6.1	83.1	7.1	9.1	12.2
172	6.1	3.7	76.7	5.7	17.2	2.9
173	3.5	4.1	74.6	9.3	21.9	5.5
174	1.8	4.3	66.1	2.2	32.1	4.0
175	2.0	8.6	59.1	12.5	38.9	10.7
176	0.3	1.3	54.3	3.5	45.4	2.9
177	0.5	1.7	45.6	5.7	53.9	4.5
178	0.1	0.5	40.3	5.8	59.6	6.3
179	1.5	3.4	35.6	9.2	62.9	5.8
180	0.2	0.9	27.5	2.5	72.2	1.6
181	0.4	0.9	25.3	5.6	74.3	4.9
182	0.3	1.3	20.4	3.6	79.3	2.6
183	0.5	2.2	26.3	4.1	73.2	3.5
184	0.6	2.5	29.8	1.7	69.6	4.1
185	0.0	0.0	35.7	7.1	64.3	7.1
186	0.8	3.3	40.0	9.7	59.2	7.0
187	0.0	0.0	45.8	4.2	54.2	4.2
188	0.8	2.9	53.3	9.2	45.9	7.1
189	0.0	0.0	57.4	5.2	42.6	5.2
190	0.0	0.0	63.5	5.3	36.4	5.3
191	1.4	0.8	71.4	8.3	27.2	7.9
192	1.9	4.3	76.0	4.9	22.1	2.2
193	3.6	6.0	82.7	9.8	13.7	5.1
194	4.0	3.6	86.0	6.6	9.9	10.1
195	4.1	6.2	89.8	5.2	6.1	1.3
196	6.1	1.7	90.5	5.6	3.4	5.4

Table A.2: Mean composition and 95% confidence level of N-GST combinatorial libraries used in Chapter 5.

Point #	Ge / at. %		Sb / at. %		Te / at. %		N / at. %	
	Mean	Error	Mean	Error	Mean	Error	Mean	Error
1	32.2	16.2	17.9	13.8	42.7	2.8	7.2	3.3
2	30.8	3.1	18.4	6.4	44.3	3.4	6.6	2.4
3	31.1	5.2	16.6	12.1	45.7	13.8	6.6	3.5
4	29.5	8.0	17.3	10.8	45.9	3.0	7.4	1.5
5	28.3	13.2	17.5	15.7	48.1	4.1	6.1	1.6
6	27.6	3.0	16.2	4.6	48.1	5.9	8.1	2.9
7	27.5	16.1	15.1	9.5	50.3	7.0	7.1	0.0
8	26.0	18.2	15.1	15.3	51.4	3.1	7.5	0.3
9	25.2	3.3	14.8	2.0	54.7	4.8	5.4	1.3
10	24.7	10.3	13.5	1.5	54.8	10.5	7.1	0.4
11	24.5	3.1	13.3	0.5	56.9	3.1	5.2	1.4
12	23.2	9.4	12.3	6.4	59.3	6.2	5.2	3.3
13	22.5	3.7	11.9	8.1	60.8	11.2	4.8	3.3
14	22.3	3.0	12.1	4.8	61.4	5.9	4.2	1.7
15	30.4	9.4	21.3	8.7	39.9	2.0	8.4	4.8
16	29.7	2.2	20.5	3.9	42.2	5.1	7.7	2.9
17	28.9	8.6	19.7	2.6	42.5	6.8	8.9	4.4
18	28.4	5.0	19.0	2.1	44.8	3.4	7.9	2.0
19	27.6	6.2	17.9	7.8	45.9	2.6	8.6	2.7
20	27.2	5.5	17.1	1.8	48.0	5.2	7.8	0.8
21	27.0	4.9	17.2	12.2	50.0	8.0	5.9	0.5
22	25.4	9.7	15.9	11.7	51.3	2.4	7.4	0.2
23	25.3	2.5	15.4	4.5	53.2	2.6	6.2	0.5
24	25.1	4.3	14.2	4.3	55.5	2.7	5.3	3.2
25	23.8	2.1	13.5	4.9	56.6	6.8	6.1	1.4
26	22.1	3.1	13.7	4.6	57.4	5.1	6.8	1.2
27	21.5	5.7	13.2	7.0	59.2	7.5	6.1	0.6

Continued on next page...

Point #	Ge / at. %		Sb / at. %		Te / at. %		N / at. %	
	Mean	Error	Mean	Error	Mean	Error	Mean	Error
28	21.1	7.8	12.9	1.3	60.5	6.8	5.4	2.6
29	29.7	2.8	21.8	7.0	39.8	4.5	8.8	4.1
30	29.0	3.1	21.1	0.3	41.2	3.2	8.8	4.2
31	29.3	2.4	20.8	5.4	41.6	3.1	8.3	2.9
32	28.8	5.3	19.6	6.1	43.8	3.8	7.8	2.8
33	27.2	5.1	19.6	5.0	46.0	0.3	7.2	1.8
34	26.5	2.4	19.1	1.7	47.2	3.6	7.2	1.7
35	26.0	4.6	16.9	6.0	49.3	9.4	7.9	2.2
36	25.1	5.6	15.9	2.4	50.4	8.0	8.6	1.4
37	24.0	8.9	15.9	4.3	52.4	6.9	7.7	0.7
38	23.3	2.3	16.1	2.0	54.6	1.6	6.1	1.2
39	22.4	6.1	14.5	4.6	57.6	10.7	5.6	2.0
40	22.0	4.7	14.0	6.5	58.1	1.9	5.9	2.8
41	21.1	7.5	13.8	4.7	60.7	2.8	4.4	2.9
42	20.7	2.6	13.0	6.6	60.6	4.8	5.8	1.3
43	28.5	2.0	23.8	6.7	40.2	6.0	7.5	4.4
44	29.5	5.6	22.1	7.0	39.9	2.0	8.5	2.9
45	28.1	8.9	21.5	4.0	42.1	8.3	8.4	3.2
46	27.3	2.3	21.3	1.5	43.4	2.1	8.1	2.2
47	25.5	3.9	20.1	9.5	45.7	5.7	8.6	3.3
48	26.1	3.9	19.1	3.1	47.2	3.1	7.6	0.3
49	24.5	4.4	18.4	3.5	48.1	1.3	9.0	2.4
50	23.3	2.5	16.6	1.5	50.7	3.7	9.4	1.9
51	23.2	6.9	16.6	1.8	52.5	5.2	7.8	0.0
52	22.0	4.8	16.3	8.3	54.0	5.5	7.7	1.7
53	21.1	4.4	14.8	7.7	56.5	4.9	7.6	0.3
54	20.3	8.4	14.9	5.3	57.8	9.2	7.2	0.0
55	19.5	2.2	14.5	5.5	60.0	3.9	6.0	1.4
56	18.8	4.6	14.2	9.7	61.4	10.6	5.6	1.2
57	28.2	2.9	23.8	3.5	39.0	1.3	9.0	4.9

Continued on next page...

Point #	Ge / at. %		Sb / at. %		Te / at. %		N / at. %	
	Mean	Error	Mean	Error	Mean	Error	Mean	Error
58	27.9	8.7	23.6	3.7	39.5	5.1	9.0	4.8
59	26.7	9.6	22.9	9.1	41.7	1.5	8.8	3.5
60	26.4	4.5	21.0	1.2	43.3	5.7	9.3	4.2
61	25.3	3.2	19.9	4.6	45.3	7.3	9.5	2.9
62	24.6	11.1	19.3	9.6	46.8	11.3	9.4	2.2
63	23.3	7.3	19.4	9.2	48.9	4.1	8.3	1.9
64	23.4	0.6	18.6	4.6	50.9	5.1	7.2	0.3
65	22.5	4.0	18.0	3.5	52.6	0.7	6.9	0.6
66	20.5	2.3	16.4	5.5	54.6	3.4	8.5	1.4
67	20.5	2.2	16.1	3.9	56.7	6.2	6.8	0.2
68	18.9	3.7	15.4	8.9	58.6	5.2	7.2	0.2
69	18.7	9.0	14.7	2.8	60.6	11.6	6.0	2.1
70	18.2	6.8	15.5	2.7	61.9	6.5	4.4	3.1
71	27.2	4.1	24.5	6.8	37.7	4.3	10.6	5.8
72	26.8	6.0	23.9	10.3	39.6	5.2	9.7	5.0
73	26.3	3.9	23.3	4.7	41.1	1.7	9.3	4.1
74	25.7	3.8	22.4	1.5	43.7	3.3	8.3	2.3
75	24.0	4.4	21.8	6.5	44.9	4.5	9.4	4.1
76	23.5	6.8	21.9	11.3	47.5	4.7	7.1	1.0
77	23.0	4.9	19.5	4.5	47.6	0.8	9.9	2.7
78	22.0	5.9	19.0	8.6	50.8	10.8	8.2	1.0
79	21.2	2.1	19.2	3.0	53.0	5.0	6.7	0.3
80	19.7	5.5	17.2	12.8	54.3	7.4	8.7	2.0
81	19.0	3.0	17.5	2.1	56.3	2.5	7.2	1.1
82	18.4	1.8	16.5	3.7	60.1	2.0	5.0	1.7
83	17.1	4.9	15.7	5.9	60.6	10.6	6.7	0.0
84	16.5	3.9	15.6	3.5	62.8	7.1	5.1	2.2
85	26.6	11.8	26.0	1.7	38.4	10.2	9.0	5.0
86	26.6	1.8	24.4	1.8	39.5	1.2	9.5	5.9
87	25.1	2.2	23.9	5.3	40.4	6.8	10.6	5.0

Continued on next page...

Point #	Ge / at. %		Sb / at. %		Te / at. %		N / at. %	
	Mean	Error	Mean	Error	Mean	Error	Mean	Error
88	24.0	4.2	23.6	1.6	42.1	2.5	10.3	3.8
89	23.0	1.7	22.3	4.4	45.3	2.9	9.5	3.1
90	22.3	2.7	20.8	3.9	47.0	1.6	10.0	3.3
91	21.5	4.4	20.8	1.2	48.7	3.8	9.1	2.8
92	20.8	5.4	20.2	8.2	49.8	5.2	9.2	1.8
93	19.6	9.9	19.9	5.8	53.6	6.6	6.9	1.0
94	19.3	3.5	19.2	9.0	55.8	7.8	5.8	0.9
95	17.1	2.9	18.8	3.8	57.0	6.3	7.1	0.5
96	16.7	5.2	17.6	3.9	58.3	4.3	7.3	0.2
97	15.9	1.7	17.1	8.4	61.2	7.4	5.8	1.2
98	15.1	3.0	16.2	5.1	63.2	4.2	5.6	1.4
99	25.1	3.3	27.3	9.9	37.4	6.8	10.2	7.1
100	26.4	6.1	26.4	10.7	39.3	6.5	7.9	2.9
101	23.7	0.6	24.5	7.8	40.6	8.0	11.2	6.1
102	23.2	2.2	24.5	3.3	42.6	5.4	9.6	3.7
103	21.9	1.0	24.0	2.1	44.7	2.6	9.4	4.7
104	21.6	5.2	23.2	2.3	46.3	5.5	8.8	2.8
105	20.7	5.2	21.8	8.2	49.3	3.0	8.3	1.4
106	19.5	8.5	21.3	4.8	50.3	4.7	9.0	2.4
107	17.9	2.8	20.5	7.5	53.1	4.7	8.5	1.7
108	16.8	3.4	19.8	4.7	54.6	5.9	8.8	1.1
109	16.2	1.2	19.5	3.7	58.0	4.6	6.3	1.0
110	15.7	2.7	18.0	4.3	60.4	6.5	5.9	1.8
111	14.0	1.6	18.2	6.1	61.3	6.1	6.6	1.0
112	13.9	3.0	17.4	3.2	62.0	5.9	6.7	0.7
113	23.5	3.7	28.1	2.9	37.5	2.7	10.9	6.5
114	23.9	6.8	26.4	7.0	39.5	0.8	10.2	5.8
115	21.8	0.4	27.3	2.6	41.6	3.0	9.4	5.1
116	21.8	1.9	26.0	6.1	41.8	5.6	10.3	3.8
117	20.8	4.1	24.7	1.5	44.7	5.0	9.8	3.8

Continued on next page...

Point #	Ge / at. %		Sb / at. %		Te / at. %		N / at. %	
	Mean	Error	Mean	Error	Mean	Error	Mean	Error
118	20.3	5.0	24.2	9.4	48.3	4.6	7.2	1.8
119	19.1	5.3	23.1	6.4	49.3	1.5	8.6	2.7
120	17.8	1.9	22.1	0.8	50.5	1.8	9.6	3.5
121	17.3	2.7	21.0	2.0	52.8	2.7	8.9	1.9
122	16.0	3.7	21.1	6.4	55.2	3.5	7.6	0.6
123	14.9	2.9	20.4	6.1	56.8	5.1	7.9	0.3
124	13.7	5.0	19.4	10.6	60.3	6.2	6.5	2.4
125	13.1	7.7	19.1	5.6	62.1	5.0	5.7	1.1
126	12.1	3.8	18.9	3.3	62.6	1.2	6.4	1.5
127	22.9	5.3	29.0	6.5	38.0	6.1	10.1	5.4
128	22.5	1.0	27.8	0.8	39.6	1.7	10.1	5.5
129	21.9	1.9	27.4	6.8	41.7	7.1	9.1	2.1
130	20.8	2.4	27.0	7.2	43.9	4.8	8.4	2.5
131	20.0	5.3	26.1	3.1	45.5	5.8	8.4	2.7
132	18.7	4.4	24.6	3.7	47.4	6.7	9.3	2.8
133	16.9	2.9	24.6	9.5	49.0	9.3	9.5	2.2
134	17.0	8.6	23.8	6.5	51.4	3.3	7.8	1.2
135	15.6	2.0	22.4	3.0	53.8	2.3	8.3	1.5
136	14.5	3.8	22.1	3.5	56.7	5.5	6.7	0.2
137	13.0	3.0	21.5	2.4	58.4	2.5	7.1	0.3
138	12.6	5.0	20.1	7.3	59.9	7.2	7.5	0.5
139	11.3	3.4	19.1	3.8	62.0	2.1	7.6	0.6
140	10.6	6.1	19.2	7.2	63.4	2.6	6.8	0.7
141	21.6	3.1	30.2	11.6	39.0	9.3	9.2	4.5
142	20.6	5.7	28.9	6.3	39.3	4.3	11.2	6.5
143	19.7	1.1	28.2	3.9	41.1	4.8	11.0	5.3
144	19.1	1.5	27.5	1.7	43.2	1.1	10.2	3.9
145	17.5	1.3	26.7	3.6	44.9	4.7	10.9	3.3
146	17.2	3.9	26.6	1.5	47.7	4.4	8.6	2.6
147	15.9	6.0	24.8	7.4	48.6	6.0	10.7	3.9

Continued on next page...

Point #	Ge / at. %		Sb / at. %		Te / at. %		N / at. %	
	Mean	Error	Mean	Error	Mean	Error	Mean	Error
148	14.8	1.4	24.7	1.7	52.3	1.4	8.3	1.5
149	14.2	4.5	23.2	6.8	54.1	5.2	8.6	1.0
150	12.7	6.8	23.6	3.6	56.6	6.4	7.1	0.5
151	12.0	2.7	22.8	5.0	58.4	6.5	6.9	0.4
152	10.8	3.4	20.8	3.8	60.5	5.0	8.0	0.9
153	9.5	3.0	20.5	3.7	62.6	6.7	7.4	0.3
154	9.3	1.8	20.4	4.0	63.5	5.3	6.8	1.6
155	20.6	1.5	31.0	3.9	38.1	2.9	10.3	6.0
156	18.8	4.5	31.1	3.8	40.5	1.8	9.6	5.5
157	18.3	1.0	28.7	2.7	41.4	1.7	11.7	5.6
158	17.2	2.9	29.3	0.7	43.6	3.6	9.9	3.9
159	16.1	7.0	28.9	15.3	44.8	8.6	10.2	4.0
160	15.5	2.8	26.3	8.7	47.4	6.0	10.9	4.1
161	14.6	5.1	26.5	3.2	50.3	2.3	8.6	2.0
162	13.1	5.5	25.8	1.0	51.7	5.6	9.4	2.6
163	12.2	1.8	25.1	4.4	52.9	6.0	9.9	3.2
164	11.4	2.7	24.0	5.2	56.7	7.6	7.9	1.4
165	10.2	2.0	23.6	5.3	58.2	3.3	8.0	0.7
166	9.3	2.2	22.2	4.4	60.9	4.0	7.7	1.4
167	8.3	2.4	21.9	1.6	62.2	2.4	7.6	0.1
168	7.4	1.4	21.0	4.0	63.6	3.5	8.0	0.5
169	19.7	4.2	30.8	3.5	39.2	5.4	10.3	4.8
170	17.4	4.1	31.3	6.2	40.1	3.3	11.2	6.3
171	17.1	1.8	30.6	1.1	43.2	2.9	9.1	3.8
172	16.0	2.0	30.3	1.7	43.2	1.3	10.5	4.7
173	14.8	2.3	28.6	4.7	46.3	6.7	10.3	4.5
174	14.0	1.3	28.0	6.3	47.5	7.4	10.6	4.6
175	12.9	3.8	27.0	4.9	49.9	3.3	10.2	3.5
176	11.7	6.1	26.7	4.0	51.4	2.2	10.3	4.0
177	10.9	1.8	25.9	5.0	55.6	3.4	7.6	0.8

Continued on next page...

Point #	Ge / at. %		Sb / at. %		Te / at. %		N / at. %	
	Mean	Error	Mean	Error	Mean	Error	Mean	Error
178	10.1	2.6	26.0	3.7	58.1	6.3	5.9	0.0
179	8.8	3.1	24.1	4.0	59.9	3.9	7.2	0.0
180	7.6	3.0	23.0	1.9	60.5	4.7	8.9	0.8
181	6.5	4.4	23.2	3.6	61.7	3.5	8.6	0.7
182	6.1	2.3	21.4	2.6	64.3	0.4	8.2	1.1
183	17.4	5.0	31.5	7.7	39.5	2.7	11.6	7.6
184	16.7	5.5	33.4	6.6	41.2	2.0	8.7	3.3
185	15.5	1.1	31.6	8.1	43.6	9.1	9.3	4.0
186	14.1	1.8	31.5	5.0	44.1	4.4	10.2	4.8
187	13.0	5.5	30.8	10.3	46.1	4.8	10.1	3.5
188	11.8	3.4	29.1	2.7	49.3	0.7	9.8	4.3
189	11.1	5.1	28.6	1.5	50.4	6.3	10.0	3.3
190	9.9	7.8	27.2	0.7	52.7	8.1	10.1	4.3
191	9.4	1.0	26.9	3.1	55.0	2.2	8.8	2.7
192	8.1	4.5	26.6	8.5	58.7	6.4	6.7	1.5
193	7.3	7.3	25.6	5.0	59.6	2.3	7.5	1.6
194	6.7	1.6	24.4	1.1	61.4	0.5	7.6	0.1
195	4.9	3.8	23.2	1.6	63.5	5.1	8.4	0.1
196	4.5	2.5	23.4	3.6	64.0	5.2	8.1	0.4

Appendix B

14 × 14 Plots

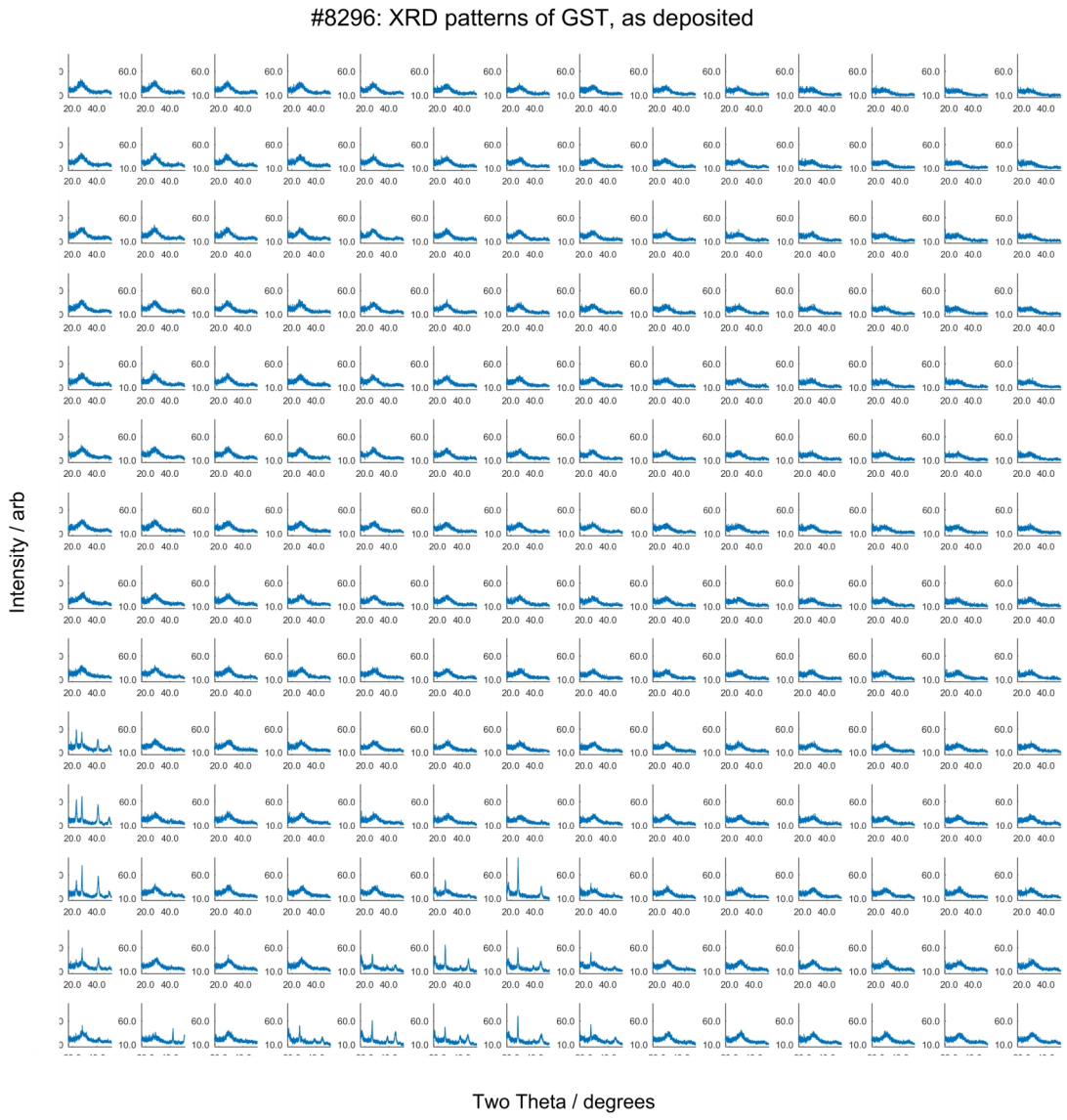

Figure B.1: XRD patterns of GST sample #8296, as deposited.

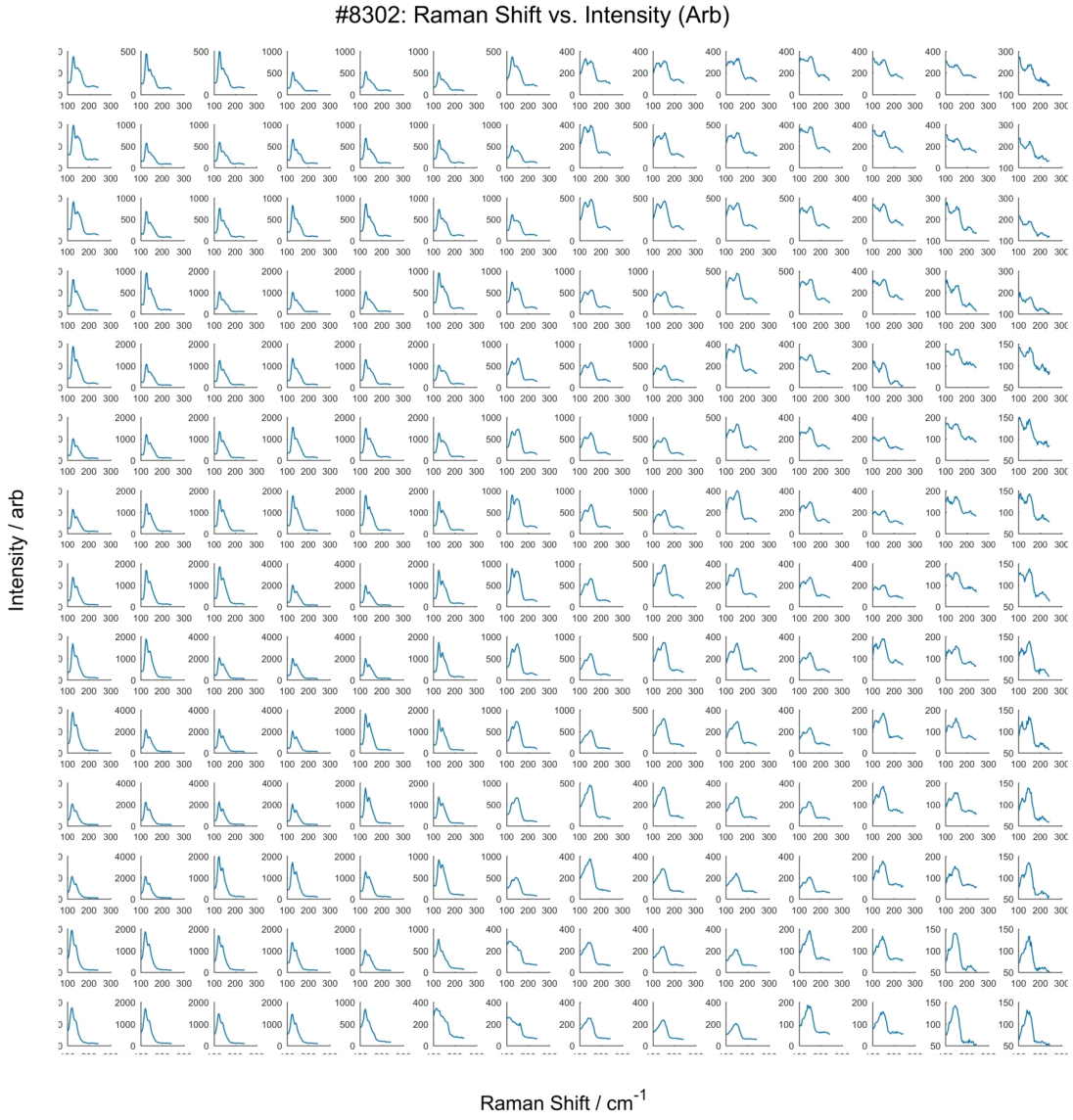

Figure B.2: Raman spectra of GST sample #8302, as deposited.

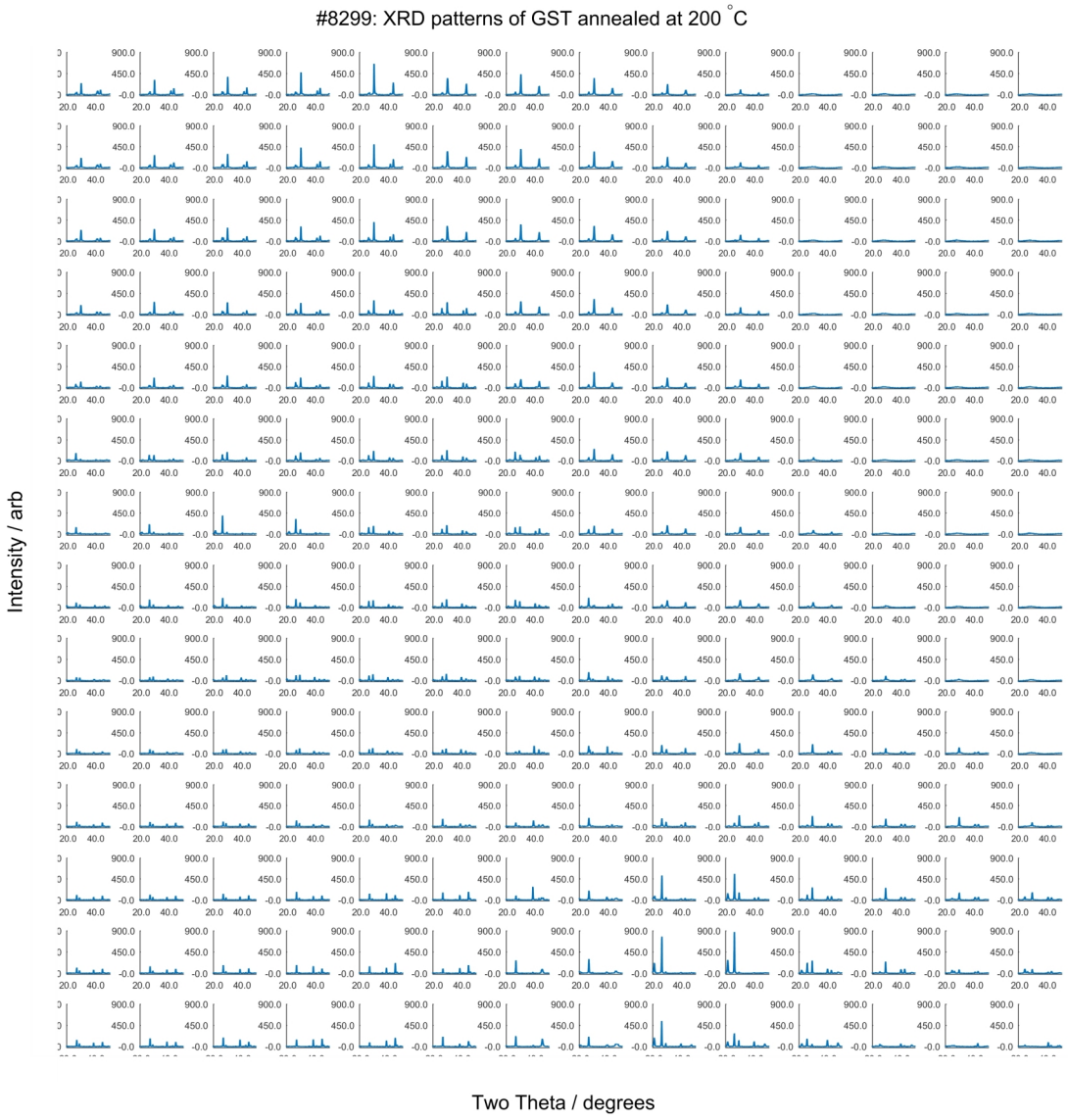

Figure B.3: XRD patterns of GST sample #8299, annealed *in vacuo* at 200 °C for 20 min.

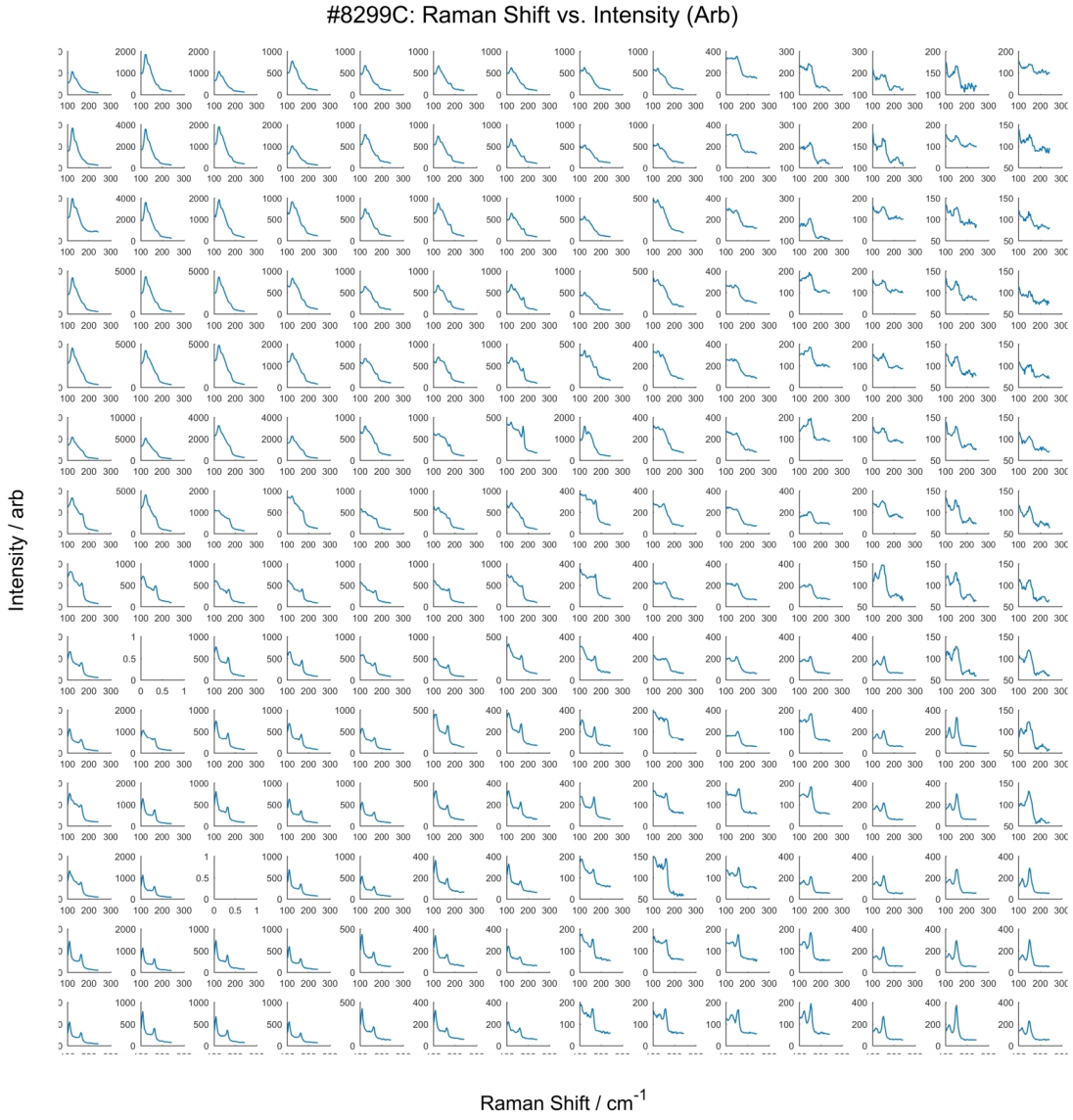

Figure B.4: Raman spectra of GST sample #8299, annealed *in vacuo* at 200 °C for 20 min.

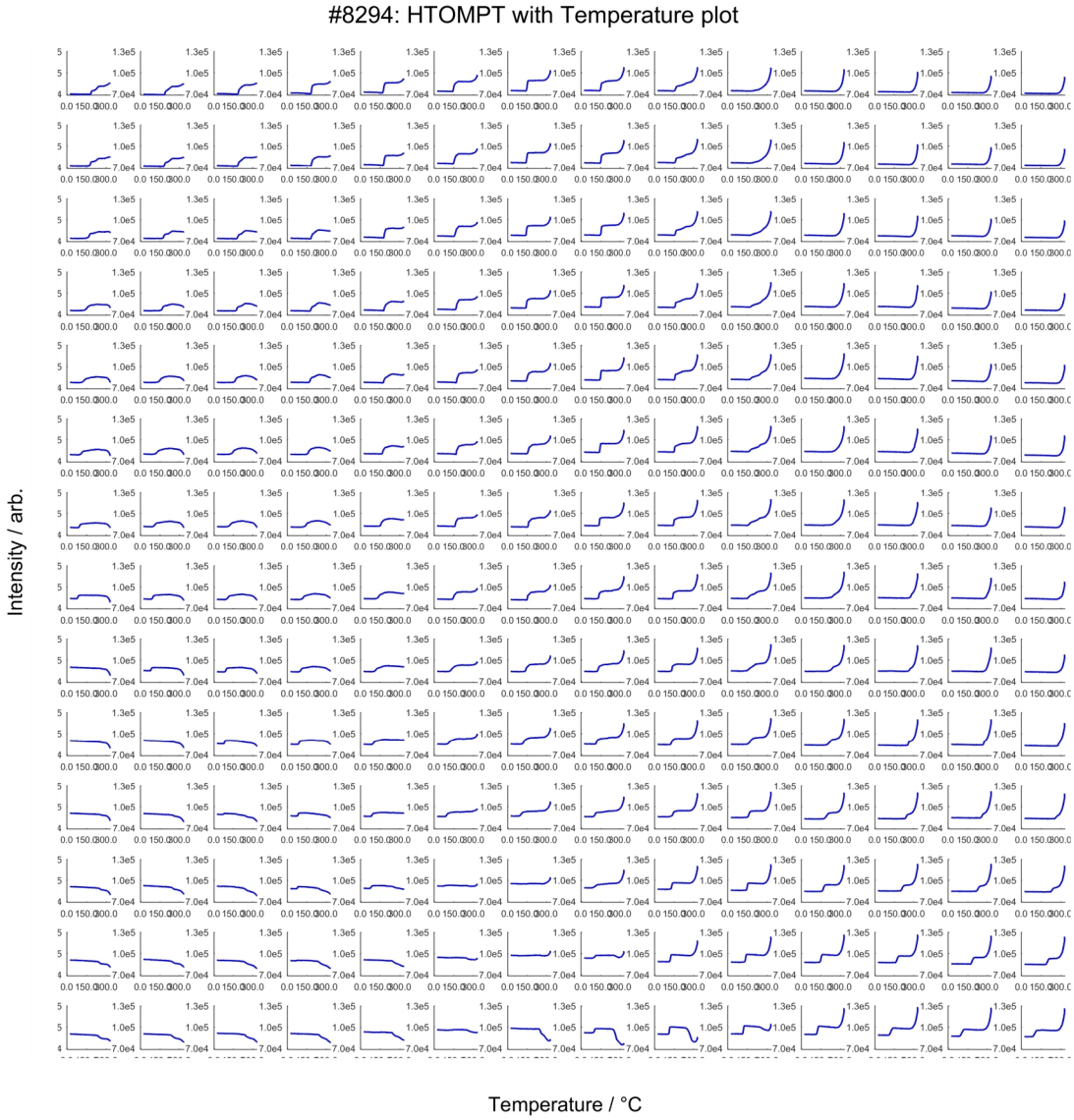

Figure B.5: HTOMPT intensity versus temperature plots of GST sample #8294.

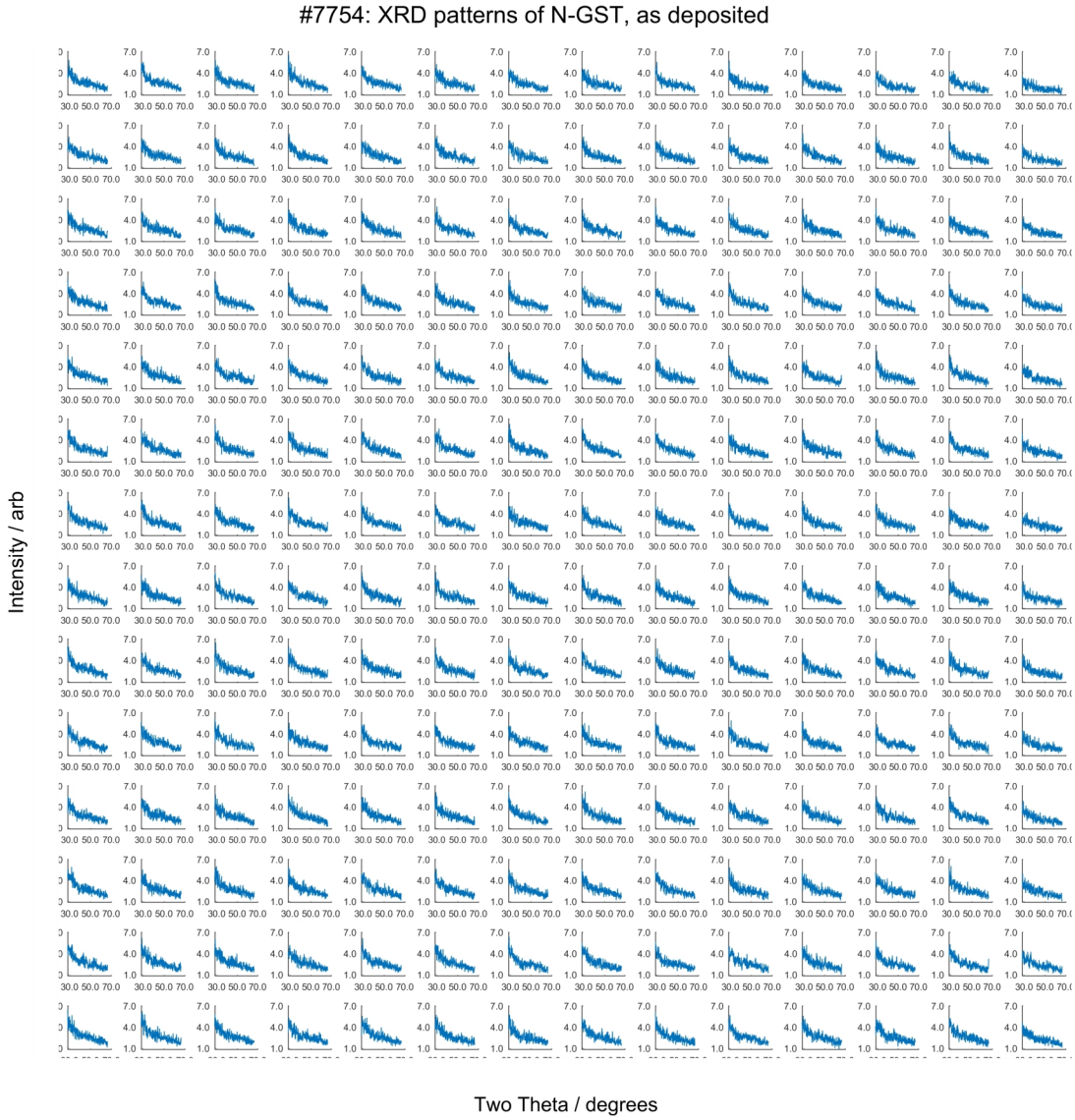

Figure B.6: XRD patterns of N-GST sample #7754, as deposited.

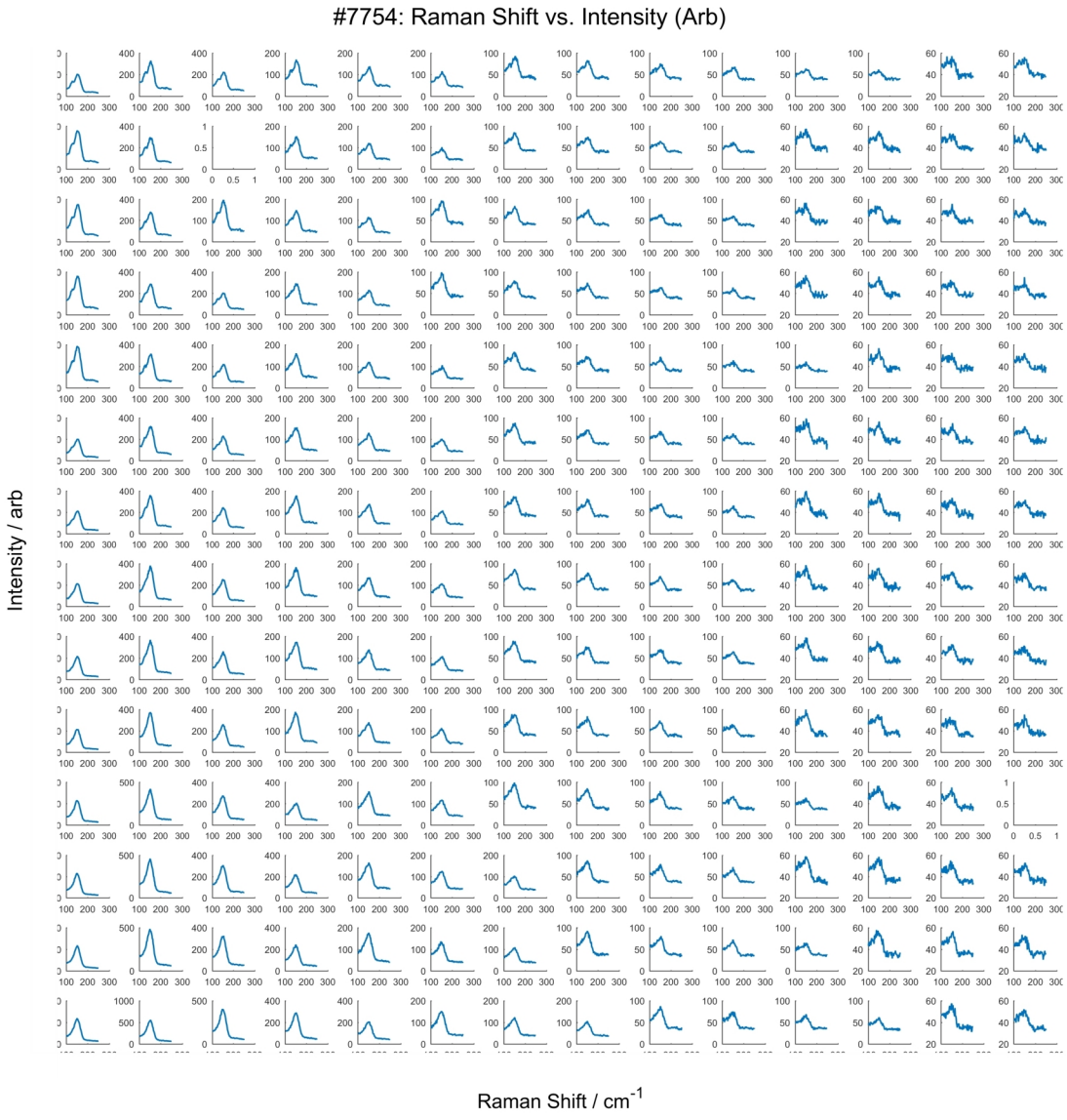

Figure B.7: Raman spectra of N-GST sample #7754, as deposited.

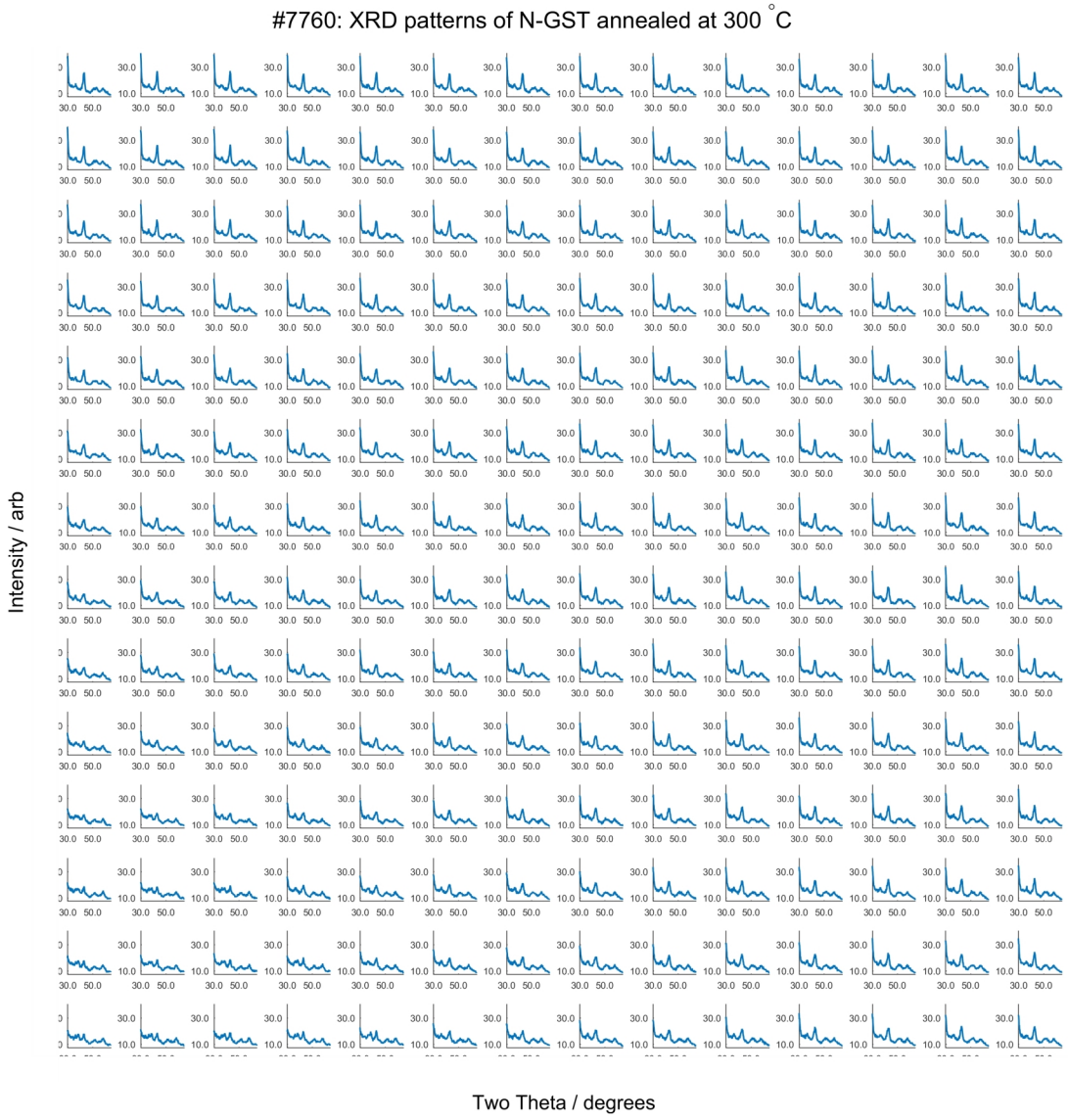

Figure B.8: XRD patterns of N-GST sample #7760, annealed *in vacuo* at 300 °C for 20 min.

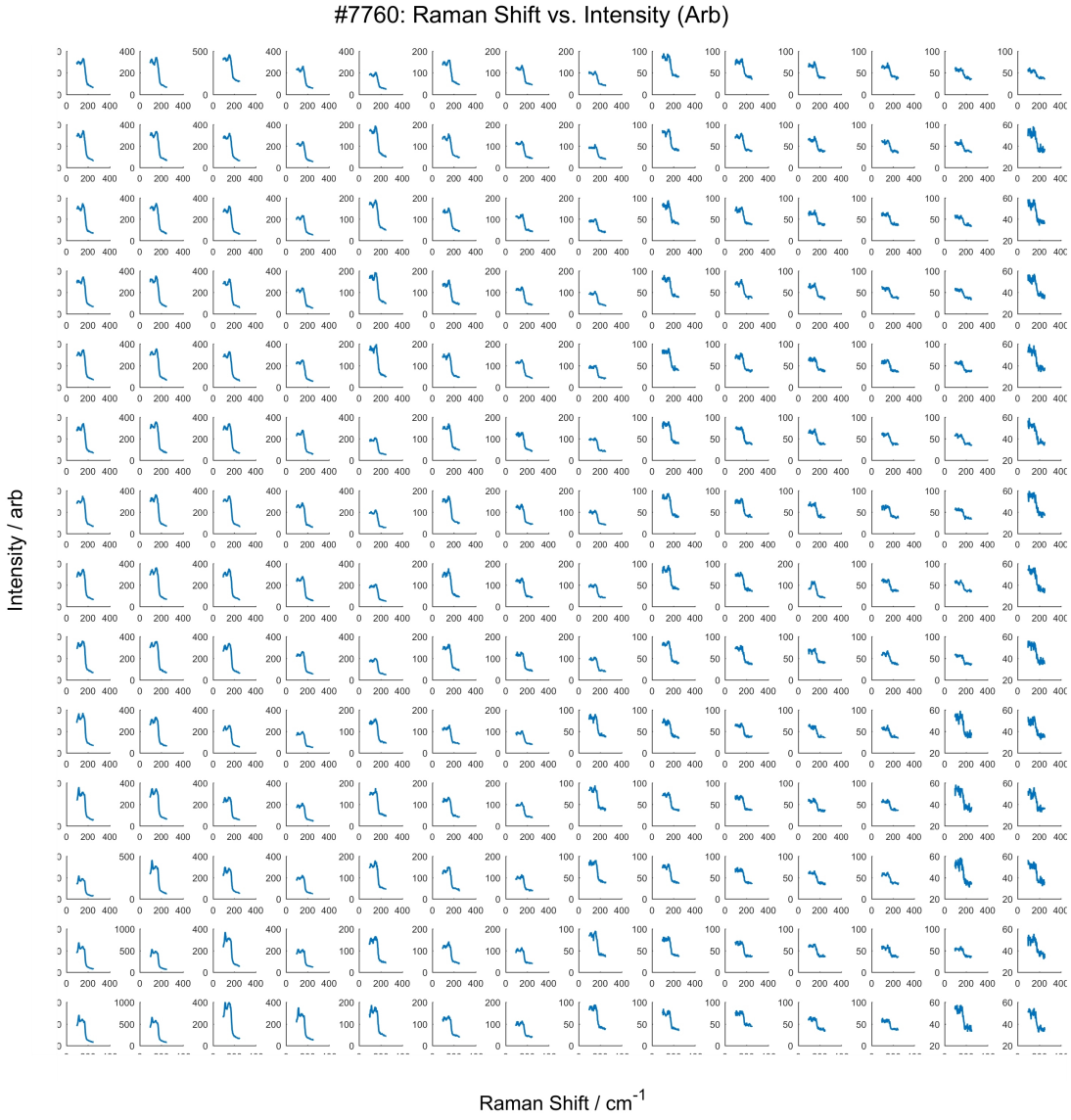

Figure B.9: Raman spectra of N-GST sample #7760, annealed *in vacuo* at 300 °C for 20 min.

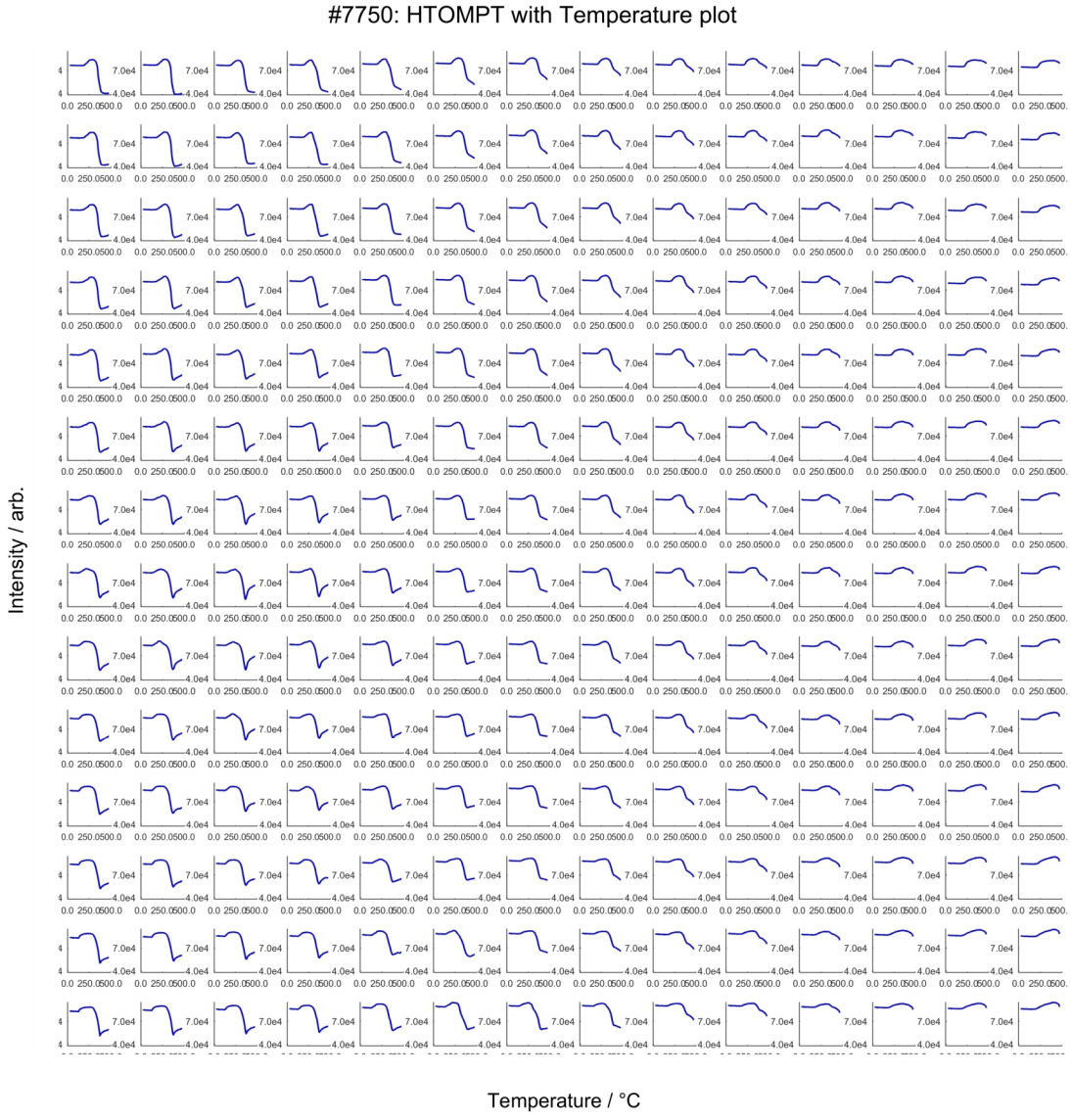

Figure B.10: HTOMPT intensity versus temperature plots of N-GST sample #7750.

Appendix C

Microfabrication of Si_3N_4 Deposition Masks

A newly designed chip has been fabricated (Mir Enterprises Ltd.) made up of multiple windows of low-stress, low-pressure CVD silicon nitride membranes supported by a 450 µm-thick polycrystalline silicon substrate. The chip footprint conforms to a geometry required in relation to the holders and masking system incorporated in the HT-PVD system. Different silicon nitride membrane thicknesses were selected (300 nm and 600 nm) for testing.

Square windows of 1.2 × 1.2 mm arranged in a 12 × 12 array were created using silicon back-side wet etching technique. Wet etching using KOH is the most frequently used method in bulk micromachining for fabrication of micromechanical structures due to its simplicity and relatively low cost.[286] The process etches silicon anisotropically with an etch rate being dependent on crystal orientation and temperature. This forms slopes at a 54.7° angle from the surface (Figure C.1) resulting in a V-shaped groove from the edge of the square opening in the etch mask. An etch-resistant mask is used to protect the areas of the silicon chip that will remain to provide structural support for the membranes.

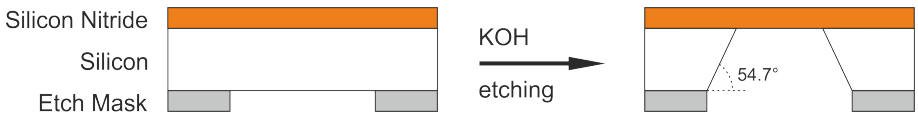

Figure C.1: Cross-section schematic of the back-side wet silicon etch process shown for a single window. The exposed area of the membranes is a square 1.2 mm by side. Diagram is not to scale.

The design of the chip was drawn in-house using the latest version of the Tanner Tools software. This design was sent to Mir Entreprises who deposited the Si_3N_4 membranes and carried out the KOH etching process.

Further processing of the chips into deposition masks was done in the clean room facilities belonging to the Optoelectronics Research Centre (ORC) of the University of Southampton.

This involved the use of UV lithography and related microfabrication techniques in order to create the features on the silicon nitride windows through which the contact pads would be deposited. Dr Behrad Gholipour kindly assisted with this process.

A photomask with the desired patterns was drawn using the Tanner Tools software. The finished designs were sent to Compugraphics International Ltd. for manufacturing.

The photolithography process may be broken down into four broader steps:

1. Ashing of the Si_3N_4 membrane surface using reactive ion etching (RIE) to remove any dust and trace impurities.
2. Patterning and development of the photolithography mask onto the photoresist-coated membrane.
3. Etching of the developed pattern using RIE.
4. Photoresist stripping and final ashing step to remove any remaining impurities.

Specific details for each step are shown in Figure C.2. The equipment used for each process is listed below:

- Reactive Ion Etching: Oxford Instruments Plasmalab 80 Plus, using high purity BOC gases.
- Resist coating: Primus STT 15 spin coater, using Shipley Microposit S1813 photoresist.
- Mask alignment and UV photolithography: SUSS MicroTec MA6 Mask Aligner.
- Development: On a wet-bench using MICROPOSIT MF-319 developer.

Figure C.3 shows an array of the smallest circle patterns that were successfully fabricated. The micrograph is at 10x magnification and shows circle of 10 µm diameter at a 20 µm pitch. A number of observations can be made off this micrograph. First, the pattern was successfully created on the membrane; almost all the pads are well defined and are free from obstruction, despite the remaining traces of photoresist. Second, there are no broken membrane sections between pads. Finally, the irregular shape of the window could be seen; this is a manufacturing defect arising from the KOH etching process and is consistent across all windows within the chip.

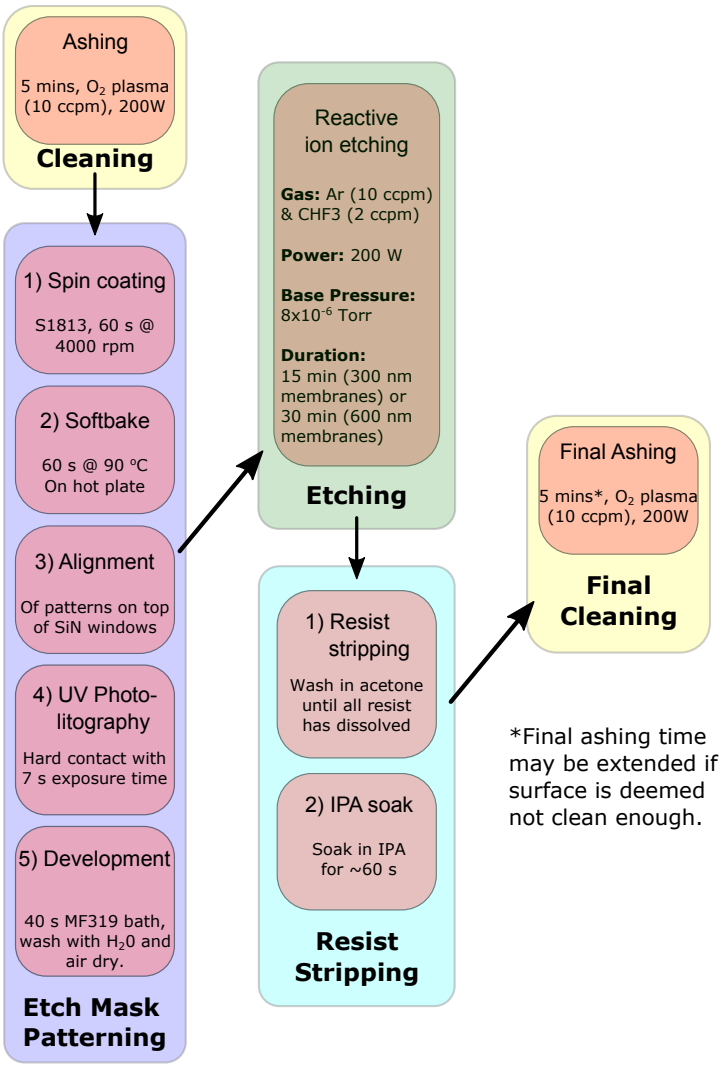

Figure C.2: Flowchart of the photolithography process devised to create deposition masks through silicon nitride membranes. Process designed in collaboration with Dr Behrad Gholipour.

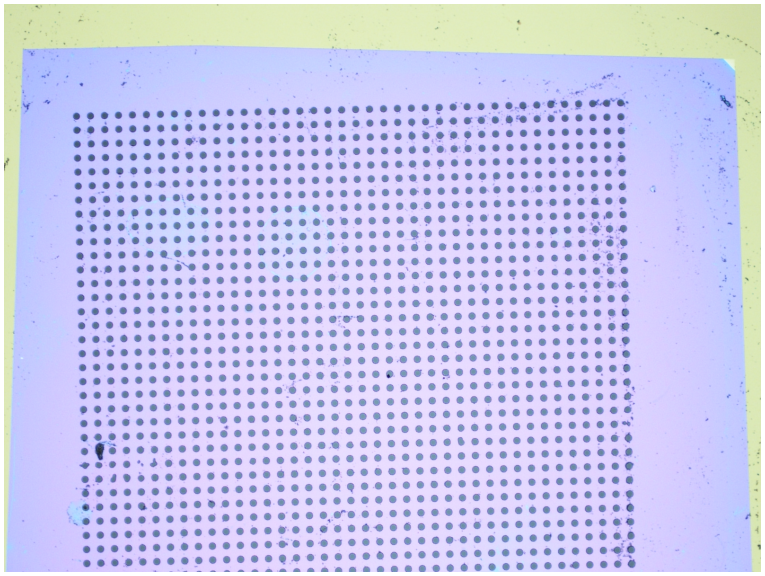

Figure C.3: Optical micrograph showing an array of circles with 10 µm diameter at a 20 µm pitch. Membrane (blue background) is ~1.2 mm across. Notice the irregular window shape created during KOH etching. Also relevant are the traces of photoresist left on the chip, seen here as dirt. Finally, feature size and shape is consistent across the array.

Bibliography

(1) Fullerton, E. E.; Childress, J. R. *P. IEEE* **2016**, *104*, 1787–1795.

(2) Kryder, M. H.; Chang Soo, K. *IEEE T. Magn.* **2009**, *45*, 3406–3413.

(3) Grochowski, E.; Halem, R. D. *IBM Syst. J.* **2003**, *42*, 338–346.

(4) Chung, A.; Deen, J.; Jeong-Soo, L.; Meyyappan, M. *Nanotechnology* **2010**, *21*, 412001.

(5) ITRS *The International Technology Roadmap for Semiconductors, 2013 Edition*; Report; 2014.

(6) Youngdon, C.; Ickhyun, S.; Mu-Hui, P. et al. In *Solid-State Circuits Conference: Digest of Technical Papers, 2012 IEEE International*, 2012, pp 46–48.

(7) Servalli, G. In *Electron Devices Meeting, 2009. IEDM Technical Digest. IEEE International*, 2009, pp 1–4.

(8) Guerin, S.; Hayden, B. E. *J. Comb. Chem.* **2006**, *8*, 66–73.

(9) Von Neumann, J. *IEEE Ann. Hist. Comput.* **1993**, *15*, 27–75.

(10) Backus, J. *Commun. ACM* **1978**, *21*, 613–641.

(11) Wuttig, M. *Nat. Mater.* **2005**, *4*, 265–266.

(12) Bruce, J.; Spencer, N.; Wang, D., *Memory Systems : Cache, DRAM, Disk*, 1st ed.; Morgan Kaufmann: Burlington, M.A., U.S.A., 2007.

(13) Waser, R., *Nanoelectronics and Information Technology*, 3rd ed.; Wiley-VCH: Berlin, Germany, 2012, p 1040.

(14) McAdams, H. P.; Acklin, R.; Blake, T. et al. *IEEE J. Solid-St. Circ.* **2004**, *39*, 667–677.

(15) Sbiaa, R.; Meng, H.; Piramanayagam, S. N. *Phys. Status Solidi-R* **2011**, *5*, 413–419.

(16) Miura, K.; Kawahara, T.; Takemura, R. et al. In *VLSI Technology, 2007 IEEE Symposium on*, 2007, pp 234–235.

(17) Baek, I. G.; Lee, J.; Oh, S. C. et al. Memory devices including multi-bit memory cells having magnetic and resistive memory elements and related methods., US 7,952,914 B2, Patent, 2008.

(18) Noguchi, H.; Kushida, K.; Ikegami, K. et al. In *VLSI Technology, 2013 IEEE Symposium on*, 2013, pp C108–C109.

(19) Raoux, S.; Xiong, F.; Wuttig, M.; Pop, E. *MRS Bull.* **2014**, *39*, 703–710.

(20) Nirschl, T.; Philipp, J. B.; Happ, T. D. et al. In *Electron Devices Meeting, 2007. IEEE International*, 2007, pp 461–464.

(21) Masuoka, F.; Iizuka, H. Semiconductor memory device and method for manufacturing the sam., US 4,531,203 A, Patent, 1985.

(22) Ovshinsky, S. R. Symmetrical Current Controlling Device., US 3,271,591 A, Patent US 3,271,591 A, 1966.

(23) Ovshinsky, S. R. *Phys. Rev. Lett.* **1968**, *21*, 1450–1453.

(24) Dewald, J.; Northover, W.; Pearson, A.; Peck, W. In *Advances in Glass Technology*, 1st; Plenum Press: New York, N.Y., U.S.A., 1962, pp 357–356.

(25) Sie, C. H. Memory Cell Using Bistable Resistivity in Amorphous As-Te-Ge- Film., Ph.D. Thesis, Iowa State University, 1969.

(26) Uttecht, R.; Stevenson, H.; Sie, C. H. et al. *J. Non-Cryst. Solids* **1970**, *2*, 358–370.

(27) Sie, C. H. A Cinematic Study of Mechanisms of Phase Change Memory., `http://www.youtube.com/watch?v=0bgVs0k17vw` (accessed 2016).

(28) Battle, J. H.; Lighty, P. E.; Shanefield, D. J. Solid state element comprising semiconductive glass composition exhibiting negative incremental resistance., US 3,448,425 A, Patent, 1969.

(29) Shanks, R.; Davis, C. In *Solid-State Circuits Conference: Digest of Technical Papers. 1978 IEEE International*, 1978; Vol. XXI, pp 112–113.

(30) Feinleib, J.; deNeufville, J.; Moss, S. C.; Ovshinsky, S. R. *Appl. Phys. Lett.* **1971**, *18*, 254–257.

(31) Chen, M.; Rubin, K. A.; Marrello, V. et al. *Appl. Phys. Lett.* **1985**, *46*, 734–736.

(32) Chen, M.; Rubin, K. A.; Barton, R. W. *Appl. Phys. Lett.* **1986**, *49*, 502–504.

(33) Ohta, T.; Uchida, M.; Yoshioka, K. et al. In *Proc. SPIE*, 1989; Vol. 1078, pp 27–35.

(34) Yamada, N.; Ohno, E.; Nishiuchi, K. et al. *J. Appl. Phys.* **1991**, *69*, 2849–2856.

(35) Iwasaki, H.; Harigaya, M.; Nonoyama, O. et al. *Jpn. J. Appl. Phys.* **1993**, *32*, 5241.

(36) Savransky, S. D.; Wei, T.-C. *J. Ovonic Res.* **2005**, *1*, 31–37.

(37) Foong, A.; Hady, F. In *Memory Workshop, 2016 IEEE 8th International*, IEEE: 2016, pp 1–4.

(38) Rios, C.; Stegmaier, M.; Hosseini, P. et al. *Nat. Photon.* **2015**, *9*, 725–732.

(39) Skelton, J. M.; Loke, D.; Lee, T. H.; Elliott, S. R. *ACS Appl. Mater. Interfaces* **2015**, *7*, 14223–14230.

(40) Loke, D.; Skelton, J. M.; Wang, W. J. et al. *P. Natl. Acad. Sci.* **2014**, *111*, 13272–13277.

(41) Hosseini, P.; Wright, C. D.; Bhaskaran, H. *Nature* **2014**, *511*, 206–211.

(42) Kolobov, A. V.; Tominaga, J., *Chalcogenides Metastability and Phase Change Phenomena*, 1st ed.; Springer Series in Materials Science; Springer: New York, N.Y., U.S.A., 2012.

(43) Krebs, D.; Raoux, S.; Rettner, C. T. et al. *Appl. Phys. Lett.* **2009**, *95*, 082101.

(44) Wong, H. S. P.; Raoux, S.; SangBum, K. et al. *P. IEEE* **2010**, *98*, 2201–2227.

(45) Kim, I. S.; Cho, S. L.; Im, D. H. et al. In *VLSI Technology, 2010 IEEE Symposium on*, 2010, pp 203–204.

(46) Mott, N. In *Nobel Lecture*, 1977, pp 1–11.

(47) Adler, D.; Shur, M. S.; Silver, M.; Ovshinsky, S. R. *J. Appl. Phys.* **1980**, *51*, 3289–3309.

(48) Karpov, V. G.; Kryukov, Y. A.; Savransky, S. D.; Karpov, I. V. *Appl. Phys. Lett.* **2007**, *90*, 1–3.

(49) Bogoslovskiy, N. A.; Tsendin, K. D. *Semiconductors* **2012**, *46*, 559–590.

(50) Waterman, A. T. *Philos. Mag.* **1917**, *33*, 225–247.

(51) Waterman, A. T. *Phys. Rev.* **1923**, *21*, 540–549.

(52) Yamada, N.; Ohno, E.; Akahira, N. et al. *Jpn. J. Appl. Phys.* **1987**, *26*, 61–66.

(53) Lencer, D.; Salinga, M.; Grabowski, B. et al. *Nat. Mater.* **2008**, *7*, 972–977.

(54) Lencer, D.; Salinga, M.; Wuttig, M. *Adv. Mater.* **2011**, *23*, 2030–2058.

(55) Wuttig, M.; Raoux, S. *Z. Anorg. Allg. Chem.* **2012**, *638*, 2455–2465.

(56) Jensen, W. B. *J. Chem. Educ.* **1997**, *74*, 1063.

(57) Kim, J.; Ko, C.; Frenzel, A. et al. *Appl. Phys. Lett.* **2010**, *96*, 213106.

(58) Boyd, D. C.; Danielson, P. S.; Thompson, D. A. et al. In *Kirk-Othmer Encyclopedia of Chemical Technology*, 4th; John Wiley and Sons, Inc.: New York, N.Y., U.S.A., 1998.

(59) Elliott, S. R. In *Materials Science and Technology: A Comprehensive Treatment*. Zarzycki, J., Ed., 1st; VCH Verlagsgesellschaft mbH: Weinheim, Germany, 1991; Chapter 7, pp 375–454.

(60) Tanaka, K. In *Reference Module in Materials Science and Materials Engineering*, 1st; Elsevier: Published Online, 2015.

(61) Raoux, S.; Wuttig, M., *Phase Change Materials: Science and Applications*, 1st ed.; Springer: New York, N.Y., U.S.A., 2010.

(62) Gibbs, J. H.; DiMarzio, E. A. *J. Chem. Phys.* **1958**, *28*, 373–383.

(63) Turnbull, D.; Cohen, M. H. *J. Chem. Phys.* **1970**, *52*, 3038–3041.

(64) Goldstein, M. *J. Chem. Phys.* **1977**, *67*, 2246–2253.

(65) Angell, C. A.; Rao, K. J. *J. Chem. Phys.* **1972**, *57*, 470–481.

(66) Wuttig, M.; Yamada, N. *Nat. Mater.* **2007**, *6*, 824–832.

(67) Turnbull, D. *Contemp. Phys.* **1969**, *10*, 473–488.

(68) Loke, D.; Lee, T. H.; Wang, W. J. et al. *Science* **2012**, *336*, 1566–1569.

(69) Kalb, J. A.; Spaepen, F.; Wuttig, M. *J. Appl. Phys.* **2005**, *98*, 054910.

(70) Lee, T. H.; Elliott, S. R. *Phys. Rev. Lett.* **2011**, *107*, 145702.

(71) Coombs, J. H.; Jongenelis, A. P. J. M.; Vanesspiekman, W.; Jacobs, B. A. J. *J. Appl. Phys.* **1995**, *78*, 4906–4917.

(72) Van Pieterson, L.; Lankhorst, M. H. R.; van Schijndel, M. et al. *J. Appl. Phys.* **2005**, *97*, 083520.

(73) Akola, J.; Jones, O. In *NIC Symposium 2012*, ed. by Binder, K.; Muenster, G.; Kremer, M., John von Neumann Institut für Computing (NIC): 2012; Vol. 45, pp 207–214.

(74) Kolomiets, B. T. *Phys. Status Solidi B* **1964**, *7*, 713–731.

(75) Mott, N. F. *Adv. Phys.* **1967**, *16*, 49–144.

(76) Zachariasen, W. H. *J. Am. Chem. Soc.* **1932**, *54*, 3841–3851.

(77) Anderson, P. W. *Phys. Rev. Lett.* **1975**, *34*, 953–955.

(78) Mott, N.; Davis, E., *Electronic Processes in Non-Crystalline Materials*, 2nd ed.; Oxford University Press: Oxford, U.K., 1979.

(79) Street, R. A.; Mott, N. F. *Phys. Rev. Lett.* **1975**, *35*, 1293–1296.

(80) Kastner, M.; Adler, D.; Fritzsche, H. *Phys. Rev. Lett.* **1976**, *37*, 1504–1507.

(81) Kolobov, A. V.; Fons, P.; Tominaga, J. *Sci. Rep.* **2015**, *5*, 13698.

(82) Robertson, J.; Xiong, K.; Peacock, P. W. *Thin Solid Films* **2007**, *515*, 7538–7541.

(83) Pirovano, A.; Lacaita, A. L.; Benvenuti, A. et al. *IEEE T. Electron. Dev.* **2004**, *51*, 452–459.

(84) Kolobov, A. V. *J. Non-Cryst. Solids* **1996**, *198–200, Part 2*, 728–731.

(85) Edwards, A. H.; Pineda, A. C.; Schultz, P. A. et al. *Phys. Rev. B* **2006**, *73*, 045210.

(86) Phillips, J. C. *J. Non-Cryst. Solids* **1979**, *34*, 153–181.

(87) Paesler, M. A.; Baker, D. A.; Lucovsky, G. et al. *J. Phys. Chem. Solids* **2007**, *68*, 873–877.

(88) Micoulaut, M.; Raty, J. Y.; Otjacques, C.; Bichara, C. *Phys. Rev. B* **2010**, *81*, 174206.

(89) Micoulaut, M. *J. Phys.-Condens. Mat.* **2010**, *22*, 285101.

(90) Jóvári, P.; Kaban, I.; Steiner, J. et al. *Phys. Rev. B* **2008**, *77*, 035202.

(91) Baldé, L.; Legendre, B.; Balkhi, A. *J. Alloy. Compod.* **1995**, *216*, 285–293.

(92) Agarwal, S. C.; Paesler, M. A.; Baker, D. A. et al. *Pramana-J. Phys.* **2008**, *70*, 245–254.

(93) Cheng, H. Y.; Hsu, T. H.; Raoux, S. et al. In *Electron Devices Meeting, 2011. IEEE International*, 2011, pp 3.4.1–3.4.4.

(94) Kooi, B. J.; De Hosson, J. T. M. *J. Appl. Phys.* **2002**, *92*, 3584–3590.

(95) Simpson, R. E. Chalcogenide thin film materials for next generation data storage., Ph.D. Thesis, University of Southampton, 2008.

(96) Wuttig, M.; Lusebrink, D.; Wamwangi, D. et al. *Nat. Mater.* **2007**, *6*, 122–128.

(97) Kolobov, A. V.; Fons, P.; Frenkel, A. I. et al. *Nat. Mater.* **2004**, *3*, 703–708.

(98) Shportko, K.; Kremers, S.; Woda, M. et al. *Nat. Mater.* **2008**, *7*, 653–658.

(99) Lucovsky, G.; White, R. M. *Phys. Rev. B* **1973**, *8*, 660–667.

(100) Littlewood, P. B. *J. Phys. C Solid State* **1979**, *12*, 4459.

(101) Hyot, B.; Biquard, X.; Poupinet, L. In *European/Phase Change and Ovonics Symposium 2001*, 2001.

(102) Andrikopoulos, K. S.; Yannopoulos, S. N.; Kolobov, A. V. et al. *J. Phys. Chem. Solids* **2007**, *68*, 1074–1078.

(103) Hosokawa, S.; Ozaki, T.; Hayashi, K. et al. *Appl. Phys. Lett.* **2007**, *90*, 131913.

(104) Kohara, S.; Kato, K.; Kimura, S. et al. *Appl. Phys. Lett.* **2006**, *89*, 201910.

(105) Akola, J.; Jones, R. O. *Phys. Rev. B* **2009**, *79*, 134118.

(106) Caravati, S.; Bernasconi, M.; Kühne, T. D. et al. *Appl. Phys. Lett.* **2007**, *91*, 171906.

(107) Hegedüs, J.; Elliott, S. R. *Nat. Mater.* **2008**, *7*, 399–405.

(108) Xu, M.; Cheng, Y. Q.; Sheng, H. W.; Ma, E. *Phys. Rev. Lett.* **2009**, *103*, 195502.

(109) Sun, Z.; Pan, Y.; Zhou, J. et al. *Phys. Rev. B* **2011**, *83*, 113201.

(110) Nardone, M.; Simon, M.; Karpov, I. V.; Karpov, V. G. *J. Appl. Phys.* **2012**, *112*, 071101–20.

(111) Chong, T. C.; Shi, L. P.; Zhao, R. et al. *Appl. Phys. Lett.* **2006**, *88*, 122114.

(112) Boniardi, M.; Redaelli, A.; Pirovano, A. et al. *J. Appl. Phys.* **2009**, *105*, 084506.

(113) Ielmini, D.; Lavizzari, S.; Sharma, D.; Lacaita, A. L. *Appl. Phys. Lett.* **2008**, *92*, 193511.

(114) SangBum, K.; Byoungil, L.; Asheghi, M. et al. In *Reliability Physics Symposium, 2010 IEEE International*, 2010, pp 99–103.

(115) Lankhorst, M. H. R.; Ketelaars, B. W. S. M. M.; Wolters, R. A. M. *Nat. Mater.* **2005**, *4*, 347–352.

(116) Horii, H.; Yi, J. H.; Park, J. H. et al. In *VLSl Technology, 2003 IEEE Symposium on*, 2003, pp 177–178.

(117) Privitera, S.; Rimini, E.; Zonca, R. *Appl. Phys. Lett.* **2004**, *85*, 3044–3046.

(118) Privitera, S.; Rimini, E.; Bongiorno, C. et al. *Nucl. Instrum. Meth. B* **2007**, *257*, 352–354.

(119) Wang, W. H.; Loke, D.; Shi, L. P. et al. *Sci. Rep.* **2012**, *2*, 1–6.

(120) Dimitrov, D.; Shieh, H. P. D. *Mat. Sci. Eng. B-Solid* **2004**, *107*, 107–112.

(121) Kölpin, H.; Music, D.; Laptyeva, G. et al. *J. Phys.-Condens. Mat.* **2009**, *21*, 435501.

(122) Sipeng, G.; Lisong, H. In *Advanced Optical Storage Technology, Conference on*, ed. by Xu, D.; Ogawa, S., SPIE: 2002; Vol. 4930, pp 367–371.

(123) Watabe, K.; Polynkin, P.; Mansuripur, M. *Appl. Optics* **2004**, *43*, 4033–4040.

(124) Wang, K.; Wamwangi, D.; Ziegler, S. et al. *J. Appl. Phys.* **2004**, *96*, 5557–5562.

(125) Skelton, J. M.; Pallipurath, A. R.; Lee, T. H.; Elliott, S. R. *Adv. Funct. Mater.* **2014**, *24*, 7291–7300.

(126) Zhou, G. F. *Mat. Sci. Eng. A-Struct* **2001**, *304–306*, 73–80.

(127) Song, K.-H.; Kim, S.-W.; Seo, J.-H.; Lee, H.-Y. *J. Appl. Phys.* **2008**, *104*, 103516.

(128) Hirotsune, A.; Miyauchi, Y.; Terao, M. *Jpn. J. Appl. Phys.* **1995**, *35*, 346.

(129) Qiao, B.; Feng, J.; Lai, Y. et al. *Appl. Surf. Sci.* **2006**, *252*, 8404–8409.

(130) Cai, Y.; Zhou, P.; Lin, Y. et al. *Chinese Phys. Lett.* **2007**, *24*, 781.

(131) Kojima, R.; Yamada, N. *Jpn. J. Appl. Phys.* **2001**, *40*, 5930.

(132) Huang, Y. J.; Tsai, M. C.; Wang, C. H.; Hsieh, T. E. *Thin Solid Films* **2012**, *520*, 3692–3696.

(133) Guoxiang, W.; Xiang, S.; Qiuhua, N. et al. *J. Phys. D Appl. Phys.* **2012**, *45*, 375302.

(134) Raoux, S.; Salinga, M.; Jordan-Sweet, J. L.; Kellock, A. *J. Appl. Phys.* **2007**, *101*, 044909.

(135) Seung Wook, R.; Ho-Ki, L.; Jong Ho, L. et al. *Nanotechnology* **2011**, *22*, 254005.

(136) Shin, H. J.; Kang, Y. S.; Benayad, A. et al. *Appl. Phys. Lett.* **2008**, *93*, 021905–3.

(137) Hirota, K.; Ohbayashi, G. *Jpn. J. Appl. Phys.* **1998**, *37*, 1847–1851.

(138) Kojima, R.; Okabayashi, S.; Kashihara, T. et al. *Jpn. J. Appl. Phys.* **1998**, *37*, 2098.

(139) Jeong, T. H.; Kim, M. R.; Seo, H. et al. *Jpn. J. Appl. Phys. 1* **2000**, *39*, 2775.

(140) Seo, H.; Jeong, T. H.; Park, J. W. et al. *Jpn. J. Appl. Phys. 1* **2000**, *39*, 745–751.

(141) Kim, Y.; Hwang, U.; Cho, Y. J. et al. *Appl. Phys. Lett.* **2007**, *90*, 021908.

(142) Kim, K.-H.; Park, J.-C.; Chung, J.-G. et al. *Appl. Phys. Lett.* **2006**, *89*, 243520.

(143) Caravati, S.; Colleoni, D.; Mazzarello, R. et al. *J. Phys.-Condens. Mat.* **2011**, *23*, 265801.

(144) Lee, T. H.; Loke, D.; Elliott, S. R. *Adv. Mater.* **2015**, *27*, 5477–5483.

(145) Shelby, R. M.; Raoux, S. *J. Appl. Phys.* **2009**, *105*, 104902.

(146) Lai, Y.; Qiao, B.; Feng, J. et al. *J. Electron. Mater.* **2005**, *34*, 176–181.

(147) Lankhorst, M. H. R. *J. Non-Cryst. Solids* **2002**, *297*, 210–219.

(148) Barton, R. W.; Davis, C. R.; Rubin, K. A.; Lim, G. *Appl. Phys. Lett.* **1986**, *48*, 1255–1257.

(149) Mikla, V. I.; Mikhalko, I. P.; Mikla, V. V. *Mater. Sci. Eng. B-Adv.* **2001**, *83*, 74–78.

(150) Yoon, S.-M.; Lee, N.-Y.; Ryu, S.-O. et al. *IEEE Electr. Device L.* **2006**, *27*, 445–447.

(151) Wakkad, M. M.; Shokr, E. K.; Abd El Ghani, H. A.; Awad, M. A. *J. Phys. D Appl. Phys.* **2007**, *40*, 7572.

(152) Kumar, P.; Sathiaraj, T. S.; Thangaraj, R. *Phil. Mag. Lett.* **2010**, *90*, 183–192.

(153) Al-Agel, F. A. *Opt. Laser Technol.* **2013**, *54*, 208–213.

(154) Al-Agel, F. A.; Al-Arfaj, E. A.; Al-Marzouki, F. M. et al. *Mat. Sci. Semicon. Proc.* **2013**, *16*, 884–892.

(155) Lee, H. K.; Kang, D.-H.; Tran, L. *Mater. Sci. Eng. B-Adv.* **2005**, *119*, 196–201.

(156) Yu, B.-G.; Ju, S.; Sun, X. et al. *Appl. Phys. Lett.* **2007**, *91*, 133119.

(157) Loireau-Lozac'h, A.-M.; Guittard, M.; Flahaut, J. *Mater. Res. Bull.* **1976**, *11*, 1489–1496.

(158) Mairaj, A. Optical waveguides and lasers in improved gallium lanthanum sulphide glass., Ph.D. Thesis, University of Southampton, 2003.

(159) West, Y. D.; Schweizer, T.; Brady, D. J.; Hewak, D. W. *Fiber Integrated Opt.* **2000**, *19*, 229–250.

(160) Li, R. H.; Furniss, D.; Bagshaw, H.; Seddon, A. B. *J. Mater. Res.* **1999**, *14*, 2621–2627.

(161) Sámson, Z. L.; MacDonald, K. F.; De Angelis, F. et al. *Appl. Phys. Lett.* **2010**, *96*, 143105.

(162) Benazeth, S.; Tuilier, M. H.; Loireau-Lozac'h, A. M. et al. *J. Non-Cryst. Solids* **1989**, *110*, 89–100.

(163) Gholipour, B. Novel Chalcogenide Optoelectronic and Nanophotonic Information Storage and Processing Devices., Ph.D. Thesis, University of Southampton, 2012.

(164) Kumta, P. N.; Risbud, S. H. *J. Mater. Sci.* **1994**, *29*, 1135–1158.

(165) Takebe, H.; Brady, D. J.; Hewak, D. W.; Morinaga, K. *J. Non-Cryst. Solids* **1999**, *258*, 239–243.

(166) Simpson, R. E.; Mairaj, A.; Huang, C. C. et al. *Electron. Lett.* **2007**, *43*, 830–831.

(167) Curtarolo, S.; Hart, G. L. W.; Nardelli, M. B. et al. *Nat. Mater.* **2013**, *12*, 191–201.

(168) Hegedüs, J.; Elliott, S. R. *Phys. Status Solidi A* **2010**, *207*, 510–515.

(169) Skelton, J. M.; Lee, T. H.; Elliott, S. R. *Appl. Phys. Lett.* **2012**, *101*, 024106.

(170) Skelton, J. M.; Elliott, S. R. *J. Phys.-Condens. Mat.* **2013**, *25*, 205801.

(171) Kalyva, M.; Orava, J.; Siokou, A. et al. *Adv. Funct. Mater.* **2012**, *23*, 2052–2059.

(172) Bartlett, P. N.; Benjamin, S. L.; de Groot, C. H. et al. *Mater. Horiz.* **2015**, *2*, 420–426.

(173) Milliron, D. J.; Raoux, S.; Shelby, R. M.; Jordan-Sweet, J. L. *Nat. Mater.* **2007**, *6*, 352–356.

(174) Ritala, M.; Pore, V.; Hatanpää, T. et al. *Microelectron. Eng.* **2009**, *86*, 1946–1949.

(175) Hanak, J. J. *J. Mater. Sci.* **1970**, *5*, 964–971.

(176) Persidis, A. *Nat. Biotech.* **1998**, *16*, 691–693.

(177) Cawse, J. N. *Accounts Chem. Res.* **2001**, *34*, 213–221.

(178) Xiang, X. D.; Sun, X.; Briceño, G. et al. *Science* **1995**, *268*, 1738–1740.

(179) Wang, J.; Yoo, Y.; Gao, C. et al. *Science* **1998**, *279*, 1712–1714.

(180) Xiang, X. D. *Biotechnol. Bioeng.* **1999**, *61*, 227–241.

(181) Danielson, E.; Golden, J. H.; McFarland, E. W. et al. *Nature* **1997**, *389*, 944–948.

(182) Ramberg, C.; Wang, Y.; Fan, Q. et al. *Mat. Res. Soc. Symp. Proc.* **2004**, *803*, 1–6.

(183) Kyrsta, S.; Cremer, R.; Neuschutz, D. et al. *Thin Solid Films* **2001**, *398 - 399*, 379–384.

(184) Laurenzis, M.; Heinrici, A.; Bolivar, P. H. et al. *IEE P.-Sci. Meas. Tech.* **2004**, *151*, 394–397.

(185) Guerin, S.; Hayden, B. E.; Lee, C. E. et al. *J. Comb. Chem.* **2004**, *6*, 149–158.

(186) David, A.; Guerin, S.; Hayden, B. E. et al. *Cryst. Growth Des.* **2013**.

(187) Saleh-Subaie, J. Electrochemistry and Electrocatalysis of Metallic Carbide Thin Films., M.Sc. Thesis, University of Southampton, 2011.

(188) Noble, R. M. High Throughput Synthesis and Screening of Photovoltaic Materials., Ph.D. Thesis, University of Southampton, 2011.

(189) Simpson, R. E.; Hewak, D. W.; Guerin, S. et al. In *European/Phase Change and Ovonics Symposium 2005*, 2005.

(190) Guerin, S.; Hayden, B. E.; Hewak, D. W.; Vian, C. *ACS Comb. Sci.* **2017**, *19*, 478–491.

(191) Gourvest, E.; Pelissier, B.; Vallée, C. et al. *J. Electrochem. Soc.* **2012**, *159*, H373–H377.

(192) Suryanarayana, C.; Norton, M., *X-Ray Diffraction: A Practical Approach*, 1st ed.; Springer: New York, N.Y., U.S.A., 2013.

(193) Van der Pauw, L. J. *Philips Tech. Rev.* **1958**, *20*, 220–224.

(194) Schroder, D., *Semiconductor Material and Device Characterization*, 3rd ed.; John Wiley and Sons Ltd.: Hoboken, N.J., U.S.A., 2006.

(195) Lee, B.-S.; Abelson, J. R.; Bishop, S. G. et al. *J. Appl. Phys.* **2005**, *97*, 093509.

(196) Kalb, J. A.; Wen, C. Y.; Spaepen, F. et al. *J. Appl. Phys.* **2005**, *98*, 054902.

(197) Konstantinov, P. P.; Shelimova, L. E.; Avilov, E. S. et al. *Inorg. Mater.* **2001**, *37*, 662–668.

(198) Sittner, E.-R.; Siegert, K. S.; Jost, P. et al. *Phys. Status Solidi A* **2013**, *210*, 147–152.

(199) Navarro, G.; Sousa, V.; Persico, A. et al. *Solid State Electron.* **2013**, *89*, 93–100.

(200) Luckas, J.; Olk, A.; Jost, P. et al. *Appl. Phys. Lett.* **2014**, *105*, 092108.

(201) Suhrmann, R.; Berndt, W. *Z. Physik* **1940**, *115*, 17–46.

(202) Fujimori, S.; Yagi, S.; Yamazaki, H.; Funakoshi, N. *J. Appl. Phys.* **1988**, *64*, 1000–1004.

(203) Lannin, J. S. *AIP Conf. Proc.* **1976**, *31*, 123–129.

(204) Pine, A. S.; Dresselhaus, G. *Phys. Rev. B* **1971**, *4*, 356–371.

(205) Nemec, P.; Nazabal, V.; Moreac, A. et al. *Mater. Chem. Phys.* **2012**, *136*, 935–941.

(206) Carria, E.; Mio, A. M.; Miritello, M. et al. *Electrochem. Solid St.* **2010**, *13*, H317–H320.

(207) Carria, E.; Mio, A. M.; Gibilisco, S. et al. *J. Electrochem. Soc.* **2011**, *159*, H130–H139.

(208) Resch-Esser, U.; Frotscher, U.; Esser, N. et al. *Surf. Sci.* **1994**, *307–309, Part A*, 597–602.

(209) Andrikopoulos, K. S.; Yannopoulos, S. N.; Voyiatzis, G. A. et al. *J. Phys.-Condens. Mat.* **2006**, *18*, 965–979.

(210) Sosso, G. C.; Caravati, S.; Bernasconi, M. *J. Phys.-Condens. Mat.* **2009**, *21*, 095410.

(211) Sosso, G. C.; Caravati, S.; Mazzarello, R.; Bernasconi, M. *Phys. Rev. B* **2011**, *83*, 134201.

(212) Först, M.; Dekorsy, T.; Trappe, C. et al. *Appl. Phys. Lett.* **2000**, *77*, 1964–1966.

(213) De Bastiani, R.; Piro, A. M.; Grimaldi, M. G. et al. *Appl. Phys. Lett.* **2008**, *92*, 241925.

(214) Baker, D. A.; Paesler, M. A.; Lucovsky, G. et al. *Phys. Rev. Lett.* **2006**, *96*, 255501.

(215) Petit, L.; Carlie, N.; Adamietz, F. et al. *Mater. Chem. Phys.* **2006**, *97*, 64–70.

(216) Daszykowski, M.; Serneels, S.; Kaczmarek, K. et al. *Chemometr. Intell. Lab.* **2007**, *85*, 269–277.

(217) Jaumot, J.; Gargallo, R.; de Juan, A.; Tauler, R. *Chemometr. Intell. Lab.* **2005**, *76*, 101–110.

(218) Wang, X.; Kunc, K.; Loa, I. et al. *Phys. Rev. B* **2006**, *74*, 134305.

(219) Richter, W.; Becker, C. R. *Phys. Status Solidi B* **1977**, *84*, 619–628.

(220) Liu, B.; Song, Z.-T.; Zhang, T. et al. *Chinese Phys.* **2004**, *13*, 1947.

(221) Vinod, E. M.; Ramesh, K.; Sangunni, K. S. *Sci. Rep.* **2015**, *5*, 8050.

(222) Bermejo, D.; Cardona, M. *J. Non-Cryst. Solids* **1979**, *32*, 405–419.

(223) Germain, P.; Zellama, K.; Squelard, S. et al. *J. Appl. Phys.* **1979**, *50*, 6986–6994.

(224) Golovchak, R.; Choi, Y. G.; Kozyukhin, S. et al. *Appl. Surf. Sci.* **2015**, *332*, 533–541.

(225) Dieker, H.; Wuttig, M. *Thin Solid Films* **2005**, *478*, 248–251.

(226) Dahshan, A. *J. Non-Cryst. Solids* **2008**, *354*, 3034–3039.

(227) Morales-Sánchez, E.; Lain, B.; Prokhorov, E. et al. *Vacuum* **2010**, *84*, 877–881.

(228) Morales-Sánchez, E.; Prokhorov, E.; J., G.-H.; A., M.-G. *Thin Solid Films* **2005**, *471*, 243–247.

(229) Czubatyj, W.; Hudgens, S. J.; Dennison, C. et al. *IEEE Electr. Device L.* **2010**, *31*, 869–871.

(230) Lu, Y.; Zhang, Z.; Song, S. A. et al. *Appl. Phys. Lett.* **2013**, *102*, 241907.

(231) Song, S. A.; Yao, D.; Song, Z. T. et al. *Nanoscale Res. Lett.* **2015**, *10*, 1–5.

(232) Cabral, C.; Krusin-Elbaum, L.; Bruley, J. et al. *Appl. Phys. Lett.* **2008**, *93*, 071906.

(233) Raoux, S.; Muñoz, B.; Cheng, H.-Y.; Jordan-Sweet, J. L. *Appl. Phys. Lett.* **2009**, *95*, 143118.

(234) Friedrich, I.; Weidenhof, V.; Njoroge, W. et al. *J. Appl. Phys.* **2000**, *87*, 4130–4134.

(235) Das, V. D.; Soundararajan, N. *J. Appl. Phys.* **1989**, *65*, 2332–2341.

(236) Cheng, L.; Wu, L.; Song, Z. T. et al. *J. Appl. Phys.* **2013**, *113*, 044514.

(237) Cheng, L.; Wu, L.; Song, Z. T. et al. *Mater. Lett.* **2012**, *71*, 98–100.

(238) Osiac, M.; Tiron, V.; Iacobescu, G. E. In *Phenomena in Ionised Gases, XXXII International Conference on*, 2015.

(239) Kim, H. K.; Lee, S. Y.; Choi, D. J. *J. Korean Phys. Soc.* **2009**, *55*, 1896–1900.

(240) Hayden, B.; Lee, C.; Smith, D. et al. Vapour deposition process for the preparation of a chemical compound., US 9,067,790 B2, Patent, 2015.

(241) Jung, M.-C.; Lee, Y. M.; Kim, H.-D. et al. *Appl. Phys. Lett.* **2007**, *91*, 083514.

(242) Raoux, S.; Jordan-Sweet, J. L.; Kellock, A. J. *J. Appl. Phys.* **2008**, *103*, 114310.

(243) Zhu, M.; Wu, L.; Rao, F. et al. *J. Alloy. Compd.* **2011**, *509*, 10105–10109.

(244) Kim, K.-H.; Park, J.-C.; Lee, J.-H. et al. *Jpn. J. Appl. Phys.* **2010**, *49*, 101201.

(245) Kim, M. S.; Cho, S. H.; Hong, S. K. et al. *Ceram. Int.* **2008**, *34*, 1043–1046.

(246) Liu, B.; Song, Z. T.; Zhang, T. et al. *Thin Solid Films* **2005**, *478*, 49–55.

(247) Chivers, T., *A Guide to Chalcogen-Nitrogen Chemistry*, 1st ed.; World Scientific Publishing: Singapore, Singapore, 2005.

(248) Speight, J., *Lange's Handbook of Chemistry*, 16th ed.; McGraw-Hill Education: New York, N.Y., U.S.A., 2005.

(249) Cottrell, T., *The Strengths of Chemical Bonds*, 1st ed.; Butterworths Publications: London, U.K., 1958.

(250) Kim, Y.; Jeong, K.; Cho, M.-H. et al. *Appl. Phys. Lett.* **2007**, *90*, 171920.

(251) Yin, Y.; Sone, H.; Hosaka, S. *J. Appl. Phys.* **2007**, *102*, 064503.

(252) Steigmeier, E. F.; Harbeke, G. *Solid State Commun.* **1970**, *8*, 1275–1279.

(253) Deb, S. K.; Dong, J.; Hubert, H. et al. *Solid State Commun.* **2000**, *114*, 137–142.

(254) Soignard, E.; McMillan, P. F. *Chem. Mater.* **2004**, *16*, 3533–3542.

(255) Jeong, T. H.; Kim, M. R.; Seo, H. et al. *J. Appl. Phys.* **1999**, *86*, 774–778.

(256) Jang, M. H.; Park, S. J.; Lim, D. H. et al. *Appl. Phys. Lett.* **2009**, *95*, 012102.

(257) Raoux, S.; Burr, G. W.; Breitwisch, M. J. et al. *IBM J. Res. Dev.* **2008**, *52*, 465–479.

(258) Burr, G. W.; Breitwisch, M. J.; Franceschini, M. et al. *J. Vac. Sci. Technol. B* **2010**, *28*, 223–262.

(259) Kado, H.; Tohda, T. *Appl. Phys. Lett.* **1995**, *66*, 2961–2962.

(260) Bae, B.-J.; Hong, S.-H.; Hwang, S.-Y. et al. *Semicond. Sci. Tech.* **2009**, *24*, 075016.

(261) Hong, S.-H.; Bae, B.-J.; Lee, H. *Nanotechnology* **2010**, *21*, 025703.

(262) Yang, F.; Xu, L.; Fang, L. et al. *Appl. Phys. A* **2013**, *112*, 663–667.

(263) Pandian, R.; Kooi, B. J.; Palasantzas, G. et al. *Adv. Mater.* **2007**, *19*, 4431–4437.

(264) Bhaskaran, H.; Sebastian, A.; Despont, M. *IEEE T. Nanotechnol.* **2009**, *8*, 128–131.

(265) Bhaskaran, H.; Sebastian, A.; Drechsler, U.; Despont, M. *Nanotechnology* **2009**, *20*, 105701.

(266) Wright, C. D.; Hosseini, P.; Vazquez Diosdado, J. A. *Adv. Funct. Mater.* **2013**, *23*, 2248–2254.

(267) Shen, L.; Kong, J., *Applied Electromagnetism*, 3rd ed.; CL Engineering: Boston, Massachusetts, U.S.A., 1995.

(268) Bruns, G.; Merkelbach, P.; Schlockermann, C. et al. *Appl. Phys. Lett.* **2009**, *95*, 043108.

(269) Miao, X. S.; Shi, L. P.; Lee, H. K. et al. *Jpn. J. Appl. Phys.* **2006**, *45*, 3955.

(270) Frenkel, J. *Phys. Rev.* **1938**, *54*, 647–648.

(271) Xu, L.; Tong, L.; Geng, L. et al. *J. Appl. Phys.* **2011**, *110*, 013703.

(272) Prokhorov, E.; Gervacio-Arciniega, J. J.; Luna-Bárcenas, G. et al. *J. Appl. Phys.* **2013**, *113*, 113705.

(273) Savransky, S. D.; Prokhorov, E. F. *Mater. Res. Soc. Symp. Proc.* **2006**, *918*, 0918-H07-06-G08-06.

(274) Karpov, I.; Savransky, S.; Karpov, V. In *Non-Volatile Semiconductor Memory Workshop, 2007 22nd IEEE*, 2007, pp 56–57.

(275) Liu, B.; Song, Z. T.; Feng, S. L.; Chen, B. *Microelectron. Eng.* **2005**, *82*, 168–174.

(276) Raoux, S.; Cabrera, D.; Devasia, A. et al. In *European/Phase Change and Ovonics Symposium 2011*, 2011.

(277) Shin, D.-H.; Song, M.-J.; Kim, J.-W. et al. *Jpn. J. Appl. Phys.* **2014**, *53*, 031402.

(278) Lee, S. Y.; Cho, S. H.; Kim, H. K.; Oh, J. H. *J. Ceram. Process. Res.* **2009**, *10*, 433–436.

(279) Fantini, A.; Sousa, V.; Perniola, L. et al. In *Electron Devices Meeting (IEDM), 2010 IEEE International*, 2010, pp 29.1.1–29.1.4.

(280) Navarro, G.; Souiki, S.; Persico, A. et al. *Microelectron. Reliab.* **2012**, *52*, 1928–1931.

(281) Wright, C. D.; Liu, Y.; Kohary, K. I. et al. *Adv. Mater.* **2011**, *23*, 3408–3413.

(282) Lee, T. H.; Loke, D.; Huang, K. J. et al. *Adv. Mater.* **2014**, *26*, 7493–7498.

(283) Keysight Technologies Scanning Microwave Microscopy Solutions for Quantitative Semiconductor Device Characterization. Application Note., `http://literature.cdn.keysight.com/litweb/pdf/5992-1659EN.pdf` (accessed 2016).

(284) Vazquez-Mena, O.; Villanueva, L. G.; Savu, V. et al. *Nanotechnology* **2009**, *20*, 415303.

(285) Feynman, R. *Engineering and Science* **1960**, *23*, 22–36.

(286) Madou, M., *Fundamentals of Microfabrication: The Science of Miniaturization*, 1st ed.; CRC press: Boca Raton, Florida, U.S., 2002.